Quantitative imaging of plasmid DNA in human airway epithelial cells following non-viral gene transfer

Charanjit Singh

Department of Gene Therapy

National Heart and Lung Institute

Imperial College London

PhD

2013

Abstract

The UK CF Gene Therapy Consortium is interested in non-viral gene therapy for cystic fibrosis (CF). To provide insight into the intracellular bottlenecks plasmid DNA (pDNA) encounters on its way to the nuclei of airway epithelial cells, I sought to quantitatively describe the intracellular fate of non-virally transferred pDNA using a clinically relevant human airway epithelial cell air-liquid-interface (ALI) model. Plasmid DNA was tagged with nanogold particles or fluorescent quantum dots (QDots) for use in transmission electron microscopy (TEM) or confocal microscopy studies, respectively. Conjugation of pDNA with either nanogold or QDots did not affect the biological activity. The number of cells showing cytoplasmicaly-localised nanogold-conjugated pDNA increased with increasing transfection time. Interestingly, there was an equal distribution of pDNA in cytoplasm and nuclei of cells transfected for 60 minutes. In the parallel confocal study, QDot-pDNA was visible in nuclei (~12 μm below the apical surface) after transfection for only 15 minutes, consistent with our earlier observations. Approximately 8% (n= 349 nuclei from 9 independent ALIs) of nuclei contained QDot-pDNA in ALIs transfected for 15 minutes. I next collected *z*-stacks of QDot-pDNA-transfected ALIs every 10 minutes up to a maximum of 120 minutes. As expected, some QDot-pDNA remained on the apical surface throughout the transfection period. Importantly, by 60 minutes, there was a time-dependent net movement of the QDot-fluorescence downwards through the epithelium with the number of nuclei containing QDot-pDNA increasing as early as 30 minutes reaching maximum levels of 8.2±4.8% (n=256 nuclei from 7 ALIs). In conclusion, the results from the TEM and confocal studies showed good agreement for the numbers of nuclei containing pDNA at early transfection times (15, 30 and 60 minutes). These data, in a clinically relevant model, should help focus efforts on increasing gene transfer efficiency by finding the strategies to overcome cytoplasmic and nuclear barriers.

Declaration of Originality

I hereby declare that the work presented in this thesis is my own. Work undertaken by others and described in this thesis is appropriately referenced.

Copyright Declaration

Acknowledgements

I would like to thank Professor Eric Alton for giving me the opportunity to carry out a PhD at the Department of Gene Therapy, Imperial College London. Especially, I would like to thank him and Drs Stephen Smith and Felix Munkonge for the commitment and excellent supervision I have received throughout my PhD.

I would also like to thank my colleagues, both at the Department of Gene Therapy, Imperial College London, and in the UK Cystic Fibrosis Gene Therapy Consortium. Especially, I am grateful to Drs Uta Griesenbach and Marguerite Wasowicz, for their invaluable technical, theoretical, constructive criticism and moral support.

Special thanks to Ms Ann Dewar, Dr Andy Rogers, Dr Raffa Carzaniga and Dr Tillmann Pape for assisting with the electron transmission microscope and associated laboratory techniques.

Finally, but definitely not least, I would like to thank my wife Parmjit, and children, Kirandeep and Sandeep, who provided much-needed support and made many valuable comments.

Dedicated to my Parents

Abbreviations

2-D	2-dimensional
3-D	3-dimensional
A	Adenine
AAV	Adeno-associated viruses
ABC	Adenosine triphosphate (ATP)-binding cassette
AC	Artificial chromosome
AdV	Adenoviruses
AEAA	L = *N*-(2-aminoethyl) aspartic acid
AMP	Adenosine monophosphate
ANOVA	One-way analysis of variance
ASL	Airway surface liquid
ATP	Adenosine triphosphate
AuNPs	Gold nanoparticles
BAC	Bacterial artificial chromosome
BFP	Blue fluorescent proteins
BHK	Baby hamster kidney
BrdU	5-bromo-2'-deoxyuridine
c	Cysteine
Caco-2	Colon adenocarcinoma
cAMP	Cyclic adenosine mono phosphate
CCD	Charge-coupled device
CdSe	Cadmium selenide
CF	Cystic fibrosis
CFP	Cyan fluorescent proteins
CFTR	CF transmembrane conductance regulator
CFTR cDNA	*CFTR* complementary DNA
CHO	Chinese hamster ovary -K1
CLSM	Confocal laser scanning microscopy
CMV	Cytomegalovirus
CO_2	Carbon dioxide
COS-1	SV40-transfected kidney fibroblast
COS-7	African Green Monkey SV40-transfected kidney fibroblast cell line
CpG	Cytosine/guanine dinucleotides
CTT	Cytosine/thymidine/thymidine
DAPI 4',6'	Diamidino-2-phenylindole
DC-Chol	3β[N-(N,N-dimethylamminoethane)-carbamoyl] cholesterol
ΔF508	Deletion of a phenylalanine residue at position 508
DMEM	Dulbecco's modified Eagle's medium
DMPE	Dimyristoylphosphatidylethanol-amine
DMRIE	N-(2-hydroxyethyl)-N,N-dimethyl-2,3-bis(tetra-decyloxy)-1-propanaminium bromide
DODAB	Dimethyldioctadecyl-ammonium bromide
DOPE	Dioleoyl phosphatidyl-ethanolamine
DOTAP	N-[1-(2,3-dioleoyloxy)propyl]-N,N,N-trimethylammonium chloride
DOTMA	N-[1-(2,3-dioleyloxy)propyl]-N,N,N-trimethylammonium chloride
ε	Molar extinction coefficient in $M^{-1}cm^{-1}$

EDTA	Ethylenediaminetetraacetic acid
EF1α	Elongation factor 1 alpha
EGTA	Ethyleneglycol-bis-(β-aminoethyl ether)-N,N-tetraacetic acid
ENaC	Epithelial sodium channel
FABP	Fatty acid binding protein
FBS	Foetal bovine serum
Fluc	*Firefly* luciferase reporter gene
G	Guanine
GCVs	Genomic context vectors
GFP	Green fluorescent proteins
GL67A	Genzyme lipid 67A
Gluc	*Gaussia* luciferase reporter gene
GMP	Good manufacturing practice
GTAs	Gene transfer agents
GTP	Guanosine triphosphate
hCEFI	Human CMV enhancer and the elongation factor 1α promoter
HEK	Human embryonic kidney
IL-8	Interleukin-8
J	Psuedocytosine
K-S	Kolmogorov–Smirnov
kb	Kilo base
MAP	Microtubule associated proteins
MCF7	Human breast carcinoma
MEA	Mercaptoethylamine hydrochloride
mRNA	Messenger RNA
MSD	Membrane spanning domain
NaCl	Sodium chloride
NBD	Nucleotide binding domain
NBF	Nucleotide binding fold
NBF1	First NBD
NHBE	Normal human bronchial epithelial
NLSs	Nuclear localisation signals
NPC	Nuclear pore complex
NPD	Nasal potential difference
ODNs	Oligodeoxynucleotides
PBS	Phosphate buffered saline
pCIKCFTR	CFTR plasmid
pCIKFluc	*Firefly* luciferase reporter plasmid
pCIKGluc	*Gaussia* luciferase reporter plasmid
PD	Potential difference
PEG	Polyethylene glycol
PEI	Polyethylenimine
PFC	Perfluorocarbon
pGM169	CpG-free *CFTR* expression plasmid
PNA	Peptide nucleic acid
PTFE	Polytetrafluoroethylene
QDot	Quantum dot
QDot-pDNA	Quantum dot-conjugated plasmid DNA
R domain	Regulatory domain
RFP	Red fluorescent proteins

RLU	Relative light units
rpm	Revolutions per minute
SDCM	Spinning disk confocal laser microscopy
SeV	Sendai viruses
T	Thymine
TCEP	Tris (2-carboxyethyl) phosphinehydocloride
TEM	Transmission electron microscopy
TNF-alpha	Tumour necrosis factor-alpha
UbC	Ubiquitin C
UKCFGTC	UK CF Gene Therapy Consortium
UNC	University of North Carolina
UV	Ultraviolet
w:w	weight:weight
WFI	Water for injection
YAC	Yeast artificial chromosome
YFP	Yellow fluorescent proteins
ZnS	Zinc sulphide

List of figures

List of tables

Chapter 1: Introduction

1.1 Overview of cystic fibrosis disease

The inherited autosomal recessive gene disorder cystic fibrosis (CF), common among Caucasians, affects approximately 1 in 2500 newborns and there are currently around 70,000 people affected worldwide [1]. The expected average life of CF patients is approximately 37 years [2]. CF is a monogenic disease and is caused by a mutation in the CF transmembrane conductance regulator (*CFTR*) gene. The gene responsible for CF encodes CFTR protein which is a cyclic adenosine mono phosphate (cAMP)-regulated chloride channel responsible for transport of chloride ions across airway epithelial cells [3-5]. Although several organs are affected (e.g. gut, pancreas, liver, reproductive organs) by the mutation of the *CFTR* gene, morbidity and mortality in CF disease is mainly related to the progressive lung disease [6]. The faulty CFTR protein causes abnormal water and ion transport across the airway epithelial cells. This results in depletion of the periciliary fluid layer called airway surface liquid (ASL) covering the airway epithelia and in turn affects the clearance of mucus [7;8]. Consequently, any inhaled bacteria trapped in the dehydrated thick mucus are not cleared properly leading to chronic infections with consequent inflammation, bronchiectasis and eventual respiratory failure [9]. Even though, there is no effective cure for CF, numerous treatments such as antibiotics, steroids, mucolytics, enzyme replacement and physiotherapy have now been developed to improve the quality of life of CF individuals [10]. However none of these treatments addresses the underlying causative molecular defect. As CF is caused by a single gene defect, augmentation with a correct copy by gene therapy provides the best potential approach to ameliorate CF disease.

1.2 The CF gene

In 1985, polymorphic DNA markers genetically linked to CF gene were identified and found to be located on chromosome 7 [3;11]. Four years later in 1989, the CF gene was cloned and characterised. It contains 27 exons and spans approximately 250 kilo base (kb) pairs on the long arm of chromosome 7 at q31.2 [4;5]. The *CFTR* gene expresses CFTR protein on the apical cell membrane of epithelial cells lining the organs of digestive, reproductive and respiratory systems and is also expressed in the ducts of sweat, submucosal and salivary glands [12;13]. A member of the adenosine triphosphate (ATP)-binding cassette (ABC) super-family, CFTR acts as a chloride channel, transporting chloride ions across the cell membrane. Additionally, CFTR chloride channel also plays an important role in many other regulatory functions including the regulation of sodium ions via the epithelial sodium channel (ENaC) located on the epithelial cell apical surface membranes [14].

A multi-domain glycoprotein comprising 1485 amino acids and 180 kDa in size, the CFTR protein consists of two repeated motifs (Figure 1). Each motif consists of a membrane spanning domain (MSD) and a nucleotide binding fold (NBF). Each MSD consists of six transmembrane segments which are hydrophobic and arranged in such a way to form a channel across the epithelial cell apical surface membrane. While both MSDs are located on the apical surface membrane, the NBFs present in the cytoplasm bind and hydrolyse ATP. Both motifs are joined via an intracellular regulatory (R) domain that contains many phosphorylation sites, necessary for the activation of CFTR channel together with NBFs [15].

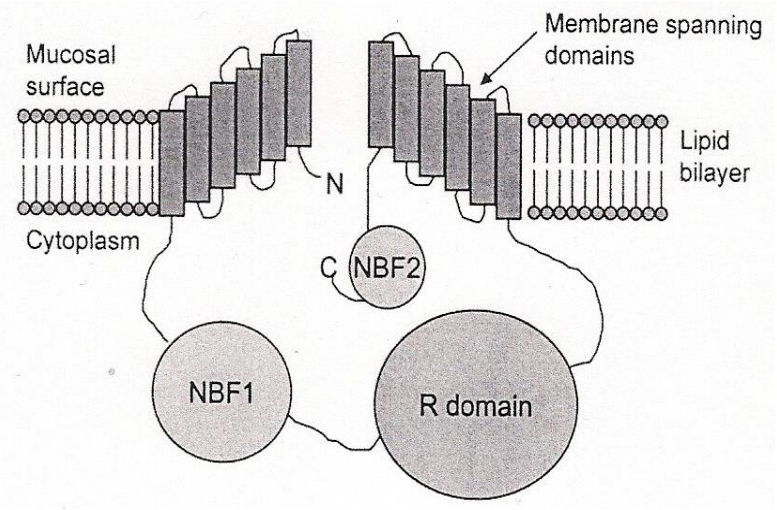

Figure 1: Schematic diagram illustrating the predicted structure of cystic fibrosis transmembrane conductance regulator protein

The cystic fibrosis transmembrane conductance regulator (CFTR) protein consists of two repeated motifs which are joined together via an intracellular regulatory domain (R domain). Each motif contains a membrane spanning domain and a nucleotide binding fold (NBF).
C: C-terminus; N: N-terminus. Adapted from Alton *et al* [16].

1.3 CFTR gene mutations

To date, more than 1800 mutations of CFTR have been identified either within the exons or at the boundaries of the introns and exons (http://www.genet.sickkids.on.ca/Home.html). There are five classes of CFTR mutations depending on their effect on the CFTR protein. These mutations are shown in Figure 2 and classified as:

Class I mutations are nonsense, frame shift and splice site mutations that result in the formation of premature termination codons, thus producing truncated defective CFTR protein.

Class II mutations are missense mutations that hinder the correct post-translational processing of the codon in the endoplasmic reticulum as a result of which abnormal CFTR protein is made. The abnormal CFTR protein is retained in the endoplasmic reticulum and is degraded. The most common example of this type of mutation is the ΔF508 mutation.

Class III mutations, for example G551D, are missense mutation that results in substitution of an amino acid leading to the expression of protein that reach the apical surface but the activity of the channel is not regulated normally.

Class IV mutations are similar to class III, but occur in the MSDs; as a result conductance of chloride ions through CFTR channel is reduced.

Class V, the last type of mutation is due to splicing or point mutations in the promoter sequence that affect the correct transcription or translation thus results in reduced amount of functional protein [17].

The most common mutation ΔF508 (deletion of a phenylalanine residue at position 508), accounts for approximately 70% of all CF alleles worldwide, with the highest frequency among Caucasian population. ΔF508 occurs in the first NBD (NBF1) in the CFTR protein due to loss of a cytosine/thymidine/thymidine (CTT) nucleotide triplet in exon 10. As a result the mutated protein is abnormally folded and therefore retained and degraded in the endoplasmic reticulum.

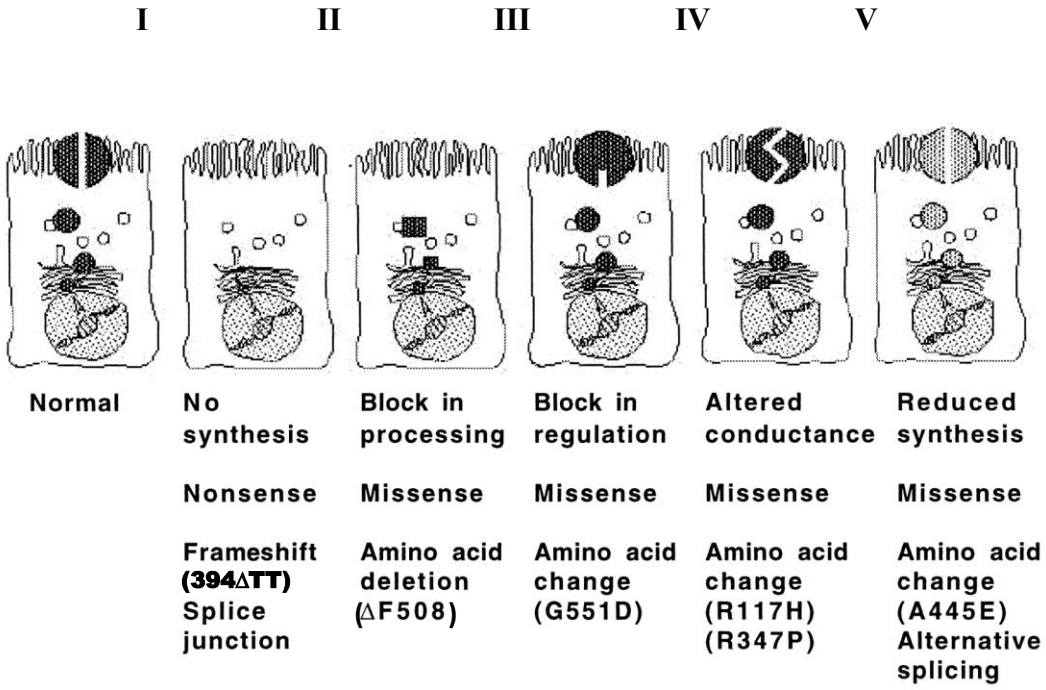

Figure 2: Schematic diagram illustrating the cystic fibrosis transmembrane conductance regulator mutations

The five classes (I-V) of mutations and their effect on protein production. Adapted from Pier *et al* [18].

1.4 Expression of CFTR protein in human airways

As mentioned above, death from CF is primarily caused by airway disease. The human respiratory tract consists of conducting large and small airways leading to lung parenchyma where the exchange of gases takes place in the alveoli. The large airways, lined with a pseudostratified epithelium, consist of a mixed population of ciliated and non-ciliated columnar cells (goblet or mucous cells, serous cells and basal cells). The small or distal airway consists of a single layer of cuboidal cells (ciliated cells and non-ciliated Clara cells) [19]. CFTR is expressed at higher levels in serous cells of submucosal glands of the proximal cartilaginous airways [20-22]. It has also been reported that CFTR is expressed in ciliated cells of the surface epithelium of larger airways, and in a small population of non-ciliated cells in distal airways with a negligible amount expressed in cells of lung parenchyma [12;23]. The ciliated columnar cells of the human respiratory tract, the main locus of the aberrant CFTR expression and dysfunction, represent an attractive site for manipulation of the *CFTR* gene in order to correct CF disease at the molecular level.

1.5 Gene therapy

Gene therapy can be broadly defined as a method to introduce genetic informations into a patient's somatic cells in order to produce specific therapeutic proteins to correct or modulate disease. Several gene therapy approaches have been used to treat medical conditions such as 1) the direct attack on tumour cells with cytotoxic metabolites, inactivating or restoring function of oncogenes or mutated tumour suppressor genes, by using immune responses to tumour antigens, via delivery of cytokines, anti-tumour-associated antigen vaccines, upregulation of major histocompatibility complex (MHC) or co-stimulatory molecules, or

inhibition of immunosuppressive molecules, as in cancer gene therapy 2) the local and systemic production of secreted proteins such as factors VIII and IX, erythropoietin, and apolipoprotein for protein replacement therapy for inherited and acquired diseases 3) an introduction of anti-HIV genes into hematopoietic cells to produce a population that is protected from the effects of HIV.

The central dogma of molecular biology states that DNA containing the genetic code is transcribed in the nucleus to produce messenger RNA (mRNA) transcripts. The transcripts are then translated at the ribosmes following export into the cytoplasm prior to the biosynthesis of the encoded protein. So, in our case, in order to produce correctly functioning CFTR protein to augment the mutated CFTR, we need to deliver the therapeutic DNA into the nucleus for transcription and subsequent translation. For CF, the nucleic acid coding for the CFTR protein can be introduced in a number of forms. For instance, the code for the specific protein can, theoretically, be introduced by the addition of appropriate mRNA, without the requirement of delivery of pDNA to the nucleus for initial transcription. However, the direct delivery of mRNA to the target cells is short-lasting because of the short half-life of mRNA and its instability. The exogenous DNA can also be engineered into genomic context vectors (GCVs) namely bacterial artificial chromosomes (BACs), yeast artificial chromosomes (YACs) and mammalian artificial chromosomes (ACs). Large genomic fragments that contain all the long-range control elements should, in theory, permit tissue-specific gene expression at the physiological level [24]. GCVs carrying large *CFTR* transgenes with relevant regulatory regions have been designed, but their delivery and hence transfection efficiency is hampered by their large size.

Therapeutic pDNA such as that coding for CFTR protein is currently the most practical option in gene therapy strategies. A plasmid is essentially a closed circular extra chromosomal bacterial DNA molecule which has the potential to accommodate exogenously introduced specific DNA sequences. Based on this principle plasmid has been engineered for the successful synthesis of transgenes.

The exogenous DNA, in whatever form, has to overcome physical barriers. Strategies to enable the cell to take up the pDNA are therefore of great importance. Viral or non-viral vectors currently represent the best options for the introduction of the correct version of the defective gene in a clinical setting. These vectors, also called gene transfer agents (GTAs), will be introduced later on in this chapter.

1.6 Cystic fibrosis gene therapy

Despite the increased lifespan of CF patients due to improved antibiotic and conventional medical treatment in recent years, there is still no treatment for the CF basic defect. CF is an ideal candidate for gene therapy because of the following reasons:

a) The single defective gene is known, and is therefore more amenable to manipulation compared to polygenic conditions such as asthma where the genes responsible for it are complex or unknown [25].

b) The airway epithelium lining the lungs, in contrast to deeply located submucosal glands, is easily accessible via topical administration thus avoiding invasive transfection procedures.

The basic goal of CF gene therapy is to introduce a normal copy of the *CFTR* gene into the target airway epithelial cells. This was initially demonstrated by the correction of dysfunctional chloride secretion in the early 1990s using ΔF508 CFTR immortalised epithelial cells [26] and CF mouse models [27;28] transfected with normal copies of *CFTR* complementary DNA (*CFTR* cDNA). Our laboratory, and others, then undertook a series of proof-of-mechanism and proof-of-concept studies and demonstrated correction of ~25% of the chloride defect [29-41]. Although gene transfer efficiency to the lung after topical administration using viral GTAs is higher than that with non-viral GTAs, the viral GTAs have been shown to be unsuited for repeated dosing, as an anti-viral immune response reduces the effectiveness of each subsequent dose [42-45]. Non-viral approaches, using cationic liposomes or polymers, appear to be more suited for repeated dosing [46]. In this context, the UK CF Gene Therapy Consortium (UKCFGTC) have developed a CpG-free *CFTR* expression plasmid (pGM169) engineered for prolonged transgene expression complexed with the cationic Genzyme lipid 67A (Lipid GL67A), the most efficient GTA for airway epithelial cells [33;47]. Clinical studies aimed at topically administering a non-viral gene transfer formulation consisting of pGM169-Lipid GL67A complex to the lungs and noses of subjects with CF by aerosol are currently underway. Previous laboratory and clinical studies have shown that non-viral GTAs are less effective overall, when compared to their viral GTAs counterparts, likely due to extra- and intracellular obstacles to the delivery of the therapeutic pDNA to the nucleus of the target cell for CF gene therapy, the terminally differentiated ciliated airway epithelial cells. With this in mind, and in line with the UKCFGTC's pre-clinical efforts to identify potential sources of materials that will provide a further pipeline of new non-viral vectors, I have therefore focussed my research on characterising the fate of pDNA in human airway epithelial cells following non-viral gene

transfer. Insights gained will hopefully facilitate the rationale development of gene transfer materials and protocols for CF gene transfer applications.

1.7 Vectors for airway gene transfer

Over decades many viral and non-viral vectors carrying the functional copy of *CFTR* gene have been developed and tested for their potential to correct the CF defect [44]. These are discussed below.

1.7.1 Viral vectors

Viruses have evolved to subvert their host cell's defence machinery in order to deliver their genome. Conceptually, viral vectors, designed to exploit this property, exhibit very high transduction efficiencies compared to non-viral strategies. A number of viral approaches have been used to deliver therapeutic pDNA to human airway epithelial cells. The DNA viruses, adenoviruses (AdV) and adeno-associated viruses (AAV) have been tested in CF clinical trials for their efficacy, safety and repeat-administration and shown to produce an immune response on repeat-administration [35;42,43;48-53]. Non-integrating RNA viruses, namely Sendai viruses (SeV) have also been assessed for their potential to transfer CFTR gene *in vivo* [35]. SeV successfully transduced 80% of airway epithelial cells in ferret lung and partially restored the chloride transport in the nasal epithelium of CF knockout mice [32;54]. The gene expression is strong and transient but, again, repeat administration triggers the immune response [35;55]. RNA retro- and lenti- viruses have also been tested for their transduction efficacy. Crucially, lenti viruses can transfect non-dividing fully differentiated airway epithelial cells, compared to retroviruses. Several studies have shown, not only long-

lasting gene expression in murine airway epithelium (18-25 months) by lentiviruses due to integration of cDNA into the host cell genome, but also repeat administration with minimal immune responses [44]. However, the main drawback is that the lentiviruses have the potential to integrate randomly into the cellular genome resulting in the activation of a proto-oncogene [56;57]. Therefore more research is needed to meet the safety requirements using this virus for airway gene transfer.

1.7.2 Non-viral vectors

Though viral vectors are more efficient in gene delivery, development of immune responses and their potential to integrate into the host genome on repeat-administration have restricted their use. As an alternative, various non-viral *CFTR* gene vectors have been designed and assessed in clinical trials for their transfection efficiency and safety [35;36]. The majority of these clinical trials have shown partial correction of the chloride transport in nasal epithelium but further study is required to assess whether they can ameliorate the CF lung disease, as assessed by appropriate clinically relevant endpoints such as bacterial infection and inflammation. Non-viral vectors are generally less efficient for airway gene transfer compared to viral vectors because of the lack of natural mechanisms for cellular entry, endosomal escape and nuclear delivery. However, their low immunogenicity, low toxicity, ease of bulk preparation and stability in clinically used nebuliser delivery systems makes them good candidates suitable for repeat administrations of the *CFTR* gene to the human airway epithelium [44]. Four main types of non-viral vectors have been used for gene delivery to the airway. These are naked pDNA, cationic polymer/pDNA complexes (polyplexes), cationic liposome/pDNA complexes (lipoplexes) and DNA nanoparticles.

1.7.2.1 Naked plasmid DNA

Intra-tracheal administration of naked pDNA has been reported to transfect the airway epithelial cells in both mice and rats [58]. In both animal models, the transgene expression was found to be transient when driven by a cytomegalovirus (CMV) promoter. Another study by Gill *et al* has shown persistent expression in mice lungs for up to 8 weeks post instillation of plasmid containing human promoters such as ubiquitin C (UbC) or elongation factor 1 alpha (EF1α) [59]. This demonstrated that the long-lasting gene expression depends upon the right choice of promoters. Therefore, a number of eukaryotic or hybrid promoters (e.g. CMV enhancer/UbC promoter) containing human and viral regulatory elements have been assessed recently for their ability to transfect airway epithelial cells [33]. It has previously been reported that unmethylated CpG motifs on the plasmid backbone activate the immune system via toll-like receptors thus inducing inflammatory responses (cytokines) [33;60;61]. The UKCFGTC has recently shown that the complete removal of unmethylated CpG motifs from a plasmid results in longer-lasting pulmonary gene expression in mice due to reduced inflammation [33]. Naked pDNA has not been taken forward into clinical trials because of its unsuitability for the purposes of aersolisation into the human airway owing to its instability in clinically-used nebulisers (Dr Uta Griesenbach, Department of Gene Therapy, Imperial College London - personal communication).

1.7.2.2 Cationic polymers

Among cationic polymers, polyethylenimine (PEI) is the most commonly used to deliver pDNA to airway epithelial cells. Its ability to bind negatively charged pDNA, via electrostatic interactions, results in condensation of pDNA thus makes it not only favourable

for efficient airway gene transfection, both *in vitro* and *in vivo*, but also protecting the pDNA against degradation [62]. Further, the overall positive charge on the PEI/DNA complex due to excess of polycations allows the binding of complex to the anionic proteoglycans present on the cell membrane. This not only favours the solubilisation of PEI/DNA complex but also promotes cellular entry via endocytosis [63-65]. Another advantage of PEI is that it acts as a proton sponge due to the protonation of nitrogen atoms it contains [62]. This leads to the osmotic swelling and eventually rupturing of the PEI/DNA complex-containing endosomes, due to the accumulation of chloride ions, thereby releasing the pDNA into the cytoplasm [66].

Two types of PEI have been assessed for their ability to transfect airway epithelial cells. Higher levels of transient gene expression were achieved *in vitro* and *in vivo* following nasal instillation to the lungs of mice and rabbits with linear 22 kDa PEI compared to branched 25 and 50 kDa PEI. Furthermore, the repeat administration of linear PEI/DNA complex did not trigger immune responses even though a reduction in gene expression was observed [67;68]. Bragonzi *et al* reported that a linear PEI was distributed into the alveolar region, while branched PEI was localised to the bronchial epithelial cells following intertracheal injection of PEI/DNA complex to the mouse lung [69].

Gene transfer efficiency was also compared following nebulisation, a clinically relevant delivery technique, of linear or branched PEI/DNA complexes. Higher expression was achieved with branched 25 kDa PEI [36;70] compared to the linear form. It has also been reported that the delivery of branched PEI/DNA complexes to the mouse lung via whole body aerosolisation can transfect the airway epithelial cells effectively and safely without producing inflammation [71-73] as compared to nasal instillation that cause moderate to

severe inflammation [74;75]. Another study by Rudolph *et al* showed 15-fold higher gene transfection efficiency with PEI via nebulisation as compared to intra-tracheal intubation [76]. However, PEI/DNA complex formulation is limited by precipitation and hence loss of efficacy when pDNA concentrations exceed 0.5 mg/ml in the PEI/DNA formulation. Davies *et al* overcame this limitation by introducing a filtration step during the preparation of PEI and prepared a stable branched 25 kDa PEI at concentrations at 8 mg/ml pDNA which is expressed more efficiently following nebulisation into the murine lung [75]. Finally, a level of reporter gene expression similar to that achieved by PEI was achieved on intra-tracheal delivery of another biodegradable, linear cationic polymer called chitosan when complexed with pDNA [77]. However, the high toxicity of PEI is still an issue making it an unfavourable candidate to take forward to clinical trial.

1.7.2.3 Cationic liposomes

Cationic liposomes have also been used to transfect airway epithelial cells *in vitro, in vivo* and *ex vivo*. Cationic liposome/pDNA complexes, also called lipoplexes, are the most commonly used non-viral vectors. Lipoplexes consist of three components: a cationic lipid, a neutral helper lipid and pDNA which are described in detail below.

A cationic lipid, as shown in Figure 3 (upper panel), comprises a positively charged head group and a linker molecule which stabilises the lipid via linkage of the head group to the lipid hydrophobic anchor group (tail) resulting in the formation of cationic lipid vesicles as shown in Figure 3 (lower panel). The head group is positively charged due to the presence of a protonated positively-charged nitrogen containing group and the linker molecule contains the neutral alkyl ether group (Figure 3A). The positively charged head group interacts

electrostatically with negatively charged pDNA resulting in the formation of a lipoplex (Figure 4). The lipid's hydrophobic anchor group interacts with the cell membrane and neutral helper lipids facilitate transfection efficiency of liposome/pDNA complex, possibly by destabilisation of lipid bilayers of the cell membrane thus enhancing the cellular entry as well as endosomal escape of pDNA. Dependence of the transfection efficiency of lipoplexes on the helper lipid type was demonstrated by Fasbender *et al* [78]. They showed that the cationic lipid dioleoyl phosphatidyl-ethanolamine (DOPE) and helper lipid 3β[N-(N,N-dimethylamminoethane)-carbamoyl] cholesterol (DC-Chol) together gave higher levels of reporter gene expression *in vitro* compared to the N-(2-hydroxyethyl)-N,N-dimethyl-2,3-bis(tetra-decyloxy)-1-propanaminium bromide (DMRIE) helper lipid.

A number of cationic lipid formulations have been evaluated for *in vivo CFTR* gene transfer. One of the earliest studies demonstrated the correction of chloride ions transport defects on topical administration of human *CFTR*/ lipofectamine complexes to the lungs of CFTR null mice [27]. However, the major drawback using lipofectamine is its higher toxicity. Therefore, Alton *et al* next demonstrated the restoration of chloride ions secretion in the airway to 50 % of wild type levels in null mice on nebulisation of lipoplexes consisting of CFTR and the cationic formulation DC-Chol/DOPE [28]. Another study by the same group showed that repeat administration of DC-Chol/DOPE/CFTR lipoplex in CF null mice retained transgene expression and the DC-Chol/DOPE formulation was therefore taken forward into clinical trials [79]. In these studies, a partial correction of the chloride defect to 25 % of wild type levels was demonstrated on topical administration of liposome/hCFTR complex to the nose of CF patients. The correction was transient, peaking 3 days post-administration, and disappeared by day 7 because of short acting CMV promoter/enhancer [80]. Although the life span of a ciliated cell can be over one year (17-18 months) the gene expression was transient

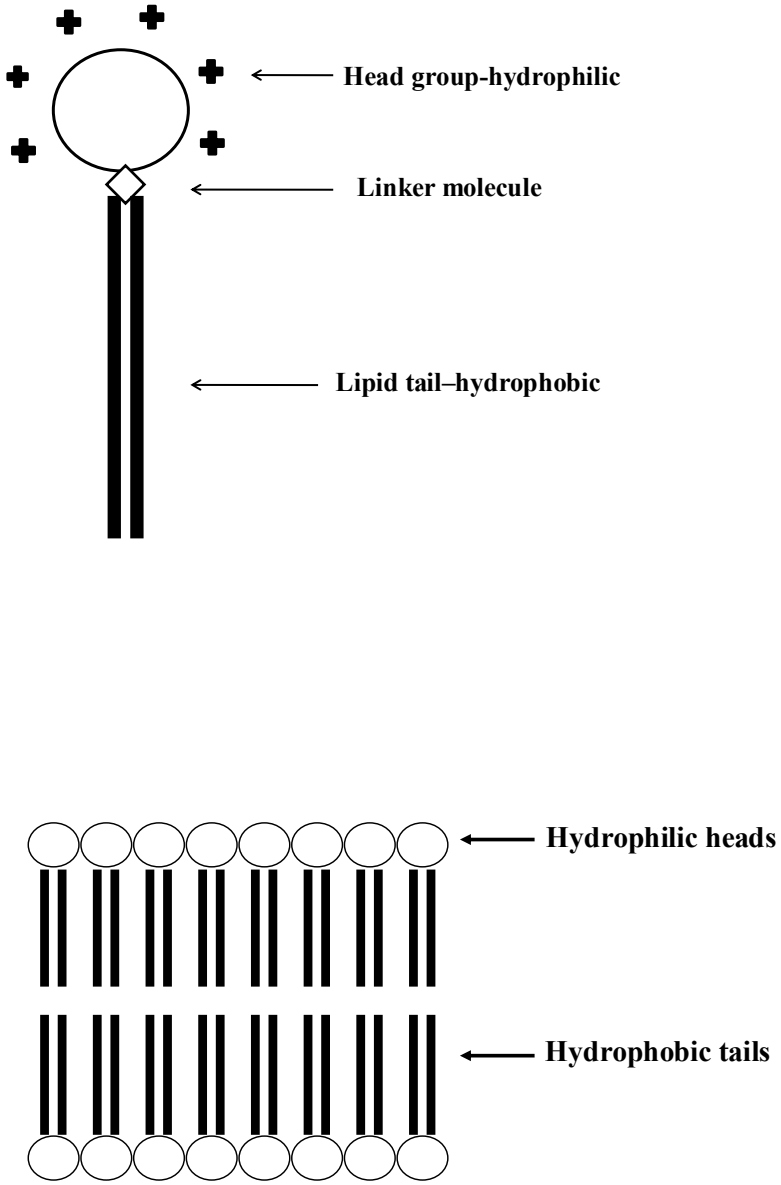

Figure 3: Basic structure of cationic lipid (upper panel) and cationic lipid vesicle formation (lower panel)

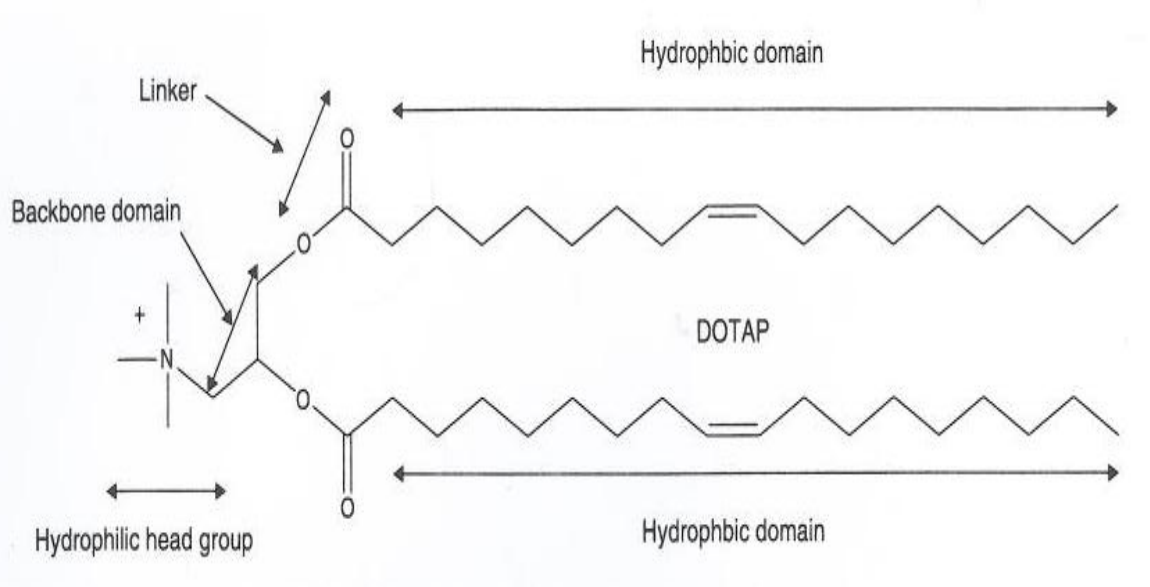

Figure 3A: The three basic domains of cationic lipids

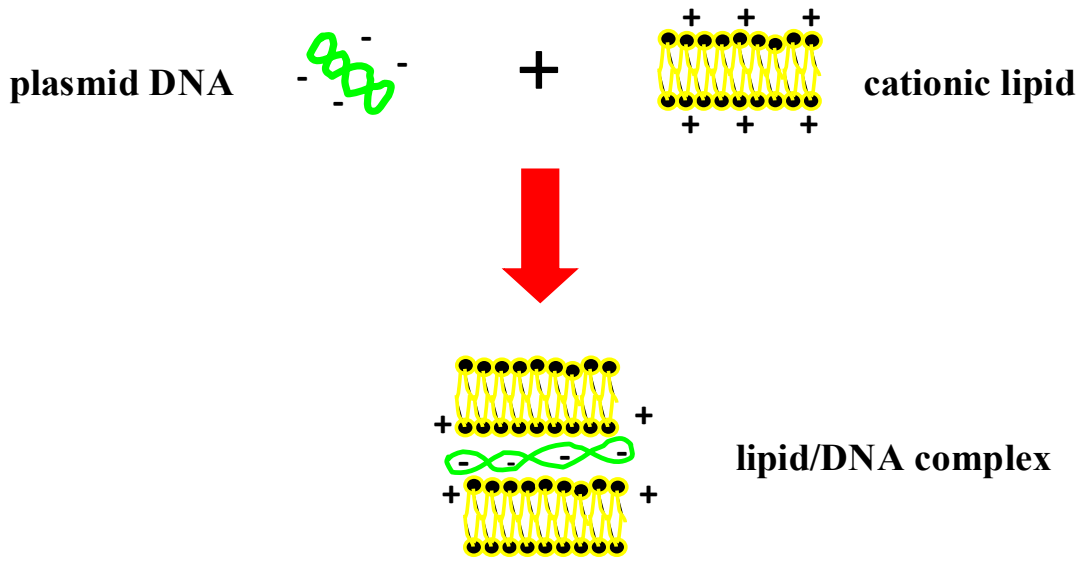

Figure 4: Cationic lipid-plasmid DNA complex (lipoplex)
The negatively charged plasmid DNA interacts electrostatically with positively charged cationic lipid to form lipid/DNA complex.

because pDNA did not integrate in the host genome [80a]. In an another study using DC-Chol/DOPE, Gill *et al*, showed that a second administration of different doses of DC-Chol/DOPE complexed with CFTR plasmid resulted in the correction of nasal PD for up to 15 days, at least in one subject [81]. This study was further extended and interestingly, it was shown that three doses of the lipoplex, repeatedly administered to the nose of CF subjects, retained efficacy [46]. However, repeat administration of DC-Chol/ DOPE formulation retained transfection efficiency, but it was not taken forward because another formulation that uses cationic Genzyme Lipid 67A (GL67A) (Genzyme Corporation, Framingham, USA) was found to be more effective (discussed below).

The cationic lipid GL67A (Figure 4A) is now established as the most efficient lipid for delivery of pDNA to the airway epithelium. It consists of a T-shaped spermine headgroup joined to a cholesterol anchor group via a carbamate linker molecule [82]. Its formulation comprises of charged lipid DOPE and dimyristoylphosphatidylethanol-amine (DMPE) helper lipid, linked to a small amount of polyethylene glycol (PEG5000). Addition of DMPE-PEG5000 resulted in stabilisation of the GL67A/pDNA complex thus making it suitable for aerosol delivery to the human lung [82;83]. A number of studies have now successfully used the GL67A/pDNA formulation in *vitro* and *in vivo* settings.

Preclinical evaluation of GL67A in mouse models of CF revealed encouraging results. Lee *et al* reported a 1,000-fold higher level of reporter gene expression compared to naked pDNA alone in the mouse lung, peaking between 1-4 days post-administration with GL67/pDNA complexes [82]. In addition, they also reported a similar level of efficacy in the mouse lung on re-administration of a second dose of lipoplex. However, re-administration of a second

A GL67

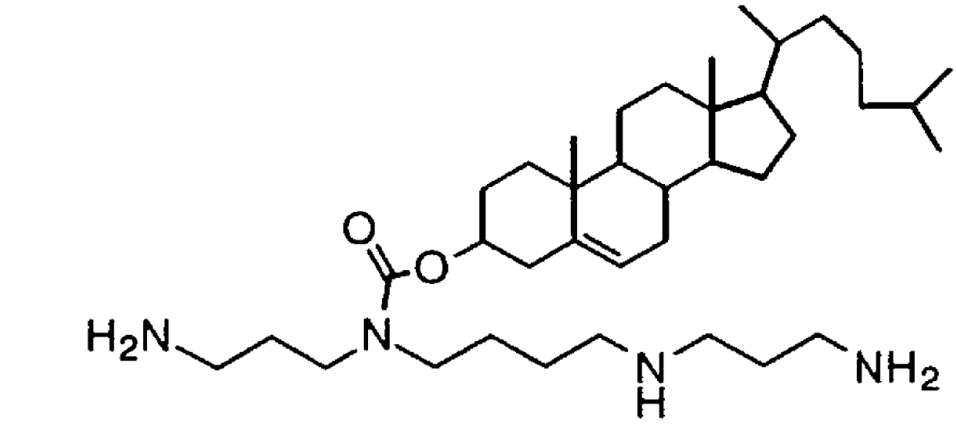

B DOPE

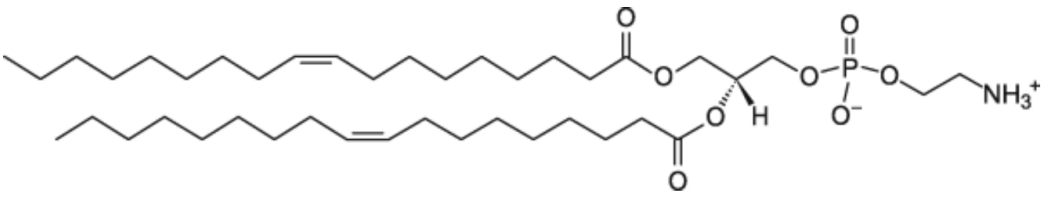

C DMPE-PEG$_{5000}$

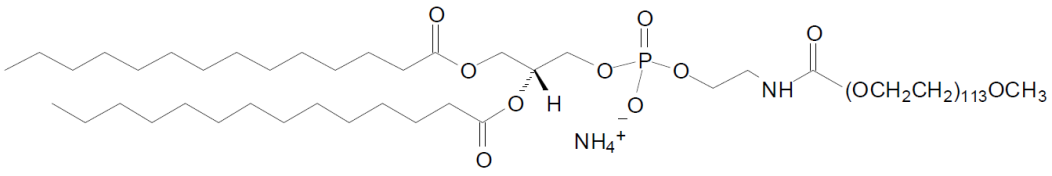

Figure 4A: Description of GL67A

The cationic lipid mixture GL67A consists of a mixture of three components-GL67 (structure shown at A), DOPE (structure shown at B) and DMPE-PEG5000 (structure shown at C), formulated at 1:2:0.05 molar ratios.

higher dose resulted in lower efficacy due to immune response against the reporter gene. In a recent study, the transfection ability of GL67A/plasmid CFTR was assessed in the mouse nasal epithelium of approximately 400 mice. The majority of mice confirmed the presence of *CFTR* mRNA but no significant improvement was observed in the CF phenotype (periciliary liquid height, bacterial colonisation and nasal potential difference) [47]. Non-viral vectors are, thus, comparatively less efficient than viral vectors in the delivery of genes but offer the advantage of re-administration without a significant inflammatory response.

Having shown positive results in CF mouse models, the GL67A formulation was taken forward into the clinical setting and used to investigate *CFTR* gene transfer to the human airway epithelium. The formulation was initially shown to transfect human airway (lung tissue) *ex vivo* [84]. The efficacy of GL67 to deliver lipoplex (GL67/CFTR pDNA) to the nose and lung of CF subjects was then assessed in clinical trials [29;85]. Alton *et al* reported a partial correction of chloride secretion in both lung and nose using bronchial PD and NPD respectively. More importantly a change was observed in some of the CF secondary clinical characteristics such as a significant reduction of inflammatory cells in sputum, and reduced bacterial colonisation in the nose and lower airways in majority of patients [29]. Interestingly, Ruiz *et al* also reported *CFTR* mRNA detection in bronchial biopsies of four out of nine CF subjects in a parallel study using GL67A [85]. However, in both studies some patients showed mild, transient flu-like symptoms post administration. These inflammatory responses are likely to be caused by unmethylated cytosine/guanine dinucleotides (CpG) in the plasmids. Despite, absence of antibodies against the pDNA or lipid an increase in level of inflammatory cytokines (IL-8, TNF-alpha) in the serum was shown [85]. Based on these findings, the UKCFGTC has selected GL67A as the best performing non-viral vector for use in ongoing clinical trials. Pre-clinical assessment showed efficacy in airway epithelial cells *in*

vivo, low toxicity and stability in a clinically-used nebuliser. In addition, preparation of the GL67A was optimised for good manufacturing practice (GMP). Recently the UKCFGTC has carried out a clinical trial programme in CF patients, involving the single administration of different doses of GL67A complexed with clinically relevant CpG-free plasmid 169 in which transgene *CFTR* is under the control of a hybrid promoter consisting of human CMV enhancer and the elongation factor 1α promoter (hCEFI). Higher doses of GL67A/*CFTR* cDNA, namely 10 ml and 20 ml resulted in a dose-related inflammatory response. However, a lower dose (5 ml) resulted in very little inflammatory response, and this dose is being taken forward into a multiple dose clinical trial to evaluate whether GL67A-mediated gene transfer can improve clinically relevant end-points after 12 repeated administration over one year.

1.8 Barriers to gene therapy in cystic fibrosis

As explained above, the ultimate objective is to deliver *CFTR* cDNA to the nuclei of fully differentiated ciliated human airway epithelial cells, the target cells for CF gene therapy, using the current best performing cationic lipid GL67A. As part of its role in respiration, the upper airway tract removes foreign bodies from the lung, a property that represents the first obstacle to both viral and non-viral GTAs. Further, the upper respiratory tract of CF individuals consists of thick mucus-bearing CF airway epithelium, and is opportunistically colonised by bacterial with related inflammation and immune cell invasion. All represent additional extracellular impediments to gene transfer. More importantly, even when the GL67A/pDNA complex finally makes its way through the extracellular obstacles to the epithelial cell surface on the airway lumen, the complex is faced with the challenge of cellular uptake and subsequent transport across the cytoplasm, via the nuclear membrane and delivery to the nucleus for transcription of the transgene [62;86-89]. In order to follow the

progress of pDNA across the terminally differentiated polarised airway epithelial cell into the nucleus, insights into the following key questions are important.

What are the target cells for CF gene therapy and where are they located?

As mentioned earlier, CFTR protein is expressed at higher levels in serous cells of submucosal glands, as well as in the cells of the surface airway epithelium. Thus, delivery of normal CFTR plasmid to these locations could potentially replace the defective *CFTR* gene via subsequent expression of functional CFTR protein. However, cells (ciliated or non-ciliated) of the surface epithelium are highly differentiated so gene expression will be lost on cell death, even if these cells are transfected with a safe integrating vector [90]. Furthermore, various studies reported that the highly differentiated cells of surface epithelium, as well as serous cells in submucosal glands, are difficult to transfect because of their reduced uptake capability [12;90;91]. Obviously, the usefulness of topical administration of the transgene via nebulisation depends on the location of these target cells, as it is unlikely that the non-viral vectors containing *CFTR* transgene could reach the serous cells of deeply located submucosal glands or basal cells of the surface airway epithelium as these cells are not exposed apically. The likelihood of hitting the apically (at the lumen of surface epithelium) located airway epithelial cells is, however, much higher. We have therefore concentrated our research on non-viral gene transfer to the ciliated airway epithelial cells as these are the most predominant cells (~70 %) and express CFTR [92;93].

How do the target ciliated airway epithelial cells internalise cationic lipid- or cationic polymer-complexed plasmid DNA?

The first and the most crucial step to the transfection of the fully differentiated ciliated epithelial cells is the successful uptake of non-viral vectors (cationic lipid and cationic polymer) into the polarised cells. The vector has to reach the cell surface membrane after overcoming the various extra-cellular barriers namely extracellular matrix, glyocalyx and mucociliary clearance which has the potential to wash away the majority of vector with the result that only a fractional amount of vector is able to reach the cell surface membrane. Since the cationic vectors are large and hydrophilic, they cannot penetrate through the cell surface membrane. Having a slight excess of positive charge, the cationic vectors have the potential to bind to the negatively charged heparan sulphate proteoglycans and integrins present on the cell surface membrane via non-specific ionic (electrostatic) interactions [94-98]. A study by Mislick *et al* demonstrated reduced binding ability of lipoplexes and polyplexes in proteoglycan-deficient cells [99]. Kopatz *et al* suggested the binding of polyplexes to the negatively charged syndecan molecules present on the surface membrane [100]. After cellular binding, it is now well established that both the non-specific and ligand-bound non-viral vectors are internalised by various endocytic and non-endocytic mechanisms outlined in Figure 5 [95;101-105].

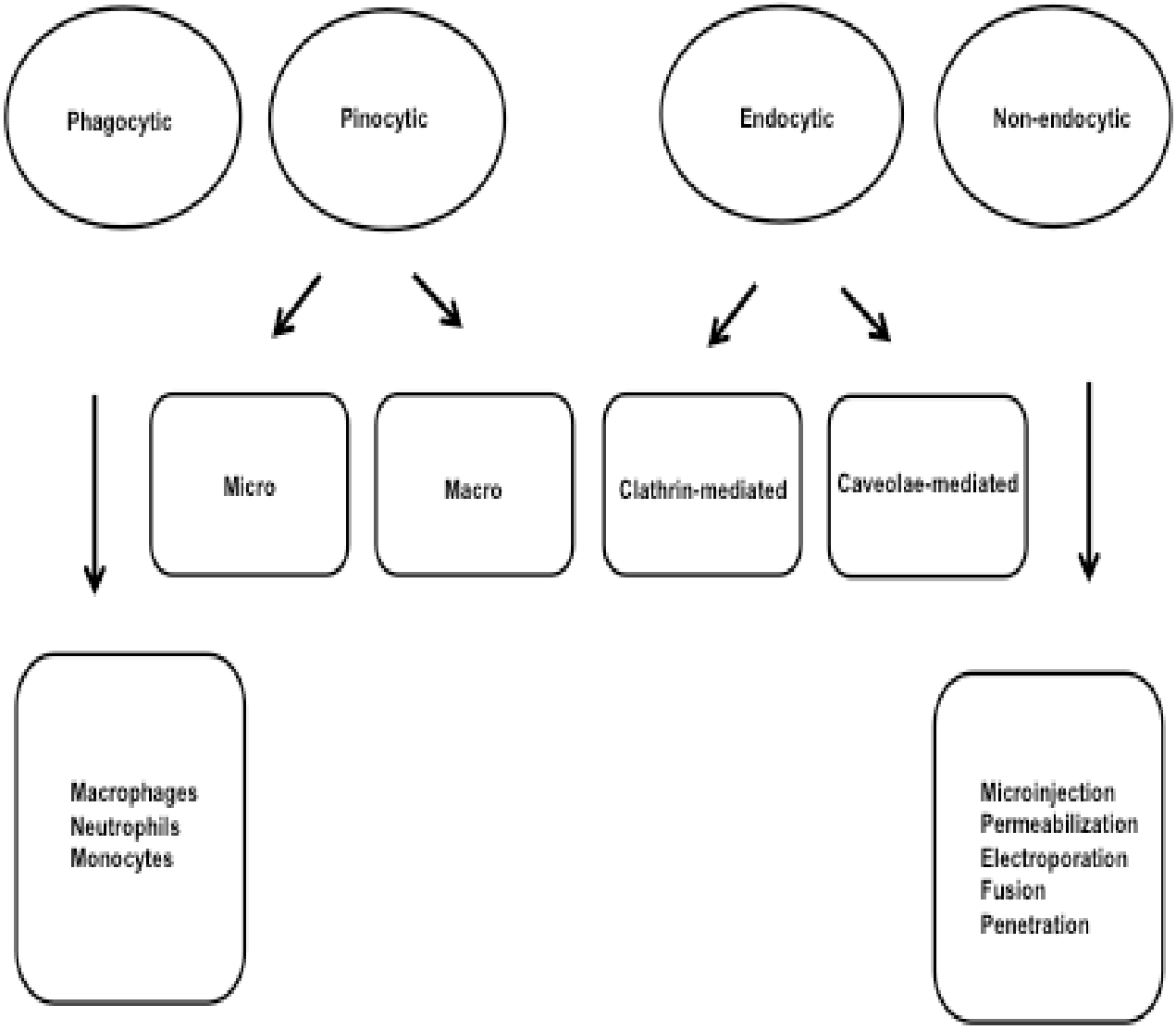

Figure 5: Various uptake routes of non-viral vectors

Phagocytosis: Phagocytosis facilitates the uptake of large particles using cell surface receptors and is strictly restricted to specialised cells such as macrophages, neutrophils or monocytes [106].

Pinocytosis: Pinocytosis takes place through two different pathways, namely micropinocytosis and macropinocytosis. The micropinocytosis pathway involves the uptake of particles no larger than 0.1 μm in diameter. Macropinocytosis involves larger particles (0.2–5 μm in diameter) and it is the result of cell surface membrane ruffles folding back on the plasma membrane. Macropinosomes are not coated with clathrin or caveolin but encircled by actin in its early stages. Macropinocytosis provides an efficient process for nonselective uptake of nutrients and solute macromolecules [107].

Endocytic uptake: Receptor-mediated endocytosis is a distinct mechanism where internalisation of a receptor and its ligand is carried out within clathrin-coated or uncoated vesicles [108;109]. Endocytosis involves the uptake of particles into membrane-bound lipid bilayer vesicles formed by invagination of the cell membrane which subsequently pinch off and are released as endosomes into the cytosol in an energy driven process. This enables the internalisation of receptors, adaptors, regulators, and other downstream proteins as a signalling complex [110]. Moreover, endocytic uptake may sometimes be accompanied by caveolae-mediated entry. Caveolae are involved in plasma membrane invaginations 50–80 nm in size including cholesterol and sphingolipids, receptors and caveolins [110;111]. In contrast, clathrin-coated pits of 100–200 nm are associated with the key protein clathrin and other scaffold proteins such as AP-2 and eps15 [112]. Plasmid DNA (~ 200 nm when fully condensed with cationic lipid) internalisation by endocytosis was demonstrated by the detection of gold-labelled DNA in intracellular vesicles using electron microscopy post-

transfection [103]. Other studies also reported the detection of lipoplexes in intracellular vesicles beneath the cell membrane in cultured cells using electron and fluorescence microscopy, suggesting the endocytic uptake of lipoplexes [110;113]. Clathrin-mediated endocytosis occurs in all mammalian cells in which clathrin-coated pits, formed by the binding of ligand to specific cell surface receptors, internalise by invagination and pinching off as clathrin-coated vesicles. The depolymerisation of the clathrin coat then results in the release of an early endosome [109;114]. The internalisation of lipoplexes and polyplexes via clathrin-mediated endocytosis has been reported [115-117]. The caveolae-mediated pathway involves the internalisation of particles by the formation of flask-shaped invaginations of cell membrane called caveolae. These pinch off the cell membrane to form caveosomes in the cytosol [118;119]. Uptake of lipoplexes and polyplexes via caveolae-mediated endocytosis has been suggested by many researchers [117;120;121].

Non-endocytic uptake: Various non-endocytic routes to deliver the pDNA to the mammalian cell nuclei have been proposed. Microinjection involves the rapid physical delivery of DNA to the cytosol or the nucleus [122;123]. Permeabilisation is another non-endocytic method that can deliver large genes directly into the cytoplasm via creation of transient transmembrane pores in the cell membrane using pore-forming agents like streptolysin-O or anionic peptides [124;125]. Electroporation is another technique that facilitates pDNA delivery into the cytosol via transient opening of pores in the cell membrane under the application of an electric field [126]. However, physical routes, such as the above, are all invasive and thus likely only suitable for *in vitro* or *ex vivo* use.

Is uptake of cationic lipid-complexed with plasmid DNA by polarised airway epithelial cells different from uptake by non-polarised cells?

The target cells for CF gene therapy, ciliated airway epithelial cells, are polarised with distinct apical, lateral and basolateral membranes. The cells are bound together via tight junctions to form a sealed epithelial sheet restricting access from the luminal to the serosal side. In contrast, non-polarised cells are not differentiated and have a relatively homogeneous cell membrane throughout, without existence of any tight junctions between them. This characteristic of non-polarised cells makes them easy to transfect, as the entire cell surface is available for vector entry compared to the restricted apical entry in the case of polarised cells [127].

It has been reported that lipoplexes carry genes efficiently into a few cell lines and primary cell cultures [102;128-131]. However, transfection activity of lipoplexes is less effective in highly differentiated airway epithelial cells, and is therefore a key focus of research for non-viral CF gene therapy [80;104;132;133]. Two similar studies conducted by Jiang *et al* and Chu *et al* demonstrated that fully differentiated polarised human airway epithelial cells, namely primary normal human bronchial epithelial (NHBE) cells grown on filter supports at an air-liquid interface, were more resistant to cationic lipid GL67-mediated transfection compared to poorly differentiated non-polarised cells grown on tissue culture plates[134;135]. They also showed that GL67-mediated transfection efficiency decreased progressively as the cells became more polarised and differentiated. These results were in agreement with those reported by Matsui *et al* in "islands" of differentiated human airway epithelial cells (i.e.NHBE cells), and also with those reported by Fasbender *et al* in human primary cultures of ciliated airway epithelial cells grown at an air-liquid interface and also

rabbit tracheal explants [104;132]. A decrease in binding ability of the cationic lipids to the surface of mature airway epithelial cells, and hence a reduced rate of internalisation of the bound complexes into these cells, resulted in lower gene transfection activity. In addition, the reduction in binding of these complexes was also explained by differences in surface charge between poorly and well-differentiated cells. Matsui *et al* also suggested that well-differentiated cells exhibited receptor-mediated endocytosis while in poorly differentiated cells lipoplexes internalised via receptor-mediated endocytosis, pinocytosis and phagocytosis [104]. Another study demonstrated a loss of cationic GL67-mediated transfection activity due to a decline in proliferative rate of the NHBE cells (measured by reduced thymidine uptake, a cell division marker) as they became more polarised and differentiated, when matured on the collagen matrix [134]. On the other hand, these cells do not polarise when cultured on tissue culture plates but show a decrease in proliferation, and hence transgene expression, as they became more confluent. Similar results have been suggested by previous workers [132;136-138]. Jiang *et al* reported that transfection efficiency of cationic lipid GL67 depends on the mitotic activity of the cells, with higher efficiency in dividing rather than non-dividing cells [134]. Another study by Leigh *et al* also demonstrated lower transgene expression following cationic lipid-mediated transfection in airway epithelium (with low mitotic activity)[139]. Interestingly, they also found higher transfection efficiency in inflamed CF lungs probably due to elevated proliferation in airway epithelial cells.

As described above, the apical surface membrane of well-differentiated polarised cells, for example NHBE, limits the internalisation of most viral and non-viral vectors due to the lack of appropriate receptors. In contrast, the basolateral membrane is rich in receptors, such as viral receptors for AdV and AAV [140;141]. Other receptors present on the basolateral surface include, the epidermal growth factor, α2-adrenergic and transferrin receptors

[142;143]. Calcium-free or calcium chelating agents, such as ethyleneglycol-bis-(β-aminoethyl ether)-N,N-tetraacetic acid (EGTA) are known to open tight junctions transiently, thus allowing the basolateral entry of vectors to the target cells [144;145]. Chu *et al* demonstrated an increased transgene expression due to enhanced uptake of lipoplexes in NHBE cells pre-treated with calcium-free medium or EGTA to disrupt the epithelium (as measured by a decrease in transepithelial resistance) [135]. Another study also showed enhanced uptake in colon adenocarcinoma (Caco-2) cells pre-treated with tight junction disruptors, namely sodium caprate, decanoylcarnitine and the calcium ion chelator ethylenediaminetetraacetic acid (EDTA) [146]. Lastly, *in vivo* studies have also demonstrated higher rates of vector internalisation using EGTA and the non-ionic detergents, polidocanol, and perfluorocarbon (PFC) [147-152].

How does internalised plasmid DNA escape from the endosomal-lysosomal pathway?

The internalised lipoplexes and polyplexes are either entrapped in the endocytic vesicles (early endosomes), or fuse with the cell surface membrane to release the pDNA directly into the cytosol. Early endosomes are then directed to the sorting endosomes where they are either re-cycled back (retrograde transport) to the cell surface and exocytosed or they fuse with late endosomes. The late endosomes either fuse with lysosomes (post-endosomal vesicles that contain acid hydrolase enzymes to break down waste materials and cellular debris) via endosomal-lysosomal pathway resulting degradation of complex or alternatively, endosmolysis, the lysis of the endosomal vesicle occurs, releasing the pDNA and thus avoiding degradation, a crucial step for successful nuclear delivery of gene [117]. Two different mechanisms, detailed below, have been proposed for endosomal escape depending

on the type of complexes: 1) lipoplexes escape the endosome via flip-flop and fusion mechanism and 2) polyplexes escape the endosome via the proton sponge mechanism.

1) **'Flip-flop and fusion' mechanism**: This mechanism describing the release of pDNA into the cytosol was proposed by Xu and Szoka [153;154]. It is based on the endosomal membrane phospholipids' ability to flip over to an opposing membrane lipid bilayer of the lipoplex and is illustrated in Figure 6. Briefly, the cationic lipoplex is internalised into the cells via endosomes. After endocytosis, the cationic lipoplex destabilises the endosomal membrane that results in 'Flip-Flop' of anionic lipids facing the cytoplasmic side of the endosome membrane to face the luminal side of the endosome. The 'flipped over' anionic lipids are then electrostatically fused with the cationic lipids of the lipoplex to form neutral ion pairs which in turn weakens the electrostatic interactions between cationic lipid and negatively charged pDNA. This re-organisation of lipids in the endosomal membrane and lipoplex displaces the pDNA from the cationic lipids of lipoplex, thus releasing the pDNA into the cytosol. Tachibana *et al* reported that addition of DOPE, a fusogenic lipid, to pH-sensitive liposomes results in release of entrapped macromolecules into the cytosol [155]. They speculated that the stable lipid bilayer formed by DOPE at physiological pH 7 changes to hexagonal form at an acidic pH 5-6 and destabilises the endosomal membrane. Similarly, addition of excess of DOPE to the cationic lipids (with weak buffering ability) such as N-[1-(2,3-dioleyloxy)propyl]-N,N,N-trimethylammonium chloride (DOTMA), N-[1-(2,3-dioleoyloxy)propyl]-N,N,N-trimethylammonium chloride (DOTAP) and DC-Chol results in release of pDNA into the cytosol.

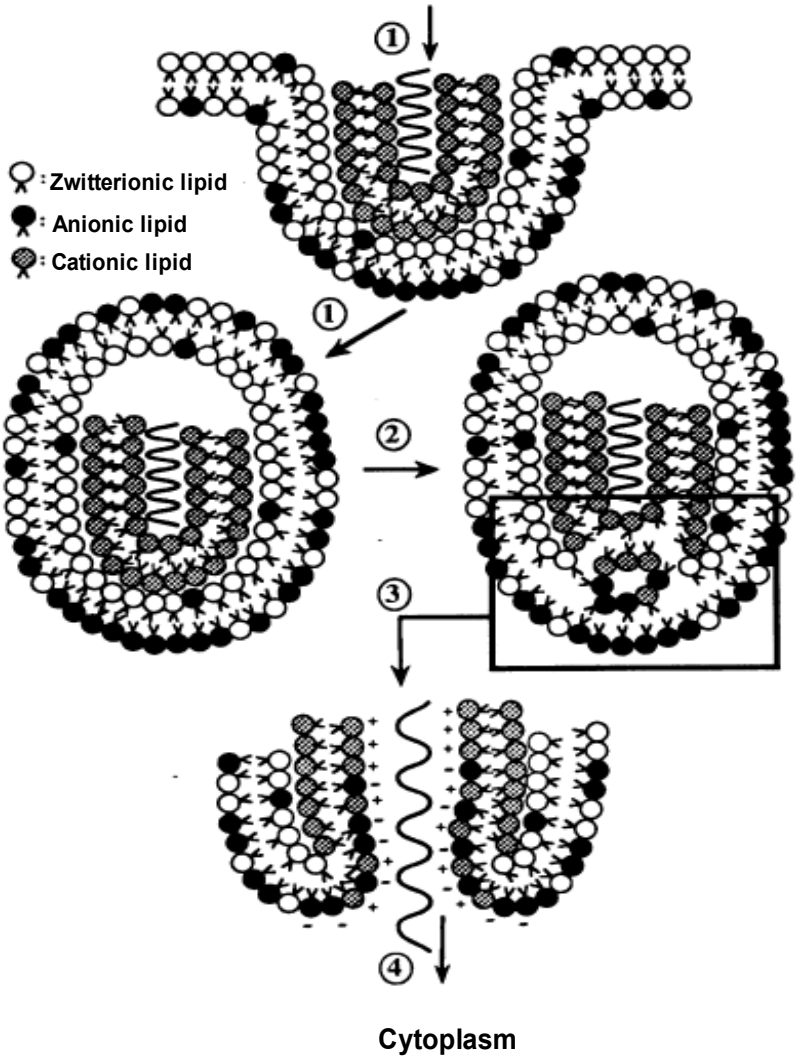

Figure 6: Schematic representation of the lipoplex uptake and "Flip-Flop and Fusion" mechanism of escape of plasmid DNA from the endosome
1) Internalisation of lipoplexes via endosomes 2) Lipoplexes destabilise the endosomal membrane which, in turn, results in the 'Flip-Flop' of anionic lipid from the cytoplasmic side towards the luminal side of the endosome 3) Diffusion of anionic lipids into the lipoplexes forms a neutral ion-pair with the cationic lipid due to electrostatic interaction 4) The plasmid DNA is then displaced from the lipoplexes and released into the cytoplasm. Adapted from Szoka *et al* [153].

2) **'Proton sponge' mechanism**: This mechanism was first proposed by Boussif *et al* [62] and is based on acidification of late endosomes by protonation of amino groups in PEI-polyplexes (Figure 7). In PEI every third atom is amino nitrogen which can be protonated during endosome acidification. Thus PEI acts as a 'proton sponge' and has a higher buffering ability. Excessive accumulation of protons within the endosomes triggers the massive influx of chloride ions which increase the ionic concentration inside the endosomes and results in osmotic swelling due to water entry. The polyplex is then released into the cytosol following endosomal lysis. A study by Sonawane *et al* also demonstrated this increase in gene delivery in Chinese hamster ovary (CHO)-K1 cells based on osmotic swelling due to protonation of PEI-polyplexes [66]. Similarly, histidylated polyplexes escape from endosomes due to protonation of imidazole during endosome acidification [156].

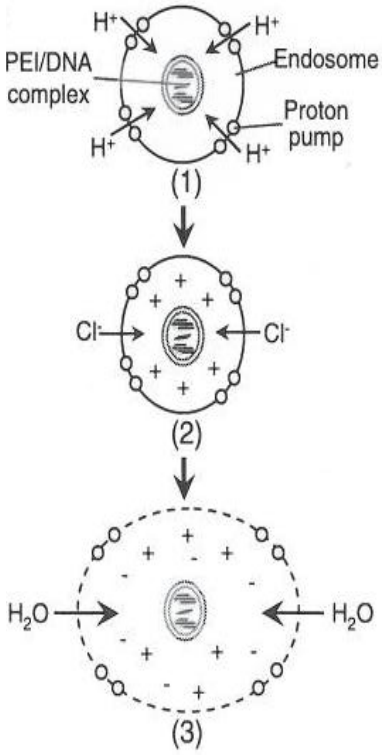

Figure 7: Schematic representation of "proton sponge" mechanism
1) Acidification of endosome due to protonation of amino groups present on PEI (i.e. influx of hydrogen ions into endosome) 2) Accumulation of hydrogen ions results in influx of chloride ions into endosome. 3) Water molecules enter the endosome because of the increased ionic strength inside; the endosome ultimately swells and releases the PEI/pDNA polyplex into the cytoplasm. Adapted from Hamm-Alvarez *et al* [157].

What is the role of the cytoplasmic transport mechanism in the translocation of the pDNA to the nuclear periphery ready for delivery to the nucleus?

As described above, pDNA is either released directly into the cytosol after fusion of lipoplex with the cell surface membrane or after endosmolysis to release intact lipoplexes from the endosomes into the cytosol. Following this cytosolic release or endosomal escape, the pDNA or intact complex must still travel some distance towards the peri-nuclear space before entry into the nucleus via the nuclear pore complex (NPC) [136;158]. It has been shown that pDNA, because of its size, is unable to diffuse freely through the mesh-like cytoplasm [159;160]. The fact that studies demonstrate successful transfection suggests the existence of a route by which pDNA enters the nucleus.

Before nuclear delivery, however, the pDNA needs to be translocated to the nuclear periphery. A number of studies now suggest that macromolecules, including exogenously introduced nucleic acids, are transported intracellulary via the cytoskeleton network in a 'rail-road' fashion. The cytoskeleton (which consists of different sized filaments namely, actin, intermediate filaments and microtubules) provides a 'railway-like' trafficking network for intracellular transport of various proteins, vesicles and their encapsulated cargo along microtubules (towards the minus-end) via dynein, a microtubule-associated retrograde motor protein [161;162]. A number of other studies have also reported the involvement of microtubules in the cytoplasmic transport of pDNA [163-165]. They also suggested that stabilisation of microtubules by taxol results in enhanced trafficking of pDNA and thus increased gene expression. Other studies also demonstrated the microtubule-mediated transport of pDNA [166;167]. Hasegawa *et al* using real time confocal laser spinning microscopy (CLSM) showed that microtubules play an important role in the intracellular

transport of lipoplexes in COS-7 cells [168]. This was further supported by another study demonstrating that PEI-polyplexes travel towards the microtubules in COS-7 cells, this being actively driven by a motor protein [169]. Interestingly, a study by Dauty *et al* found that transport of pDNA in the cytosol is impaired by unspecific binding of pDNA to actin, vimentin and keratin [170]. Thus, we can speculate that the pDNA or intact lipoplexes are potentially transported across the cytoplasm to the nuclear periphery, ready for translocation across the nuclear envelope into the nucleus, via the 'rail-like' cytoskeleton network.

What is the role of the nuclear transport mechanism in the translocation of the pDNA across the nuclear envelope?

The next important step towards delivery of the exogenously introduced pDNA is to cross the nuclear envelope, a key obstacle. It is now well established that macromolecular access to the nucleus occurs across the NPC which form aqueous channels across the double-membrane nuclear envelope and is 9-10 nm in diameter [171]. Molecules with molecular weight less than or equal to 40 kDa are able to translocate through the NPCs via passive diffusion [172]. Larger molecules (>40 kDa) are transported across the NPC into the nucleus in an energy-dependent manner. For the terminally differentiated respiratory epithelium the expection is that all nuclear entry of pDNA in these non-dividing cells occurs only through the NPC, compared to entry into dividing cell nuclei where the possibility of entry during nuclear envelope disassembly and assembly during cell division is likely.

As noted above, entry of pDNA into the nucleus could take three routes: 1) entry through the NPC via passive diffusion 2) entry when the nuclear envelope disintegrates during mitosis, and 3) entry through NPC via an active transport facilitated mechanism. Even though the

passive diffusion of small oligonucleotides (ODNs), 12 to 28 bp in size, across the NPC into the nucleus has been demonstrated, condensed pDNA which is approximately 200 nm in size is too large to cross the NPC unaided [173]. However, this is not a problem in dividing cells. In these, the pDNA enters the nucleus when the nuclear envelope breaks down at the end of mitosis. For instance, it has been shown that cells transfected in G2 or the G2-M phase of the cell cycle show much higher gene expression than those transfected in G1 suggesting that gene expression correlates with the breakdown of the nuclear membrane [174]. Evidence for the cell cycle-dependent nuclear entry of pDNA was further supported by a similar study in our laboratory in COS-7 cells [175]. The nuclear delivery of pDNA during cell division is, however, unlikely to occur in non-dividing cells (i.e. growth-arrested, confluent) or in cells with extremely low rate of mitosis such as cells of the airway epithelium [132;159;176-178]. The only other remaining route for the nuclear delivery of pDNA into non-dividing differentiated cells is therefore that requiring facilitated active transport.

It has been suggested that the transport of larger cargo molecules is mediated by nuclear localisation signals (NLSs) and in turn facilitated by soluble transport factors such as importin-β and importin-α. In the classical pathway shown in Figure 8, importin-β recognises the cargo proteins that carry NLS via the importin-α-NLS adapter molecule. The importin-α/β complex, formed by covalent binding of importin-β to importin-α, then translocates across the NPC via a still poorly understood energy-dependent mechanism, which is regulated by the nucleotide state of the Ras-family GTPase Ran [179].

Initial evidence testing whether pDNA nuclear entry could be enhanced by incorporation of NLS onto the pDNA in order to increase ‘capture’ by the nuclear import machinery have shown not only an increased nuclear delivery in *in vitro* cell-free systems, but also results in

higher transfection efficiency in cultured cell lines [180-182]. The studies have, however, been inconsistent likely due to: 1) the large size of the pDNA molecule compared to the smaller NLS peptide 2) masking of the NLS peptide by a strong electrostatic interaction between the positively charged smaller peptide and the negatively charged large pDNA molecule and 3) alteration of physiochemical properties of the cationic lipid/pDNA complexes due to incorporation of the charged NLS peptide onto pDNA [173]. Furthermore, even if the approach were to successfully enhance the nuclear entry of pDNA, the feasibility of its use in a clinical setting is unlikely because of the issue of manufacturing at clinical scale and grade.

Our laboratory, and others, have now established that because pDNA lacks NLS to permit translocation across the NPC, the pDNA is thought to bind proteins possessing NLSs and DNA-binding capacity (so called pDNA-binding nuclear shuttle proteins e.g. transcription factors) which carry pDNA, via the classical nuclear import pathway, into the nucleus as shown in Figure 9 [183].

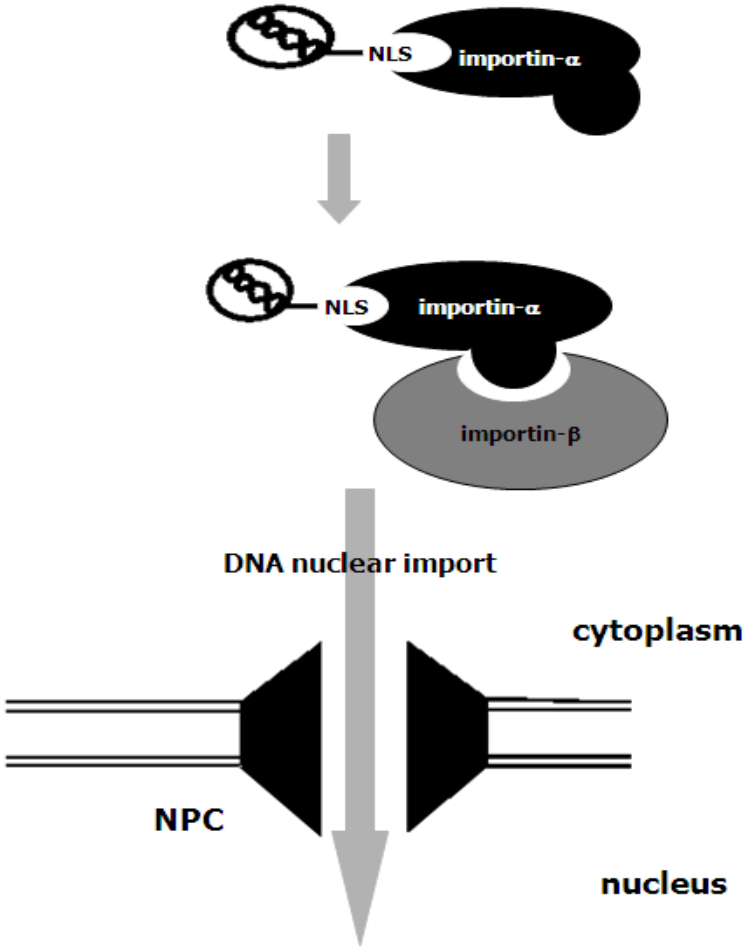

Figure 8: Schematic representation of the classical nuclear import pathway for nuclear-localising signal sequence-bearing macromolecules
Cargo macromolecules bind to importin-β via a nuclear localisation signal-importin-α conjugate to form an importin-α/β complex. This complex is then translocated across the nuclear pore complex. NLS: Nuclear localisation signal; NPC: nuclear pore complex. Adapted from Munkonge *et al* [173].

Once the pDNA successfully traverses the nuclear envelope via the NPC into the nucleus it is then ready for subsequent transcription. The next questions arising are 1) whether the pDNA dissociates from the shuttle proteins, or 2) whether it remains associated with cationic lipid, prior to accessing the transcription machinery; both are unknown and the subject of investigation by our laboratory and others. It is still not clear whether lipoplexes or polyplexes release the pDNA into the cytosol after endosomal release or if pDNA is dissociated from the cationic liposome or polymer after nuclear delivery. A study by Zabner *et al* showed that poor gene expression was obtained on microinjection of lipoplexes into the nucleus compared to the microinjection of naked pDNA, thus suggesting that separation of pDNA from the cationic liposome likely occurred in the cytosol before nuclear delivery [136]. According to Xu and Szoka, pDNA is directly released into the cytosol after endosomal escape [154]. However, in contrast to liposomes, Zabner *et al* demonstrated that similar levels of transgene expression were observed on injecting PEI-polyplexes either into the cytosol or nucleus individually, suggesting that dissociation of pDNA from the PEI-polyplex possibly occurs in the nucleus before transcription [136]. These findings are further supported by the lack of transgene expression on microinjection of cationic liposome/pDNA into the nucleus of mammalian cells, as compared to the nuclear microinjection of PEI/pDNA which results in transgene expression [184]. In the case of polyplexes, Remy *et al.*, demonstrated that pDNA is released by PEI-polyplexes in the nucleus by competitive interaction of pDNA with the genomic DNA [185].

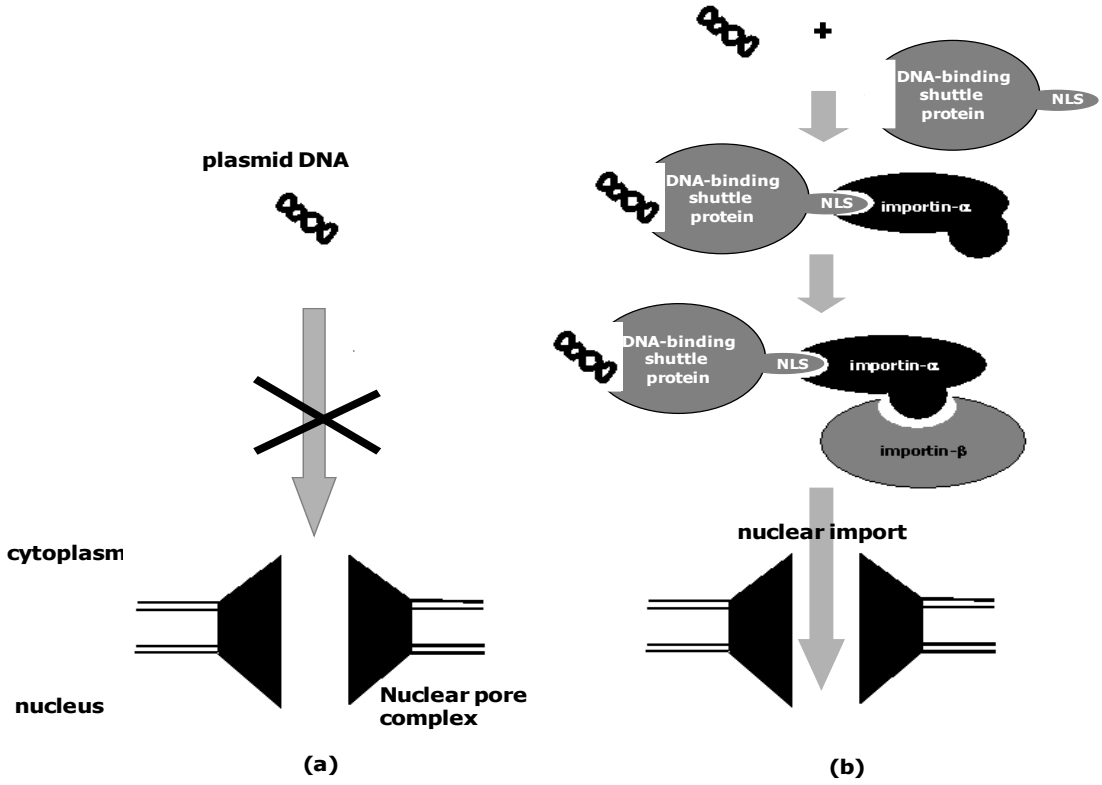

Figure 9: Schematic representation of facilitated translocation of plasmid DNA across the nuclear pore complex

The 'piggyback' model suggests that plasmid DNA molecules, which lack intrinsic nuclear targeting capability, are unable to translocate across the nuclear pore complex as free molecules (a). For plasmid DNA nuclear import to occur, the plasmid DNA cargo molecule binds to the adapter importin-α via karyophilic soluble shuttle protein possessing both DNA-binding site and nuclear localisation signal (NLS). The resulting complex then binds to the importin-β and translocates across the nucleus in the same fashion as the classical import pathway. Thus, nuclear import of plasmid DNA is facilitated via DNA-binding-NLS bearing shuttle proteins (b). Adapted from Munkonge *et al* [173].

In summary, pDNA or cationic lipid/pDNA complexes (lipoplexes or polyplexes), after overcoming the various extracellular barrier namely, extracellular matrix, mucociliary clearance and the glycocalyx of the cell surface membrane, have to circumvent a number of intracellular barriers in terminally differentiated polarised human airway epithelial cells before nuclear entry (Figure 10). The key trafficking events shown in Figure 11 include:

A) The internalisation of lipoplexes or polyplexes in the endocytic vesicles.
B) The escape of pDNA from the endosomes or degradation in lysosomes.
C) The cytoplasmic transport of released pDNA to the peri-nuclear space either via cytoskeleton microtubules or passive diffusion.
D) The active translocation of pDNA across nuclear envelope via NPC followed by transcription and translation of the transgene.

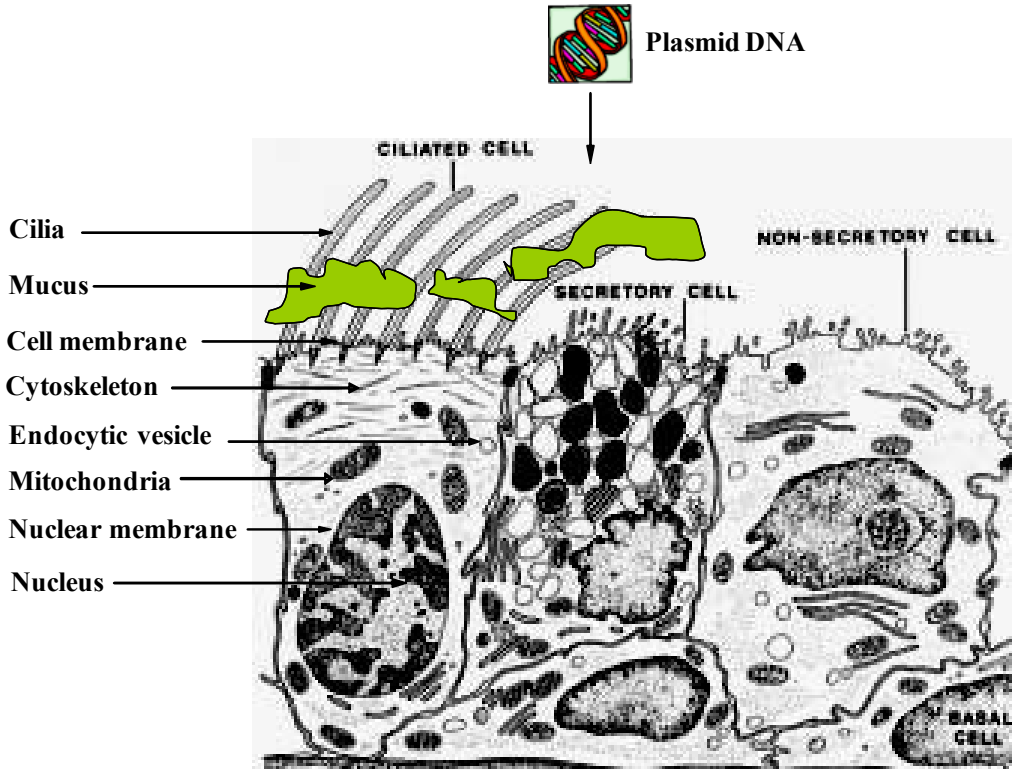

Figure 10: Schematic representation showing barriers to non-viral gene delivery
Pseudostratified epithelium consists of ciliated and non-ciliated cells (secretory, non-secretory and basal cell). Various barriers to delivery of plasmid DNA into the nucleus of ciliated epithelial cell are indicated by arrows.

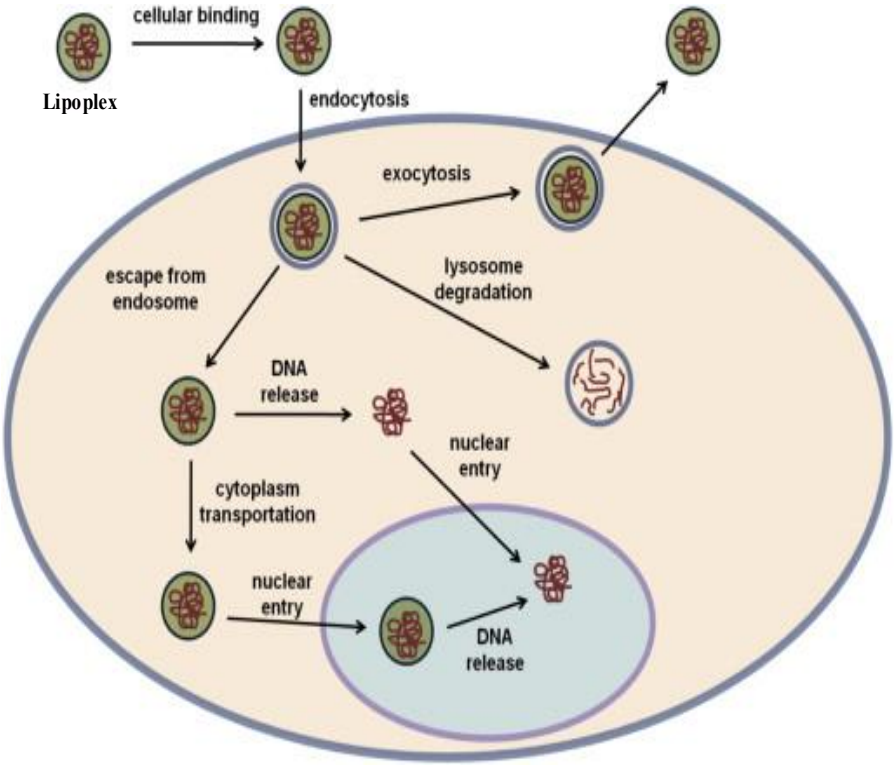

Figure 11: Schematic diagram representing intracellular trafficking of lipoplex (cationic lipid/plasmid DNA complex)
Lipoplexes bind to the cell surface membrane followed by internalisation into endosomes in the cytosol. The endosome-encapsulated lipoplexes are then either exocytosed, or mature into degradatory lysosomes, or the plasmid DNA escapes from the endosome. After endosomal escape, plasmid DNA is released by the lipoplex into the cytosol which then enters the nucleus, or the lipoplexes are delivered to the nucleus via the nuclear transport machinery. The plasmid DNA is then released from the lipoplex inside the nucleus ready for transcription. Adapted from Zhang *et al* [186].

This thesis is therefore about

a) Identifying where pDNA goes following non-viral gene transfection.
b) Quantifying relative amounts of delivered pDNA in intracellular compartments following non-viral gene transfection over time.

In order to do this, I used two parallel imaging strategies, 1) transmission electron microscopy (TEM) and 2) live-cell spinning disk confocal laser microscopy (SDCM).

As shown in Figure 12, a common feature of both the TEM and SDCM strategies to image the progress of pDNA in transfected epithelial cells was the need to label the pDNA with either an electron dense marker for TEM or fluorescent marker for SDCM. For visualisation of pDNA using TEM, on well preserved ultra-structural background of the transfected human airway epithelial cells, I labelled pDNA with 1.4 nm nanogold particles. The sequence-specific tagging of the pDNA with the nanogold particles at 1:1 stoichiometry was achieved using peptide nucleic acid (PNA) linker molecule [187]. Whilst the size of the 1.4 nm gold particles is insignificant compared to the larger pDNA molecule (~200 nm when fully condensed with cationic lipid) [188], they are, however, not sufficiently electron dense to be clearly visible on the ultrathin section from transfected airway epithelial cells using the TEM protocols. Thus, in order to clearly observe and quantitate the nanogold tagged pDNA against transfected airway epithelial cell intracellular background using the TEM method, amplification of the signal by gold-enhancement was necessary. After confirming the lack of any significant effect on the biological activity of the nanogold-conjugated pDNA, I went on to visualise and quantitate the intracellular distribution of nanogold-conjugated pDNA following transfection

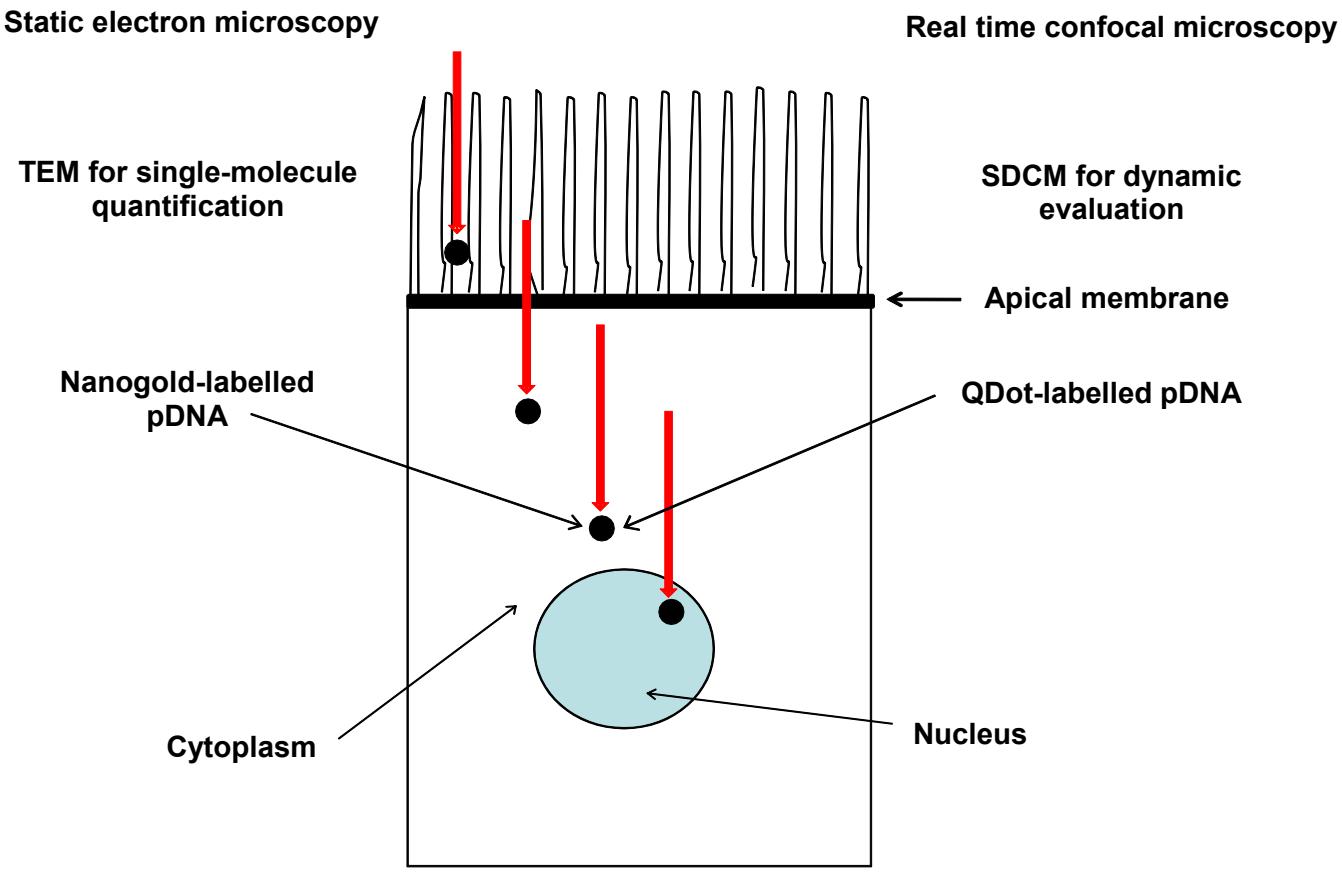

Figure 12: Parallel studies to image the intracellular fate of plasmid DNA in transfected airway ciliated epithelial cell using 1) transmission electron microscopy (TEM) and 2) spinning disc confocal laser microscopy (SDCM)

of the airway epithelial cells at different time points. In a parallel approach, I extended the above TEM study and imaged the intracellular distribution of pDNA in live human airway epithelial cells in real-time using SDCM. The pDNA was labelled in a sequence-specific manner, with ultra-bright, photo-stable fluorescent quantum dot (QDot) markers, in an identical fashion to that described for nanogold particles above. As for the nanogold labelling, the conjugation of the pDNA with QDots resulted in very little loss in biological activity. In contrast to the static snapshots obtained in fixed cells using TEM, I was able to continuously visualise the progress of the fluorescently labelled pDNA in living transfected cells over a period of 120 minutes using the combination of optical sectioning and 3-D reconstruction capabilities provided by SDCM and imaging software.

Overall study hypothesis

The hypothesis being tested is whether the nuclear delivery of plasmid DNA following non-viral gene transfer to the human airway epithelial cell is hindered by intracellular barriers.

Specific aims of the study

1. To optimise the chemical fixation technique for the preservation of intracellular ultrastructure to facilitate the visualisation of gold-labelled pDNA following non-viral gene transfer (Chapter 3).
2. To prepare and validate nanogold-conjugated pDNA for use in localisation of the gold-labelled pDNA following non-viral gene transfer (Chapter 4).
3. To assess the quantitative localisation of pDNA in human airway epithelial cells at different transfection time points using TEM (Chapter 5).
4. To assess real time quantitative localisation of pDNA in human airway epithelial cells at different transfection time points using SDCM (Chapter 6).

Chapter 2: Materials and Methods

The following chapter describes the general materials and methods used in this study. Specific materials and methods used in different experiments are described in detail in the relevant chapters. All chemicals, reagents and doubly distilled de-ionised water used throughout the experiments were of analytical grade.

2.1 Cell lines and air-liquid-interface cultures

2.1.1 Cell lines

The human embryonic kidney (HEK) 293T cells (ATCC LGC Promochem, London, UK) were maintained in Dulbecco's modified Eagle's medium (DMEM) (Sigma-Aldrich Com. Ltd, Poole, UK) supplemented with 10 % heat-inactivated foetal bovine serum (FBS) (Sigma-Aldrich Com.Ltd., Poole, UK) and 1 % penicillin/streptomycin (Sigma-Aldrich Com.Ltd., Poole, UK). To reduce phenotypic variability, only cells between passages 1 to 10 were used in this study. Cells were cultured in a humidified atmosphere at 37°C with 5 % CO_2. HEK293T cells were seeded at a density of 1×10^5 cells/well in pre-coated poly-D-lysine 6-well (35-mm diameter) plates (BD Biosciences, Oxford, UK) 24 hours before transfection.

2.1.2 Air-liquid interface cultures

Human pseudo-stratified respiratory epithelia grown at an air-liquid interface (ALI) were used in this study. Briefly, primary human airway epithelial cells were isolated from nasal polyps or bronchial biopsies. These were then seeded onto semi-permeable supports

(Transwell insert, 6.5 mm in diameter, 0.4 μm pore size). After proliferation in submerged conditions, differentiation was induced by maintaining the airway epithelial cells at an ALI [189]. Fully differentiated ALI cultures (MucilAir^{TM}) were purchased from Epithelix SARL (Geneva, Switzerland). On arrival, these were cultured in MucilAir^{TM} culture medium (700 μl/insert; in the basolateral compartment) (Epithelix) under humidified atmosphere at 37°C with 5 % CO_2 in a standard tissue culture incubator according to manufacturer's recommendation. The MucilAir^{TM} culture medium (700 μl/insert) in the basolateral compartment was replaced every 2-3 days. Viability of the ALI was routinely monitored by visual inspection of beating cilia using a light microscope (Nikon TMS-F, Japan, magnification x20). A representative image of each ALI was routinely acquired for comparison with a reference "gold standard" ALI image.

2.2 Animals and anaesthesia

Fatty acid binding protein (FABP) CF mice [190] were obtained from the University of North Carolina (UNC) and maintained at the Imperial College animal house facility. All animal studies had been approved by local Animal Ethics Committees at Imperial College and were carried out according to the UK Home Office Animals (Scientific Procedures) Act 1986.

FABP mice (8-10 weeks old) were anaesthetised with a combination of Hypnorm (Roche, Switzerland), Hypnovel (Roche) and water for injection (B Braun Melsungen AG, Melsungen, Germany) at a ratio of 1:1:4 by volume (100 μl per 10 g mouse were administered). Mice were opened ventrally and a dorsal arterio-section was performed. The nose is highly vascular, and therefore, it was important to drain out the blood completely otherwise the dissection of the nasal tissue will be obscured. The animal was turned over on

to its back and exsanguinated onto layers of absorbent tissue. The skin was removed from the head. The snout and cartilage were removed to expose the nasal cavity and the bone covering the arch of the nose was removed to expose the septum. The nasal tissue was then removed carefully from either side of the septum.

2.3 Preparation of airway epithelial tissue for transmission electron microscopy

2.3.1 Chemical fixation and processing

The airway epithelial tissue was fixed in pre-warmed 1 ml fixative 2.5% glutaraldehyde (Electron Microscopy Sciences, Hatfield PA, USA) made in phosphate buffered saline (PBS) without calcium and magnesium (Invitrogen.com/Gibco), pH 7.0 at 37°C for 30 minutes. This was further incubated at ambient temperature for 2.5 hours and finally stored overnight at 4°C. Next day, fixed sample was processed for TEM. Briefly, glutaraldehyde fixed tissue was washed with in 0.05 M, pH 7.4 sodium cacodylate buffer (Sigma-Aldrich Com.Ltd., Poole, UK) for 15 minutes (x3) followed by post fixation in osmium tetroxide (1%) (TAAB Ltd., Aldermaston, UK) made in 0.05 M sodium cacodylate buffer for 1.5 hours at room temperature. Osmium tetroxide post-fixed tissue was then washed with distilled water for 10 minutes (x2). The washed tissue was dehydrated in graded series of methanol (VWR International Ltd., Leicester, UK) i.e. 70% (15 minutes), 90% (15 minutes), 100% (15 minutes), 100% (30 minutes) under rotation (2 rotations/minute) followed by immersion in 100% propylene oxide (VWR International Ltd., Leicester, UK) , a mixture of propylene oxide and araldite (1:1 by volume) and 100% araldite (Agar Scientific Ltd., Stansted, UK), rotated for 30 minutes, 30 minutes and overnight, respectively. Next day the araldite infiltrated tissue was embedded in 100% fresh araldite followed by polymerisation of the resin at 60^{o}C for 2-3 days.

2.3.2 Sectioning of araldite embedded tissue and staining of ultrathin sections

The polymerised araldite blocks were cut with the help of a glass knife on an ultra microtome (Ultracut E, Reichert-Jung, Leica, Milton Keynes, UK). Silver-gold ultrathin sections (120 nm) were collected on copper grids (TAAB Ltd., Aldermaston, UK) for general visualisation or on nickel grids (TAAB Ltd), if the ultrathin sections were treated with gold enhancement mix. Sections were then stained with uranyl acetate (TAAB Ltd.) and lead citrate (TAAB Ltd.) as follows:

Grids were immersed with the section facing up in 1 % uranyl acetate solution filtered on a glass dish. After 7 minutes incubation at room temperature the grids were washed in 100% methanol (x4) and were dried using Whatman filter paper (Whatman International Ltd, Maidstone, England). The dried grids with the section facing down were next stained by floating on filtered drops of lead citrate for 5 minutes at room temperature. The grids were washed in distilled water (x4) and blotted dry. Finally the stained sections were observed under TEM (Hitachi 7000, Nissei Sangyo Co. Ltd., Tokyo, Japan) and pictures were captured by a digital camera fitted to TEM. The processing of biological samples for TEM is outlined in Figure 13.

Tissue

↓

Primary fixation in 2.5% glutaraldehyde (made in PBS) at 37^{o}C for 30 minutes, followed by further incubation at ambient temperature for 2.5 hours

↓

Wash with sodium cacodylate buffer for 15 minutes (x3)

↓

Secondary fixation in 1.0% osmium tetroxide for 1 hour

↓

Wash with distilled water for 10 minutes

↓

Sequential dehydration with graded methanol (at 70%, 90%, and 100%)

↓

Dehydration with propylene oxide for 30 minutes

↓

Infiltration with propylene oxide and araldite (1:1 V/V) for 30 minutes

↓

Infiltration with araldite overnight

↓

Polymerisation in araldite at 60^{o}C for two days

↓

Cut sections on ultra microtome

↓

Sections collected on grids, stained with uranyl acetate and lead citrate.

↓

Observed by TEM and image captured by a digital camera

Figure 13: Work flow of optimised chemical fixation for mouse nasal tissue for visualisation by Transmission Electron Microscope

2.4 Monomaleimido-nanogold

The 1.4 nm monomaleimdo-nanogold was purchased from Nanoprobes, Inc., New York, USA. Molecular weight =15,000 Da and extinction coefficient at 420 nm = 155,000 $M^{-1}cm^{-1}$

2.5 Peptide nucleic acid

Bis-peptide nucleic acid (PNA) with a terminal cysteine residue was purchased from Panagene, Cambridge, UK (Molecular weight = 6776 Da and extinction coefficient at 260 nm = 153.6 ml μmol^{-1} cm^{-1}. The synthesised PNA contains the following sequence: cLLLTTTCTCCCTTCLLLJTTJJJTJTTT (where c = cysteine, L = *N*-(2-aminoethyl) aspartic acid (AEAA) linker, C = cytosine, T = thymine, J = psuedocytosine). Figure 14 shows that the two 11-mer sequences are linked covalently via three linker molecules (LLL) and the N terminus of the PNA containing the cysteine (c) is also linked to one of the arm of 11-mer via three linker units. PNA can be linked covalently to any probe (electron-dense or fluorescent) via the monomaleimide functional group.

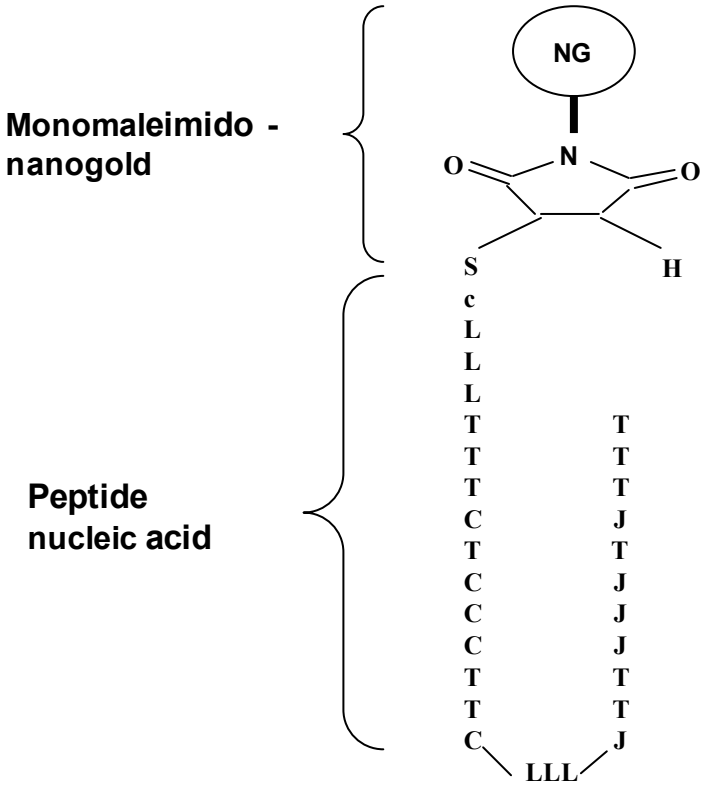

Figure 14: Schematic representation of bis-peptide nucleic acid

The bis-peptide nucleic acid (PNA) contains two 11-mer sequences which are covalently linked via three linker molecules (LLL). The cysteine (c) is located on one arm of 11-mer sequences also via three linker units (LLL). The terminal cysteine thiol group on the PNA was covalently linked with the maleimide moiety on the monomaleimido-Nanogold (NG) to produce a PNA-Nanogold-conjugate. L = *N*-(2-aminoethyl) aspartic acid (AEAA) linker, C = cytosine, T = thymine, J = psuedocytosine). Adapted from Hilary *et al* [187].

2.6 Gene transfer materials

2.6.1 Plasmid DNA

Three different plasmids carrying eukaryotic regulatory elements were used in this study.

- pCIKFluc: The pCIKFluc plasmid (subsequently referred to as pCMV-Fluc;) used in this study was provided by Dr. Deborah Gill (Gene Medicine Group, University of Oxford, UK). It carries the *Firefly* luciferase (Fluc) reporter gene under control of the eukaryotic immediate/early CMV promoter/ enhancer. The pCIKFluc plasmid map showing the specific PNA target site containing the 8-mer sequence (AAGGGAGA) and restriction sites are shown in Figures 15 and 16 respectively. The DNA concentration was measured by UV absorption at 260 nm.

- pCIKGluc: The pCIKGluc plasmid (subsequently referred to as pCMV-Gluc1) carrying secreted *Gaussia* luciferase (Gluc) reporter gene under control of the eukaryotic immediate/early CMV promoter/ enhancer was purchased from Aldevron (Fargo, ND, USA). It was prepared using a strategy described previously in which Fluc reporter gene in pCIKFluc plasmid was replaced with the Gluc reporter gene [59].

- pCIKCFTR: The pCIKCFTR plasmid was kindly obtained from Dr. Deborah Gill (Gene Medicine Group, University of Oxford, UK). The plasmid contains the human *CFTR* cDNA under the control of the eukaryotic CMV immediate-early promoter/enhancer and served as a negative control throughout this study.

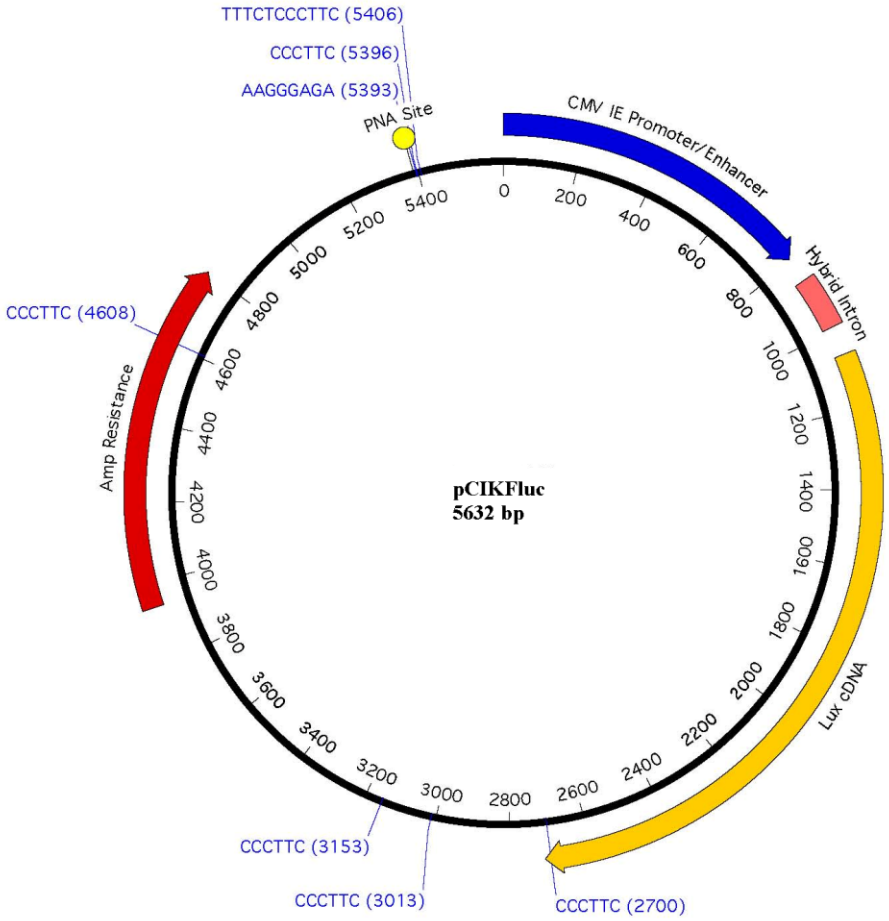

Figure 15: The pCIKFluc plasmid map showing Peptide Nucleic Acid target site
The nanogold-conjugated PNA hybridises to pCIKFluc via an 8-bp (AAGGGAGA) specific target sequence at position 5393 (bp).

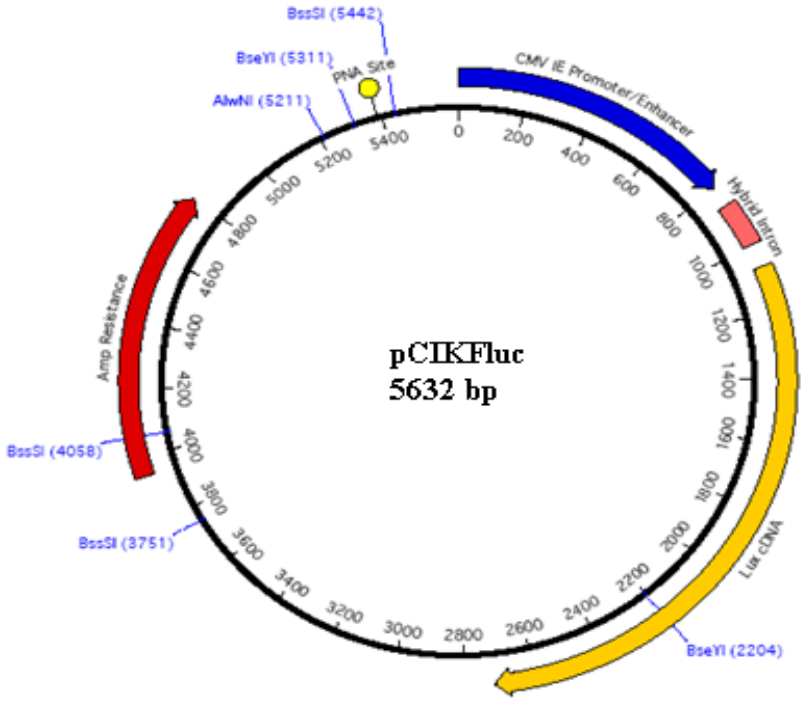

Figure 16: Plasmid CIKFluc restriction enzyme map
The pCIKFluc plasmid restriction map indicating the potential restriction fragments, including the 131-bp (5442-5311) fragment containing the nanogold-PNA conjugate hybridisation site, generated from digestion by the endonucleases BssSI and BseY1.

2.6.2 Cationic liposomes and their formulation with plasmid DNA

Two different types of cationic liposomes were used in this study:

Genzyme Lipid 67A (GL67A): The cationic lipid GL67A (Genzyme Corporation, Framingham, USA), optimised for airway gene transfer, comprises the cationic lipid GL67 {Cholest-5-en-3-ol(3beta)-,3-[(3-aminopropyl)[4-[(3-aminopropyl) amino]butyl]carbamate]} (Genzyme Haverhill, UK), DOPE (1,2-dioleoyl-sn-glycero-3-phosphoethanolamine) and DMPE-PEG5000 (1,2-Dimyristoyl-sn-Glycero-3-Phosphoethanolamine-N-[methoxy (Polyethylene glycol)5000]) (Avanti, Alabaster, Alabama, USA) [29;41]. GL67A was generated using the three lipids formulated at 1:2:0.05 (GL67:DOPE:DMPE-PEG5000) molar ratios and freeze-dried by OctoPlus (Leiden, The Netherlands). GL67A was used for *in vitro* transfection of ALIs. GL67A was re-suspended in water for injection (WFI) (B.Braun Medical Ltd., Sheffield, UK) to a final concentration of 11.4 mM at room temperature. This was vortexed for approximately 45 minutes at 2400 rpm (revolutions per minute) (DVX-2500 Multi-Tube Vortexer, VWR International, Lutterworth, UK) to give a homogeneous suspension. Lipid GL67A/pDNA complexes for ALI culture experiments were prepared as previously described at 6:8 lipid: DNA molar ratio containing approximately 2.65 mg pDNA/ml final formulation [33]. The same formulation was used in previous clinical studies [29]. Lipid GL67A/pDNA complexes, as previously described at 1:4 (lipid:DNA) molar ratio containing approximately 0.8 mg pDNA/ml final formulation, used for mouse nasal instillation and perfusion experiments, were also generated [82]. Briefly, equal volumes of re-suspended GL67A (11.4 mM) and pDNA (15.2 mM, 5 mg/ml, based on an average molecular weight per nucleotide 330 g/mol) equilibrated at 30°C for 5 min were mixed to achieve a molar ratio of 6:8 (GL67A: pDNA). The complexes were then incubated at room temperature for 15 minutes before use. For the generation of 1:4 molar ratio, re-suspended GL67A (11.4

mM) was diluted to a final concentration of 1.2 mM in WFI followed by mixing of equal volumes of re-suspended GL67A (1.2 mM) and pDNA (4.8 mM, 1.6 mg/ml, based on an average molecular weight per nucleotide 330 g/mol) as described for 6:8 molar ratio.

Lipofectamine: Lipofectamine™ 2000 (Invitrogen, Paisley, UK), was used for *in vitro* transfection of HEK 293T cell line. Briefly, equal volumes of pDNA and lipofectamine™ 2000 were complexed at a weight:weight (w:w) ratio of 1:2.5 (pDNA: lipofectamine), in OptiMEM (Invitrogen, Paisley, UK) and incubated for 15 minutes at room temperature according to manufacturer's recommendations.

2.7 Covalent linkage of nanogold to peptide nucleic acid and hybridisation of the resultant conjugate to plasmid DNA

Cysteine-terminated PNA was reduced by incubation for 1 hour at room temperature with 1.5 mg of mercaptoethylamine hydrochloride (MEA) (Sigma-Aldrich Com. Ltd., Poole, UK) dissolved in 1 ml of 0.1 M sodium phosphate buffer, pH 6.0, containing 5 mM EDTA. The unreacted MEA was removed by membrane centrifugation using micro concentrator (cut-off limit 3000 Da; Millipore, UK). The monomaleimide terminated nanogold, reconstituted in 1 ml de-ionised water, was added immediately to the reduced cysteine terminated PNA at a 15 molar excess and incubated at room temperature for 16 hours with end-to-end mixing. The resulting PNA–nanogold conjugate was then hybridized to pDNA at a molar ratio of 100:1 (PNA–nanogold: pDNA) in sterile TE hybridization buffer (10 mM Tris, 1 mM EDTA, pH 6.5) overnight at 37°C, where the molarity of the pDNA was 0.5 μM. At this stage an equal amount of monomaleimide terminated nanogold reconstituted in 1 ml de-ionised water was also added immediately to the same amount of controlled pDNA and both preparations were treated in the same way. The unbound PNA–nanogold was removed by membrane

centrifugation using a micro concentrator (cut-off limit 10,000 Da; Millipore, UK). The nanogold-PNA-pCIKFluc conjugate (nanogold-conjugated pDNA) was precipitated using *n*-butanol, followed by centrifugation at 14,400 *g* for 10 minutes at 4°C. The supernatant was removed and nanogold-conjugated pDNA was re-precipitated by adding potassium acetate (3 M) followed immediately by addition of 70% (v/v) ethanol. The pellet (nanogold-conjugated pDNA) collected after re-centrifugation was air-dried and re-suspended in sterile 150 mM sodium chloride (NaCl) overnight at 4°C. The work flow of the preparation of nanogold-conjugated pDNA is shown in figure 17.

2.8 Spectrophotometric analysis of nanogold-conjugated plasmid DNA

The sample (2 μl) was added to 150 mM NaCl (500 μl) in duplicate in a quartz cuvette and gently mixed by inversion. The absorbance of pDNA and the nanogold was measured at 260 nm and 420 nm respectively using a Unicam UV1 spectrophotometer Thermospectronic, Cambridge, UK) with a 1 nm bandwidth. The concentration of pDNA and nanogold in the nanogold-conjugated pDNA, and the concentration of pDNA in the control unconjugated pDNA were determined from the absorbance values measured at 260 nm and 420 nm respectively.

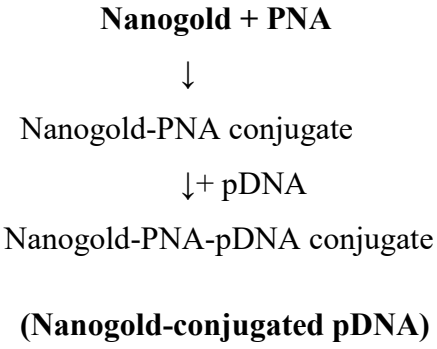

Figure 17: Work flow of the preparation of nanogold-conjugated plasmid DNA
The peptide nucleic acid is covalently linked with monomaleimido nanogold to form the nanogold-PNA conjugate which is then hybridised to the target site on a plasmid DNA in a sequence-specific manner. Control plasmid DNA is mixed with nanogold without PNA and is subjected to the similar purification steps as nanogold-conjugated plasmid DNA.

2.9 Visualisation of nanogold-conjugated pDNA using super-resolution TEM

Nanogold-labelling of pDNA was visualised directly using a super resolution TEM (Philips CM 200 FEG, Eindhoven, Holland). Nanogold-conjugated pDNA, unconjugated pDNA or nanogold was put on a Formvar-carbon coated copper grid (Agar Scientific Limited, Essex, UK) for 2 minutes followed by washing with de-ionised water. The grid was then stained with uranyl acetate. The residual uranyl acetate was then blotted off using Whatman filter paper. The grid was then air-dried and observed under TEM.

2.10 Spot test to detect nanogold in nanogold-conjugated plasmid

This test for the detection of nanogold in a given sample was recommended by Nanoprobes. Briefly, a drop containing equal amount of nanogold, nanogold-conjugated pDNA and a control unconjugated pDNA was applied on a nitrocellulose membrane (1 cm x 1 cm) individually. The samples were dried for 30 minutes followed by quick immersion of the nitrocellulose membrane, using tweezers, in de-ionised water. The nitrocellulose membrane is then placed in a petri dish followed by addition of 30 µl of freshly prepared gold-enhancement mix. The colour change was observed on the nitrocellulose membrane and pictures were taken before, and after, treatment with gold-enhancement mix.

2.11 Agarose gel electrophoresis

Loading buffer (cyan-orange dye x6000, 3 µl) (Invitrogen, Paisley, UK) was added to samples (1 µl at 1 mg DNA/ml) of nanogold-conjugated pDNA, unconjugated pDNA, a physical mix of unconjugated pDNA with nanogold particles, or pure nanogold particles

alone. Samples were loaded onto a 0.9% agarose gel containing Gel Red 10,000x in water (Biotium, Inc., California, USA). A 2-16 kbp super-coiled ladder (1 µl at 1 mg DNA/ml) (Invitrogen, Paisley, UK) was also loaded as a reference marker. The electrophoresis was run at 90 volts until the cyan-orange marker dye band reached the bottom edge of the gel. The resolved bands of pDNA, stained with Gel Red, were visualised using a 2UV Transilluminator and Multi Doc-It Digital Imaging System (UVP, Inc., California, USA) and images were captured using a digital camera.

Endonuclease restriction enzyme digestion

A double digestion using the endonucleases *BssSI* and *BseYI* was carried out according to the supplier's instructions (Biolab, England). Briefly, the digestion mix (20 µl) was composed of nanogold conjugated pDNA (1 µl at 1 mg DNA/ml) or unconjugated pDNA (1 µl at 1 mg DNA/ml), water for injection (15 µl), digestion buffer N3 x10 (2 µl), restriction enzyme *BseYI* (1 µl) and restriction enzyme *BssSI* (1 µl) was digested at 37°C for 1.5 hours. The resultant digestion fragments were then dissolved in the above agarose electrophoresis loading buffer and run on 3% agarose gel containing Gel Red as described previously with a 25 bp size ladder (1 µl at 1 mg/ml) (Invitrogen, Paisley, UK). The restriction fragments of pDNA stained with Gel Red were visualised and images were acquired using a digital camera.

2.12 Visualisation of nanogold attached to plasmid DNA on agarose electrophoresis gels by silver enhancement

Equal amounts of initiator and enhancer were mixed and incubated at room temperature for 30 minutes. Undigested pDNA or restriction fragments were run on agarose gels as described

above. The agarose gel was observed in an UV illuminator. The gel was then washed 5 times in de-ionised water for 3 minutes, observed under UV light and images taken using a digital camera. The gel was then transferred to a pre-washed glass tray filled with 50 ml silver-enhancement mix (Nanoprobes, NY, USA). Colour development was observed for 30 minute, prior to the acquisition of images.

2.13 Transfection of human embryonic kidney cells and preparation of cell lysates for *Firefly* luciferase reporter gene assay

HEK293T cells were seeded onto a pre-coated poly-D-lysine 6-well (35-mm diameter) plate at a density of 300,000 cells/ well and cultivated with 2 ml of growth medium (DMEM) supplemented with 10% heat-inactivated foetal bovine serum (FBS) and 1% penicillin/streptomycin for 24 hours at 37°C until 60–70% confluent. Next day the media in each well was replaced with fresh DMEM supplemented with 10% heat-inactivated foetal bovine serum (FBS) and 1% penicillin/streptomycin. The transfection complex (pDNA/lipofectamine) was freshly prepared as described in section 2.6.2. The cells were transfected with 400 µl (per well) of the transfection complex containing 1 µg of nanogold-conjugated pCIKFluc (or the unconjugated pCIKFluc and pCIKCFTR controls) and 2.5 µl lipofectamine™ 2000 reagents. After 6 hours incubation, the transfection media was replaced with fresh media and the cells were incubated for a further 19 hours prior to harvesting for reporter gene activity measurement. The culture medium was removed and cells washed with PBS buffer prior to mixing with 300 µl of reporter gene assay lysis buffer (1x) (Roche Diagnostics GmbH, Manheim, Germany). After three freeze-thaw cycles (−80°C for 30 minute and 37°C for 20 minutes, respectively), the cell lysates were centrifuged at 14,000 rpm and 4°C for 10 minutes to remove cell debris and the supernatant was collected.

The supernatant was used for luciferase expression and total protein determination (determined by Bio-Rad protein assay (Bio-Rad Labs, Hertfordshire, UK)) immediately, or stored at -80°C for analysis at a later time.

2.14 Quantification of *Firefly* luciferase expression

The cell lysates obtained as described above were assayed for luciferase expression according to the manufacturer's recommendations (Luciferase assay Kit, Promega, Southhampton, UK). The assay, as shown in Figure 18, is based on measuring the light units produced when the substrate benzothiazole (beetle luciferin) is converted into oxy-luciferin by *Firefly* luciferase. Briefly, 100 µl Luciferase assay mixture (Luciferase Assay substrate and Luciferase Assay Buffer) was added to 20 µl cell lysates in a 96 well plate and its fluorescence intensity in terms of relative light units (RLU) was immediately measured using a luminometer (Appliskan; Thermo Electron Corporation, Vantaa, Finland). All the samples were assayed in duplicate and required further dilution with lysis buffer in order to make sure that they fell within the linear detection range of the equipment. The relative light unit (RLU) readings were normalised against protein concentration to give the specific activity (RLU/mg cell lysate protein).

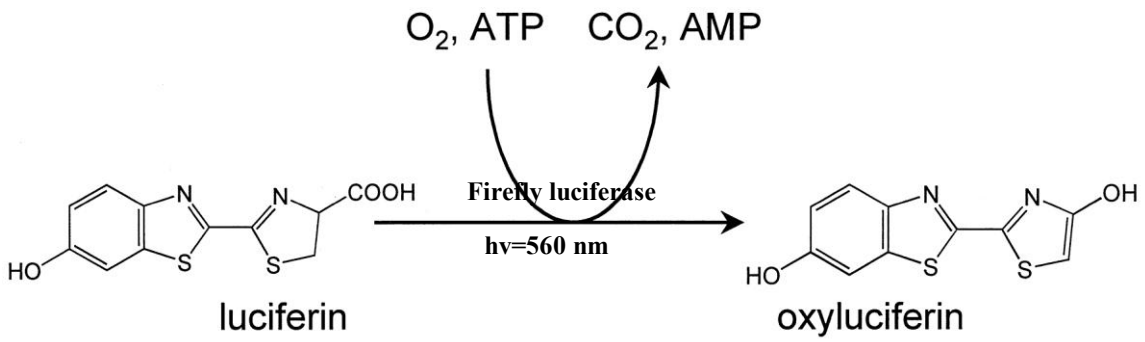

Figure 18: The photo-oxidation catalysed by *Firefly* luciferase
Firefly luciferase, a luciferase reporter from *Photinus pyralis,*catalyses the oxidation of the substrate luciferin in a reaction that produces yellow-green light at 560 nm. Modified from Gomi and Kajiyama [191].

2.15 Transfection of human airway epithelial cells with *Gaussia* luciferase reporter plasmid

Fully differentiated ALI cultures were transfected apically at 37^{o}C with 100 µl complex (per ALI) of cationic lipid GL67A and pCIKGluc in 1:4 or 6:8 molar ratios, made in OptiMEM (Invitrogen.com). Untransfected ALI cultures served as negative controls. The transfection complexes were removed from the apical side at indicated time points after transfection, the medium in the basolateral compartment was replaced and ALI cultures were further incubated at 37^{o}C. After 48 hours of incubation, 100 µl of MucilAir^{TM} culture medium was added to the apical side and incubated for 1 hour at 37^{o}C. The apical medium was harvested after washing the ALI cultures by gently pipetting the medium up and down five times. Care was taken not to pierce the pipette tip through the membrane support on which the ALI cultures grow. The basolateral media were also harvested at the same time. The harvested apical and basolateral media were centrifuged at 14,000 rpm for 10 minutes at 4^{o}C. The supernatants collected were either used immediately for Gluc reporter gene expression or stored at -80^{o}C for analysis at a later time.

2.16 Quantification of *Gaussia* luciferase expression

Gluc activity was determined according to manufacturer's recommendations (*Gaussia Luciferase* Assay Kit, New England BioLabs Inc. Herts, UK). The assay is based on measuring the intensity of blue-green light which is emitted at approximately 475 nm when the enzyme *Gaussia* luciferase, secreted into the culture medium, catalyses the oxidation of the substrate coelenterazine producing coelenteramide and carbon dioxide as shown in Figure 19. In brief, 50 µl of *Gaussia* luciferase assay solution (50 µl Gluc substrate and 5 ml Gluc

assay buffer) was added to 15 µl culture medium in a 96 well plate and luciferase activity was measured at 470 nm using a luminometer (Appliskan plate reader) (Thermo Fisher Scientific, Basingstoke, UK). All the samples were assayed in duplicate. The reporter gene expression was expressed as Gluc (RLU/µl medium).

2.17 Statistical analysis

Unless otherwise indicated, data are expressed as medians for the indicated number of experiments. The Kolmogorov–Smirnov (K-S) normality test was performed to assess the normality of distribution of the data. A parametric unpaired *t*-test or a non-parametric Mann-Whitney test was carried out for two group comparisons of normal and not normally distributed samples respectively. One-way analysis of variance (ANOVA) followed by Bonferroni *post-hoc* corrections (parametric) or a Kruskal-Wallis with Dunn's Multiple *post-hoc* corrections (non-parametric) were used for more than two group comparisons. Please note that all data are expressed as medians for convenience. In all cases the null hypothesis was rejected at $p < 0.05$. All analysis was performed using GraphPad Prism4 (GraphPad Software, Inc., La Jolla, CA, USA).

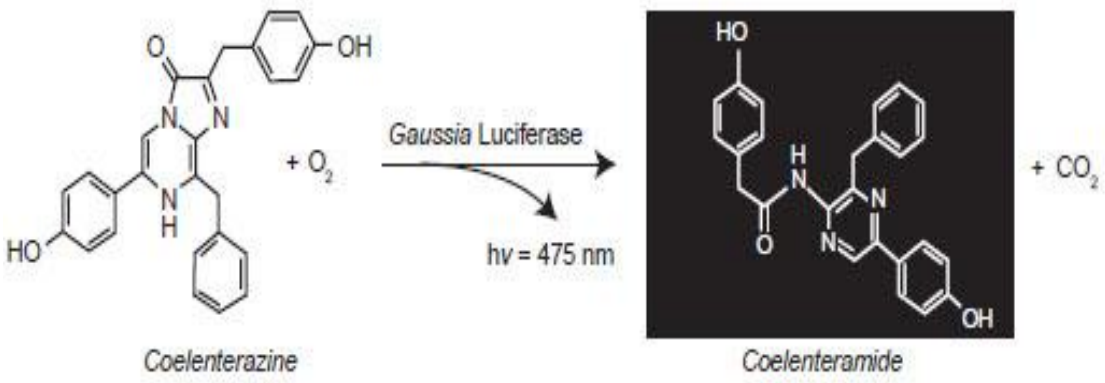

Figure 19: The photo-oxidation catalysed by *Gaussia* luciferase
Gaussia luciferase, a luciferase reporter protein secreted by the marine copepod *Gaussia princeps,* catalyses the oxidation of the substrate coelenterazine in a reaction that produces blue-green light at 475 nm. Adapted from www.neb.com.

Chapter 3: Optimisation of the chemical fixation of airway tissue to preserve intracellular structure

3.1 Introduction

In order to visualise pDNA inside the cell, we needed to preserve as much of the relevant ultrastructure as possible. For example, cellular elements involved in the intracellular transport of pDNA such as the cytoskeleton or endocytic vesicles are not very well preserved after conventional TEM pre-processing. Thus, I initially set out to optimise the conventional tissue fixation protocol to enable the preservation of key features involved in intracellular transport of pDNA following non-viral gene transfer to the ciliated airway epithelial cells.

Whilst we, and others, have historically used the *ex vivo* mouse nasal epithelium as a convenient model for studies of human airway structure, electrophysiology and gene transfer, it has become apparent that the model is far from ideal [192]. The human airway epithelial cells grown at the air-liquid interface (ALI) culture model consisting of primary human airway epithelial cells grown on permeable supports to form pseudostratified epithelia represent a superior laboratory experimental model in which to study gene transfer [189;193]. Recently ALI cultures have become commercially available from Epithelix Sarl (Epithelix Sarl, Geneva, Switzerland). These cultures have an excellent shelf life of at least one year and mimic the morphological and functional characteristics of human airway respiratory epithelium. Briefly, these cultures are developed by seeding human airway epithelial cells, isolated from nasal polyps or bronchial biopsies of healthy volunteers, onto a semi-permeable membrane. While keeping human airway epithelial cells submerged, they proliferate and reach confluency. Then differentiation is induced by removing the medium from the apical

side and exposing the apical membrane to air. The ALI culture with a basolateral side exposed to nutrient medium and an apical side exposed to air is shown in Figure 20. It comprises a pseudostratified epithelium of ciliated and non-ciliated cells (goblet cells), thus resembling the native human airway epithelium.

I, therefore, completed the chemical fixation method optimisation, initially performed in mouse nasal epithelium, by fine-tuning it to preserve ultrastructure in ALI. The polytetrafluoroethylene (PTFE) permeable-supports on which the primary cells are grown on in ALI are susceptible to degradation by methanol and propylene oxide; these reagents were therefore replaced with ethanol for the dehydration of glutaraldehyde fixed samples during TEM processing.

Hypothesis

Cytoskeleton stabilising or mild permeablising agents preserve the intracellular ultrastructure of airway epithelium.

Aims

To optimise the chemical fixation technique for the preservation of intracellular ultrastructure to facilitate the visualisation of gold-labelled pDNA following non-viral gene transfer.

Assessed the effect of:

1) fixation in glutaraldehyde made in PBS
2) fixation in glutaraldehyde made in cytoskeleton stabilising buffer
3) taxol on microtubule stabilisation
4) saponin permeabilisation

on preservation of intracellular ultrastructure of airway epithelium.

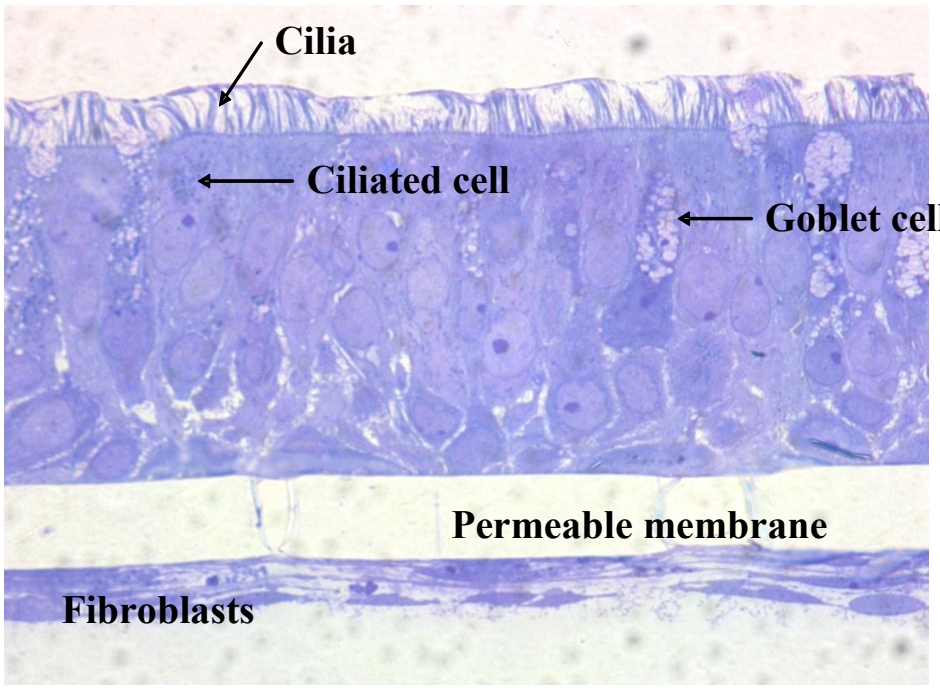

Figure 20: Human airway epithelial cells grown at an air-liquid interface
Cross-section of pseudostratified ALI on a permeable membrane support which is in contact with basolateral growth medium (original magnification x100).

3.2 Materials and Methods

Described in detail in Materials and Methods Chapter 2

3.2.1 Chemical fixation of mouse nasal epithelium and processing for TEM

The mouse nasal tissue was removed and processed for TEM as described under Sections 2.2 and 2.3 respectively and outlined in Figure 13.

3.2.2 Effect of cytoskeletal buffer on preservation of microtubule ultrastructure during chemical fixation of mouse nasal epithelial tissue

The excised mouse nasal tissue was fixed in 1 ml 2.5% glutaraldehyde made in cytoskeletal buffer, pH 7.0 (Cytoskeleton Inc., Denver, USA) for 30 minutes at 37°C. This was further incubated at ambient temperature for 2.5 hours and finally stored overnight at 4°C. Next day, fixed epithelial tissues were processed for TEM as outlined in Figure 13.

3.2.3 Effect of taxol on preservation of microtubule ultrastructure during chemical fixation of mouse nasal epithelial tissue

The excised mouse nasal tissue was treated with taxol (Sigma-Aldrich Com.Ltd., Poole, UK) at two different concentrations (2 μM and 10 μM) for 15 minutes at 37°C followed fixation by adding 2.5% glutaraldehyde made in PBS without calcium and magnesium, pH 7.0 for 30 minutes (163;202). This was further incubated at ambient temperature for 2.5 hours and

finally stored overnight at 4°C. Next day, fixed epithelial tissues were processed for TEM (Figure 13).

3.2.4 Effect of saponin on preservation of overall cytoskeleton ultrastructure during chemical fixation of mouse nasal epithelial tissue

The excised mouse nasal tissue was treated with saponin (Sigma-Aldrich Com.Ltd., Poole, UK) at three different concentrations (0.01%, 0.02% and 0.05%) for 15 minutes at 37°C followed by adding 2.5% glutaraldehyde made in PBS without calcium and magnesium, pH 7.0 for 30 minutes (205;206). This was further incubated at ambient temperature for 2.5 hours and finally stored overnight at 4°C. Next day, fixed epithelial tissues were processed for TEM as outlined in Figure 13.

3.2.5 Chemical fixation of human airway epithelial cells grown at an air-liquid interface

Fully differentiated ALIs were obtained as described previously (Section 2.1.2). The ALIs were fixed in 2.5% glutaraldehyde made in PBS without calcium and magnesium, pH 7.0 at 37°C for 30 minutes followed by a further incubation at ambient temperature for 2.5 hours. These were further fixed overnight at 4°C. Next day, fixed epithelial cells were processed for TEM as outlined in Figure 13 with replacement of both methanol and propylene oxide by ethanol.

3.3 Results

Conventionally tissue preparation for TEM is fixed at ambient temperature with 2.5% glutaraldehyde made in 0.2 M, pH 7.4 sodium cacodylate buffer [194]. Replacement of sodium cacodylate buffer with phosphate buffer saline (PBS) has been shown to yield better retention of intracellular structure (basic protocols for TEM). We therefore fixed the tissue at 37^{o}C for 30 minutes in 2.5% glutaraldehyde made in PBS without calcium and magnesium, pH 7.0 followed by further incubation for 2.5 hours at an ambient temperature. Other additions to the modified chemical fixation method protocol were: 1) cytoskeleton buffer, 2) taxol and 3) non-ionic detergents such as saponin.

3.3.1 Chemical fixation of mouse nasal epithelial tissue in glutaraldehyde made in phosphate buffer saline at 37°C

Fixing the mouse nasal epithelial tissue at 37^{o}C in 2.5% glutaraldehyde dissolved in PBS resulted in preserved ultrastructure. At low magnification, the mouse nasal epithelium comprises well differentiated polarised cells with distinct apical and basolateral surfaces. The pseudostratified epithelium consists of ciliated and non-ciliated goblet cells, along with basolaterally-located basal cells (Figure 21A). Various intracellular structures, notably, cytoskeleton components such as the microtubules network along with comparatively thinner filaments, well preserved mitochondria with cristae, assorted vesicles, nucleus with nuclear matrix and well defined nuclear membrane were clearly visible at higher magnifications (Figure 21B and 21C).

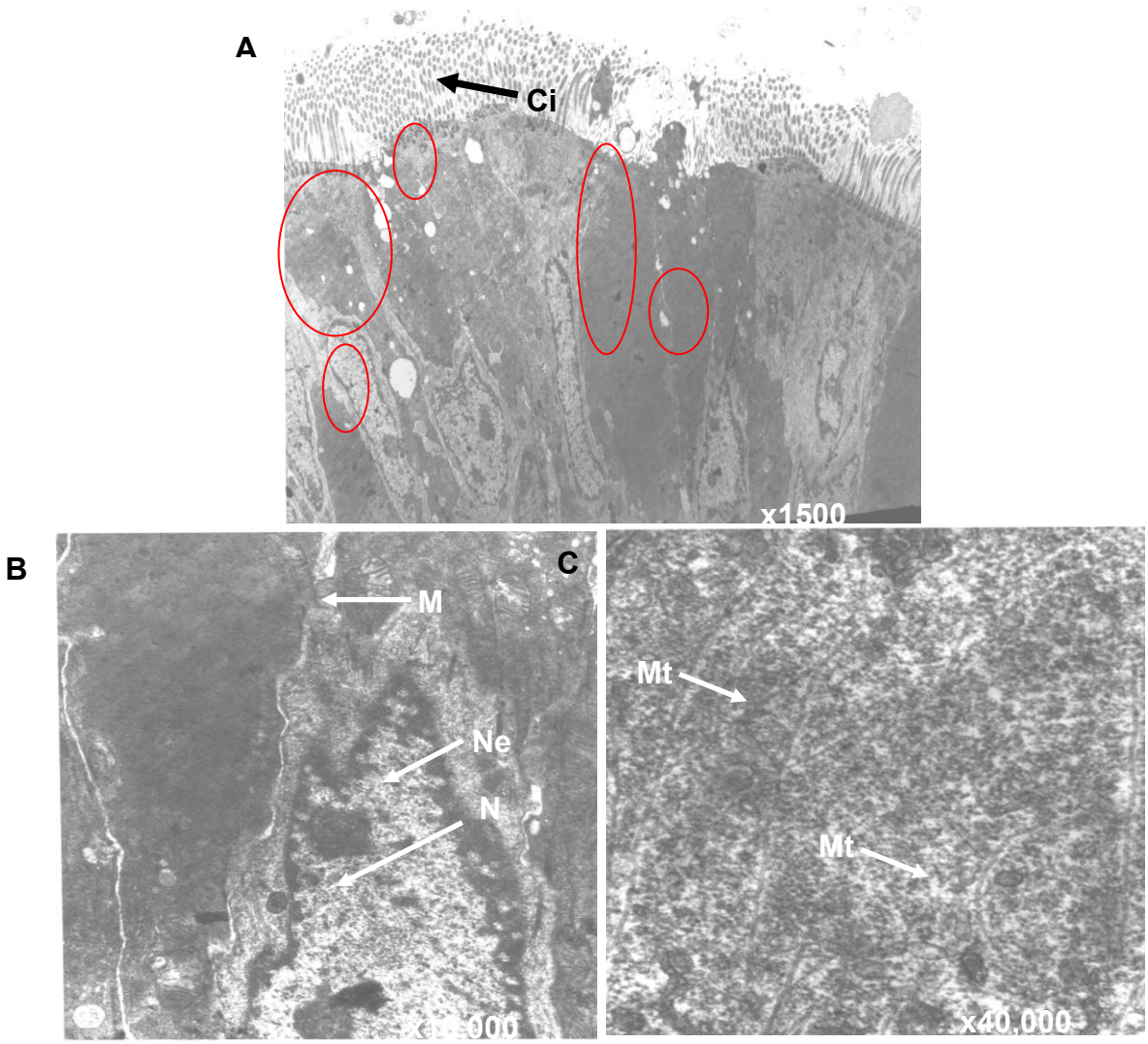

Figure 21: Representative transmission electron micrograph of mouse nasal tissue fixed in glutaraldehyde

Mouse nasal epithelium was fixed with 2.5% glutaraldehyde in PBS at 37^{o}C for 30 minutes followed by further incubation at room temperature for 2.5 hours. The fixed mouse nasal epithelium was processed for TEM. Ultrathin sections stained with uranyl acetate and lead citrate were observed under TEM at low (x1500) magnification (*A*) , higher (x10,000) magnification (B) and (x40,000) magnification C) showing cilia (Ci), mitochondria (M) and microtubule (Mt) in the cytoplasm and nucleus (N) with a well defined nuclear envelope (Ne) all indicated by arrows labelled accordingly. Circles indicate artefacts resulting from cutting of fixed tissue with ultramicrotome. Representative of three independent experiments.

3.3.2 Effect of cytoskeletal buffer on preservation of microtubule ultrastructure during chemical fixation of mouse nasal epithelial tissue

No improvement in the preservation of microtubule ultrastructure was observed on fixing mouse nasal epithelial tissue in glutaraldehyde made in cytoskeletal buffer at 37°C compared to fixation in 2.5% glutaraldehyde made in PBS (Figure 22).

3.3.3 Effect of taxol on preservation of microtubule ultrastructure during chemical fixation of mouse nasal epithelial tissue

The preservation of microtubules was not enhanced on treating mouse nasal epithelial tissue with taxol prior to fixation in glutaraldehyde made in PBS at 37°C compared to fixation in 2.5% glutaraldehyde made in PBS (Figure 23).

3.3.4 Effect of saponin on preservation of overall cytoskeleton ultrastructure during chemical fixation of mouse nasal epithelial tissue

Again, I found that treatment of mouse nasal epithelial tissue with different concentrations of saponin prior to fixation in glutaraldehyde made in PBS at 37°C did not improve the preservation of cytoskeleton ultra structure compared to fixation in 2.5% glutaraldehyde made in PBS (Figure 24).

In summary, results from the work done to optimise the preservation of microtubules in mouse nasal epithelium under different conditions are summarised in Table 1.

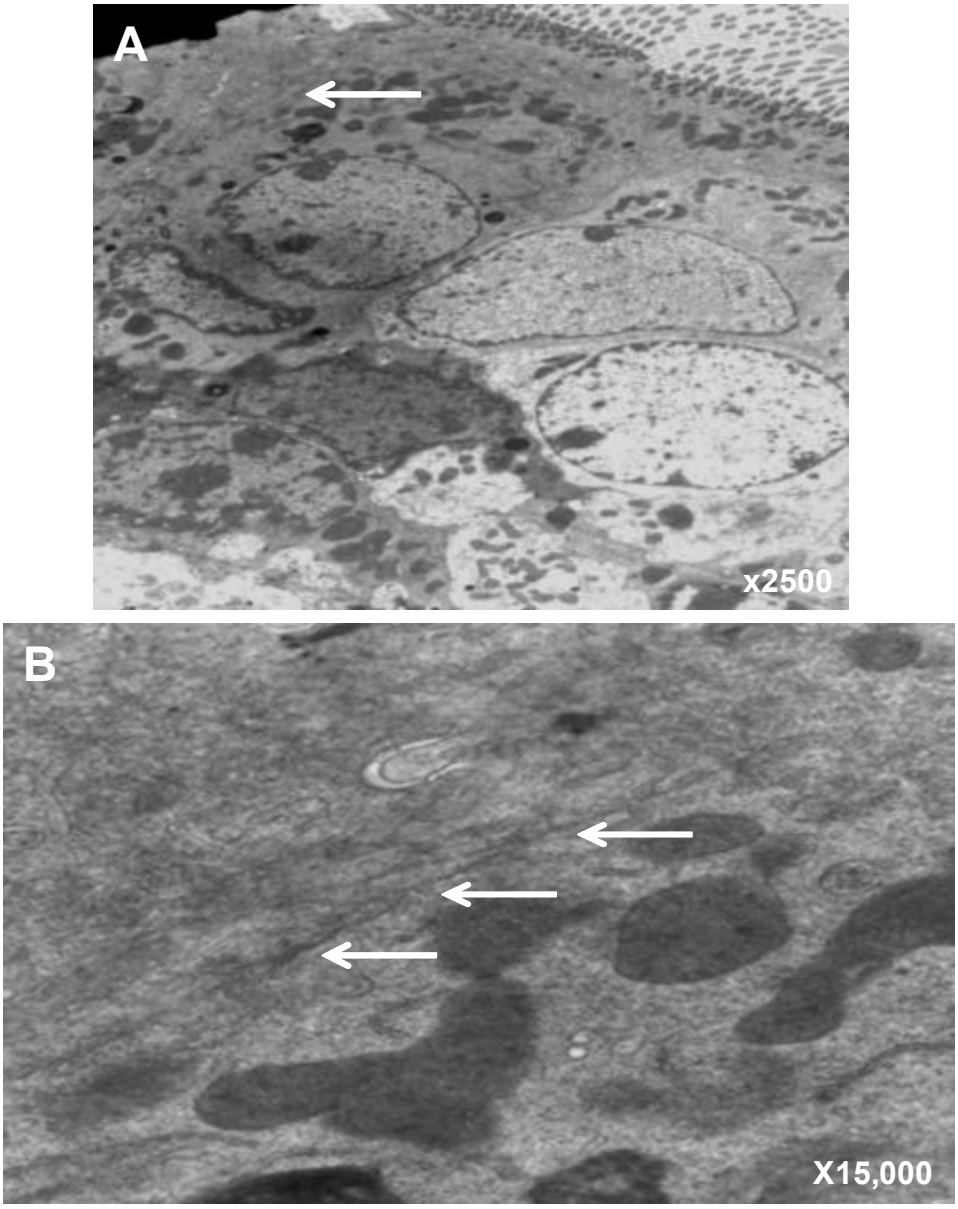

Figure 22: Representative transmission electron micrograph of mouse nasal tissue fixed in glutaraldehyde made in cytoskeletal buffer

Mouse nasal epithelium was fixed with 2.5% glutaraldehyde made in cytoskeletal buffer at 37^{o}C for 30 minutes followed by further incubation at room temperature for 2.5 hours. The fixed mouse nasal epithelium was processed for TEM. Ultrathin sections stained with uranyl acetate and lead citrate were observed under TEM at low (x2500) magnification (*A*), higher (x15,000) magnification (B) showing microtubules (white arrows). Representative of three independent experiments.

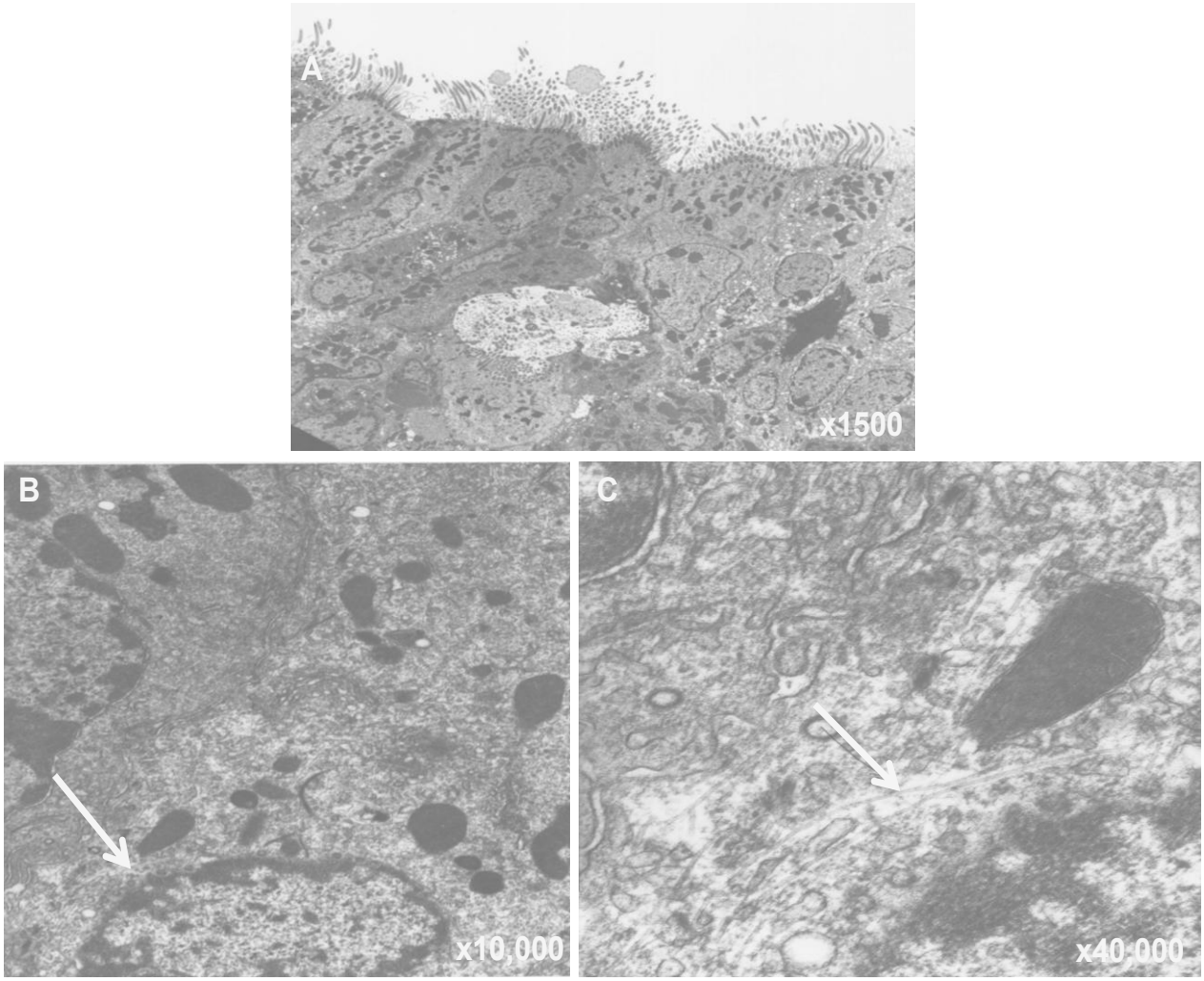

Figure 23: Representative transmission electron micrograph of mouse nasal tissue treated with taxol prior to fixation in glutaraldehyde

Mouse nasal epithelium was treated with taxol (10 μM) at 37^{o}C for 15 minutes prior to fixation in 2.5% glutaraldehyde in PBS at 37^{o}C for 30 minutes followed by further incubation at room temperature for 2.5 hours. The fixed mouse nasal epithelium was processed for TEM. Ultrathin sections stained with uranyl acetate and lead citrate were observed under TEM at low (x1500) magnification (*A*), higher (x10,000) magnification (B) and (x40,000) magnification C) showing microtubules (white arrows). Representative of three independent experiments.

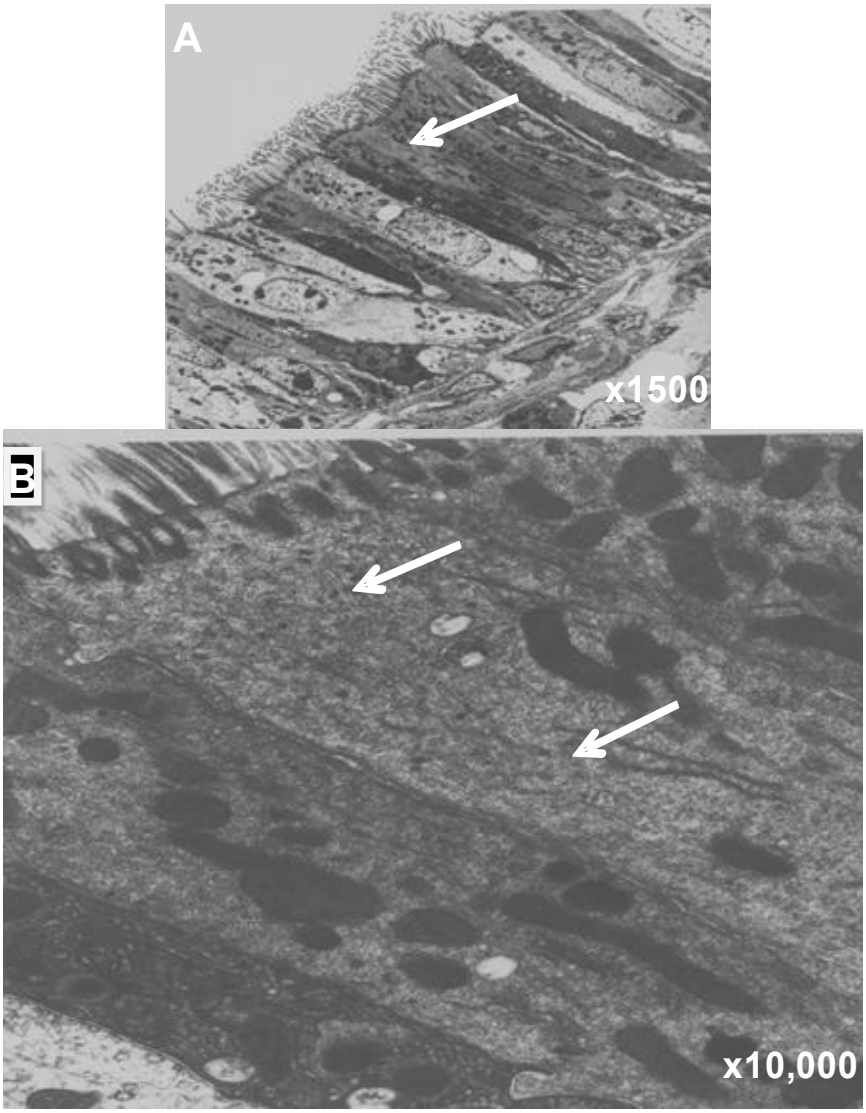

Figure 24: Representative transmission electron micrograph of mouse nasal tissue treated with saponin prior to fixation in glutaraldehyde

Mouse nasal epithelium was treated with saponin (0.02%) at 37^{o}C for 15 minutes prior to fixation in 2.5% glutaraldehyde in PBS at 37^{o}C for 30 minutes followed by further incubation at room temperature for 2.5 hours. The fixed mouse nasal epithelium was processed for TEM. Ultrathin sections stained with uranyl acetate and lead citrate were observed under TEM at low (x1500) magnification (*A*), higher (x10,000) magnification (B) showing microtubules (white arrows). Representative of three independent experiments.

Conditions	Microtubules
2.5% GLU in PBS buffer	+++
2.5% GLU in cytoskeletal buffer	+
Taxol (2 μM) + 2.5% GLU in PBS Taxol (10 μM) + 2.5%GLU in PBS	+ ++
Saponin (0.01%) + 2.5% GLU in PBS Saponin (0.02%) + 2.5% GLU in PBS Saponin (0.05%) + 2.5% GLU in PBS	+ ++ ++

Table 1: The preservation of microtubules in mouse nasal epithelium fixed under different conditions in glutaraldehyde at 37° C
For experimental details see Materials and Methods section 3.2.

GLU = Glutaraldehyde, PBS = Phosphate buffer saline

+ = Poor preservation

++ = Good preservation

+++ = Best preservation

3.3.5 Preservation of ultrastructure in human airway epithelial cells grown at an air-liquid interface

I further translated this improved chemical fixation procedure (fixation of mouse nasal epithelium in 2.5% glutaraldehyde made in PBS) to process ALI epithelium. Figure 25A shows a representative TEM micrograph of fixed human ALI. Again, cilia along with microvilli, apical and basolateral surface membranes, cytoskeleton elements such as the microtubules, mitochondria, assorted vesicles (Figure 25B); nucleus, nuclear pores and nuclear matrix (Figure 25C) were well preserved.

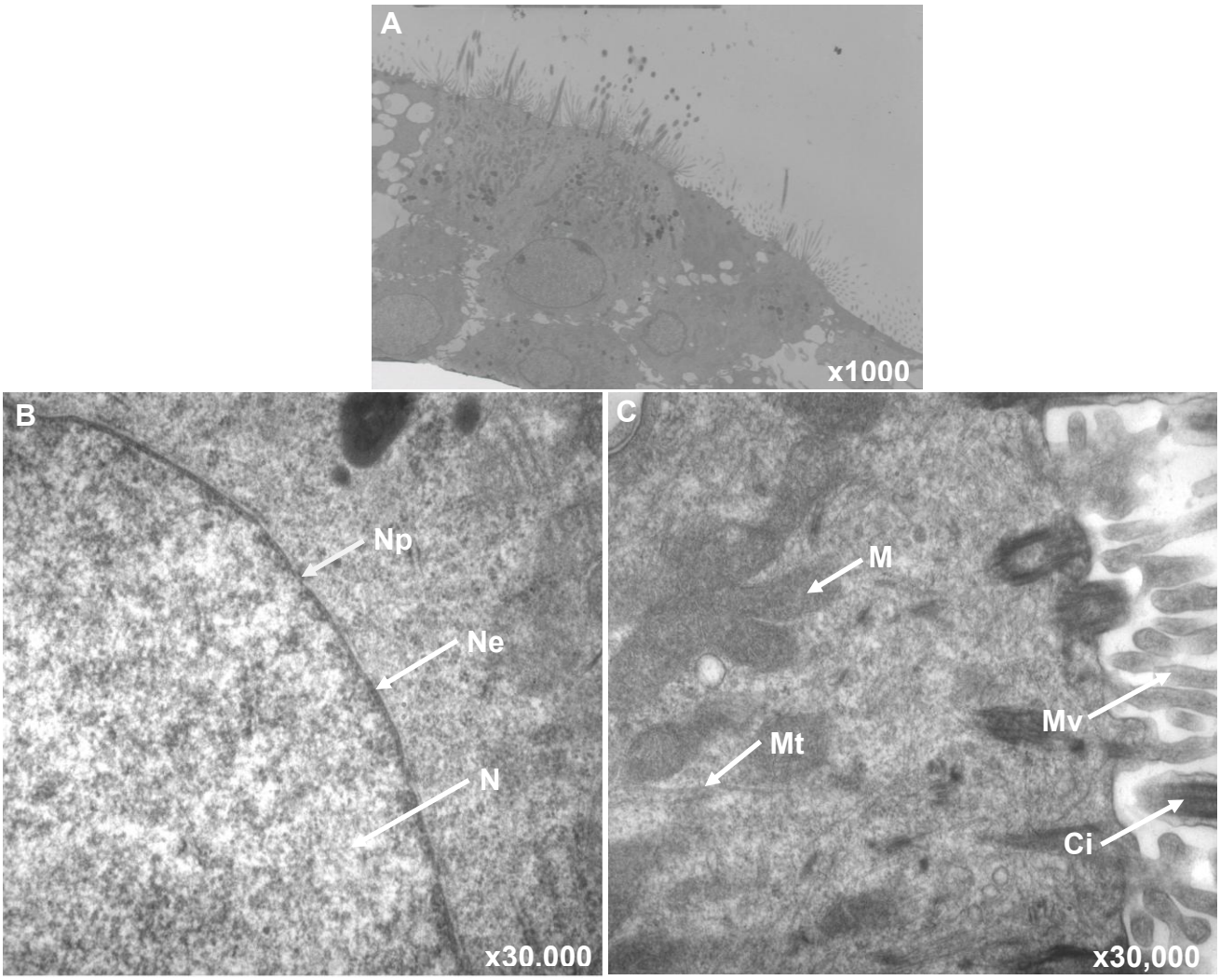

Figure 25: Representative transmission electron micrograph of human airway epithelial cells grown at the air-liquid interface

Human ALI was fixed with 2.5% glutaraldehyde in PBS at 37^{o}C for 30 minutes followed by further incubation at room temperature for 2.5 hours. The fixed ALIs were processed for TEM. Ultrathin sections stained with uranyl acetate and lead citrate were observed under TEM at low (x1000) magnification (*A*), higher (x10,000) magnification (B) and (x30,000) magnification C) showing cilia (Ci), microvilli (Mv) mitochondria (M) and microtubule (Mt) in the cytoplasm; and nucleus (N) with a well defined nuclear envelope (Ne) and nuclear pore (Np) all indicated by arrows labelled accordingly. Representative of 3 independent experiments.

3.4 Discussion

Conventional protocols for the chemical fixation of samples for detection by TEM inevitably result in degradation (poor preservation) of intracellular ultrastructure, which in turn leads to ambiguous identification of sub-cellular structures. It was, therefore, important to optimise a TEM chemical fixation protocol that preserved the ultracellular structures involved in the intracellular transport of pDNA such as the cytoskeleton or endocytic vesicles. I initially optimised the chemical fixation protocol in mouse nasal epithelial tissue and concentrated on the preservation of the cytoskeleton, a key cellular component involved in the intracellular transport of pDNA following non-viral gene transfection [163;165;168;170;195-198]. Previously, fixation temperature has been shown to be a key factor in the preservation of cytoskeleton since microtubules depolymerise at a lower temperature [199-203]. I found that preservation of ultrastructure especially microtubules was improved by fixing mouse nasal tissue in glutaraldehyde at 37˚C. After optimising the fixation protocol for temperature, I next sought to improve the preservation of cytoskeleton ultrastructure. The literature also suggests that generic 'tubulin buffer', also called cytoskeletal buffer, containing guanosine triphosphate (GTP) has been shown to stabilise the cytoskeleton filaments [200;204]. I, therefore, incubated mouse nasal tissue in 'tubulin buffer', as well as taxol, a microtubule stabiliser, prior to fixation in glutaraldehyde at 37˚C for 15 minutes [163;202;204]. Unfortunately, neither the addition of 'tubulin buffer' or taxol improved the preservation of microtubule any further.

Finally, extracting cytoplasmic soluble proteins using non-ionic detergent such as triton or saponin has been shown to permit clear visualisation of cytoskeletal filaments [203;205;206]. I therefore further sought to improve the preservation of cytoskeleton filaments in a similar

way by treating the mouse nasal tissue with mild non-ionic detergent saponin. Saponin (selectively) permeabilises the cell membrane; it is also likely that microtubule associated proteins (MAP) such as the cytoskeletal motor proteins, kinesin and dynein, that carry the cargo (for example pDNA) along the microtubules could be removed from the cells depending on the concentrations of the saponin treatment [202;207]. Therefore I tested three different concentrations of saponin ranging from 0.01 to 0.05%. Again, the preservation of cytoskeletal filaments was not improved any further after treatment with different concentrations of saponin.

In conclusion, after evaluating several cytoskeleton-interacting compounds for the preservation of ultrastructure, I found that simply replacing sodium cacodylate buffer with PBS for making glutaraldehyde in the conventional chemical fixation technique and incubating at 37˚C, gave optimal preservation of key intracellular structures. Thus original hypothesis was rejected. This optimised protocol was then successfully translated to the fixation of human ALIs.

Chapter 4: Preparation and validation of nanogold-conjugated plasmid DNA

4.1 Introduction

Having established an optimal protocol for observation of airway epithelial cells with well preserved ultrastructure, as described in the previous chapter, I next sought to visualise intracellularly-localised pDNA against this well-preserved background. Since pDNA is not electron-dense enough to be detected by TEM, it was necessary to label the pDNA with TEM-opaque gold nanoparticles. The gold-labelled pDNA would thus permit visualisation of the fate of pDNA in human airway epithelial cells following non-viral gene transfer.

Conventionally, gold probes (i.e. colloidal gold particles) can be attached, via random adsorption to bio-molecules such as antibodies, peptides and proteins via electrostatic and van der Waal's attractions [208-213]. In early studies, we and others used similar strategies to label pDNA with colloidal gold particles [214;215]. A further development of this mode of labelling is the incorporation of 5-bromo-2'-deoxyuridine **(**BrdU**),** a thymidine analogue, into the pDNA to permit subsequent detection of primary anti-BrdU antibodies with colloidal gold-labelled secondary antibodies [215-218]. Additionally, other workers have used colloidal gold-tagged avidin or streptavidin to detect biotinylated pDNA [136;214;219;220]. In another TEM study, digoxigenin-labelled oligodeoxynucleotides (ODNs) were detected using colloidal gold labelled anti-digoxigenin antibody [221].

The key pitfall in all the above approaches is that the attachment of colloidal gold is random and not specifically targeted on to the pDNA. To circumvent this limitation, Nanoprobes

(www.nanoprobes.com) introduced conjugation strategies permitting the covalent linkage of uncharged metal clusters and nanoparticles to specific sites on bio-molecules. Thus, it is possible to link any bio-molecule containing a reactive group (proteins, DNA and lipids) with metal clusters and nanoparticles in a targeted manner away from biologically important active sites so that linkage does not interfere with the activity of the particular bio-molecule, a feature that is not possible with colloidal gold. The monomaleimido group is specifically reactive towards sulfhydryl groups in an irreversible manner and is therefore widely used to covalently link (maleimide-derivatised) molecules, such as fluorophores, to target thiol-terminated proteins, peptides and oligonucleotides. Our laboratory, and others, have previously used this approach to link an Oregon-Green fluorescent probe to β-galactosidase reporter plasmid, pCMVβ-DTS in a sequence-specific manner, via a thiol-terminated peptide nucleic acid (PNA) linker molecule while retaining most of the super-coiled pDNA biological activity [187;222-226].

Using a similar approach, I have conjugated the pCIKFluc with 1.4 nm monomaleimdo Nanogold particles, in a sequence-specific manner using the cysteine-PNA. The terminal cysteine thiol group on the PNA peptide backbone was reacted with the maleimide moiety on the Nanogold to produce a PNA-nanogold-conjugate, which in turn was hybridised to an 8 base pair (bp) target sequence (located at a transcriptionally inactive region) on the plasmid to produce the final nanogold-PNA-pCIKFluc conjugate (nanogold-conjugated pDNA), the TEM probe for experiments to visualise pDNA in human airway epithelial cells following non-viral gene transfections.

Importantly for these experiments, the 1.4 nm monomaleimido nanogold is relatively small compared to the 200 nm of cationic-lipid condensed super-coiled pDNA and is uniform in

size [227;228]. In addition, it is not adsorbed to bio-molecules like colloidal gold, but is instead covalently linked to specific sites, away from the biologically active sites thus allowing biomolecule to retain their activity. Critically, tagging pDNA via PNA containing a single target sequence to a single maleimide-terminated nanogold particles results in 1:1 stoichiometric labelling (with respect to pDNA and nanogold). Binding stoichiometries of proteins conventional labelled with colloidal gold clusters vary from 0.2 to 10 (www.nanoprobes.com) [228]. As mentioned above, the size of our 1.4 nm nanogold particle tags in relation to the pDNA (200 nm; fully condensed pDNA) means the small nanogold tag is not likely to interfere with normal pDNA uptake and intracellular trafficking.

However, a major drawback of the small size of the 1.4 nm nanogold particles is that the particles are not sufficiently electron-dense enough to be observed by TEM intracellularly. Gold enhancement to amplify the signal was therefore necessary, as recommended by Nanoprobes [229]. Gold enhancement by selective deposition of gold onto nanogold particles (autometallography) has several advantages over conventional silver-enhancement (www.nanoprobes.com) [230-232]. Thus, enhancement with gold results in higher electron density, and therefore better contrast and low background staining compared to enhancement with silver. Unlike silver, gold is not etched by osmium tetroxide, so further treatment such as toning with gold tetrachloride solution is not necessary. In addition, gold enhancement is compatible with physiological buffers, as it is not precipitated by halides.

Hypothesis

Plasmid DNA hybridises (conjugates) to monomaleimido-nanogold thiol-linked to cysteine-PNA (containing 11-bps binding site) in a sequence-specific manner.

Aims

To prepare and validate nanogold-conjugated pDNA for use in localisation of the gold-labelled pDNA following non-viral gene transfer.

1. Prepared nanogold-conjugated pDNA using cysteine-PNA as a linker molecule including a physical mix of pDNA and nanogold (control unconjugated pDNA) in the absence of PNA.
2. Determined stoichiometric ratio of nanogold to pDNA in the nanogold-conjugated pDNA.
3. Validated conjugation of pDNA to nanogold biochemically.
4. Assessed the effect of nanogold conjugation on transcriptional activity of pDNA.
5. Visualised the intracellularly localised nanogold-conjugated pDNA in HEK293T monolayers, mouse nasal epithelium and ALI by TEM.

4.2 Materials and Methods

Described in detail in Materials and Methods Chapter 2

4.2.1 Gold-enhancement of 1.4 nm nanogold on ultrathin sections

To visualise the nanogold conjugated to pDNA, ultrathin sections containing the sample epithelia were collected on nickel grids, and the 1.4 nm nanogold particles enhanced using a gold-enhancement kit according to manufacturer's recommendations (Nanoprobes). Briefly, the sections were jet washed with de-ionised water for 1 minute and were further washed by floating on a 40 µl drop of de-ionised water for 5 minutes (x5). During this floating period, an equal amount of reagent A (enhancer) and reagent B (activator) were mixed for 30 seconds. After 5 minutes of incubation at room temperature, an equal amount of reagent C (initiator) was added followed immediately by the addition of an equal amount of reagent D (buffer). After mixing, the residual water on the grids was blotted off using Whatman filter paper and enhancement was initiated by floating the grid (with section facing downward) on a drop of gold enhancement mix (30 µl/ grid) for the required time. To terminate the reaction, the residual gold enhancement mix was blotted off, and the grids washed on a drop of de-ionised water five times as described above. Finally the sections were stained with uranyl acetate followed by lead citrate as described previously under Section 2.3.2. The gold enhanced sections were then ready for visualisation under TEM.

4.2.2 Visualisation of nanogold-conjugated pDNA following transfection of Human Embryonic Kidney 293T cells

Briefly, HEK293T cells were seeded at a density of 1×10^5 cells/well in pre-coated poly-D-lysine 6-well (35-mm diameter) plates (BD Biosciences, Oxford, UK) 24 hours before transfection. Plasmid DNA (1 μg) and lipofectamine™ 2000 (2.5 μl) reagent were diluted in 400 μl of serum-free Opti-MEM medium (Invitrogen) and were incubated for 15 minutes at room temperature. This transfection mix was then applied to the cells per well and incubated in a humidified atmosphere at 37°C with 5 % CO_2. After 6 hours, the transfection mix was discarded and replaced with 1 ml Opti-MEM medium supplemented with 10 % FBS. The Opti-MEM/FBS medium was changed after 18 hours and further incubated at 37°C with 5 % CO_2 for 24 hours. The cells were washed gently with PBS three times and the cells pelleted by centrifugation at 4500 rpm at 4°C for 10 minutes followed by fixation in 2.5% glutaraldehyde as described in Chapter 2. The pellet was then resuspended in 1 % molten agarose, immediately centrifuged, prior to cooling at 4°C for 15 minutes. The resultant agarose block containing the dispersed cells was sliced into 4 equal pieces and processed for TEM using our optimised fixation protocol (Figure 13). Ultra-thin sections (120 nm) cut from the agarose block using an ultra microtome were then collected on nickel grids prior to gold enhancement, as described earlier**.** The gold-enhanced sections were then stained *en bloc* with 2 % uranyl acetate followed by 2 % lead citrate prior to visualisation by TEM.

4.2.3 Visualisation of nanogold-conjugated plasmid DNA following transfection of human airway epithelial cells grown at an air-liquid interface

Human ALIs were transfected with a 100 µl complex of nanogold-conjugated pDNA and cationic lipid GL67A in a 1:4 molar ratio for 1 hour at 37^{o}C. Human ALIs identically transfected with a complex of unconjugated pDNA and GL67A served as controls. After transfection, the complex was removed and ALIs were washed four times with pre-warmed PBS followed by fixation in 2.5 % glutaraldehyde for 30 minutes at 37^{o}C. After a further incubation at room temperature for 2.5 hours, the fixed samples were stored at 4^{o}C prior to subsequent processing (Figure 13). The ultra-thin sections (120 nm) were enhanced with gold enhancement mix for 15 minutes at room temperature followed by *en bloc* staining with 2 % uranyl acetate and 2 % lead citrate, prior to visualisation by TEM as described earlier.

4.2.4 Statistical analysis

Raw data were $\log_{10}$ transformed and expressed as medians for the indicated number of experiments. Normal distribution of the data was assessed by the K-S normality test. A non-parametric Kruskal-Wallis with Dunn's Multiple Tests *post-hoc* corrections was performed for comparison of more than two groups, when the assumptions were not met after transformation. In all cases the null hypothesis was rejected at $p < 0.05$. All analysis was performed using GraphPad Prism4 (GraphPad Software, Inc., La Jolla, CA, USA).

4.3 Results

4.3.1 Determination of the stoichiometry of nanogold to plasmid DNA in the nanogold-PNA-pCIKFluc conjugate using spectrophotometry

My ultimate goal was to quantitate the localisation of pDNA in ALIs following non-viral gene transfection. Therefore, it was important to know the exact amount of nanogold covalently linked to the pDNA. With this in mind, I sought accurately to determine the stoichiometry of pDNA to nanogold in the nanogold-PNA-pCIKFluc conjugate. A stoichiometry of 0.92 μmols nanogold-PNA attached to 0.72 μmols of pCIKFluc (approximately 1 molecule of nanogold-PNA conjugates to 1 molecule of pCIKFluc) was determined from spectrophotometric data in the following way:

A. Quantitation of pCIKFluc in the nanogold-PNA-pCIKFluc conjugate

1) 50 μg/ml of DNA = 1.0 absorbance unit ($A_{260\ nm}$).
2) 2 μl of nanogold-PNA-pCIKFluc conjugate sample in 500 μl of de-ionised water is equal to 0.2892 absorbance units ($A_{260\ nm}$) from three replicates.
3) Concentration of pCIKFluc in 2 μl conjugate sample is equal to 3.6 mg/ml as calculated from:

   Concentration of DNA = $A_{260\ nm}$ x dilution factor x 50 μg/ml.
4) pCIKFluc (5632 bp); therefore, the concentration of pCIKFluc in the nanogold-PNA-pCIKFluc conjugate sample = 0.72 μM (i.e. 0.72 nmol/ml).

B. Quantitation of nanogold in the nanogold-PNA-pCIKFluc conjugate

Number of molecules of nanogold calculated using the Beer-Lambert's law (equation 1):

$A = \varepsilon CL$ - *equation 1*

Where:

A = absorbance measured at 420 nm

ε = molar extinction coefficient in $M^{-1}cm^{-1}$

C = concentration (M or mmol/ml)

L= cuvette path length which is 1 cm

1) Molar extinction coefficient of nanogold at $A_{420\ nm}$ is equal to 155,000 $M^{-1}cm^{-1}$.
2) 2 µl of nanogold-PNA- pCIKFluc conjugate sample in 500 µl of de-ionised water had an absorbance of 0.1426 units (at $A_{420\ nm}$) from three replicates.
3) Therefore, the concentration of nanogold particles in the nanogold-PNA- pCIKFluc conjugate, calculated using equation 1 was 0.92 µM (i.e. 0.92 nmol/ml).
4) Thus, the stoichiometry of nanogold to pDNA in the final nanogold-PNA- pCIKFluc conjugate was 0.72 nmol to 0.92 nmol (approximate molar ratio of 1:1).

In two early attempts at sequence-specific covalent conjugation of pDNA to mono-maleimide-terminated nanogold particles using the strong reducing agent, tris (2-carboxyethyl) phosphinehydrochloride (TCEP), to activate the PNA linker molecule terminal cysteine groups, the nanogold particles precipitated out into a brown clump due to reaction with residual TCEP, even after purification by extensive ultrafiltration. To solve this problem, I took advice from Nanoprobes, the suppliers of the nanogold reagents, and replaced the TCEP with a milder reducing agent, mercaptoethylamine hydrochloride (MEA). I was,

thus, able to successfully remove all the MEA, after reduction of PNA terminal disulphide bond for reaction with the maleimide-terminated nanogold particles, without destructive precipitation of nanogold. All together, two successful conjugation reactions were used to generate sufficient pDNA conjugated to nanogold particles for use in the entire study. As mentioned, pDNA conjugated to nanogold particles preparations were stored and snap frozen as single-use aliquots at -80^{o}C.

4.3.2 Spot test to detect nanogold in nanogold-conjugated plasmid DNA

Using a "spot test" colorimetric assay recommended by Nanoprobes, I next set out to determine whether the pDNA was directly linked to the nanogold particles (in a 1:1 stoichiometry). To test this hypothesis, I, therefore, sought to co-localise the nanogold staining with that of the plasmid in a spot of the final nanogold-PNA-pCIKFluc conjugate. However, after careful evaluation of several nanogold and pDNA stains, I was unable to find a pair of dyes that were compatible for co-staining for pDNA and nanogold on the same spot. As an alternative strategy, I stained (i.e. gold-enhanced to permit visualisation) for nanogold in separate spots containing the nanogold-PNA-pCIKFluc conjugate (nanogold-conjugated pDNA) and compared them to parallel spots containing unconjugated pDNA (physically mixed nanogold and pCIKFluc) and pure nanogold control.

Gold enhancement of the spot containing pure nanogold particles (Figure 26A) revealed a positive purple stain compared to the spot before gold enhancement (Figure 26D). The spot containing the control unconjugated pDNA did not stain for gold before, or after, gold-enhancement (Figure 26B and 26E, respectively). Gold-enhancement revealed positive staining (indicated by a purple halo around the light brown spot) in the spot containing the

nanogold-conjugated pDNA (Figure 26C). Light brown (not purple positive staining) stain was seen in the spot containing nanogold-conjugated pDNA before gold enhancement (Figure 26F), likely due to the presence of the PNA in the nanogold-PNA-pCIKFluc conjugate. Unfortunately, I could not include a pure PNA spot to control for this observation due to the cost of custom PNA synthesis.

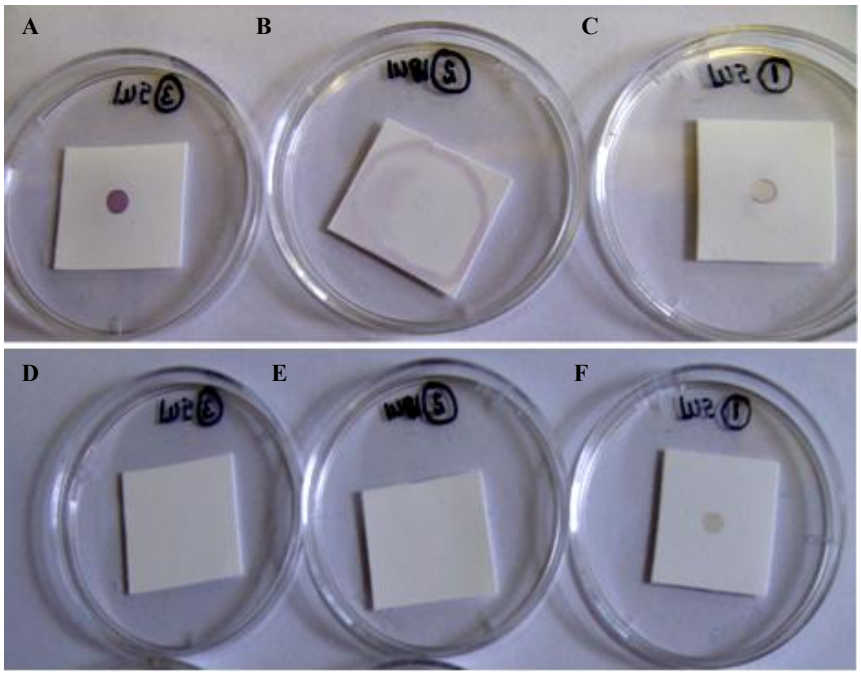

Figure 26: Evaluation of the linkage of nanogold to plasmid DNA in nanogold-PNA-pCIKFluc conjugate spotted on a nitrocellulose membrane
Pure nanogold, unconjugated pDNA (physically mixed nanogold and pCIKFluc) and nanogold-conjugated pDNA containing equal amounts of nanogold and pDNA, where appropriate, were placed onto nitrocellulose membrane, air-dried at room temperature on a petri-dish followed by gold enhancement. Gold enhanced pure nanogold (A), unconjugated pDNA (B) and nanogold-conjugated pDNA (C) compared to pre-gold enhancement of pure nanogold (D), unconjugated pDNA (E) and nanogold-conjugated pDNA (F). Representative of three independent experiments.

4.3.3 Evaluating the linkage of nanogold with plasmid DNA using agarose gel electrophoresis

The localisation of nanogold particles in the spot containing nanogold-conjugated pDNA in the above "spot test" analysis is not in itself an absolute confirmation of direct covalent pDNA-nanogold linkage. I, therefore, set out to show this direct covalent linkage by assessing the effect of nanogold conjugation on the electrophoretic mobility of the nanogold-conjugated pCIKFluc compared with unconjugated pCIKFluc (physically mixed nanogold and pCIKFluc) and wild type pCIKFluc controls, using agarose gel electrophoresis. Equal amounts of nanogold-conjugated pCIKFluc, unconjugated pCIKFluc, wild type pCIKFluc and pure nanogold particles were run on a 0.9 % agarose electrophoresis gel. Staining for DNA with Red Gel revealed all three forms of super-coiled, open-circular and linear pDNA in the nanogold-conjugated, unconjugated and wild type pDNA (Figure 27; lanes 2, 3 and 4). As expected there was no DNA present in the sample containing nanogold alone (lane 5). There was no difference in the electrophoretic mobilities of all three DNA conformations in all three samples namely nanogold-conjugated, unconjugated and wild type pCIKFluc.

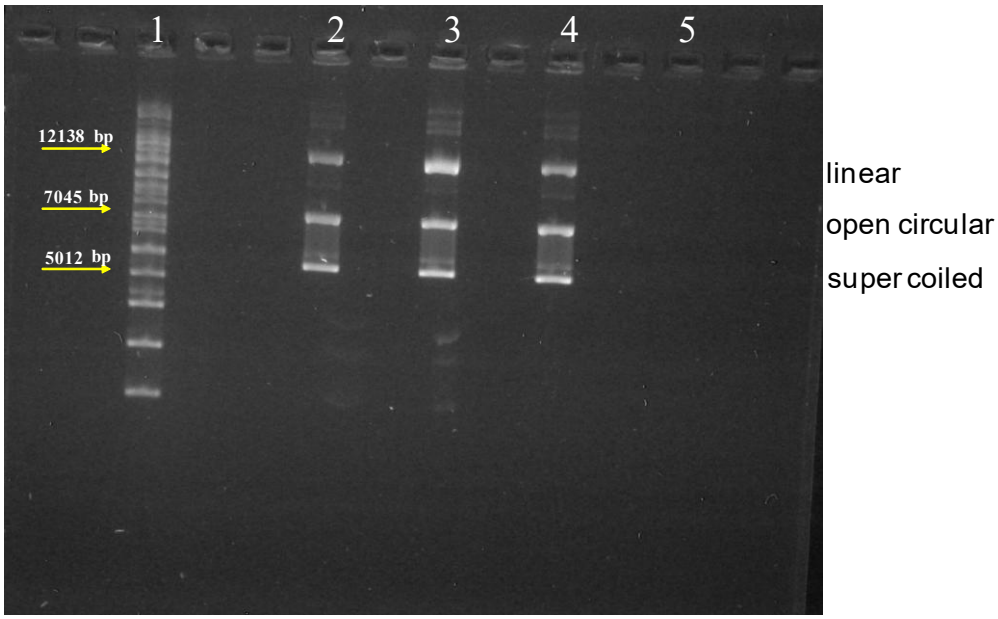

Figure 27: Agarose gel electrophoresis of nanogold-conjugated plasmid DNA and unconjugated plasmid DNA

Equal amounts of nanogold-conjugated plasmid DNA, unconjugated plasmid DNA (a physical mixture of plasmid DNA and nanogold), plasmid DNA and pure nanogold were run on a 0.9 % agarose gel for 90 minutes. Agarose gel was stained with Gel Red (10000x) for DNA detection. Lane 1: Ladder 2-16 kb, Lane 2: nanogold-conjugated plasmid DNA, Lane 3: unconjugated plasmid DNA, Lane 4: plasmid DNA and Lane 5: pure nanogold particles. Representative of three independent experiments.

4.3.4 Evaluating the nanogold linkage to plasmid DNA by agarose gel electrophoresis of endonuclease digestion nanogold-conjugated pDNA fragment products

In the preceding experiment, I was not able to demonstrate a direct linkage of nanogold-PNA to the pDNA by comparing the electrophoretic mobilities of nanogold-conjugated pCIKFluc with control unconjugated pCIKFluc. I, therefore, refined the strategy by digesting the pCIKFluc with the endonucleases BssSI at restriction sites 3751 bp, 4058 bp and 5442 bp and BseYI at restriction sites 2204 bp and 5311 bp (Figure 16). Thus, double digestion of pCIKFluc with the endonucleases BssSI and BseYI generated 5 fragments in total. The fragments were: 131, 307, 1253, 1547, and 3080 bps in size. The 131 bps fragment contains the nanogold-PNA binding site (AAGGGAGA). The restriction fragments from nanogold-conjugated pDNA were then electrophoresed on 3 % agarose gel and compared with those generated from the control unconjugated pDNA (Figure 28). Two fragments, the first a 131 bps fragment containing the nanogold-PNA conjugate, and a second, 307 bps fragment, were resolved by agarose gel electrophoresis of the digestion products of nanogold-conjugated pDNA and unconjugated pDNA (Figure 25 lanes 2 and 3). There was no difference in the electrophoretic mobilities in 131-bp fragment containing the PNA target sequence, digested from the nanogold-conjugated pDNA compared with those from the unconjugated control. Also, there was no electrophoretic mobility shift in the 307-bp fragment from the endonuclease digestion of nanogold-conjugated pDNA compared with the control, as expected. The 3 larger restriction fragments, 1253, 1547, and 3080 bps in size, were not fully resolved on 3 % agarose gel and appeared as a broad band.

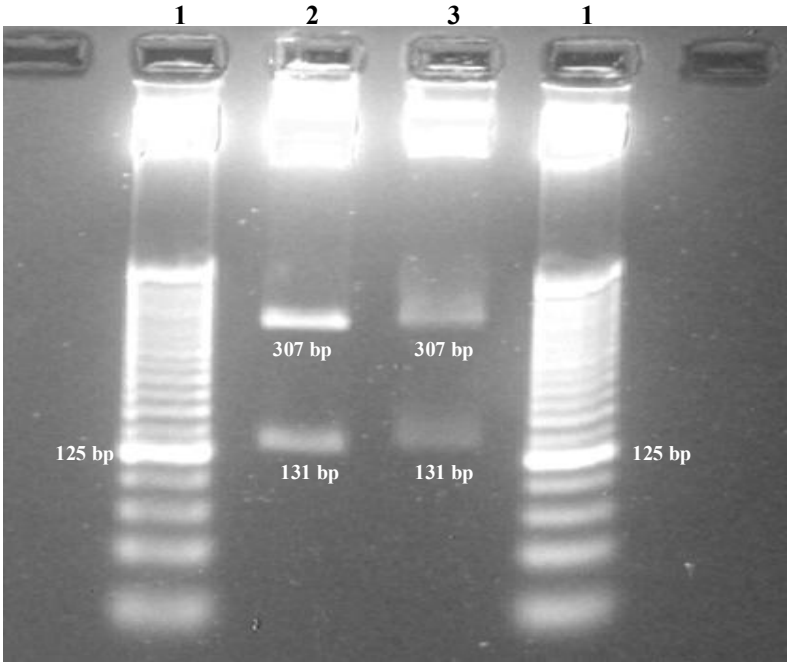

Figure 28: Agarose gel electrophoresis of restriction fragments of nanogold-conjugated plasmid DNA and unconjugated plasmid DNA

Restriction fragments of nanogold-conjugated plasmid DNA and unconjugated plasmid DNA were generated by treating nanogold-conjugated plasmid DNA and unconjugated plasmid DNA with restriction enzymes namely endonucleases BssSI and BseYI. After digestion restriction fragments were run on a 3 % agarose gel for 90 minutes. Agarose gel was stained with Gel Red (10000x) for DNA detection. Lane 1: Ladder 25-500 bp, Lane 2: Restriction fragments of nanogold-conjugated pDNA and Lane 3: Restriction fragments of unconjugated plasmid DNA. Representative of three independent experiments.

4.3.5 Effect of nanogold conjugation on the biological activity of the plasmid DNA

To evaluate the effect of nanogold conjugation on the pDNA, I next compared the transcriptional activity of nanogold-conjugated pCIKFluc with control unconjugated pCIKFluc. HEK293T cells were transfected, using lipofectamine, with nanogold-conjugated pCIKFluc, unconjugated pCIKFluc, and the CFTR-expressing pCIKCFTR negative control respectively. Cells were harvested 25 hours post-transfection, processed and assayed for luciferase reporter gene activity. The transfection efficiency was represented by a measure of relative light unit normalised to the total cell protein content (RLU/mg protein). There was no significant difference between the biological activities of nanogold-conjugated pCIKFluc and unconjugated-pCIKFluc 25 hours post-transfection of HEK293T cells (Figure 29). Only background luminescence was observed when HEK293T cells were transfected with the negative control pCIKCFTR. In samples treated with nanogold-conjugated pDNA or unconjugated pDNA, luminescence was higher compared to the background luminescence ($p<0.001$).

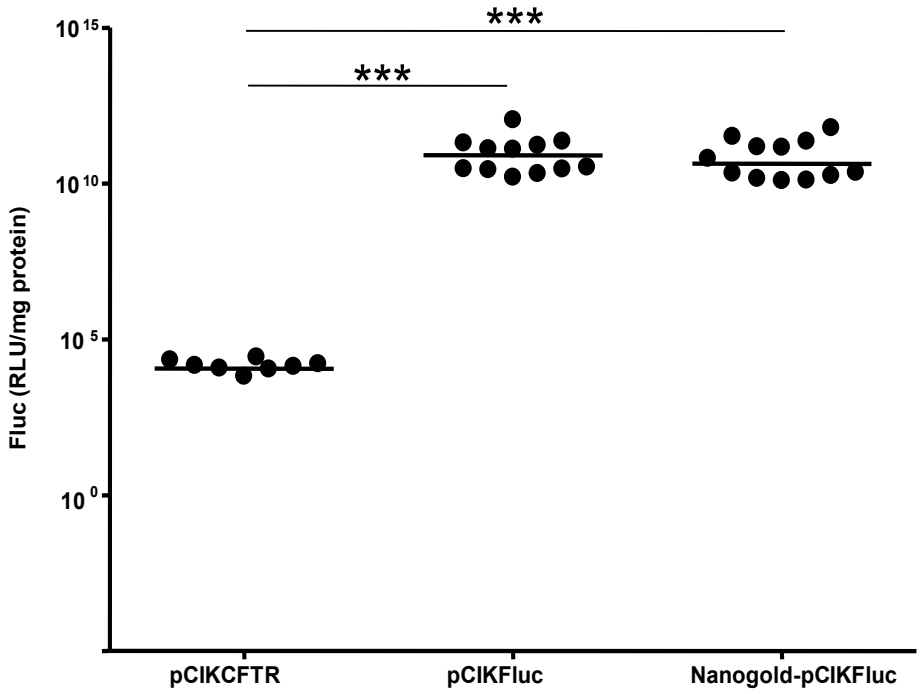

Figure 29: Luciferase expression in Human embryonic kidney 293T cell culture 25 hours post-transfection

Human embryonic kidney 293T cells were transfected with lipofectamine/pDNA complex (n=12 wells). Complex was removed after 6 hours and replaced by fresh media. The cells were harvested and assessed for luciferase expression 25 hours post-transfection. Data from two independent experiments were pooled together. Each data point represents the luciferase activity in each well. The horizontal bar represents the median. *** = $p < 0.001$ pCIKCFTR compared to pCIKFluc and nanogold-pCIKFluc respectively.

4.3.6 Direct visualisation of nanogold in the nanogold-conjugated plasmid DNA

Nanogold-conjugated pDNA (compared to unconjugated pDNA and pure nanogold) was next visualised using super-resolution TEM (Philips CM200) on Formvar-carbon coated copper grids. At this resolution, the nanogold particles were visible as dark spots (Figure 30A). No dark spots were visible in unconjugated pDNA (Figure 30B) compared to nanogold-conjugated pDNA (Figure 30C). In both the grids containing nanogold-conjugated pDNA and unconjugated pDNA respectively, the pDNA was visible as long white striations (i.e. thread like structures).

4.3.7 Visualisation of nanogold-conjugated plasmid DNA in transfected Human Embryonic Kidney 293T cultured cells by TEM

Having evaluated the integrity of nanogold-conjugated pDNA, I next sought to see whether we could visualise the nanogold-conjugated pDNA in cultured HEK293T cells following transfection. HEK293T cells were transfected with a complex of lipofectamine and nanogold-conjugated pDNA. These were then harvested and processed 48 hours post-transfection for TEM (using the optimised protocol) as described in materials and methods section 4.2.2. Figure 31A shows the representative electron micrograph of gold enhanced nanogold-conjugated pDNA-transfected HEK293T cells at low magnification. At higher magnification (Figure 31B), the cell shows well preserved mitochondria distributed within the cytoplasm. The nucleus is very large and occupies most of the cell space. A well defined nuclear envelope and condensed chromatin is clearly visible inside the nucleus. The black spots represent gold enhanced nanogold-conjugated pDNA seen inside the nucleus. No dark spots were observed when HEK293T cells were transfected with control unconjugated pDNA (Figure 31C and 31D).

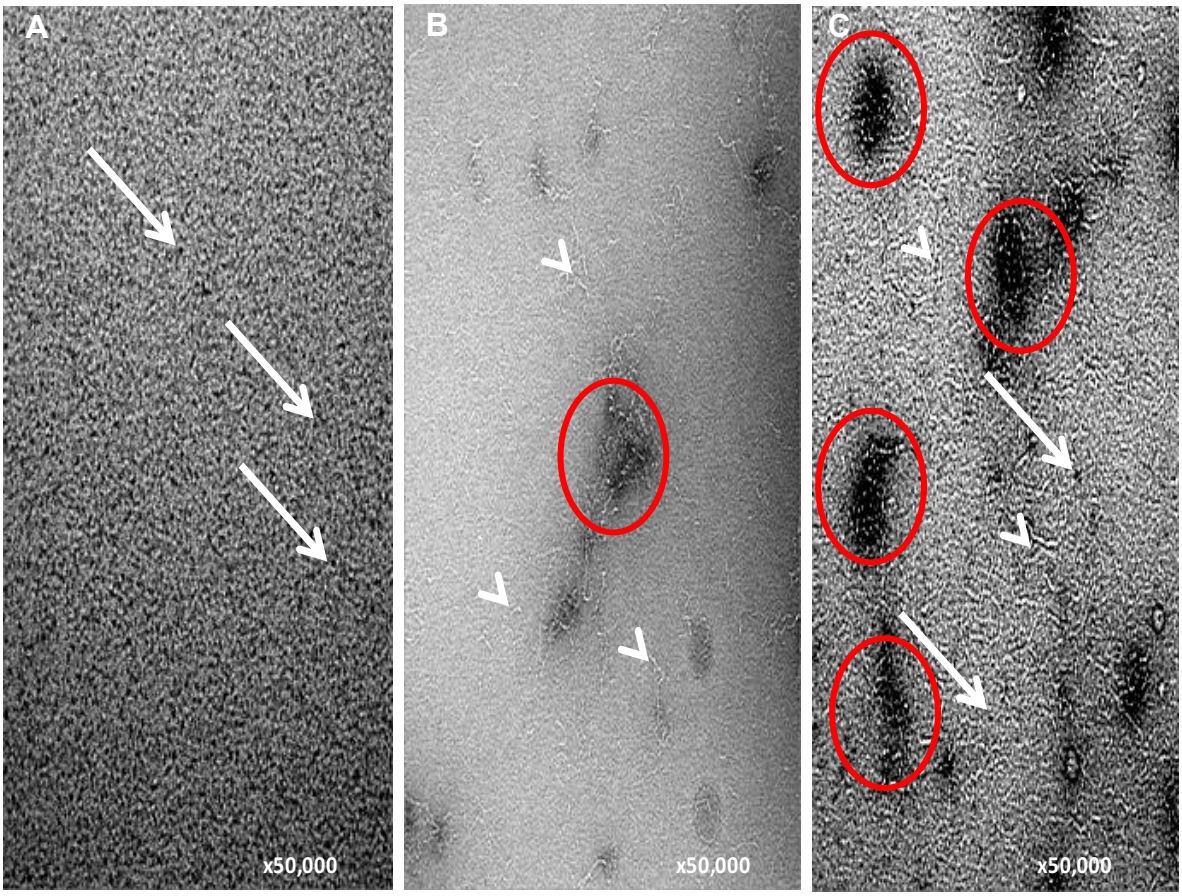

Figure 30: Visualisation of nanogold, unconjugated plasmid DNA and nanogold-conjugated plasmid DNA using high-resolution transmission electron microscopy
Equal amounts of nanogold (Figure A), unconjugated plasmid DNA (Figure B) and nanogold-conjugated plasmid DNA (Figure C) in 2 µl were spotted onto Formvar-carbon coated copper grids. After one minute incubation at room temperature, the grids were washed with distilled water, stained with uranyl acetate and observed by high-resolution TEM. Arrows indicate pure nanogold particles (Figure A), arrowheads indicate unconjugated plasmid DNA (Figure B) and nanogold-conjugated plasmid DNA represented by arrowheads and arrows (Figure C). Circles indicate artefacts resulting from carbon glow discharging of Formvar coated grids. Representative of three independent experiments.

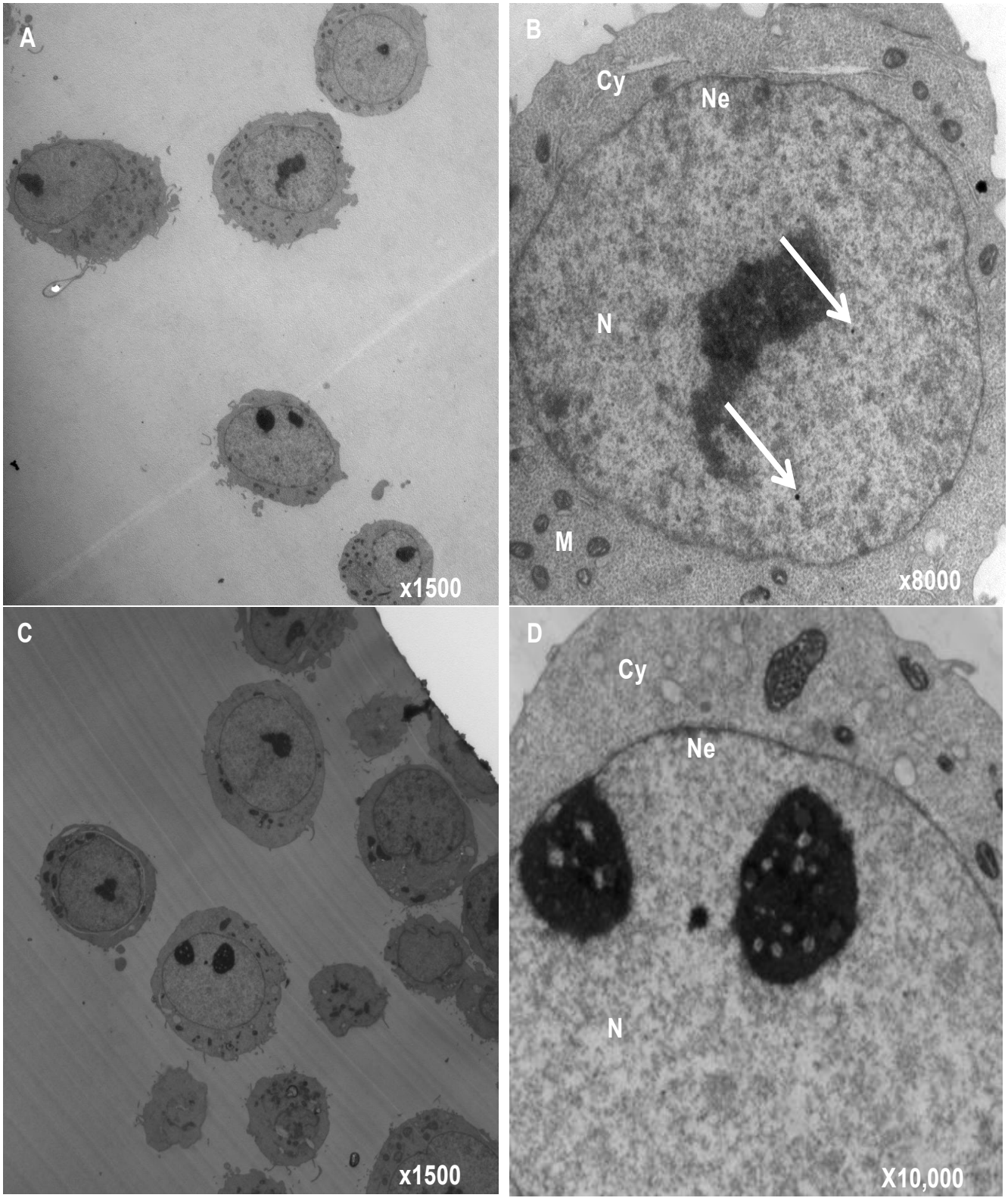
A
x1500
B
Cy
Ne
N
M
x8000
C
x1500
D
Cy
Ne
N
X10,000

Figure 31: Transmission electron micrographs of Human Embryonic Kidney 293T cultured cells transfected with nanogold-conjugated plasmid DNA for 48 hours at 37^{o}C
Human Embryonic Kidney 293T cells were transfected with a complex of lipofectamine/nanogold-conjugated plasmid DNA. After transfection, the cells were washed with PBS at 37^{o}C and processed for TEM using the optimised chemical fixation protocol described in Materials and Methods. Panel A shows cells at low magnification. Panel B shows nanogold-conjugated plasmid DNA visible as black spots inside the nucleus at higher magnification indicated by white arrows. Panel C and Panel D show absence of black spots in cells transfected with control unconjugated plasmid DNA at low and high magnification respectively. The cytoplasm (Cy), mitochondria (M), nuclear envelope (Ne) and nucleus (N) are labelled. Representative of six independent experiments.

4.3.8 Visualisation of nanogold-conjugated plasmid DNA following non-viral gene transfection in human airway epithelial cells

Having optimised our protocol for the visualisation of nanogold-conjugated pDNA in transfected cultured HEK 293T cells; I next sought to translate this approach to the visualisation of nanogold-conjugated pDNA in transfected human airway epithelial cells. Human ALIs were transfected with a complex of cationic lipid GL67A and nanogold-conjugated pDNA for 1 hour and processed for TEM as described in the Material and Method Section. A complex of cationic lipid GL67A and unconjugated pDNA served as a control. Figure 32A shows the well preserved pseudostratified epithelium with ciliated and non-ciliated cells at low magnification. However, at higher magnification, gold-enhanced nanogold-conjugated pDNA were visible as black spots on the cilia (Figure 32B). Black spots were also observed in the cytoplasm, as well as in the nucleus (Figure 32C). In the control ALIs transfected with unconjugated pDNA, we also observed randomly dispersed black spots (Figures 33).

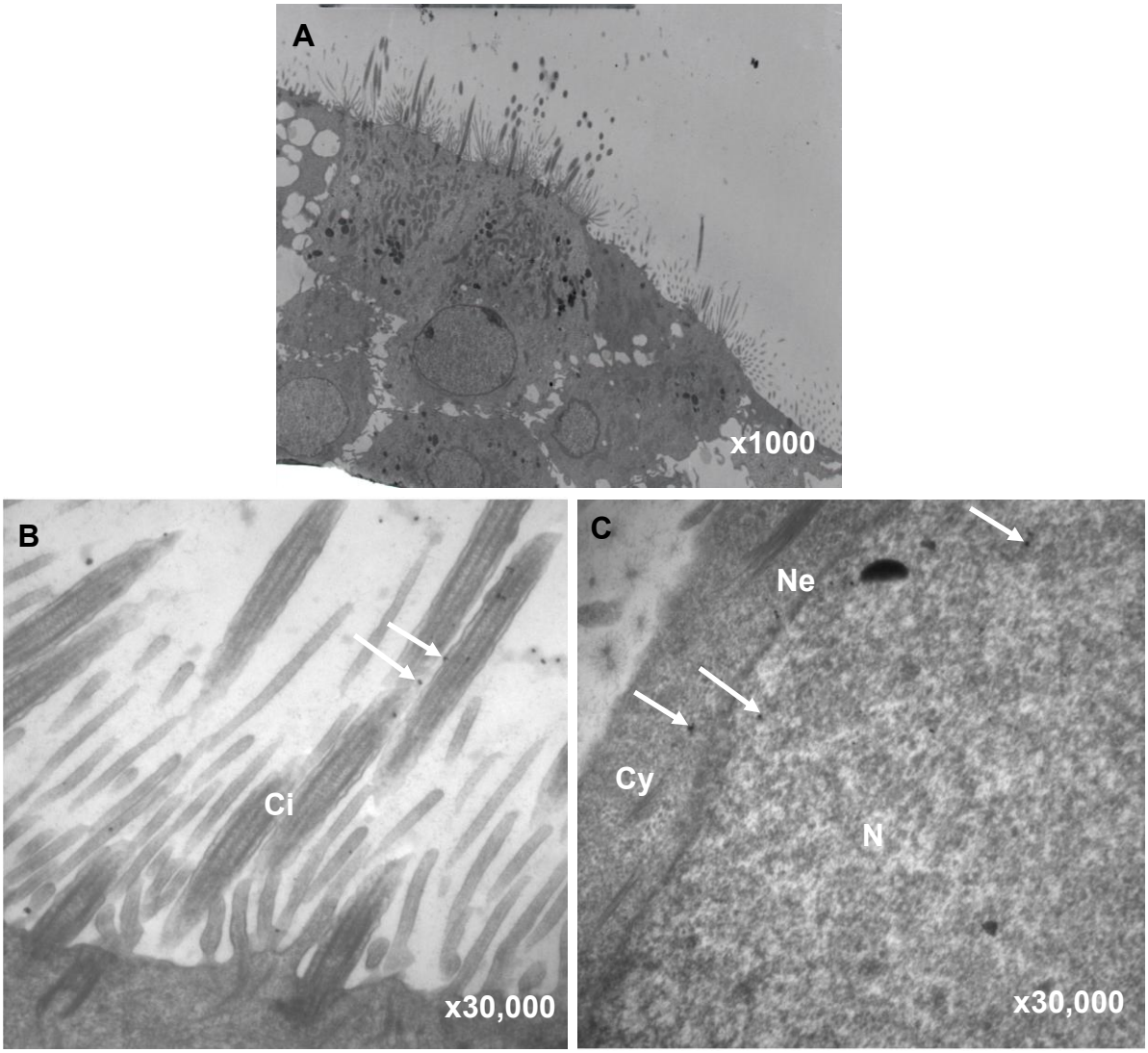

Figure 32: Representative transmission electron micrographs of human airway epithelial cells grown at an air-liquid interface transfected with nanogold-conjugated plasmid DNA for 1 hour at 37^{o}C

Human airway epithelial cells grown at an air-liquid interface (ALI) were transfected with a complex of cationic lipid GL67A/nanogold-conjugated plasmid DNA. After transfection, the cells were washed with PBS at 37^{o}C and processed for TEM using the optimised chemical fixation protocol described in Materials and Methods. Pseudostratified ALIs comprising ciliated and non-ciliated cells were visualised by TEM at x1000 magnification (Figure 32*A*). Black spots representing gold-enhanced nanogold-conjugated plasmid DNA were localised on the cilia, in the cytoplasm as well as in the nucleus at x30,000 magnification indicated by white arrows (Figure 32B and 32C). The cilia (Ci) cytoplasm (Cy), nuclear envelope (Ne) and nucleus (N) are labelled. Representative of six independent experiments.

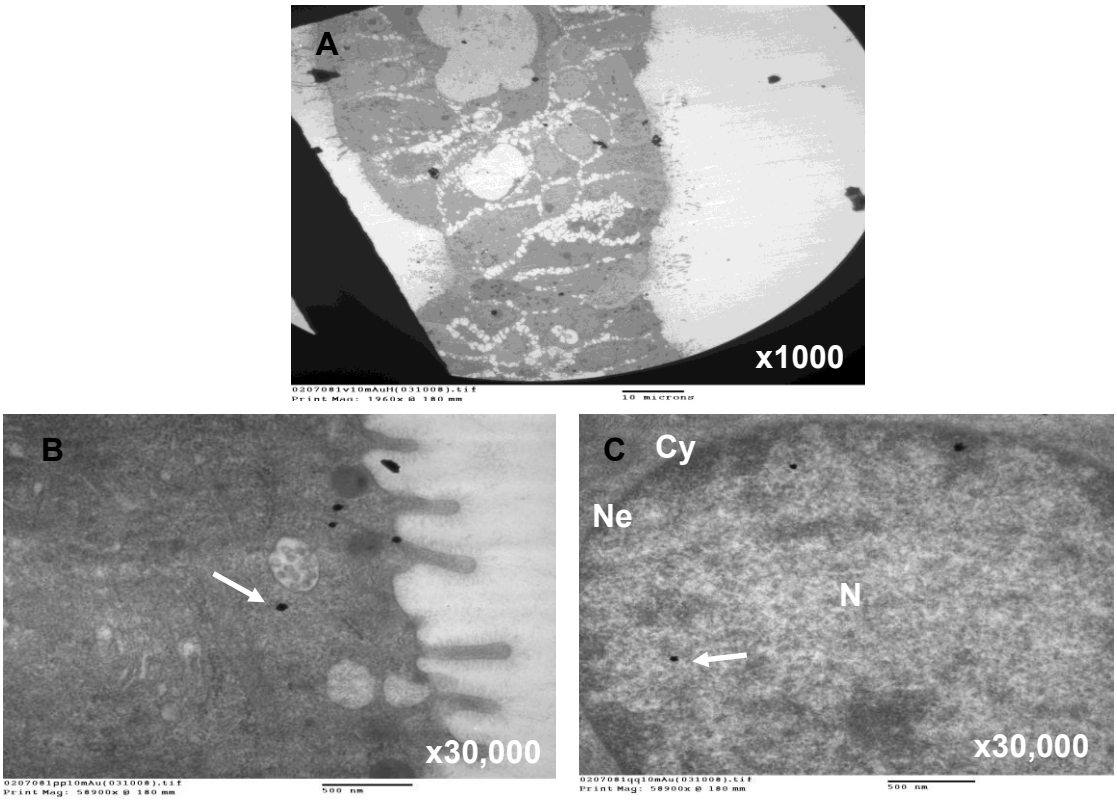

Figure 33: Transmission electron micrographs of human airway epithelial cells grown at an air-liquid interface transfected with control unconjugated plasmid DNA for 1 hour at 37^{o}C

Human airway epithelial cells grown at an air-liquid interface (ALI) were transfected with a complex of cationic lipid GL67A/unconjugated plasmid DNA. After transfection, the cells were washed with PBS at 37^{o}C and processed for TEM using the optimised chemical fixation protocol described in Materials and Methods. ALIs were visualised by TEM at x1000 magnification (Figure 33*A*). Black spots representing background staining were seen in the cytoplasm as well as in the nucleus at x30,000 magnification indicated by white arrows (Figure 33B and 33C). The cytosol (Cy), nuclear envelope (Ne) and nucleus (N) are labelled. Representative of six independent experiments.

4.4 Discussion

The native pDNA was not sufficiently electron dense to be visualised by TEM in these studies and so I needed to introduce an electron dense marker in the form of 1.4 nm nanogold particle to achieve this. Our laboratory has previously labelled super-coiled pDNA with a fluorochrome molecule in a sequence-specific manner via hybridising a PNA (linked via a monomalemide bridge to an Oregon Green 488 fluorochrome), designed to bind away from the biologically important sites [187]. I used a similar approach to tag the pDNA with electron-dense nanogold particles for use in these studies to localise the intracellular fate of pDNA.

I first covalently linked a 1.4 nm monomaleimide terminated nanogold to PNA via a single terminal cysteine thiol group. The resultant nanogold-PNA-conjugate was then hybridised to pDNA via a single target sequence to produce a stable nanogold-conjugated pDNA. Thus, a single nanogold particle was attached to a single pDNA molecule, a prerequisite in our study to visualise intracellularly localised nanogold labelled pDNA at single molecule resolution using TEM. I used a number of biochemical methods to verify the covalent binding of nanogold-PNA to the pDNA. After purifying the final nanogold-PNA/pDNA conjugates to remove any residual unbound nanogold-PNA or free pDNA, I confirmed co-localisation of the pDNA and nanogold-PNA in samples spotted on nitrocellulose membranes. This only confirmed that nanogold-PNA was present in the same sample as the pDNA after removal of any contaminating free pDNA or free nanogold-PNA.

With this in mind, I went on to visualise directly the nanogold-conjugated pDNA on copper grids using high-resolution TEM. The nanogold-conjugated pDNA appears as black spots co-

localised with striated pDNA structures compared with the control unconjugated pDNA in which the black spots were absent. In order for the nanogold-conjugated pDNA to be of use in the TEM studies, I needed to demonstrate irreversible covalent linkage of nanogold-PNA to the pDNA to give a robust TEM probe which behaves in the same way as wild type pDNA. To this end, I compared the electrophoretic mobilities of nanogold-conjugated pDNA with that of pDNA physically mixed with nanogold (representing control unconjugated pDNA), the reasoning being nanogold particles should only co-migrate with pDNA if covalently bound to it. Thus, the nanogold and pDNA would not be expected to co-migrate in the physically mixed pDNA/nanogold control. However, I found no difference in the electrophoretic mobility of the linear, open circular and super coiled pDNA conformations of the nanogold-conjugated compared to unconjugated pDNA in the physical mixture. To further extend this assay, I next sought to co-localise the Gel-red-stained DNA bands on the agarose gels with nanogold bands detected by silver staining (recommended by Nanoprobes). I reasoned that if the conjugated pDNA was covalently bound to gold particles, the nanogold and pDNA would co-migrate and thus be co-localised. Unfortunately, silver enhancement (Nanoprobes) was not sensitive and specific enough for visualisation of the nanogold on the agarose gel after electrophoresis. Thus, I saw no difference in the electrophoretic mobility of the nanogold-conjugated pDNA and control unconjugated pDNA. This is perhaps not surprising, as the addition of the relatively small, 15 kDa, nanogold particle onto the larger pDNA molecule (pCIKFluc = 4,970 kDa) is not likely to result in a resolvable shift in mobility. I thus decided to use an alternative strategy to evaluate the direct linkage of the nanogold particle onto the pDNA, exploiting any potential alterations in its electrophoretic mobility. Our laboratory has previously assessed the direct linkage of a small fluorochrome Oregon Green 488 to pCMVβ-DTS, via a specifically targeted PNA linker molecule, by comparing the electrophoretic mobility shift of endonuclease restriction enzyme fragments of

Oregon Green 488-PNA conjugated pDNA with unconjugated pDNA [187]. In this experiment, a 1 kb fragment of pCMVβ-DTS, containing the Oregon Green 488-PNA label, was generated by double digesting using the endonucleases Sap I and AhD 1. The Oregon Green 488-PNA/pCMVβ-DTS 1 kb fragment was shifted to a band migrating slightly above the unconjugated pCMVβ-DTS due to the additional mass of the PNA (6,776 Da) and the Oregon Green 488 (463 Da) molecule.

I used a similar strategy and doubly digested the pDNA, pCIKFluc, with endonucleases BseYI and BssSI to generate five restriction fragments of sizes (bps) 131, 307, 1253, 1547 and 3080. Unfortunately, there was no difference in electrophoretic mobility of the fragment A (containing nanogold-PNA sequence) from digestion of nanogold-conjugated pDNA compared with fragment A from digestion of the control physically mixed pDNA and nanogold particles. The fragment A, 131 bps in size, contains the Nanogold-PNA sequence, and fragment B, 307 bps in size, which serves as useful mobility shift internal control on the agarose gels (Figure 28). The three other larger fragments were unresolved. Thus, agarose gel electrophoresis is not able to resolve a difference in mobility shift in the fragment A following sequence-specific nanogold-PNA conjugation. In a previously described study by Hillery *et al*, fluorescence from Oregon Green 488 allowed the direct visualisation and identification of Oregon Green 488-PNA hybridised to pCMVβ-DTS [187]. The Oregon Green 488 fluorescence was shown to co-migrate with the Oregon Green-PNA target sequence-containing 1 kb fragment, a product of the endonuclease digestion of Oregon Green 488-PNA/pCMVβ-DTS, demonstrating the stable linkage of the fluorescent PNA-Oregon Green 488 conjugate to the pDNA. In a similar fashion, but using silver-enhancement to visualise the nanogold, I set out to investigate whether I could directly visualise the nanogold-PNA conjugate linked to whole nanogold-conjugated pDNA, as well as to digestion

product fragment A (131bps), following agarose gel electrophoresis. Silver enhancement to visualise nanogold particles conjugated to pDNA, electrophoresed on agarose gels was unsuccessful due to gross non-specific staining. I was, thus, unable to achieve our objective of confirming the covalent attachment of nanogold particles to pDNA by co-localising the silver-stained nanogold and the Red-Gel-stained pDNA on the electrophoresed endonuclease digested or undigested nanogold-pDNA conjugates.

In summary, I was unable to show a mobility shift difference between the 131bp fragments (generated from the digestion of nanogold-conjugated pDNA and unconjugated pDNA respectively) by running on agarose gel of 1 %, 2 % and 3 % agarose concentrations. This shows that agarose gel electrophoresis is not sensitive enough to resolve the difference in mass between the 131 bp fragments. The 131 bp fragment generated from nanogold-conjugated pDNA is 21.8 kDa (15 kDa nanogold plus 6.8 kDa PNA) larger in mass terms compared to the smaller and faster migrating 131 bp fragment generated from unconjugated pDNA.

Linking nanogold or fluorochrome to pDNA via the PNA linker molecule in this way is superior to previously reported alternative conjugation strategies. For instance, Dowty *et al* labelled pDNA directly with colloidal gold and found that the majority of the pDNA attached to one gold particle [214]. However, some unlabelled plasmids were also present in this preparation and the amount of labelled pDNA was not known. The same direct labelling approach used by Kitson *et al* in our laboratory resulted in poor labelling of pDNA, with 10 nm colloidal gold, clustered in appearance [215]. The poor labelling efficiency of pDNA with colloidal gold can, in part, be explained by the fact that colloidal gold particles are adsorbed randomly on the surface of pDNA. However, the exact interaction of colloidal gold with

pDNA is not known. Both authors therefore used an alternative indirect approach to label pDNA with colloidal gold. Dowty *et al* labelled biotinylated pDNA to colloidal gold via streptavidin [214]. Kitson *et al* labelled pDNA with BrdU, a thymidine analogue incorporated into pDNA, which is then detected by immunogold labelling using a primary αBrdU antibody and a colloidal gold conjugated secondary antibody [215]. Both indirect approaches labelled the pDNA in a non-specific random manner. In contrast to my conjugation strategy, the biotinylation as well as the incorporation of BrdU, occurs at random sites on the pDNA molecule and there is, therefore, a high probability of perturbing potentially important transcriptional sites.

The PNA target sequence containing nanogold (linked via a monomaleimide moiety) was designed to be located away from any biologically active sequences on the pCIKFluc plasmid. I, however, still needed specifically to evaluate the effect on the transcriptional activity of the pCIKFluc following nanogold-PNA hybridisation. I thus compared the transfection efficiency of nanogold-conjugated pDNA with control unconjugated pDNA physically mixed with nanogold in HEK 293T cells. Transfection activity was assessed by measuring the luciferase reporter gene transcriptional activity 25 hours post-transfection. No significant difference was observed between the levels of luciferase expression of nanogold-conjugated pDNA compared to that of the control unconjugated pDNA physically mixed with nanogold. Thus the sequence-specific linkage of nanogold-PNA had no effect on the biological activity of the nanogold-conjugated TEM probe. In contrast to the above retention of biological activity upon attachment of nanogold to pCIKFluc, a previous report from our laboratory using a similar strategy resulted in a 45% decrease in transcription activity of pCMVβ-DTS reporter plasmid conjugated to Oregon Green 488-PNA, respectively [187]. Thus, it appears that the hybridisation of the larger 1.4 nm nanogold-PNA conjugate (15 kDa

and 6776 Da, respectively) to the plasmid, pCIKFluc, resulted in the retention of most of the native transcriptional activity compared with that obtained on hybridisation of the smaller Oregon Green 488-PNA conjugate (463 Da and 6776 Da, respectively) to pCMVβ-DTS reporter plasmid. This means that the loss of biological activity of Oregon Green 488-conjugated pCMVβ-DTS reporter plasmid is unlikely to be dependent on the size of the attached fluorescent or TEM probe. PNA was targeted to sequences at 5000-6000 bps and 5393 bps for the pCMVβ-DTS and pCIKFluc, respectively. For both of these plasmids, the PNA-target sites were, therefore, well away from any transcriptional important regions. Interestingly, the PNA-target site on the pCIKFluc is closer to the CMV promoter region than that of the pCMVβ-DTS and one would therefore expect relatively more perturbation of biological activity in the former plasmid. However, more wild-type transcriptional activity was lost following the hybridisation of the more distally located Oregon Green 488-PNA onto pCMVβ-DTS compared with the relatively insignificant loss of pCIKFluc reporter gene activity following the hybridisation with nanogold-PNA conjugate. Possible explanations for this counter intuitive finding include: 1) the reporter gene activity of the conjugated plasmids compared with their wild-type positive controls was evaluated using 2 different cell types, HeLa cells for Oregon Green 488-PNA/pCMVβ-DTS and HEK 293T cells for nanogold-PNA/pCIKFluc. 2) HeLa cells were transfected with Oregon Green 488-PNA/pCMVβ-DTS using cationic Genzyme lipid 67 (lipid GL67) or DC-cholesterol/DOPE and the HEK 293T cells with nanogold-PNA/pCIKFluc using lipofectamine 2000. As discussed earlier, the conjugation strategy differs from conventional approaches for attaching probes to plasmids which non-specifically label the entire plasmid in a random fashion. I attached nanogold probes to the plasmids via PNA, in a sequence-specific, targeted and non-disruptive manner thus accepted the original hypothesis. For example, the attachment of photoactivable biotin to a 3871 bp plasmid expression vector containing chloramphenicol acetyltransferase (CAT)

gene resulted in a 60% decrease in transcription activity following transfection into mouse fibroblasts [233]. The loss of biological activity compared to wild-type plasmid was due to random covalent linkage of biotin to the transcriptional cassette of the biotinylated plasmid which significantly perturbed transgene expression. Unlike my approach, the linkage was random and non-specific and, therefore, there was no control over the placement site on the plasmid away from the transcription site.

Having established an optimal protocol for observation of ciliated epithelial cells with well preserved ultrastructure, I next set out to visualise using TEM, the intracellularly localised nanogold-conjugated pDNA following non-viral gene transfer. To this end, I first attempted to use cultured HEK293T cells as a convenient tractable test-bed prior to translation into a more complex *in vitro* model. However, it quickly became apparent that this approach was just as complex and labour-intensive as testing directly in primary airway epithelial tissue. I thus decided to use the optimised fixation and processing protocols to visualise nanogold-conjugated pDNA in transfected ALIs. I was able to see nanogold-conjugated pDNA after one hour of transfection. Nanogold-conjugated pDNA was seen on the cilia, cell membrane, cytoplasm, nuclear envelope and inside the nucleus. I also observed black spots in the control ALI transfected with unconjugated pDNA. These randomly dispersed background black spots were likely due to previously reported auto-nucleation, a common phenomenon in which gold ions (present in the gold-enhancement kit solution) are reduced to metallic gold and subsequently grow in size during the enhancement procedure [229]. The background spots were also observed in the ALI transfected with nanogold-conjugated pDNA. I therefore decided, it would be better to compare all nanogold-conjugated pDNA quantification with this background gold staining following non-viral gene transfer in ALIs during the time-lapse studies, described in the next chapter.

Chapter 5: Quantitation of intracellularly localised nanogold-conjugated pDNA in human airway epithelial cells using transmission electron microscopy

5.1 Introduction

Following the preparation and validation of nanogold-conjugated pDNA as a *bona fide* probe for visualising pDNA against a well-preserved ultrastructure of transfected human airway epithelium (described in previous Chapter 4), I next set out to use the nanogold conjugated pDNA probe to address the key question of the study. Thus, I next sought to identify the location and quantitate the relative amounts of nanogold-conjugated pDNA delivered to the cytoplasm and the nucleus following non-viral gene transfection of human airway epithelial cells.

Before starting any experiments aimed at tracking pDNA following the non-viral transfection of ALI, it was first important to assure ourselves that the ALIs were viable and transfectable. To this end, specific batches of ALI, with beating cilia, were tested for their transfectability by assessing their ability to express *Gaussia* luciferase reporter plasmid (pCIKGluc) following lipid GL67A-mediated gene transfer. Historically, we and others have successfully used the *Firefly* or *Renilla* luciferase reporter gene (Fluc) activity as a convenient surrogate measure for transgene expression following cationic lipid-mediated transfection with pCIKFluc plasmid carrying Fluc gene under the control of the human immediate/early CMV promoter/enhancer [59;134;135]. However, I was unable to detect Fluc activity in ALIs because the assay was not sensitive enough. Recently, a secreted luciferase reporter gene *Gaussia* luciferase gene (Gluc) was isolated from *Gaussia princeps*

[234] and we have established this Gluc gene under the control of the eukaryotic CMV immediate-early promoter/enhancer as an alternative to Fluc gene [235]. Furthermore, the Gluc product, *Gaussia* luciferase, is thermostable, pH resistant and more sensitive than *Firefly* luciferase [236] or secreted alkaline phosphatase [237;238]. Thus Gluc is commonly used to study various biological processes [234;239-242]. In addition, the Gluc is secreted and can be detected in both apical and basolateral compartments so gene expression in ALIs can be followed over time without the need to harvest the cells [235].

Hypothesis

Increasing the transfection time of human ALIs with nanogold-conjugated pDNA using cationic lipid GL67A results in enhanced nuclear delivery of the gold-labelled pDNA as measured by TEM.

Aims

Assessed the quantitative localisation of pDNA in human airway epithelial cells at different transfection time points using TEM.

5.2 Materials and Methods

Described in detail in Materials and Methods Chapter 2.

5.2.1 Transfection of human airway epithelial cells by nanogold-conjugated *Firefly* luciferase reporter plasmid

Briefly, human ALIs were transfected apically at 37^{o}C with a 100 µl complex of cationic lipid GL67A and nanogold-conjugated pDNA at a 1:4 molar ratio made in OptiMEM, for the required time points. Controls were transfected with a complex of physical mix of nanogold and pDNA (unconjugated pDNA) using GL67A. The ALIs were processed for visualisation under TEM, after appropriate transfection times, as described in detail in Section 4.2.3. The black osmium tetroxide stained epithelium (ALI) in the resulting clear araldite block was exposed for sectioning by trimming with a knife (Agar Scientific). Semi-thin (1 µm) epithelial sections were then cut using an ultra-microtome (Ultracut E, Reichert-Jung, Leica, Milton Keynes, UK) and were stained with toulidine blue to visualise epithelial cells using light microscopy. Sectioning was continued until at least eight complete ciliated epithelial cells were localised within a particular section by light microscopy. Next, 120 nm ultra-thin sections were cut from this area of interest and stretched using xylene in order to avoid wrinkling of the sections. The xylene-stretched gold-silver sections were then finally collected on the nickel grids. The sections were gold enhanced for 15 minutes to amplify the size of the nanogold.

5.2.2 Quantitation of nanogold-conjugated *Firefly* luciferase reporter plasmid following transfection of human airway epithelial cells

Gold-enhanced sections were observed using TEM and digital images captured at low magnification (between x1500 to x3500) to reveal areas of interest encompassing complete ciliated airway epithelial cells. Electron-dense dark spots (at x10,000), representing gold-enhanced nanogold-conjugated pDNA, on the cilia, on the cell membrane, within the cytoplasm compartment, on the nuclear envelope and within the nucleus were manually counted in a blinded-fashion. Similarly the dark spots resulting from gold-enhancement of sections from ALIs transfected with control unconjugated pDNA, representing background staining, were also counted.

5.2.3 Statistical analysis

Unless otherwise indicated, data are expressed as medians for the indicated number of experiments. To assess normal distribution of the data the K-S normality test was performed. A parametric unpaired t-test or a non-parametric Mann-Whitney test was performed for two group comparisons of normal and not normally distributed samples respectively. ANOVA followed by Bonferroni *post-hoc* corrections (parametric) or a Kruskal-Wallis with Dunn's Multiple *post-hoc* corrections (non-parametric) were carried out for more than two group comparisons. In all cases the null hypothesis was rejected at $p < 0.05$. All analysis was performed using GraphPad Prism4 (GraphPad Software, Inc., La Jolla, CA, USA).

5.3 Results

5.3.1 Assessment of the viability of human airway epithelial cells by ciliary beating

The maturity and quality of ALI cultures purchased from Epithelix varied from batch to batch. Based on data from our laboratory, batches of ALIs not older than 65 days from the date of seeding were purchased from Epithelix [235]. Soon after their arrival, they were replaced by fresh pre-warmed MucilAir medium basolateraly and kept at 37^{o}C. After 1 hour, I observed the ALIs for ciliary beating under the light microscope at x20 magnification. All ALIs survived transportation, confirmed by visible ciliary beating.

5.3.2 Human airway epithelial cells transfectability using *Gaussia* luciferase reporter plasmid

Recent work in our laboratory has shown that the transfection efficiency of GL67A/ pCMV-Gluc complexes in younger cultures (<80 days) is significantly ($p<0.01$) higher compared to older cultures (>120 days) [235]. With this in mind, I only used ALIs of 45 to 65 days post-seeding. These ALIs, with detectable ciliary beating, were transfected with a complex of pCIKGluc (10 μg DNA/ALI) and lipid GL67A (n = 6 ALIs/group). Untransfected ALIs served as controls and were cultured side-by-side (n = 6 ALIs/group). Apical and basolateral media (100 μl) were harvested 48 hours after transfection for the quantification of Gluc expression. Figure 34 shows that significantly higher levels of Gluc expression in the media collected from the apical side were found 1 hour ($p<0.01$) and 6 hours ($p<0.05$) post-transfection under standard transfection conditions (1:4 lipid/DNA molar ratio) compared to controls. This increased Gluc gene expression was not further increased, when the lipid

GL67A/pCIKGluc ratio was increased to 6:8, the clinically relevant ratio normally used for nebulisation of the lipid/pDNA formulation to human lungs [29]. Figure 35 shows that despite a decrease in overall Gluc gene expression levels, significant differences in gene expression were found in media collected from the basolateral side of transfected ALIs compared to control untransfected ALIs. Thus pCIKGluc is a suitable reporter gene for use in assessing the transfectability of ALI cultures. Furthermore, because the levels of Gluc expression were similar following transfection for 1 hour or 6 hours with lipid/DNA molar ratios of 1:4 or 6:8, I transfected ALI cultures for 1 hour at a lipid/DNA molar ratio of 1:4 in all subsequent quality control experiments. The results from the four independent experiments were pooled together and are shown in Figures 36 and 37.

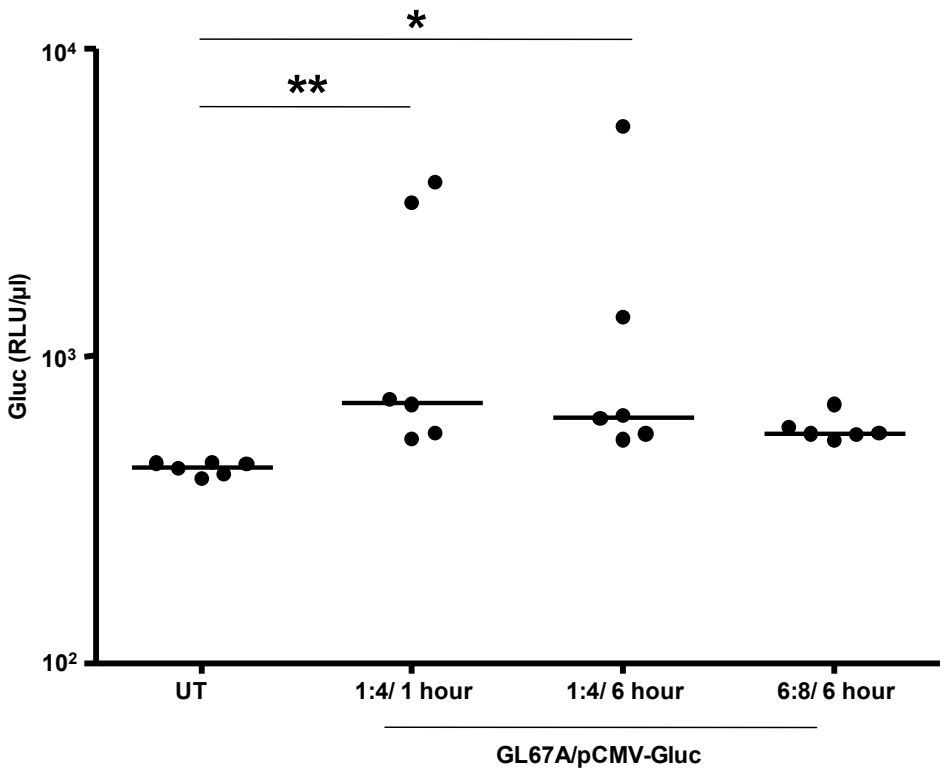

Figure 34: Apical *Gaussia* luciferase expression after transfection with GL67A/pCMV-Gluc at different molar ratios and transfection times

Human airway epithelial cells grown at an air-liquid interface (ALI) were transfected with GL67A/pCMV-Gluc at molar ratios of 1:4 for 1 hour and 6 hours and at molar ratios of 6:8 for 6 hours. Untransfected (UT) ALIs served as a negative control. Medium was added to the apical side of ALI 48 hours post-transfection and incubated for 1 hour prior to harvesting the apical medium for detection of Gluc expression. Each data point represents one ALI with the median Gluc expression of the group (n=6) shown as a horizontal line. * = $p<0.05$ GL67A/pCMV-Gluc 1:4 molar ratio transfected for 6 hours compared to UT and ** = $p<0.01$ GL67A/pCMV-Gluc 1:4 molar ratio transfected for 1 hour compared to UT.

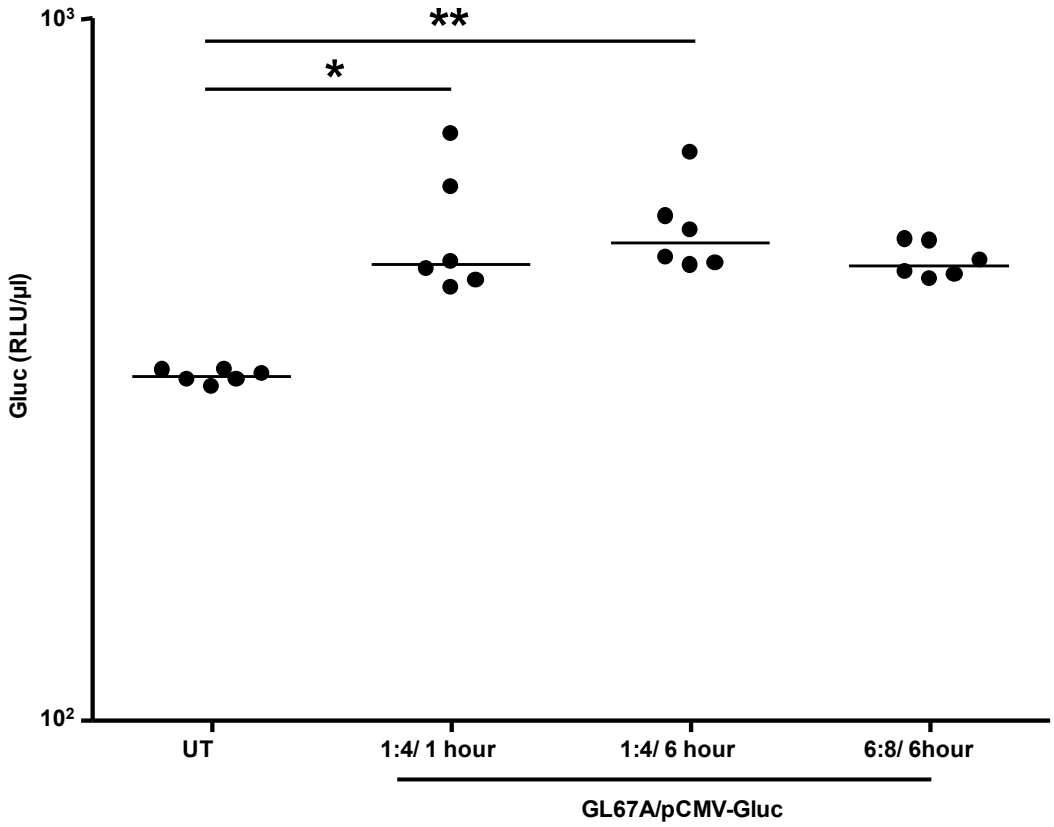

Figure 35: Basolateral *Gaussia* luciferase expression after transfection with GL67A/pCMV-Gluc at different molar ratios and transfection times
Human airway epithelial cells grown at an air-liquid interface (ALI) were transfected with GL67A/pCMV-Gluc at molar ratios of 1:4 for 1 hour and 6 hours and at molar ratios of 6:8 for 6 hours. Untransfected (UT) ALIs served as a negative control. Medium was collected from the basolateral side of ALI 48 hours post-transfection. Each data point represents one ALI with the median Gluc expression of the group (n=6) shown as a horizontal line. * = $p<0.05$ GL67A/pCMV-Gluc 1:4 molar ratio transfected for 1 hour compared to UT and ** = $p<0.01$ GL67A/pCMV-Gluc 1:4 molar ratio transfected for 6 hours compared to UT.

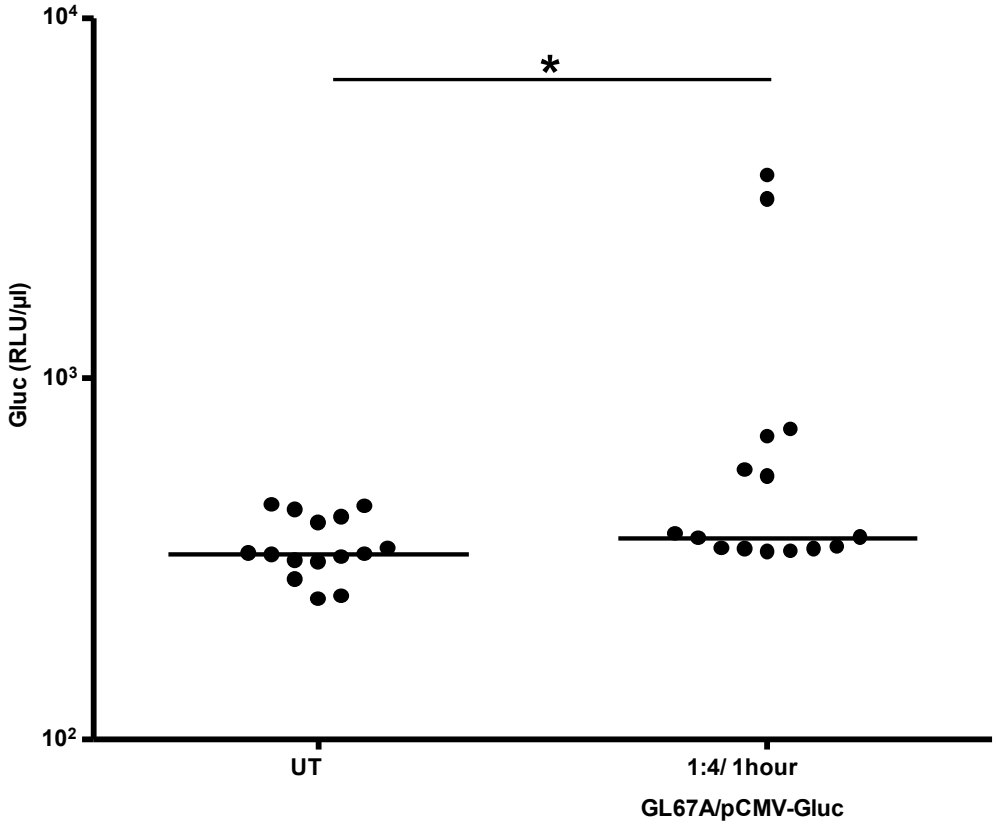

Figure 36: Apical *Gaussia* luciferase expression after transfection with GL67A/pCMV-Gluc (pooling of results from four independent experiments)
Human airway epithelial cells grown at an air-liquid interface (ALI) were transfected with GL67A/pCMV-Gluc at molar ratio of 1:4 for 1 hour. Untransfected (UT) ALIs served as a negative control. Medium was added to the apical side of ALI 48 hours post-transfection and incubated for 1 hour prior to harvesting the apical medium for detection of Gluc expression. Each data point represents one ALI with the median Gluc expression of the group (n=15) shown as a horizontal line. * = $p<0.05$ GL67A/pCMV-Gluc 1:4 molar ratio transfected for 1 hour compared to UT.

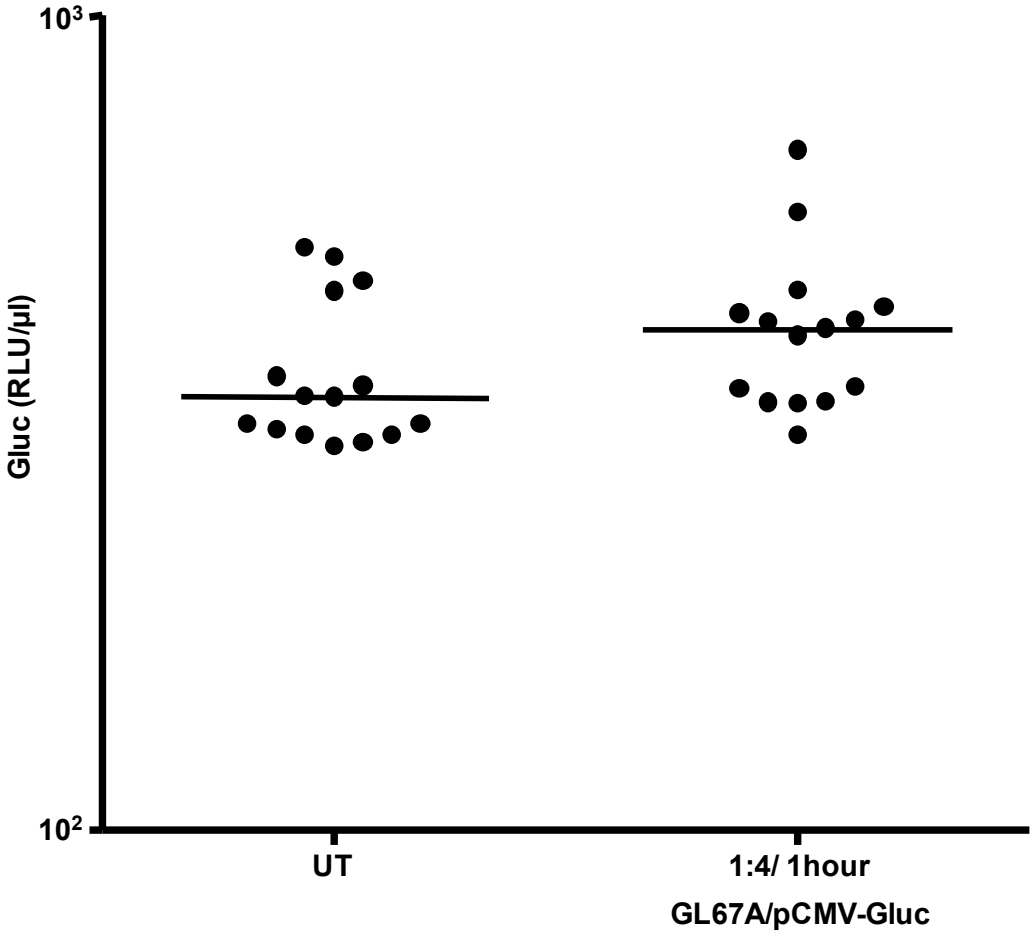

Figure 37: Basolateral *Gaussia* luciferase expression after transfection with GL67A/pCMV-Gluc (pooling of results from four independent experiments)
Human airway epithelial cells grown at an air-liquid interface (ALI) were transfected with GL67A/pCMV-Gluc at molar ratios of 1:4 for 1 hour. Untransfected (UT) ALIs served as a negative control. Medium was collected from the basolateral side of ALI 48 hours post-transfection. Each data point represents one ALI with the median Gluc expression of the group (n=6) shown as a horizontal line.

5.3.3 Quantification of intracellularly localised nanogold-conjugated plasmid DNA following non-viral gene transfection in human airway ciliated epithelial cells

Gold-enhanced nanogold particles conjugated to pDNA were seen inside the cell as electron-dense dark spots as previously shown in Chapter 4 which described the optimisation of the TEM procedure to detect nanogold-conjugated pDNA in human airway epithelial cells. In contrast, in Chapter 4, I also showed randomly localised control dark spots representing non-specific signal in epithelial cells transfected with unconjugated pDNA. The dark spots on these control unconjugated pDNA transfected cells are a likely consequence of auto-nucleation during the gold-enhancement procedure. Figure 32 shows the representative transmission electron micrograph of transfected ciliated epithelial cells with nanogold-conjugated pDNA (electron-dense dark spots) localised on the cilia, in the cytoplasmic and nuclear compartments. Background levels of dark spots were also seen in the control epithelial cells (Figure 33). In addition to the dark spots localised to the bulk cytoplasm, some appeared to be associated with vesicles and cytoskeleton filaments.

5.3.3.1 Quantification of intracellularly localised nanogold-conjugated plasmid DNA in ALIs transfected for 60 minutes

Figure 38 shows the mean number of dark spots counted in eight complete ciliated epithelial cells per gold-enhanced section from an individual ALI; including on the cilia, apical surface membrane (cell membrane), in the cytoplasm, nuclear envelope and nucleus following 60 minutes transfection with nanogold-conjugated pDNA (n=6 ALIs) compared with those transfected with control unconjugated pDNA (n=6 ALIs). The closed circles and closed diamonds shown in Figure 38 indicate gold-enhanced nanogold-conjugated pDNA- and

control unconjugated pDNA-transfected ALI sections, respectively. Each paired (i.e. grid containing nanogold-conjugated pDNA-transfected ALI section with its control grid, containing unconjugated pDNA-transfected ALI section, both processed for gold-enhancement simultaneously) ALI section is represented by the same colour. The mean number of dark spots quantified in 6 ALIs was not normally distributed, as verified using the K–S test, and are therefore represented as median values.

Taken together, it is obvious that there were more dark spots in the cytoplasm ($p<0.05$) and an increased trend in the nuclei of nanogold-conjugated pDNA-transfected ALIs compared to those seen in ALIs transfected with unconjugated pDNA control. This difference between the positive nanogold-conjugated pDNA signal compared to the control background signal in both the cytoplasm and the nucleus is better illustrated in Figures 39 and 40, which shows an increase in both the cytoplasmic- and nuclear-localised dark spots when comparing the paired ALIs. Data points of paired ALIs, defined previously as matched grid containing nanogold-conjugated pDNA-transfected ALI section with its unconjugated pDNA-transfected ALI section control grid, are joined by a line to illustrate the difference between gold enhanced sections of ALIs transfected with nanogold-conjugated pDNA compared to those transfected with unconjugated pDNA.

Having established that background levels of dark spots in gold-enhanced sections from cells transfected with control unconjugated pDNA were likely due to auto-nucleation [229], I next subtracted this background signal from our gold-enhanced nanogold-conjugated pDNA transfected cells. Figure 41 shows the distribution of background subtracted nanogold-conjugated pDNA in the cytoplasm and nucleus, as well as on the cilia, cell membrane and nuclear envelope. As noted above, the background is the median value of dark spots counted

in 6 ALIs transfected with unconjugated pDNA. Thus, following 60 minutes non-viral transfection, nanogold-conjugated pDNA is internalised, and localised in both the cytoplasm and the nucleus. No nanogold-conjugated pDNA was seen on the cilia, cell membrane and nuclear envelope based on the median values.

We know from previous investigations in our laboratory that there is considerable variability between individual ALIs and batches in gene transfer experiments [235]. In the above analysis of the nanogold-conjugated pDNA-transfected ALIs, data were presented as pooled data from an average of 8 cells per ALI section. Taking advantage of a key capability of TEM, I next looked at the above distribution of nanogold-conjugated pDNA in the cytoplasm and nucleus at the individual cell level.

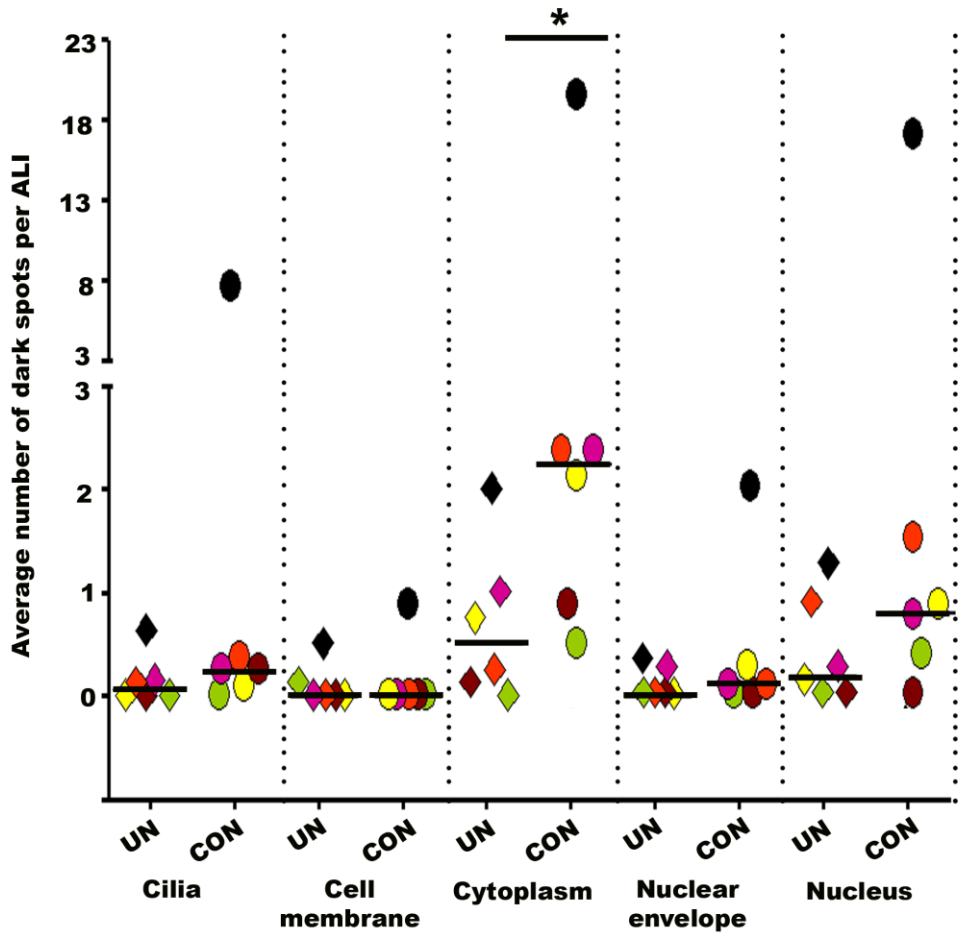

Figure 38: Quantitation of electron-dense dark spots following gold-enhancement of nanogold-conjugated plasmid DNA in human airway epithelial cells transfected for 60 minutes

Human airway epithelial cells grown at an air-liquid interface (ALI) were transfected with nanogold-conjugated plasmid DNA (circles, CON) and control unconjugated plasmid DNA (diamonds, UN) for 60 minutes. Cells were fixed and processed for TEM as described in Materials and Methods. Electron-dense dark spots on TEM micrographs of gold-enhanced sections from nanogold-conjugated pDNA- and control unconjugated pDNA-transfected cells were manually scored. Each data point represents the average number of dark spots in eight complete ciliated epithelial cells per ALI. Paired sections are indicated by colour coding. The horizontal bar represents the median of the number of dark spots in ALIs (n = 6/group), * = $p<0.05$.

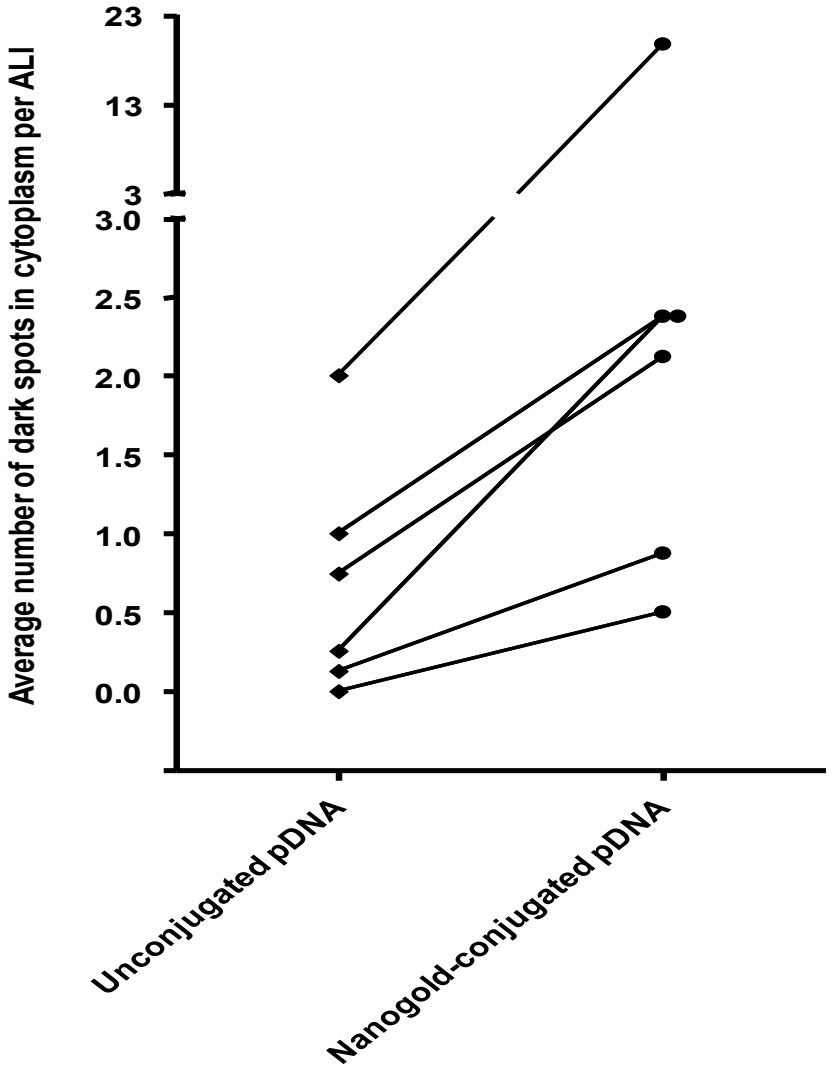

Figure 39: Localisation of electron-dense dark spots in the cytoplasm in gold-enhanced human airway epithelial cells following transfection with nanogold-conjugated or unconjugated plasmid DNA for 60 minutes

Each data point represents the average number of electron-dense dark spots in eight complete ciliated epithelial cells per ALI transfected with nanogold-conjugated pDNA (circles) compared to control unconjugated pDNA-transfected ALI (diamonds) (n = 6/group). For simplicity I defined ALIs as paired ALIs because gold enhancement of grids containing control-transfected ALI section and containing nanogold-conjugated-transfected ALI section was carried out simultaneously therefore joined by a line.

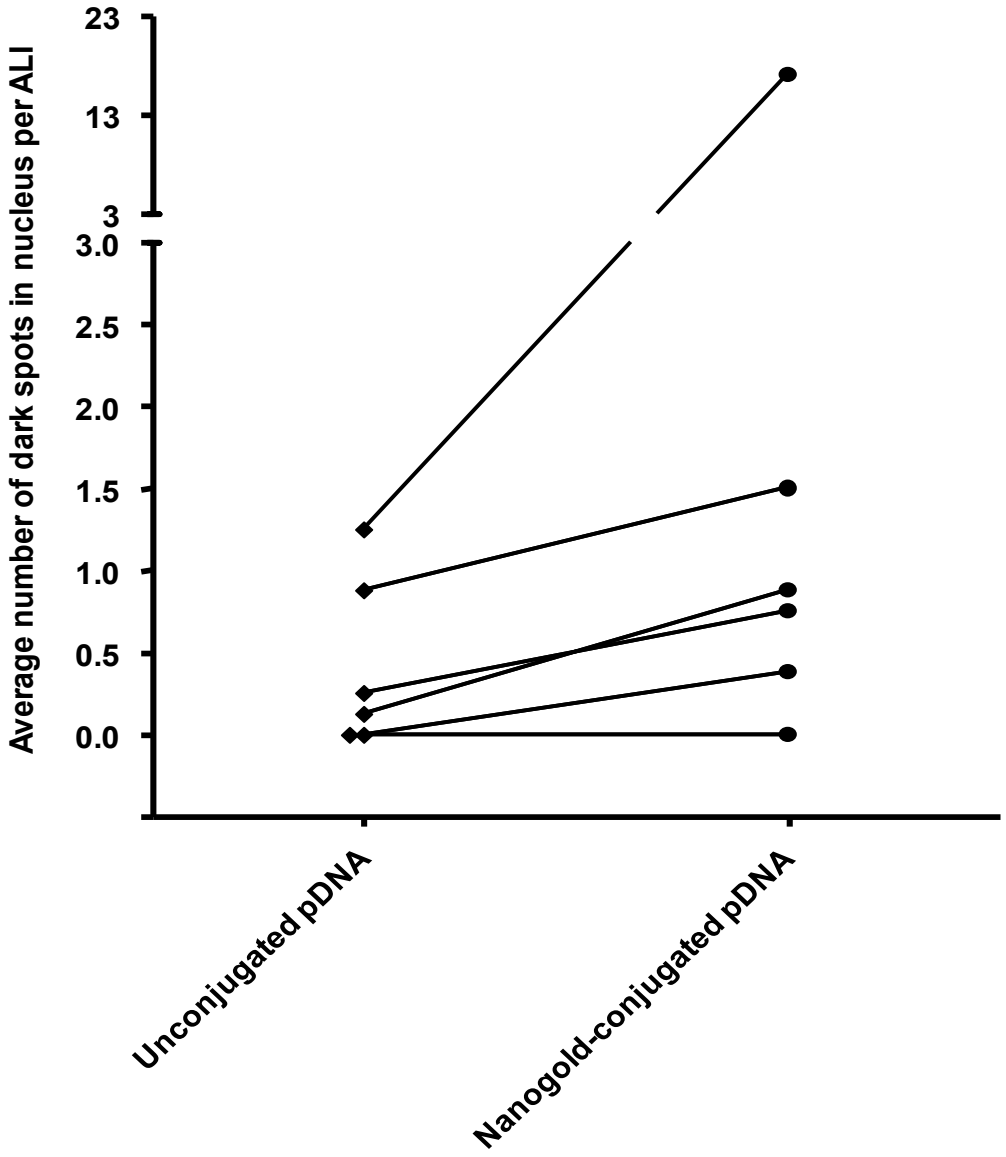

Figure 40: Localisation of electron-dense dark spots in the nucleus in gold-enhanced human airway epithelial cells following transfection with nanogold-conjugated or unconjugated plasmid DNA for 60 minutes

Each data point represents the average number of electron-dense dark spots in eight complete ciliated epithelial cells per ALI transfected with nanogold-conjugated pDNA (circles) compared to control unconjugated pDNA-transfected ALI (diamonds) (n = 6/group).

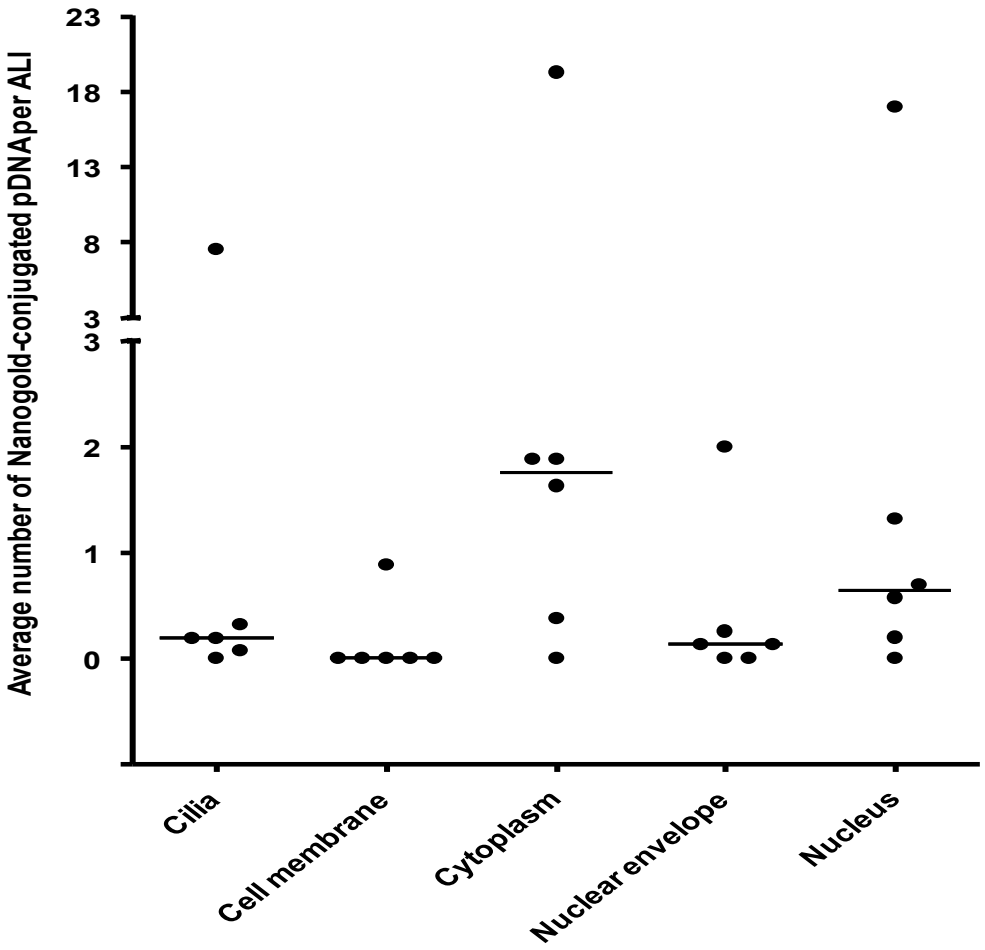

Figure 41: Quantitation of nanogold-conjugated plasmid DNA following transfection of human airway epithelial cells for 60 minutes

Background-subtracted number of nanogold-conjugated pDNAs derived from data shown in Figure 38. Each data point represents the average number of electron-dense dark spots in eight complete ciliated epithelial cells per ALI transfected with nanogold-conjugated pDNA minus the background. The background is the median of the number of dark spots counted on gold-enhanced section from eight complete cells in six ALIs transfected with control unconjugated pDNA. The horizontal bar represents the median of the number of nanogold-conjugated pDNA in ALIs (n = 6/group).

5.3.3.2 Single cell quantification of intracellularly localised nanogold-conjugated plasmid DNA in ALIs transfected for 60 minutes

The distribution of dark spots in the cytoplasm, as well as in the nucleus, of 8 individual cells transfected with nanogold-conjugated pDNA (circles) matched with its control unconjugated pDNA (diamonds) for 6 individual ALIs is shown in Figure 42 and Figure 43 respectively. In each Figure each individual cell (i.e. data point) is shown in a specific colour to permit evaluation of the distribution of dark spots in the nucleus and cytoplasm of individual cells. It is clear that both the intra-and inter-ALI dark spot distribution is highly variable. On initial inspection of these data, I found a trend towards an increase in the number of dark spots in both the cytoplasm and nuclei of cells transfected with nanogold-conjugated pDNA compared to cells transfected with control unconjugated pDNA. This suggestion was further validated on closer examination of the data and testing for significance between levels of dark spots in cells in paired nanogold-conjugated pDNA-transfected ALIs and control unconjugated-transfected ALIs. Thus, out of the 6 ALIs transfected with nanogold-conjugated pDNA for 60 minutes, 1 ALI had levels of cytoplasmic-localised and nuclear-localised dark spots higher than those seen in the control ALIs ($p<0.05$ and $p<0.01$ respectively). Taken together, and of great importance, these data show that pDNA was taken up into the cytoplasm and delivered to the nucleus of terminally differentiated cells following transfection for 60 minutes.

Figures 44 and 45 show background signal-subtracted nanogold-conjugated pDNA (i.e. the median value of dark spots counted in 8 cells in the cytoplasm or nucleus subtracted from dark spots in each individual conjugated pDNA transfected-cell cytoplasm or nucleus). Out of 6 ALIs, cytoplasmic localisation of nanogold-conjugated pDNA was seen in 5 (Figure 44)

and nuclear localisation of nanogold-conjugated pDNA in 3 ALIs (Figure 45) as indicated by median values.

Table 2 shows the number of cells in ALIs, transfected for 60 minutes, containing cytoplasmic- and nuclear-localised background-subtracted nanogold-conjugated pDNA following 60 minutes transfection. The cell numbers are expressed as the cells with internalised nanogold-conjugated pDNA in the cytoplasm, or nuclei, as a percentage of the total cell count in the 6 transfected ALIs (derived from Figures 44 and 45, respectively).

Altogether, I was able to detect cytoplasmic- and nuclear-localised nanogold-conjugated pDNA in 9 % and 8 %, respectively, of cells in ALI's transfected for 60 minutes.

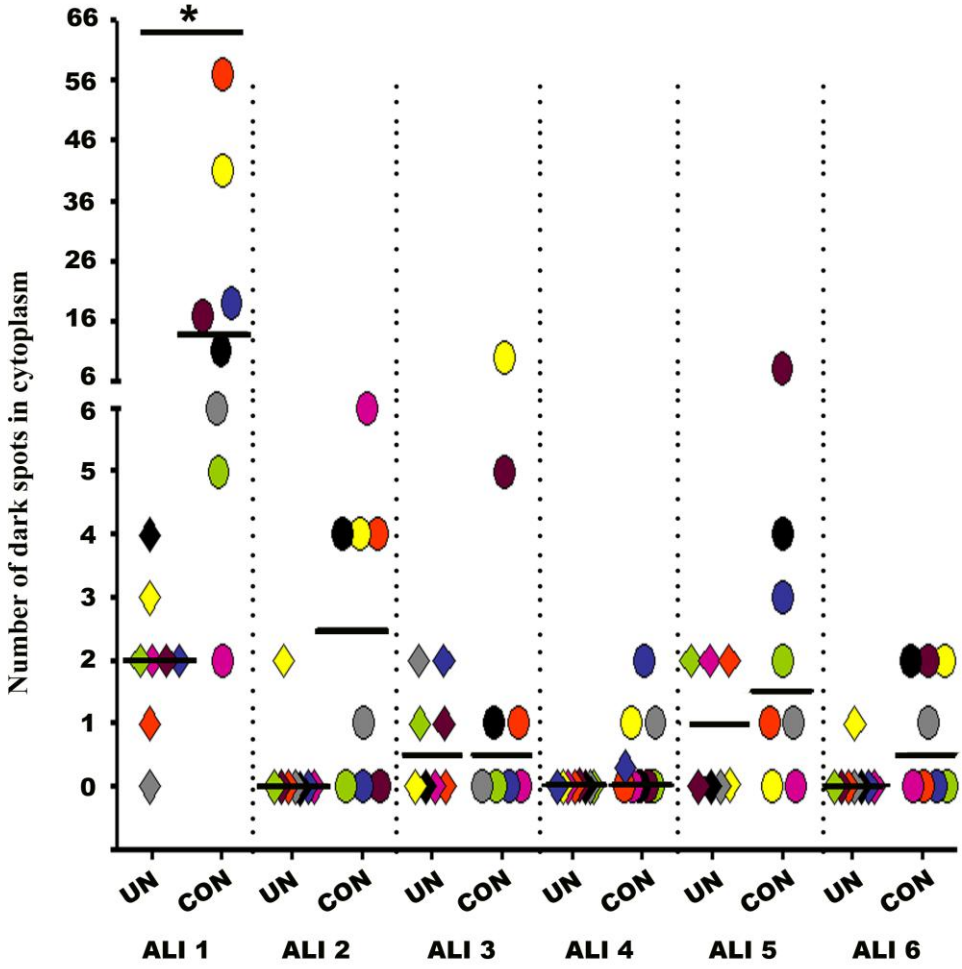

Figure 42: Distribution of dark spots in the cytoplasm following gold- enhancement of nanogold-conjugated plasmid DNA in human airway epithelial cells transfected for 60 minutes

Human airway epithelial cells grown at an air-liquid interface (ALI) were transfected with nanogold-conjugated plasmid DNA (circles, CON) and control unconjugated plasmid DNA (diamonds, UN) for 60 minutes. Cells were fixed and processed for TEM as described in Materials and Methods. Electron-dense dark spots on TEM micrographs of gold-enhanced sections from nanogold-conjugated pDNA- and control unconjugated pDNA-transfected cells were manually scored. Each data point represents the number of dark spots in the cytoplasm per complete ciliated epithelial cell. The cells were colour coded. The horizontal bar represents the median of the number of dark spots in eight cells per ALI (n = 6/group). * = $p < 0.05$

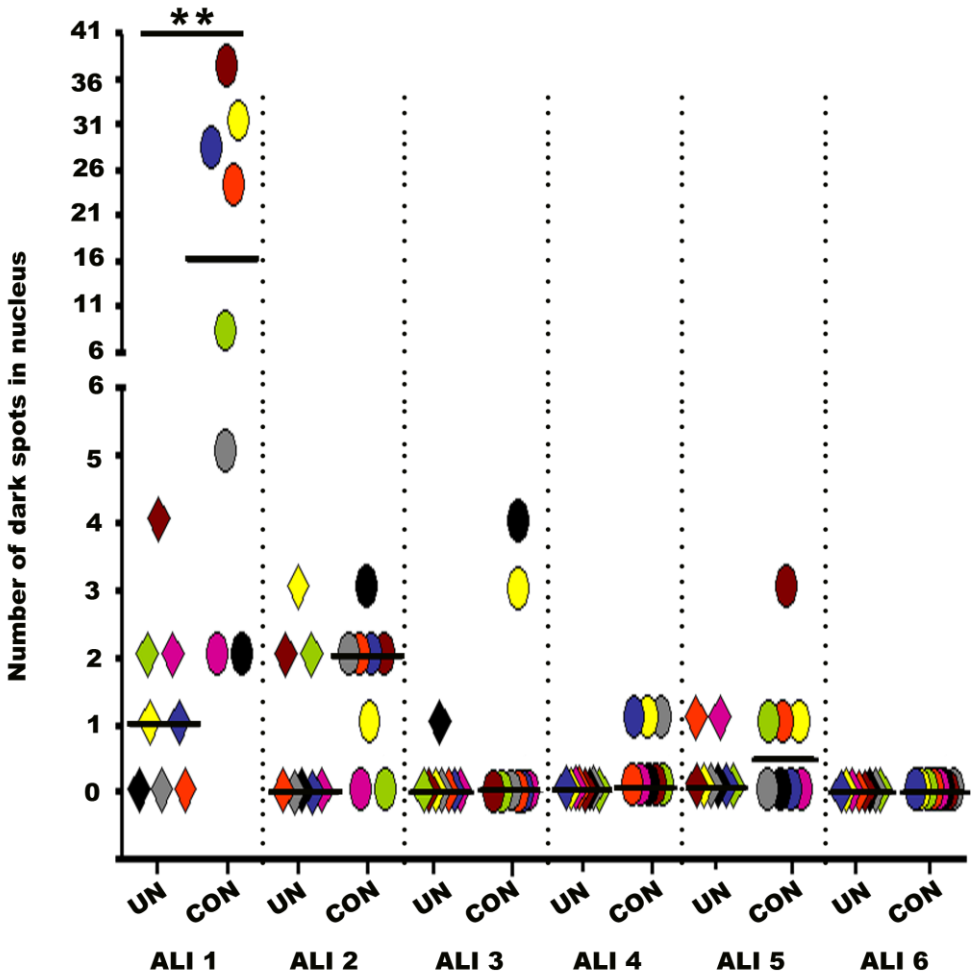

Figure 43: Distribution of dark spots in the nucleus following gold- enhancement of nanogold-conjugated plasmid DNA in human airway epithelial cells transfected for 60 minutes

Human airway epithelial cells grown at an air-liquid interface (ALI) were transfected with nanogold-conjugated plasmid DNA (circles, CON) and control unconjugated plasmid DNA (diamonds, UN) for 60 minutes. Cells were fixed and processed for TEM as described in Materials and Methods. Electron-dense dark spots on TEM micrographs of gold-enhanced sections from nanogold-conjugated pDNA- and control unconjugated pDNA-transfected cells were manually scored. Each data point represents the number of dark spots in the nucleus per complete ciliated epithelial cell. The cells were colour coded. The horizontal bar represents the median of the number of dark spots in eight cells per ALI (n = 6/group). ** = $p < 0.01$

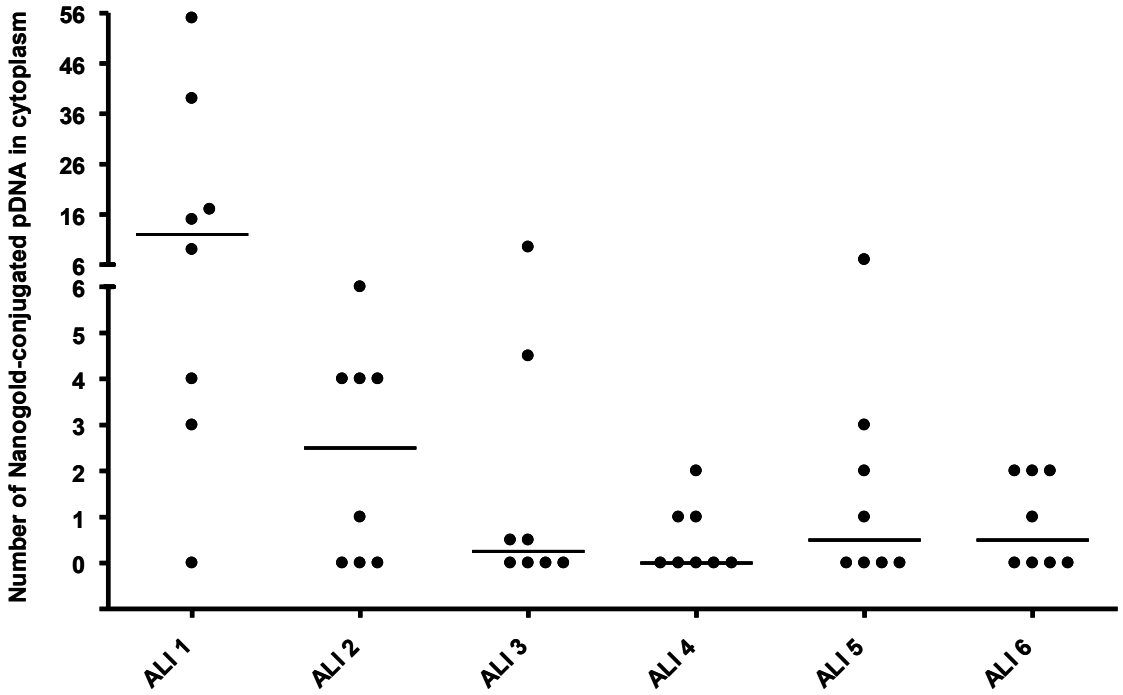

Figure 44: Distribution of nanogold-conjugated plasmid DNA in the cytoplasm following gold-enhancement of nanogold-conjugated plasmid DNA in human airway epithelial cells transfected for 60 minutes

Background subtracted nanogold-conjugated pDNA derived from data shown in Figure 42. Each data point represents the number of electron-dense dark spots in the cytoplasm per complete ciliated epithelial cell minus the background. The background is the median of the number of dark spots in eight complete ciliated epithelial cells per ALI transfected with control unconjugated pDNA. The horizontal bar represents the median of the number of nanogold-conjugated pDNA in eight cells per ALI (n = 6/group).

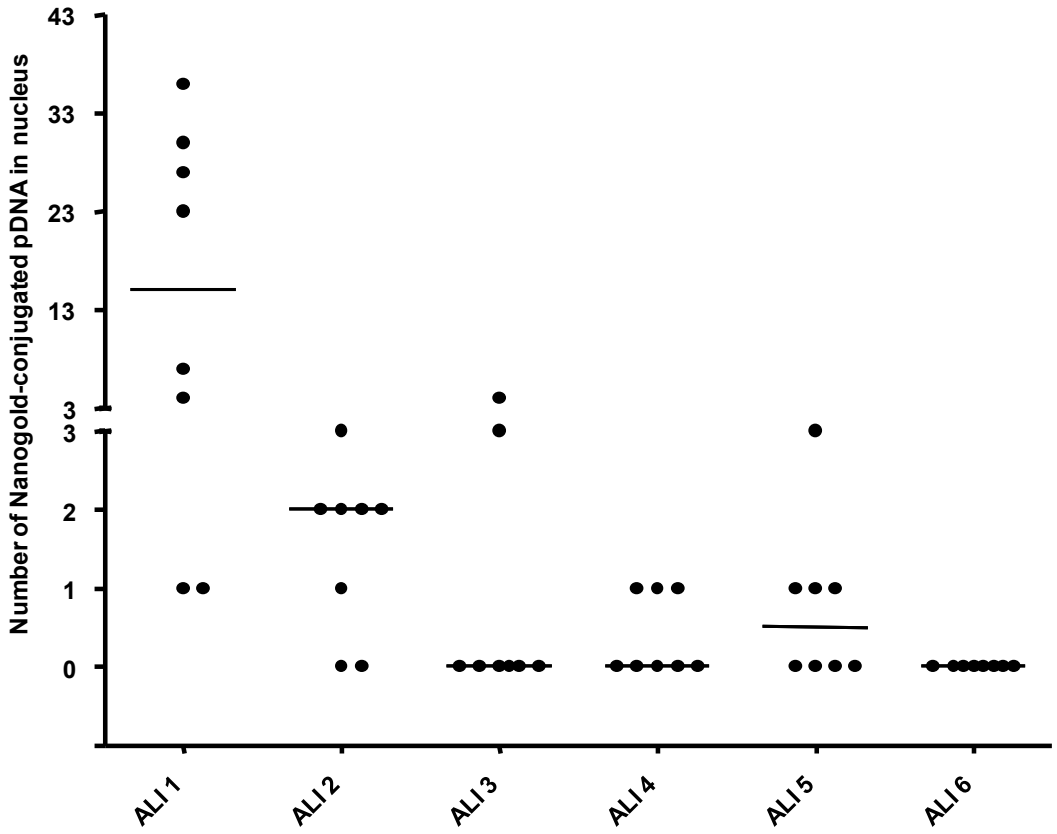

Figure 45: Distribution of nanogold-conjugated plasmid DNA in the nucleus following gold-enhancement of nanogold-conjugated plasmid DNA in human airway epithelial cells transfected for 60 minutes

Background subtracted nanogold-conjugated pDNA derived from data shown in Figure 43. Each data point represents the number of electron-dense dark spots in the nucleus per complete ciliated epithelial cell minus the background. The background is the median of the number of dark spots in eight complete ciliated epithelial cells per ALI transfected with control unconjugated pDNA. The horizontal bar represents the median of the number of nanogold-conjugated pDNA in eight cells per ALI (n = 6/group).

Cells containing nanogold-conjugated plasmid DNA (% of the total number of cells in 6 ALIs*)							Mean (%)
ALI	**1**	**2**	**3**	**4**	**5**	**6**	-
Cytoplasm	15	10	8	6	8	8	9
Nucleus	17	13	4	6	8	0	8

* The total number of 48 cells was counted in 6 ALIs.

Table 2: Number of airway epithelial cells in ALIs containing cytoplasmic- and nuclear-localised background-subtracted nanogold-conjugated plasmid DNA following 60 minutes transfection
The numbers of cells (derived from Figures 44 and 45) are expressed as the percentage of the total cells in all the 6 ALIs.

5.3.3.3 Quantification of intracellularly localised nanogold-conjugated plasmid DNA following transfection of ALIs for 15 minutes

Having determined that nanogold-conjugated pDNA was internalised, localised to the cytoplasm and delivered to the nucleus following transfection for 60 minutes, I next sought to visualise and quantitate the levels of intracellularly localised pDNA at an earlier transfection time-point in order to follow the intracellular progress of nanogold-conjugated pDNA to the nucleus as early as possible during transfection. The earliest practical time point at which the ALIs could be processed for TEM detection after the addition of the GL67A/nanogold-conjugated pDNA complex was 15 minutes. With this in mind, I therefore transfected ALI with nanogold-conjugated or control unconjugated pDNA, processed for TEM to permit visualisation and quantitative evaluation of intracellularly localised pDNA, as done for 60 minutes transfection experiments. Following 15 minutes transfection, I visualised dark spots localised to the cilia, cell membrane, cytoplasm, nuclear envelope and nucleus of ALIs transfected with nanogold-conjugated pDNA or control unconjugated pDNA. Manual counting performed in a similar fashion as for 60 minutes transfection revealed more dark spots were present in the cytoplasm and nucleus of ALIs transfected with nanogold-conjugated pDNA (circles), with levels on the cilia, cell membrane and nuclear envelope almost identical to the background-unconjugated control levels (diamonds) as shown in Figure 46. Again, as described for 60 minutes transfection, each matched pair ALI section is represented by the same colour. The mean number of dark spots quantified in 6 ALIs was normally distributed on the cilia, in the cytoplasm as well as in the nucleus but not the cell membrane and nuclear envelope, as verified using the K–S test, and are represented as

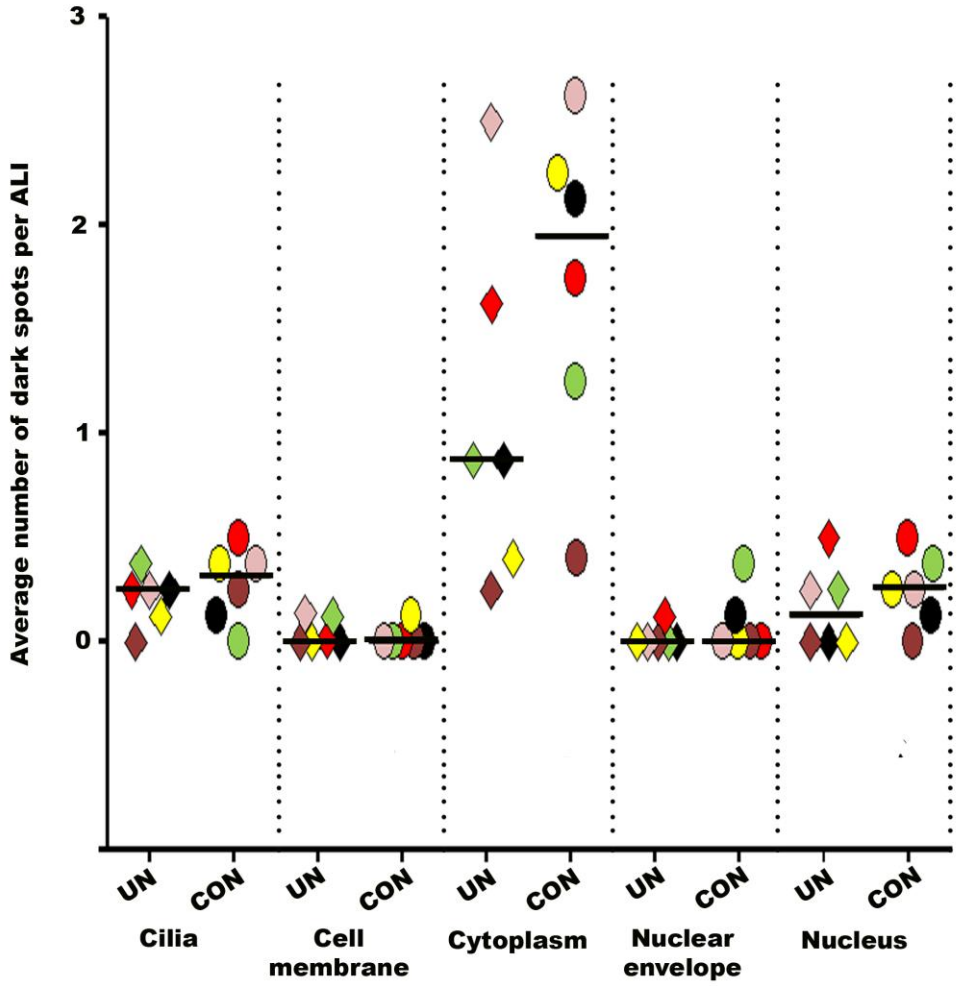

Figure 46: Quantitation of electron-dense dark spots following gold-enhancement of nanogold-conjugated plasmid DNA in human airway epithelial cells transfected for 15 minutes

Human airway epithelial cells grown at an air-liquid interface (ALI) were transfected with nanogold-conjugated plasmid DNA (circles, CON) and control unconjugated plasmid DNA (diamonds, UN) for 15 minutes. Cells were fixed and processed for TEM as described in Materials and Methods. Electron-dense dark spots on TEM micrographs of gold-enhanced sections from nanogold-conjugated pDNA- and control unconjugated pDNA-transfected cells were manually scored. Each data point represents the average number of dark spots in eight complete ciliated epithelial cells per ALI. Paired sections are indicated by colour coding. The horizontal bar represents the median of the number of dark spots in ALIs (n = 6/group).

median values (for normally distributed values means are shown). Unlike the dark spot distribution seen after 60 minutes transfection, Figures 47 and 48 illustrate that at this earlier time-point, the number of dark spots seen in the cytoplasm and nucleus of nanogold-conjugated pDNA-transfected samples showed only a slight trend above those seen in the cytoplasm and nucleus of control unconjugated pDNA-transfected ALIs.

The median background-subtracted nanogold-conjugated pDNA values (background is the median value of dark spots counted in 6 ALIs transfected with unconjugated pDNA, as defined above for 60 minutes transfection) are shown in Figure 49. Even at this early time point, significant levels of nanogold-conjugated pDNA ($p<0.05$) were observed in the cytoplasm compared to the nucleus, nuclear envelope, cell membrane and cilia.

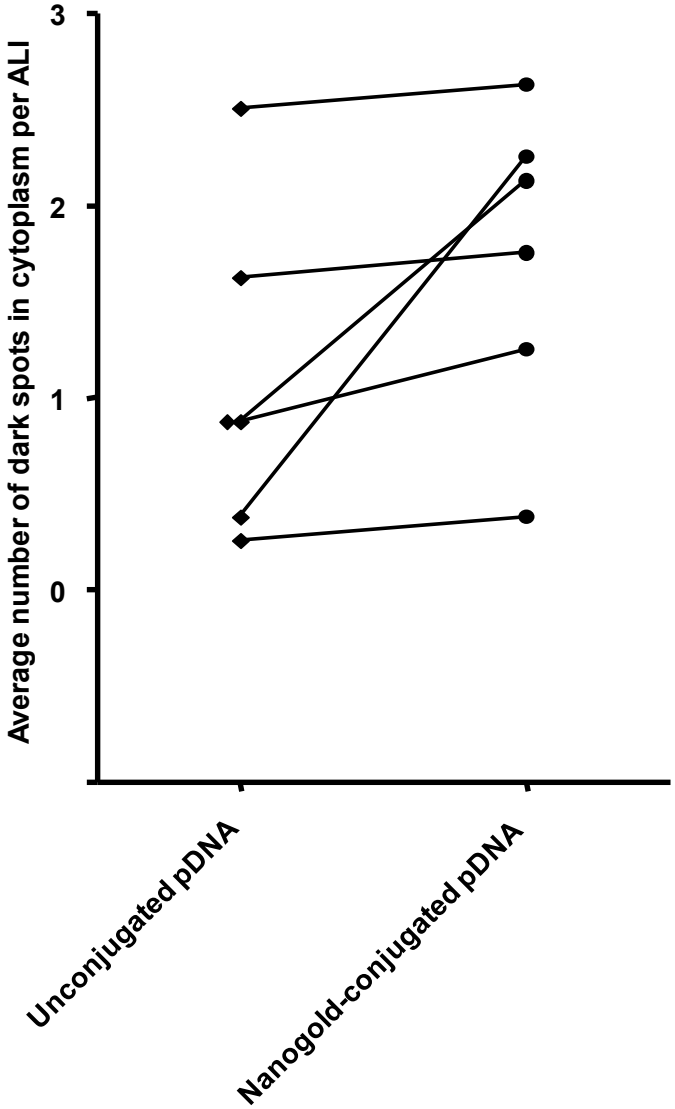

Figure 47: Localisation of electron-dense dark spots in the cytoplasm in gold-enhanced human airway epithelial cells following transfection with nanogold-conjugated or unconjugated plasmid DNA for 15 minutes

Each data point represents the average number of electron-dense dark spots in eight complete ciliated epithelial cells per ALI transfected with nanogold-conjugated pDNA (circles) compared to control unconjugated pDNA-transfected ALI (diamonds) (n = 6/group).

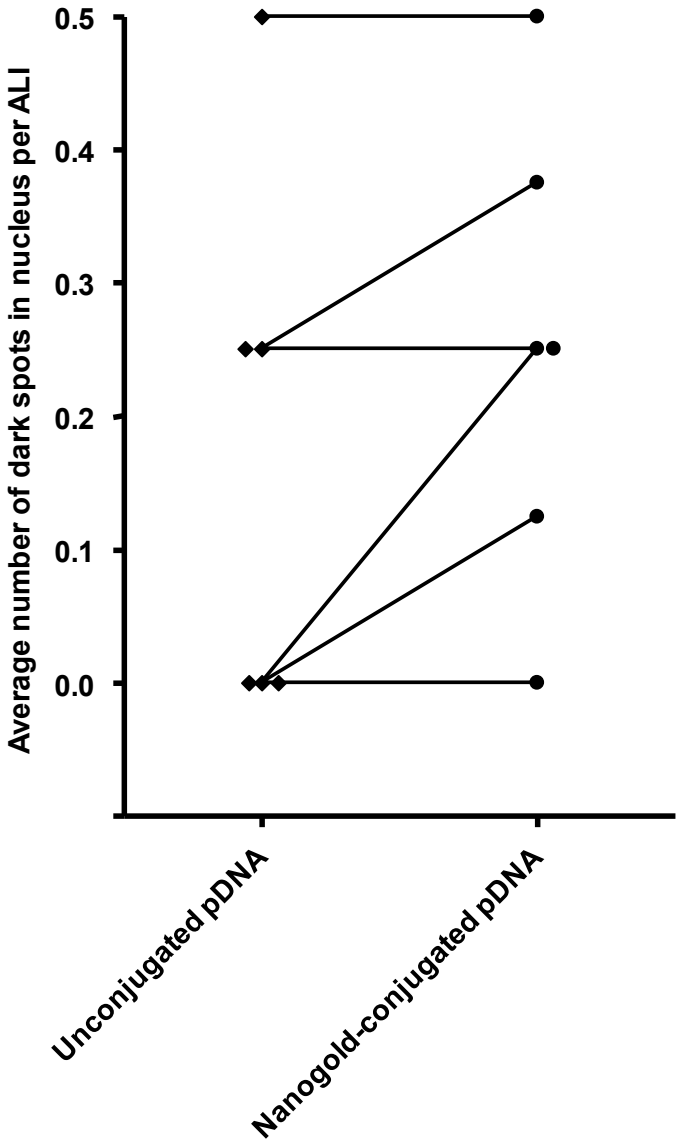

Figure 48: Localisation of electron-dense dark spots in the nucleus in gold-enhanced human airway epithelial cells following transfection with nanogold-conjugated or unconjugated plasmid DNA for 15 minutes

Each data point represents the average number of electron-dense dark spots in eight complete ciliated epithelial cells per ALI transfected with nanogold-conjugated pDNA (circles) compared to control unconjugated pDNA-transfected ALI (diamonds) (n = 6/group).

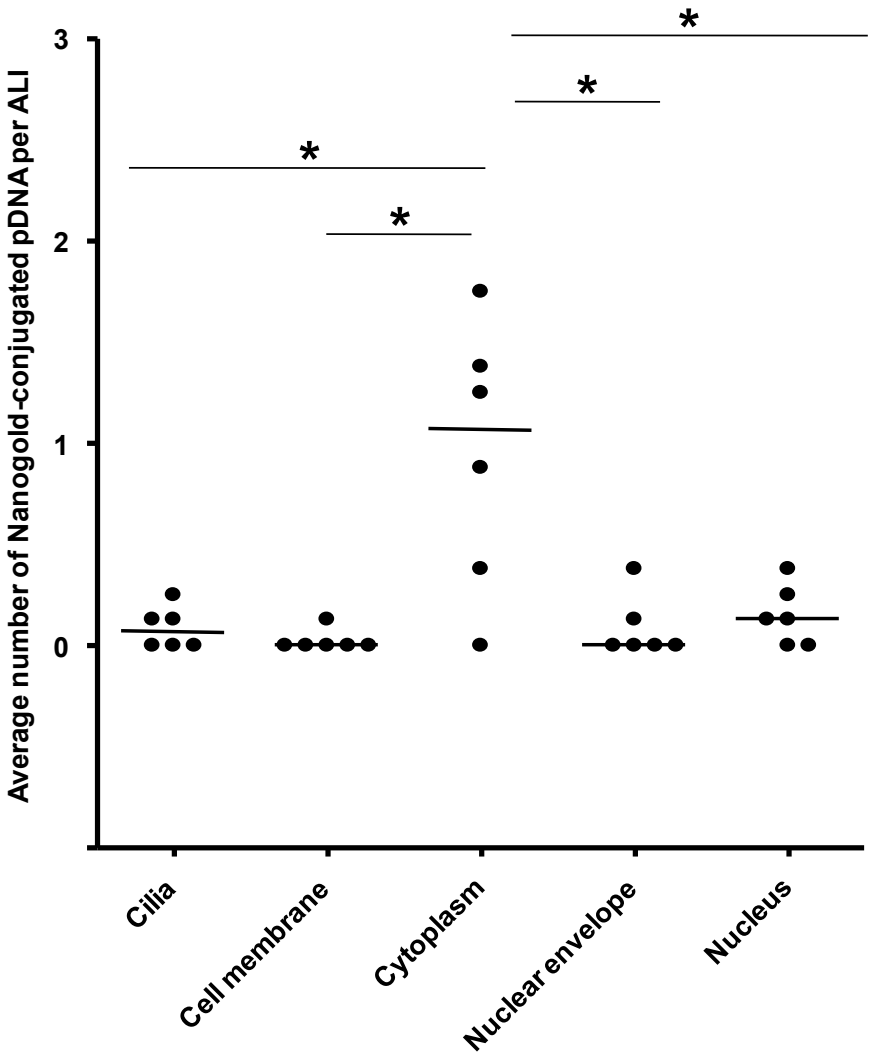

Figure 49: Quantitation of nanogold-conjugated plasmid DNA following transfection of human airway epithelial cells for 15 minutes

Background subtracted number of nanogold-conjugated pDNA derived from data shown in Figure 46. Each data point represents the average number of electron-dense dark spots in eight complete ciliated epithelial cells per ALI transfected with nanogold-conjugated pDNA minus the background. The background is the median of the number of dark spots counted on gold-enhanced section from eight complete cells in six ALIs transfected with control unconjugated pDNA. The horizontal bar represents the median of the number of nanogold-conjugated pDNA in ALIs (n = 6/group), * = $p<0.05$.

5.3.3.4 Single cell quantification of intracellularly localised nanogold-conjugated plasmid DNA in ALIs transfected for 15 minutes

As for the 60 minutes transfection, I next examined these data at the single cell level. Figures 50 and 51 show the distribution of dark spots in the cytoplasm as well as in the nucleus of 8 cells transfected with nanogold-conjugated pDNA (circles) matched with its control unconjugated pDNA (diamonds) for 6 individual ALIs. As above, each individual cell was assigned a specific colour to enable evaluation of distribution of dark spots in the nuclei and cytoplasm of individual cells. Similar to the 60 minutes transfection, Figures 50 and 51 illustrate the high variability in the intra-and inter-ALI dark spot distribution. Cells transfected with nanogold-conjugated pDNA show a trend towards higher numbers of dark spots in the cytoplasm, and to a lesser extent in the nucleus compared to cells transfected with control unconjugated pDNA, for all 6 ALIs. However, only 1 ALI out of 6 transfected with nanogold-conjugated pDNA showed significantly higher numbers of spots in the cytoplasm compared to unconjugated pDNA controls($p<0.05$). Furthermore, Figures 52 and 53 show that when the background spots (median) seen in the control unconjugated pDNA-transfected cells were subtracted from the individual spot in nanogold-conjugated pDNA-transfected cells to derive median background-subtracted nanogold-conjugated pDNA, as for the 60 minutes analysis, nanogold-conjugated pDNA was detected in the cytoplasm of cells from 3 ALIs with none in the nucleus out of 6 ALIs, as indicated by median values.

Table 3 shows the number of cells in ALIs, transfected for 15 minutes, containing cytoplasmic- and nuclear-localised background-subtracted nanogold-conjugated plasmid DNA following 15 minutes transfection. The cell numbers are expressed as the cells with

internalised nanogold-conjugated pDNA in the cytoplasm, or nuclei, as a percentage of the total cell count in the 6 transfected ALIs (derived from Figures 52 and 53, respectively).

Taken together, these data demonstrate that the level of pDNA in the nucleus as well as in cytoplasm was less than we saw following 60 minutes transfection, with cytoplasmic and nuclear delivery successful in only 8 % and 4 % of cells respectively.

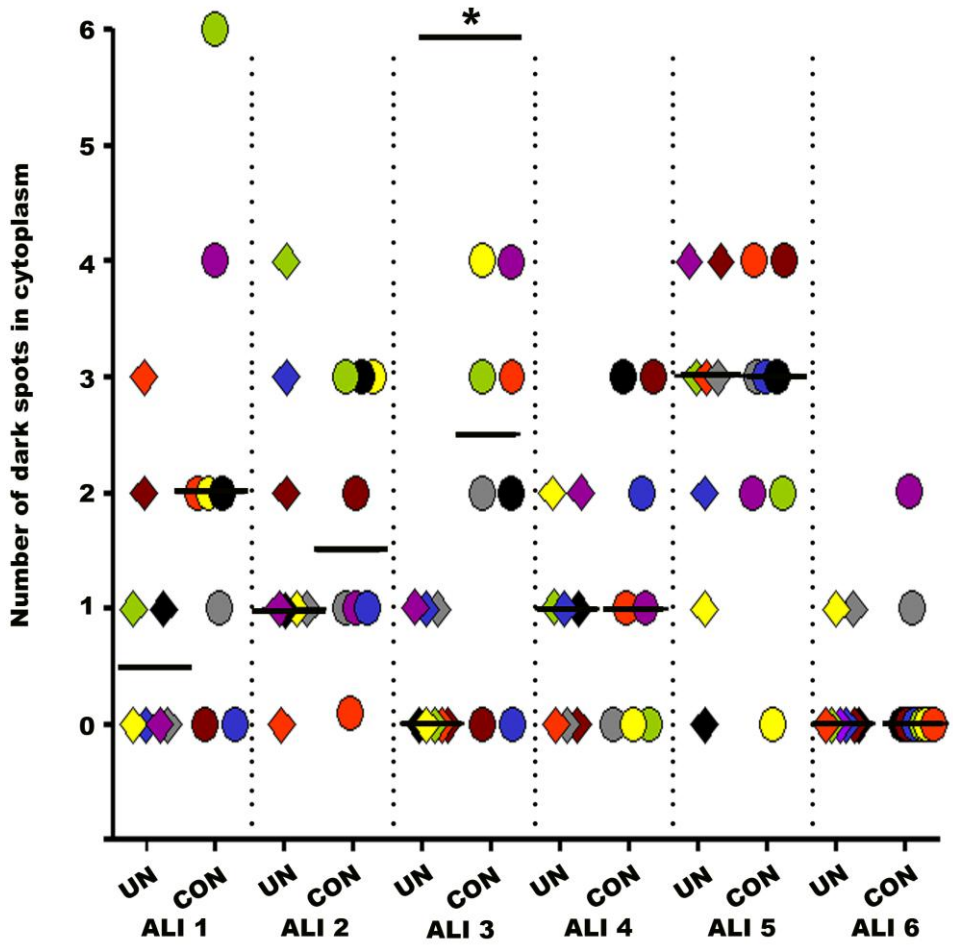

Figure 50: Distribution of dark spots in the cytoplasm following gold enhancement nanogold-conjugated plasmid DNA in human airway epithelial cells transfected for 15 minutes

Human airway epithelial cells grown at an air-liquid interface (ALI) were transfected with nanogold-conjugated plasmid DNA (circles, CON) and control unconjugated plasmid DNA (diamonds, UN) for 15 minutes. Cells were fixed and processed for TEM as described in Materials and Methods. Electron-dense dark spots on electron micrographs of gold enhanced sections from nanogold-conjugated pDNA- and control unconjugated pDNA-transfected cells were manually scored. Each data point represents the number of dark spots in the cytoplasm per complete ciliated epithelial cell. The cells were colour coded. The horizontal bar represents the median of the number of dark spots in eight cells per ALI (n = 6/group). * = $p < 0.05$

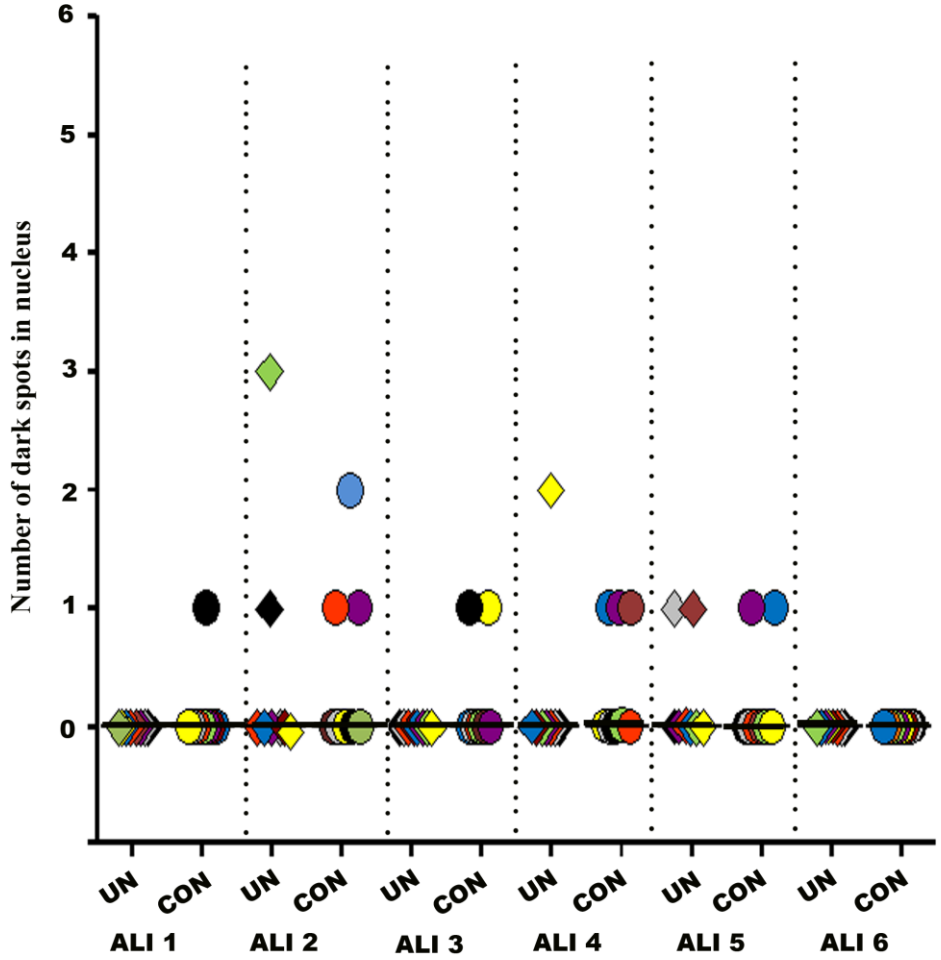

Figure 51: Distribution of dark spots in the nucleus following gold enhancement nanogold-conjugated plasmid DNA in human airway epithelial cells transfected for 15 minutes

Human airway epithelial cells grown at an air-liquid interface (ALI) were transfected with nanogold-conjugated plasmid DNA (circles, CON) and control unconjugated plasmid DNA (diamonds, UN) for 15 minutes. Cells were fixed and processed for TEM as described in Materials and Methods. Electron-dense dark spots on electron micrographs of gold enhanced sections from nanogold-conjugated pDNA- and control unconjugated pDNA-transfected cells were manually scored. Each data point represents the number of dark spots in the nucleus per complete ciliated epithelial cell. The cells were colour coded. The horizontal bar represents the median of the number of dark spots in eight cells per ALI (n = 6/group).

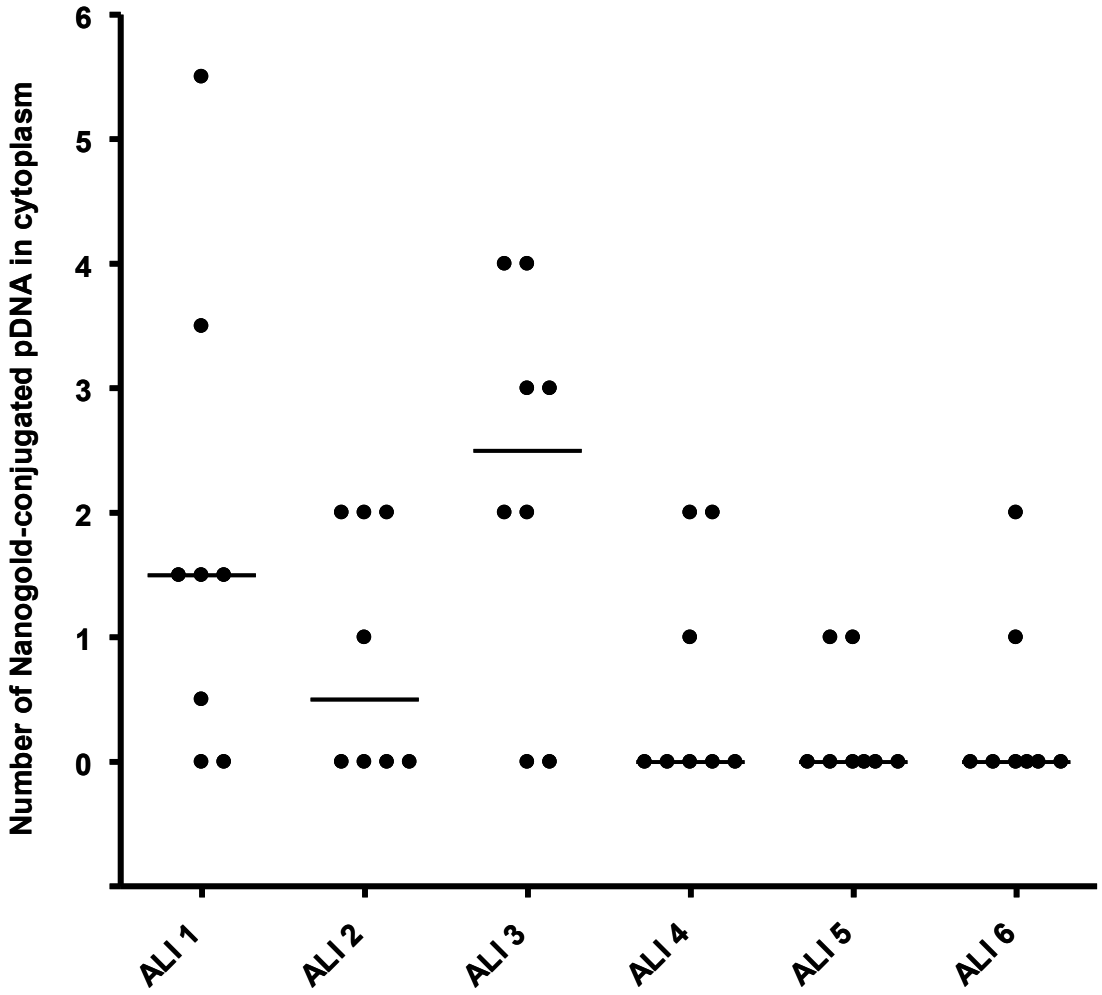

Figure 52: Distribution of nanogold-conjugated plasmid DNA in the cytoplasm following gold-enhancement of nanogold-conjugated plasmid DNA in human airway epithelial cells transfected for 15 minutes

Background subtracted nanogold-conjugated pDNA derived from data shown in Figure 50. Each data point represents the number of electron-dense dark spots in the cytoplasm per complete ciliated epithelial cell minus the background. The background is the median of the number of dark spots in eight complete ciliated epithelial cells per ALI transfected with control unconjugated pDNA. The horizontal bar represents the median of the number of nanogold-conjugated pDNA in eight cells per ALI (n = 6/group).

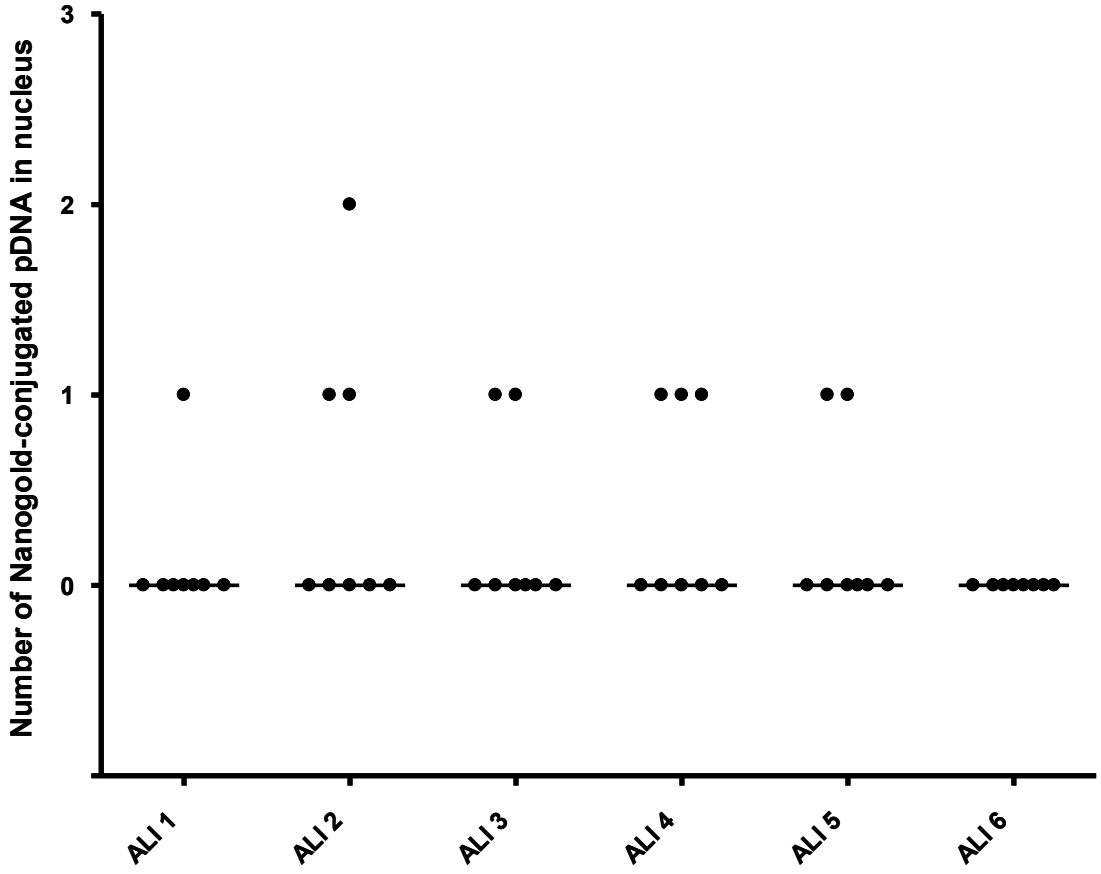

Figure 53: Distribution of nanogold-conjugated plasmid DNA in the nucleus following gold-enhancement of nanogold-conjugated plasmid DNA in human airway epithelial cells transfected for 15 minutes

Background subtracted nanogold-conjugated pDNA derived from data shown in Figure 51. Each data point represents the number of electron-dense dark spots in the nucleus per complete ciliated epithelial cell minus the background. The background is the median of the number of dark spots in eight complete ciliated epithelial cells per ALI transfected with control unconjugated pDNA. The horizontal bar represents the median of the number of nanogold-conjugated pDNA in eight cells per ALI (n = 6/group).

Cells containing nanogold-conjugated plasmid DNA (% of the total number of cells in 6 ALIs*)							Mean (%)
ALI	**1**	**2**	**3**	**4**	**5**	**6**	-
Cytoplasm	13	8	13	6	4	4	8
Nucleus	2	6	4	6	4	0	4

* The total number of 48 cells counted in 5 ALIs.

.

Table 3: Number of airway epithelial cells in ALIs containing cytoplasmic- and nuclear-localised background-subtracted nanogold-conjugated plasmid DNA following 15 minutes transfection

The numbers of cells (derived from Figures 52 and 53) are expressed as the percentage of the total cells in all the 6 ALIs.

5.3.3.5 Quantification of intracellularly localised nanogold-conjugated plasmid DNA in ALIs transfected for 360 minutes

Having established the intracellular distribution of nanogold-conjugated pDNA following transfection for 15 minutes and 60 minutes, I now assessed intracellular distribution of nanogold-conjugated pDNA transfected for an extended period of 360 minutes. Significantly higher numbers of dark spots were found in the cytoplasm and nucleus of gold-enhanced sections from ALIs transfected with nanogold-conjugated pDNA compared to control unconjugated pDNA ($p < 0.05$ for both cytoplasmic and nuclear compartment, Figure 54). The number of dark spots observed on the cilia, cell membrane and nuclear envelope of gold-enhanced sections from ALIs transfected with nanogold-conjugated pDNA was not different from the background levels seen in gold-enhanced sections from ALIs transfected with unconjugated pDNA. Again, higher levels of dark spots in the cytoplasm and nucleus of nanogold-conjugated pDNA transfected samples compared to those seen in the cytoplasm and nucleus of control unconjugated pDNA transfected ALIs were better illustrated in Figure 55 and Figure 56 respectively. This finding was further confirmed, when pDNA intracellular distribution was expressed as the median background-subtracted nanogold-conjugated pDNA. Figure 57 shows the presence of background-subtracted nanogold-conjugated pDNA in both the cytoplasm and nucleus, compared to absence on the cilia, cell membrane and nuclear envelope (based on median values) following transfection for 360 minutes. No significant difference was observed between the levels of nanogold-conjugated pDNA in the cytoplasm and the nucleus.

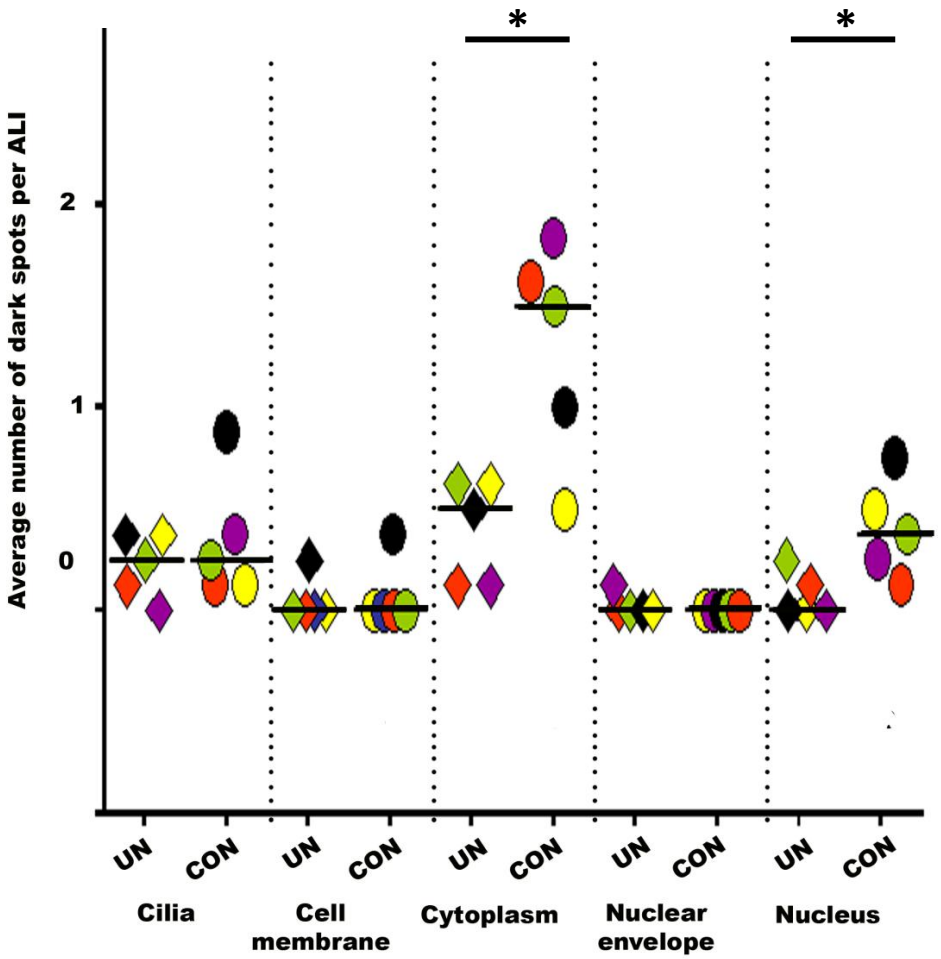

Figure 54: Quantitation of electron-dense dark spots following gold-enhancement of nanogold-conjugated plasmid DNA in human airway epithelial cells transfected for 360 minutes

Human airway epithelial cells grown at an air-liquid interface (ALI) were transfected with nanogold-conjugated plasmid DNA (circles, CON) and control unconjugated plasmid DNA (diamonds, UN) for 360 minutes. Cells were fixed and processed for TEM as described in Materials and Methods. Electron-dense dark spots on electron micrographs of gold-enhanced sections from nanogold-conjugated pDNA- and control unconjugated pDNA-transfected cells were manually scored. Each data point represents the average number of dark spots in eight complete ciliated epithelial cells per ALI. Paired sections are indicated by colour coding. The horizontal bar represents the median of the number of dark spots in the ALIs (n = 5/group), * = $p < 0.05$.

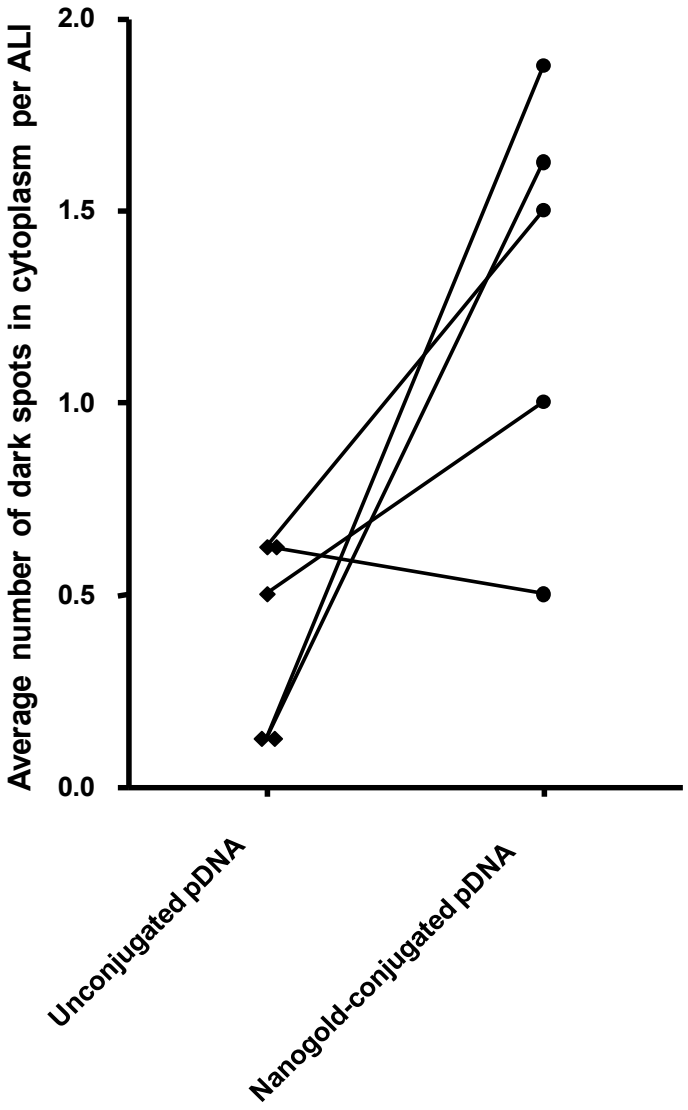

Figure 55: Localisation of electron-dense dark spots in the cytoplasm in gold-enhanced human airway epithelial cells following transfection with nanogold-conjugated or unconjugated plasmid DNA for 360 minutes

Each data point represents the average number of electron-dense dark spots in eight complete ciliated epithelial cells per ALI transfected with nanogold-conjugated pDNA (circles) compared to control unconjugated pDNA-transfected ALI (diamonds) (n = 5/group).

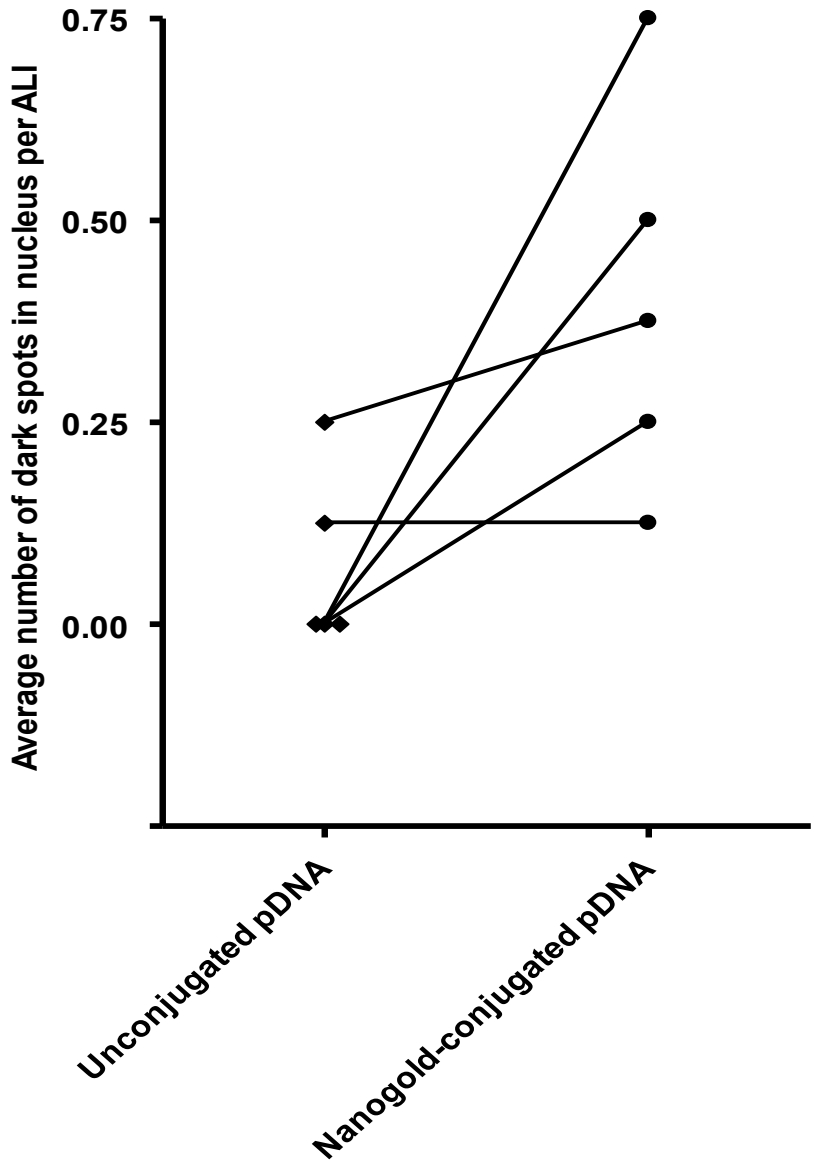

Figure 56: Localisation of electron-dense dark spots in the nucleus in gold-enhanced human airway epithelial cells following transfection with nanogold-conjugated or unconjugated plasmid DNA for 360 minutes

Each data point represents the average number of electron-dense dark spots in eight complete ciliated epithelial cells per ALI transfected with nanogold-conjugated pDNA (circles) compared to control unconjugated pDNA-transfected ALI (diamonds) (n = 5/group).

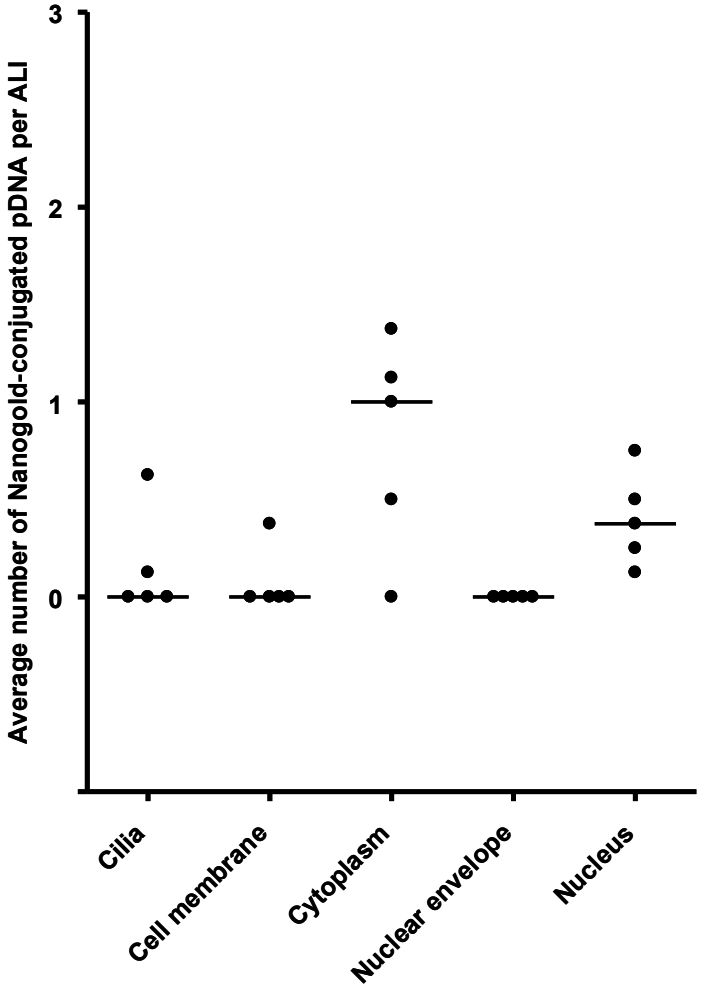

Figure 57: Quantitation of nanogold-conjugated plasmid DNA following transfection of human airway epithelial cells for 360 minutes

Background subtracted number of nanogold-conjugated pDNA derived from data shown in Figure 54. Each data point represents the average number of electron-dense dark spots in eight complete ciliated epithelial cells per ALI transfected with nanogold-conjugated pDNA minus the background. The background is the median of the number of dark spots counted on gold-enhanced section from eight complete cells in five ALIs transfected with control unconjugated pDNA. The horizontal bar represents the median of the number of nanogold-conjugated pDNA in ALIs (n = 5/group).

5.3.3.6 Single cell quantification of intracellularly localised nanogold-conjugated plasmid DNA in ALIs transfected for 360 minutes

As for the 15 and 60 minutes data, I also evaluated the distribution of dark spots in the cytoplasm and nucleus, of 8 individual cells transfected with nanogold-conjugated pDNA (circles) matched with its control unconjugated pDNA (diamonds) for 5 individual ALIs (Figures 58 and 59 respectively). As for the 15 and 60 minutes data, I found a trend towards an increase in the number of dark spots in both the cytoplasm and nuclei of cells transfected with nanogold-conjugated pDNA compared to cells transfected with control unconjugated pDNA. A significant difference in levels of dark spots was observed in the cytoplasm of 2 out of 5 ALIs ($p<0.001$). However, I found no significant differences in levels of nuclear-localised dark spots in ALIs transfected with nanogold-conjugated pDNA compared with those transfected with the control unconjugated pDNA. In addition, on subtracting the background spots, Figures 60 and 61 show that nanogold-conjugated pDNA was detected in the cytoplasm of cells from 4 ALIs although nuclear distribution was detected only in 1 ALI out of total 5ALIs respectively (based on median values). The number of cells, shown in Figures 60 and 61, with internalised nanogold-conjugated pDNA in the cytoplasm as well as in the nucleus are expressed as percentages in Table 4. Taken together and consistent with the 15 minutes and 60 minutes transfection, data again showed high variability. More pDNA was delivered to the cytoplasm (in 15 % of cells) compared to the nucleus (in 7 % of cells), following transfection of ALIs with nanogold-conjugated pDNA for 360 minutes.

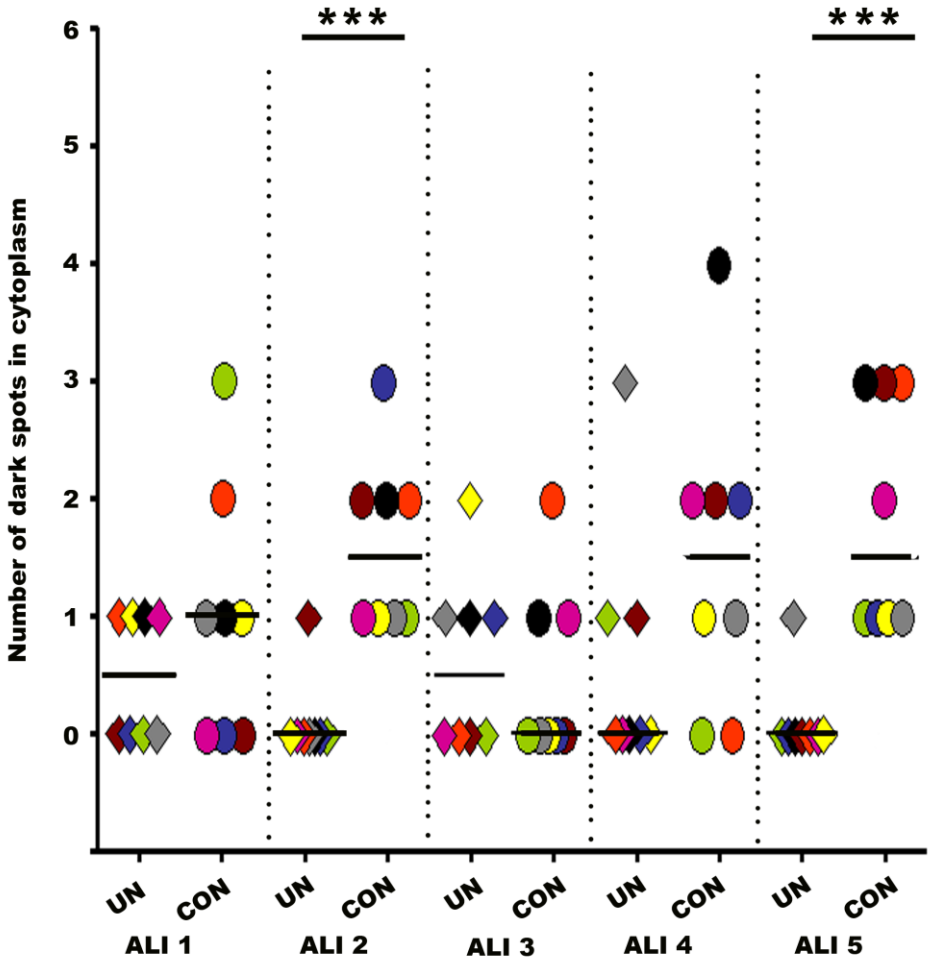

Figure 58: Distribution of dark spots in the cytoplasm following gold enhancement nanogold-conjugated plasmid DNA in human airway epithelial cells transfected for 360 minutes

Human airway epithelial cells grown at an air-liquid interface (ALI) were transfected with Nanogold-conjugated plasmid DNA (circles, CON) and control unconjugated plasmid DNA (diamonds, UN) for 360 minutes. Cells were fixed and processed for TEM as described in Materials and Methods. Electron-dense dark spots on electron micrographs of gold enhanced sections from nanogold-conjugated pDNA- and contro unconjugated pDNA-transfected cells were manually scored. Each data point represents the number of dark spots in the cytoplasm per complete ciliated epithelial cell. The cells were colour coded. The horizontal bar represents the median of the number of dark spots in eight cells per ALI (n = 5/group). *** = $p < 0.0005$

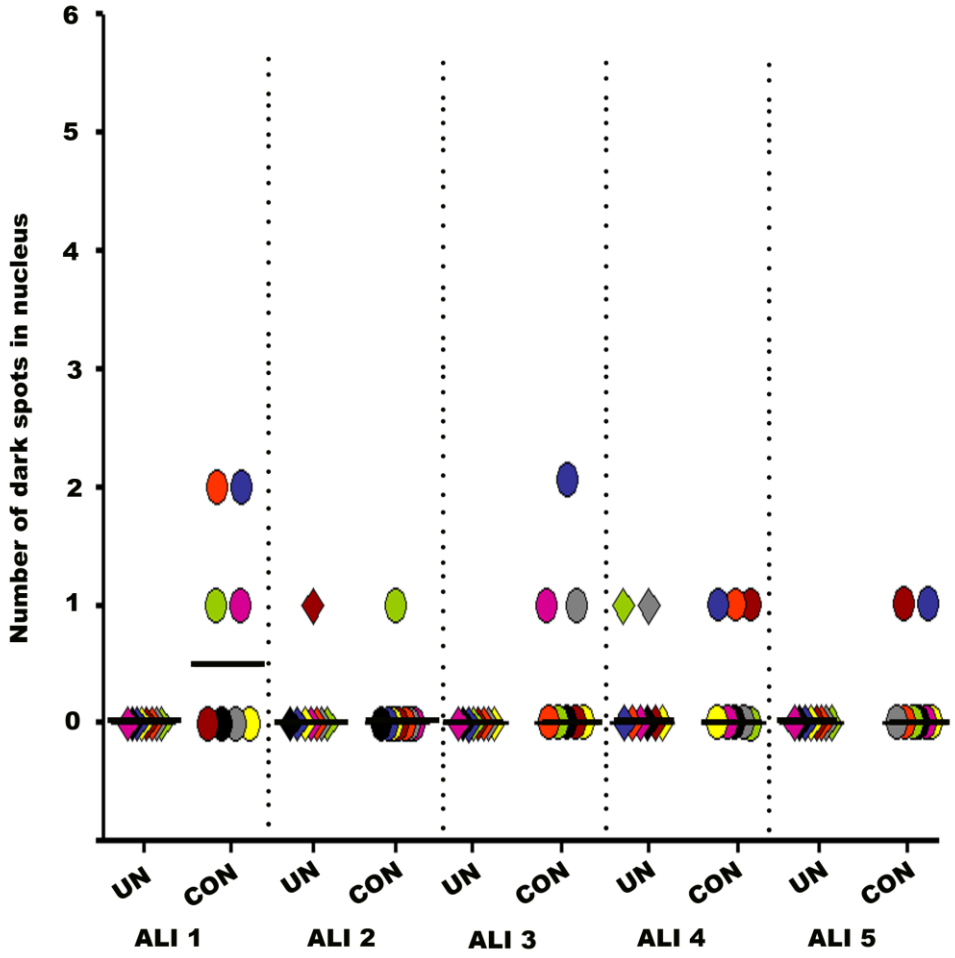

Figure 59: Distribution of dark spots in the nucleus following gold enhancement nanogold-conjugated plasmid DNA in human airway epithelial cells transfected for 360 minutes

Human airway epithelial cells grown at an air-liquid interface (ALI) were transfected with nanogold-conjugated plasmid DNA (circles, CON) and control unconjugated plasmid DNA (diamonds, UN) for 360 minutes. Cells were fixed and processed for EM as described in Materials and Methods. Electron-dense dark spots on electron micrographs of gold enhanced sections from nanogold-conjugated pDNA- and control unconjugated pDNA-transfected cells were manually scored. Each data point represents the number of dark spots in the nucleus per complete ciliated epithelial cell. The cells were colour coded. The horizontal bar represents the median of the number of dark spots in eight cells per ALI (n = 5/group).

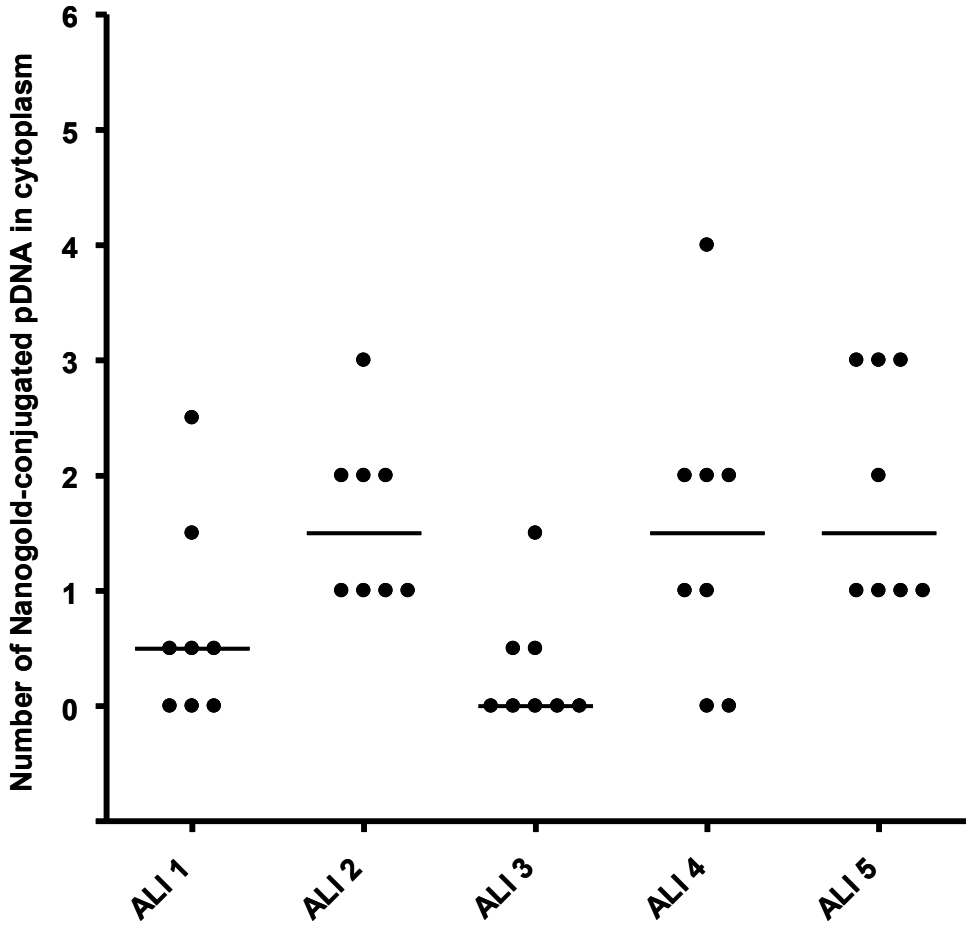

Figure 60: Distribution of nanogold-conjugated plasmid DNA in the cytoplasm following gold-enhancement of nanogold-conjugated plasmid DNA in human airway epithelial cells transfected for 360 minutes

Background subtracted nanogold-conjugated pDNA derived from data shown in Figure 58. Each data point represents the number of electron-dense dark spots in the cytoplasm per complete ciliated epithelial cell minus the background. The background is the median of the number of dark spots in eight complete ciliated epithelial cells per ALI transfected with control unconjugated pDNA. The horizontal bar represents the median of the number of nanogold-conjugated pDNA in eight cells per ALI (n = 5/group).

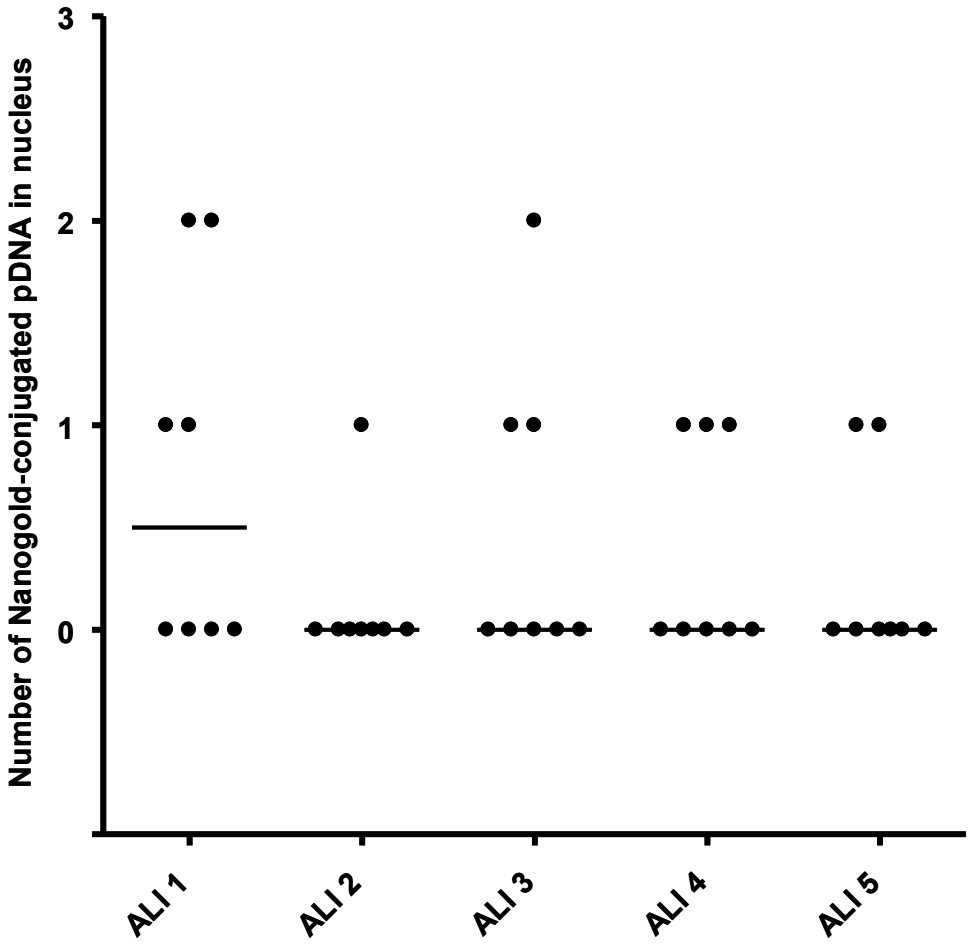

Figure 61: Distribution of nanogold-conjugated plasmid DNA in the nucleus following gold-enhancement of nanogold-conjugated plasmid DNA in human airway epithelial cells transfected for 360 minutes

Background subtracted nanogold-conjugated pDNA derived from data shown in Figure 59. Each data point represents the number of electron-dense dark spots in the nucleus per complete ciliated epithelial cell minus the background. The background is the median of the number of dark spots in eight complete ciliated epithelial cells per ALI transfected with control unconjugated pDNA. The horizontal bar represents the median of the number of nanogold-conjugated pDNA in eight cells per ALI (n = 5/group).

Cells containing nanogold-conjugated plasmid DNA (% of the total number of cells in 5 ALIs*)							Mean (%)
ALI	**1**	**2**	**3**	**4**	**5**	**6**	-
Cytoplasm	13	20	8	15	20	-	15
Nucleus	10	3	8	8	5	-	7

*The total number of 40 cells was counted in 5 ALIs.

Table 4: Number of airway epithelial cells in ALIs containing cytoplasmic- and nuclear-localised background-subtracted nanogold-conjugated plasmid DNA following 360 minutes transfection
The numbers of cells (derived from Figures 60 and 61) are expressed as the percentage of the total cells in all the 5 ALIs.

5.3.3.7 Summary of the temporal intracellular distribution of nanogold-conjugated plasmid DNA

Figure 62 shows the cellular distribution of pDNA conjugated to the nanogold TEM probe in ALIs. The percentage of cells containing median-background subtracted nanogold-conjugated pDNA is expressed as a function of transfection time (data from Tables 2-4). Strikingly as early as 15 minutes after addition of the pDNA/lipid complex, 8% nanogold-conjugated pDNA was taken up into the cytoplasm and 4% delivered to the nucleus as indicated by the mean values. At 60 minutes, there was an approximately an equal distribution of nanogold-conjugated pDNA in both cytoplasm and nucleus (in 9% and 8% of transfected cells respectively). Extended transfection times of up to 360 minutes resulted in 15% and 7% of the transfected cells with cytoplasmic- and nuclear- localised nanogold-conjugated pDNA respectively. In summary, the number of transfected cells with cytoplasmic-localised pDNA increased with increasing transfection time. Nuclear-localised pDNA was observed following transfection for 15 minutes. Further transfection for up to 60 minutes increased this nuclear-localised pDNA but there was no change after 360 minutes. Overall 4-8% of the fully differentiated ciliated epithelial cells of the transfected ALIs showed evidence for nuclear DNA deposition following non-viral gene transfer.

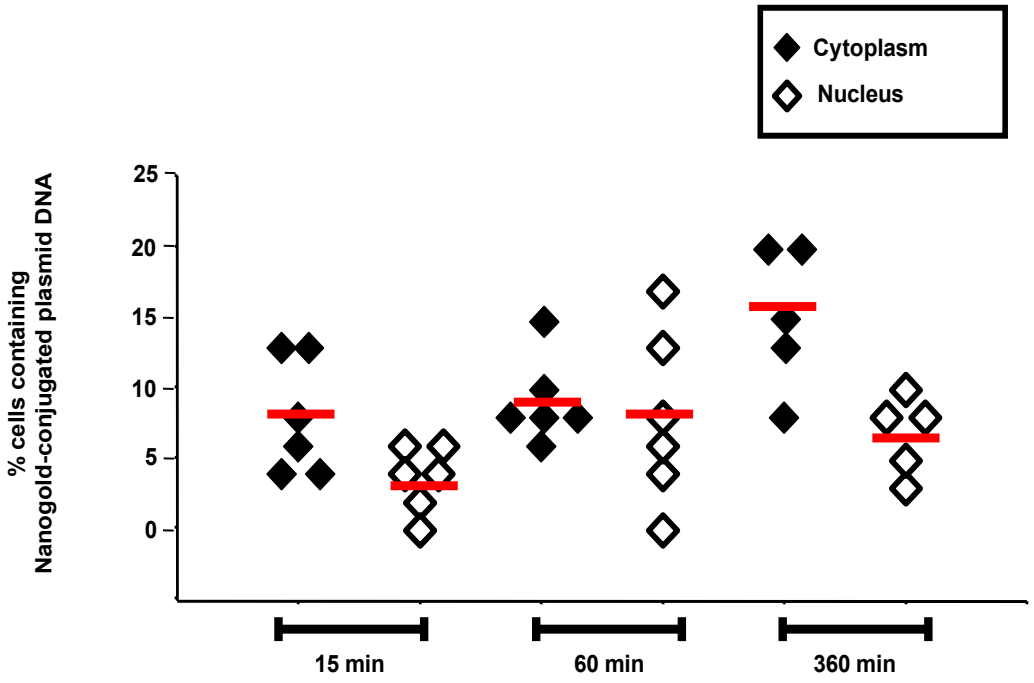

Figure 62: Time lapse study showing cellular distribution of nanogold-conjugated plasmid DNA with increased transfection time

Data from Tables 2, 3 and 4 are used to represent the temporal mean percentages of cells containing Nanogold-conjugated plasmid DNA in ALIs transfected for 15 minutes (n = 6 ALIs), 60 minutes (n = 6 ALIs) and 360 minutes (n = 5 ALIs).

5.4 Discussion

Plasmid DNA intracellular uptake and fate in non-virally transfected human airway epithelial cells was assessed at a single-molecule resolution using TEM. The resolution of light microscopy is constrained by the diffraction limit of light described by Abbe's law which states that it is only possible to resolve two adjacent points that are separated by more than approximately 200 nm. Thus, at all separation distances shorter than roughly half the wavelength of detected light from a sample, adjacent points fuse into one more or less diffuse structure [243]. As a consequence of this diffraction limitation, resolution of pDNA (200 nm when fully condensed with cationic lipid) labelled with Oregon Green 488-PNA conjugate (463 Da) was not possible at the single molecule level [187]. The resolution and diffraction are inversely proportional to each other and therefore the resolution can be improved by using shorter wavelengths and media with larger indices of refraction. Electron microscopy exploits these two facts to form high-resolution images by using extremely short wavelengths of electrons accelerated through the vacuum (refractive index of vacuum is 1) thus overcoming the resolution limitation (of light microscope) and enables resolution of 0.2 nm (i.e. 1000 fold higher than light microscopy and about 500,000 times greater than human eye). This resolution (0.2 nm) was high enough to give detailed information about the association of pDNA with intracellular components at the single molecule level.

Plasmid DNA itself is not electron-dense enough to be visualised by TEM and the plasmid had to be tagged with an electron-dense particle for use in these experiments. To this end, I conjugated the pDNA with electron-dense 1.4 nm nanogold particles via PNA as a linker molecule in a sequence-specific manner. Our laboratory has previously used this strategy to tag pDNA with organic fluorophores [183;187]. Essentially, monomaleimido-nanogold is hybridised to a specific sequence on the pDNA via a thiol-terminated PNA linker molecule.

Reporter plasmid biological activity is unaffected by this approach and conjugation results in 1:1 stoichiometry, in terms of nanogold tag and pDNA.

I used ALIs, an *in vitro* model that mimics the ion transport and histological characteristics of the normal human airway epithelium. The transfectability of these ALIs using non-viral approaches is variable and primarily dependent on the age of the cultures [189;235]. Those cultured for less than 40 days are unlikely to be fully differentiated, whilst after 75 days they accumulate excessive amounts of mucus, an impediment to non-viral gene transfer (Epithelix, personal communication). Thus only ALIs cultured for 45-70 days were used in this study. To verify the viability, and hence the transfectability, of the commercially sourced ALIs prior to use in the experiments, every batch was routinely assessed.

ALIs were incubated with the cationic lipid GL67A complexed with nanogold-conjugated or control unconjugated pDNA for 15, 60, and 360 minutes. At all time-points, pDNA was seen inside epithelial cells as dark black spots following gold-enhancement of the transfected ALI sections, on TEM micrographs generated from high resolution TEM "snapshots". As expected and consistent with our previous pre-clinical experiments and clinical trials, non-viral gene transfer to the ALIs shows variability [235].

Following transfection at all three time-points, I found that the background levels were equal or below 1 dark spot/ALI. The signal above background demonstrates that our TEM assay is sensitive enough to pick up the nanogold-conjugated pDNA in airway epithelial cells. It is worth noting the source of the background signal, comprising non-specific, randomly dispersed dark spots, in the gold-enhanced sections from unconjugated pDNA-transfected ALIs. These are a result of auto-nucleation, a phenomenon common to silver- or gold-

enhancement treatment. As well as the nanogold particles on the conjugated pDNA serving as nuclei for amplification by the enhancement process, the gold ions present in gold-enhancement solution are also reduced to atomic gold and grow in size by deposition of further gold ions (auto-nucleation) [229]. Conventionally, this background signal resulting from gold-enhancement of control sections is not usually shown. I have not only, presented TEM micrographs of control enhanced sections, but have subtracted background signal from the conjugated pDNA values in our quantitative analysis. Quantitation of the intracellular-localised dark spots representing pDNA was done by manual counting. It is important to note here that electron-dense spots (nanogold-conjugated pDNA) were counted in eight complete ciliated cells per 2-dimensional (2-D) ALI section. Obviously, serial sections of the cell would have to be analysed to obtained 3-D localisation information of the nanogold-conjugated pDNA. This was not practically possible within the time frame of this study.

Quantitative analysis revealed that pDNA accumulated in the cytoplasm of 8% cells transfected for 15 minutes. Whether this cytoplasmic-localised pDNA was associated with filamentous structures or intracellular vesicular transport organelles such as endocytes is unclear. Co-localisation of gold-labelled specific markers of filamentous structures or endocytic vesicles with the pDNA would be needed to confirm any association between filamentous structures or intracellular transport vesicles and cytoplasmic-localised nanogold-conjugated pDNA. Previous studies from other workers using an identical TEM protocol which preserves cellular ultrastructure have shown these filamentous structures to be microtubules [199;201;202;204;244]. It is thus possible to imagine the vesicle-enclosed or free pDNA travelling along these microtubular “railway tracks” on its way to the nuclear periphery prior to transport across the NPC into the nucleus.

As well as this cytoplasmic-localised pDNA, the pDNA was also delivered to the nucleus of 4% transfected cells following transfection for 15 minutes. The obvious reason for this low level of pDNA in the nucleus is insufficient lipid GL67A/pDNA complex contact (transfection) time with ALI apical surface membrane or too early to reach the nucleus. Thus, we extended the transfection time from 15 minutes to 60 minutes, and found cytoplasm-localised pDNA in more of the transfected cells (9%). Furthermore, this extended contact time resulted in increased delivery of pDNA to the nucleus, with 8% of transfected cells showing nuclear-localised pDNA. Further increasing contact time of ALI with lipid GL67A/pDNA complex from 60 to 360 minutes showed even further internalisation of pDNA into the cytoplasm of 15% of transfected cells. Interestingly, I found the nuclear delivery of pDNA decreased following transfection for 360 minutes, with only 7% of cells exhibiting nuclear-localised pDNA compared to the previous 8% following 60 minutes transfection. The likely reason for the reduced number of cells with pDNA (or loss of electron-dense signal) in their nuclei following extended transfection times up to 360 minutes could be loss of pDNA either as a result of degradation or potential separation from the Nanogold particles and their exocytosis. This result thus indicates that 60 minutes transfection time is sufficient for maximum nuclear delivery of the pDNA.

However, what is not clear is how the levels of pDNA delivered to the nucleus relate to the gene expression levels. To achieve this, levels of pDNA detected in the nucleus and subsequent gene expression would have to be determined at the appropriate transfection times. In this study, I initially assessed gene expression measuring *Firefly* luciferase activity following transfection with the luciferase reporter plasmid, pCIKFluc. A major pitfall of this measurement is that the Fluc is a cytosolic protein and therefore requires the lysis of cells before luminescence can be measured. Thus, any experiments aimed at correlating pDNA

nuclear delivery to Fluc reporter gene expression would require cell harvesting and lysis. Further, the Fluc activity is undetectable in ALI following transfection with this reporter plasmid. As previously mentioned, the introduction of *Gaussia* luciferase reporter plasmid, pCIKGluc circumvents this problem. Firstly, pCIKGluc is more sensitive than pCIKFluc and is detectable in ALIs [235]. More importantly, *Gaussia* luciferase is secreted and therefore can be easily detected in the cell media. Gluc is therefore an obvious reporter system to correlate the levels of pDNA detected in ALIs nuclei with reporter pDNA expression levels following non-viral transfection for 15, 60 and 360 minutes. Our laboratory has previously shown that Gluc reporter gene is expressed between 6 hours and 24 hours, with maximal activities at 48 hours following 6 hours transfection (contact) time [245]. I was therefore unable to directly link the detected pDNA with gene expression at the indicated transfection times. Interestingly, previous data have shown a decrease in gene expression following transfection for 24 hours compared with 6 hours transfection. This decrease in gene expression was due to epithelial damage on exposing the ALI cultures to pCIKGluc for 24 hours.

In summary, I found cytoplasmic-localised pDNA in more cells following extended transfection time after 15 minutes transfection of ALI. Transfection for 60 to 360 minutes further increased the number of cells showing successful nuclear delivery compared to that seen at 15 minutes transfection time. Interestingly, there was an equal distribution of pDNA in cytoplasmic and nuclear compartments of cells transfected for 60 minutes, with cells containing nuclear-localised pDNA decreasing following 360 minutes transfection.

My data agree broadly with findings from previous studies which have shown similar intracellular distributions of pDNA following non-viral transfection of mammalian cells

using cationic lipids. For instance, two very early studies using streptavidin-labelled colloidal gold to detect biotin-conjugated pDNA demonstrated the presence of cytoplasmic-localised pDNA in mammalian cells transfected for similar time-points to our study.

In the first study, Zabner *et al* detected colloidal gold-labelled pDNA at the African green monkey SV40-transfected kidney fibroblast (COS-1) and HeLa cell surfaces following transfection for 5 to 30 minutes [136]. Increasing the transfection to 1 and 6 hours resulted in the presence of pDNA in endocytic vesicles but none in the nucleus. They concluded that labelling of pDNA with colloidal gold could be a barrier and thus prevented the release of pDNA from the endosomes. Attempts at overcoming this obstacle by increasing the transfection time to 24 hours resulted in pDNA reaching the peri-nuclear region but failure to enter the nucleus. In a second study, using a similar colloidal gold tagging approach Friend *et al*, also showed the localisation of pDNA to the peri-nuclear region with no delivery to the nucleus following cationic- mediated transfection [103].

In a later study carried out by Kitson *et al* in our laboratory, African green monkey SV40-transfected kidney fibroblast (COS-7) cells were transfected with a complex of cationic liposome and BrdU-labelled reporter gene pCMVβ-Gal [215]. The pDNA was localised and quantitatively evaluated (by detection of BrdU label using colloidal gold-labelled anti-BrdU antibodies) following transfection for 0, 1, 10, 60, 360 and 720 minutes. In order to compare the effect of transfection time on gene expression, pCMVβ-Gal reporter gene expression was determined, in parallel, 48 hours after each of these transfection time-points. BrdU-labelled pDNA was found in the cytoplasm at all time-points compared to background levels, in agreement with my demonstration of cytoplasmic-loca1ised nanogold-conjugated pDNA following transfection for 15 to 360 minutes. Intriguingly, reporter gene expression was

observed at transfection times as early as 1 minute. This is rather surprising as BrdU-labelled pDNA was not detected in the nucleus at any time points following transfection. In order to correlate the nuclear delivery of pDNA (as determined by the levels of nuclear-localised pDNA detected) with gene expression it is clearly important that gene expression is measured at the same transfection time as the nuclear-localised reporter gene pDNA is visualised. However, in all the above studies, gene expression was measured 48 hours post-transfection. Incubation for 48 hours after the indicated transfection time most likely resulted in further redistribution and possible subsequent delivery to the nucleus explaining the expression observed at early time points.

Ouahabi *et al,* also transfected baby hamster kidney (BHK) 21 cells for 5 to 120 minutes, with a complex of BrdU-labelled pDNA and cationic lipid. The BrdU-labelled pDNA was detected by immunogold TEM [246]. They found pDNA aggregates at the surface of cells transfected for 15-30 minutes, and in the cytoplasmic compartment of cells following transfection for 2 hours. No BrdU-conjugated pDNA was detected in the nucleus at any transfection time point.

Briane *et al*, in a study visualising digoxigenin-labelled pCMV-β by immunogold TEM, found the digoxigenin-labelled pDNA in the cytoplasmic compartment of human breast carcinoma (MCF7) cells at 15 minutes, 30 minutes, 1 hours, 5 hours and 24 hours following cationic lipid-mediated transfection [247]. Interestingly, whilst I showed nuclear delivery of pDNA following transfection for 1 and 6 hours, they only found nuclear-localised pDNA following transfection for 24 hours and none at all at the earlier time points of 30 minutes, 1 hour and 5 hours. In contrast to my experiments, the digoxigenin-labelled pDNA was detected by immuno-staining with gold-labelled anti-digoxigenin-labelled antibodies. The

digoxigenin-labelling was random, not sequence-specific and required enhancement of gold-labelled anti-digoxigenin-labelled antibodies with silver. This discrepancy could likely be explained by the fact that whilst in my studies the gold probes are directly attached to the pDNA, the gold TEM probe in the Briane *et al* study was introduced post-fixation. Thus there is a potential for the masking or non-retrieval of the digoxigenin "epitopes" during the fixation and processing for immunogold TEM.

Using a different non-viral approach, Thomas and Klibanov monitored, by TEM, the intracellular trafficking of pDNA in COS7 cells transfected using PEI-based polycations covalently attached to gold nanoparticles (AuNPs) [248]. Polyplexes, presumably comprising of pDNA still attached to the AuNPs-labelled PEI, were seen as aggregates in the cytoplasmic compartment following transfection for 40 minutes but were only detectable in the nucleus upon addition of the amphophile (detergent) dodecyl.

More recently, Li *et al* successfully demonstrated the dimethyldioctadecyl-ammonium bromide (DODAB)-mediated nuclear delivery of pDNA in HEK 293 cells [249]. Briefly, HEK 293 cells were transfected with AuNPs-coated DODAB/pDNA lipoplexes. Using TEM, they were able to detect pDNA outside the cells, near the cell membrane, inside the cytoplasm as well as in the nucleus following transfection for 4 hours.

Taken together, the above studies are all in broad agreement with my finding that pDNA localise to the cytoplasmic compartment at early (15 minutes) and extended (60 to 360 minutes) non-viral transfection times. Only two studies similar to the present one (Thomas and Klibanov; Li *et al.,*) have demonstrated nuclear delivery of pDNA. In contrast to the above studies, it is worth reiterating that in my approach, I conjugated a single gold

nanoparticle to a single pDNA molecule in a sequence-specific manner, thus ensuring single-molecule TEM detection in a well preserved intracellular ultrastructure background. Also, the above studies used a variety of non-viral cationic (lipoplexes or polyplexes) mediated approaches which essentially consisted of random attachment of colloidal gold or AuNPs via streptavidin to the biotinylated pDNA, or indirect detection of BrdU-conjugated pDNA and digoxigenin-labelled pDNA using immunogold-labelling.

It would be interesting to correlate my observed bio-distribution of conjugated pDNA following 15, 60 and 360 minute's transfection times with gene expression at the same time points. Indeed, Kitson *et al* did attempt to correlate distribution of reporter plasmid indirectly labelled with colloidal gold particles with gene activity [215]. In this study, COS-7 cell lines were transfected for up to 6 hours, but, followed by an additional 48 hours incubation period, prior to subsequent evaluation of the colloidal gold-labelled reporter gene activity. This 48 hours post-transfection incubation period precluded any direct correlation of detected colloidal gold labelled pDNA with its expression. It is almost likely the additional 48 hours incubation period would have resulted in further re-distribution of the colloidal gold-labelled pDNA thus not correlated with the expression profile at the earlier ≤ 6 hour time point. In order to correlate the observed distribution of colloidal gold-labelled pDNA following appropriate transfection time with gene expression, one would need to run a parallel experiment for the evaluation of gene expression without 48 hours post-transfection incubation period.

In conclusion, to the best of our knowledge, this study provides for the first time a quantitative description of intracellular distribution of pDNA following non-viral cationic lipid mediated transfection in a clinically relevant airway epithelial model. Although no

significant increase in the number of cells containing nuclear-localised gold-labelled pDNA following non-viral transfection for 15, 60 and 360 minutes, but a trend suggesting increased nuclear delivery of pDNA was observed, tentatively supporting our original hypothesis.

Chapter 6: Quantitation of intracellularly localised quantum dot-conjugated pDNA in human airway epithelial cells using confocal microscopy

6.1 Introduction

In the previous chapter, I have described the intracellular spatial distribution of gold-labelled plasmid DNA (Nanogold-conjugated pDNA) in fixed human airway epithelial cells at the single-molecule resolution using transmission electron microscopy (TEM). In contrast to conventional lens-based optical microscopy with which resolution is limited to ~250 nm due to the diffraction limit of light, TEM uses electrons instead of light, permitting single-molecule resolution of ~0.2 nm. However, the electron microscopy technique has a number of major drawbacks including a) the need to fix samples, b) laboriousness of sample preparation with many potential artefacts, c) the need for specialist training for operation and analysis, and d) the requirement for the sample to be electron transparent and to tolerate a vacuum chamber. Finally and of major importance, for the purpose of the overarching goal of tracking the intracellular fate of pDNA following non-viral gene transfection, the major limitation of TEM is it only permits static "snap-shots" of fixed transfected airway epithelium. Thus, whilst TEM enabled me successfully to visualise and quantitate pDNA conjugated to TEM-opaque nanogold probe at high resolution, I could not monitor the intracellular progress of pDNA in living human airway epithelial cells in real time.

Recently, live-cell imaging, using confocal fluorescence microscopy, has been widely utilised to address a number of dynamic cell biology questions, such as how molecules translocate inside the cell, interact with cellular partners and respond to the local cellular signalling in this environment [250;251]. In contrast to wide field fluorescence microscopy, in which

emitted light is collected from all focal planes above and below the sample, in confocal laser scanning microscopy (CLSM) the fluorescence emission is filtered through a pinhole aperture to reject light originating from out-of-focus regions. The light is detected by a photomultiplier tube with scanning across the specimen in a serial manner to form the 2-D image generated by computer software. Although CLSM is capable of producing the highest out-of-focus discrimination of all routine optical sectioning techniques, the scanning of excitation light is slower than many intracellular transport processes, and, perhaps more importantly, for imaging of photo-labile biological macromolecules, this extended illumination time means the sample is exposed to long photo-toxic levels of the excitation light. As a way round this important drawback, in this study, I have used spinning disk confocal microscopy (SDCM) [252;253]. In contrast to CLSM, SDCM employs a rotating array of micro-lenses to focus the excitation light and a secondary array of simultaneously rotating pinholes to generate the confocality. Thus, the excitation time and energy, and therefore photo-damage to the specimen, are greatly reduced compared to CLSM. Crucially, the parallel scanning of the multiple emission pinholes in SDCM results in a real-time confocal 2-D images without the need for the point scanning as in CLSM.

Figure 63 shows that in CLSM, three-dimensional (3-D) information of the specimen is obtained by moving the objective in *z*-direction (height) via raster scanning to collect *x*,*y* (2-D) sections which are subsequently reconstructed to produce 3-D images. As mentioned above, for SDCM, multiple emission light from the multiple pinholes in the spinning disk are detected simultaneously to produce real-time 2-D images. Again, movement of the objective in the *z*-direction to collect optical sections permits *in silico* re-construction to obtain 3-D images. The representation of live cells or tissues such as our transfected human airway epithelial cells in 2-D images obtained in real-time theoretically permits the visualisation of any intracellular localised macromolecule as long as it is fluorescent. As well as providing

the capability for non-invasive optical sectioning, a key factor in the recent increase in the use of confocal fluorescence microscopy in cell biology has been the ability to tag endogenous and exogenously introduced macromolecules with fluorescent probes (such as natural fluorescent proteins and synthetic organic fluorophores) [254]. For example the fusion of the gene-encoded fluorescent probe, green fluorescent protein (GFP) from jellyfish, *Aequorea victoria*, to an increasing variety of proteins has facilitated the understanding of key cell biology questions. The recent introduction of several novel mutant spectral variants of GFP has increased the palette of the GFP toolbox. For example yellow fluorescent proteins (YFP), red fluorescent proteins (RFP), blue fluorescent proteins (BFP) and cyan fluorescent proteins (CFP) cover a broad spectral range and permit multiplexed imaging in live cells to study multiple cellular events simultaneously.

In contrast to genetically-encoded protein fluorescent probes, the real-time visualisation of exogenously introduced macromolecules, such as pDNA, with a fluorescence microscopy requires labelling with appropriate covalently linked fluorochromes [255;256]. A number of organic fluorophores have been used to label pDNA using a variety of conjugation strategies [233;257;258]. We, and others, have used a variety of small organic fluorochromes to label pDNA. These include dyes that intercalate or electrostatically bind to the DNA such as propidium iodide, acridines, ethidium bromide [259;260], 4',6'-diamidino-2-phenylindole (DAPI) and Hoechst dyes [261-264]. Other dyes are directly linked such as Texas Red and cyanine dyes (cy2,cy3,cy5,cy7) [265-267] and Oregon Green 488 [183;187].

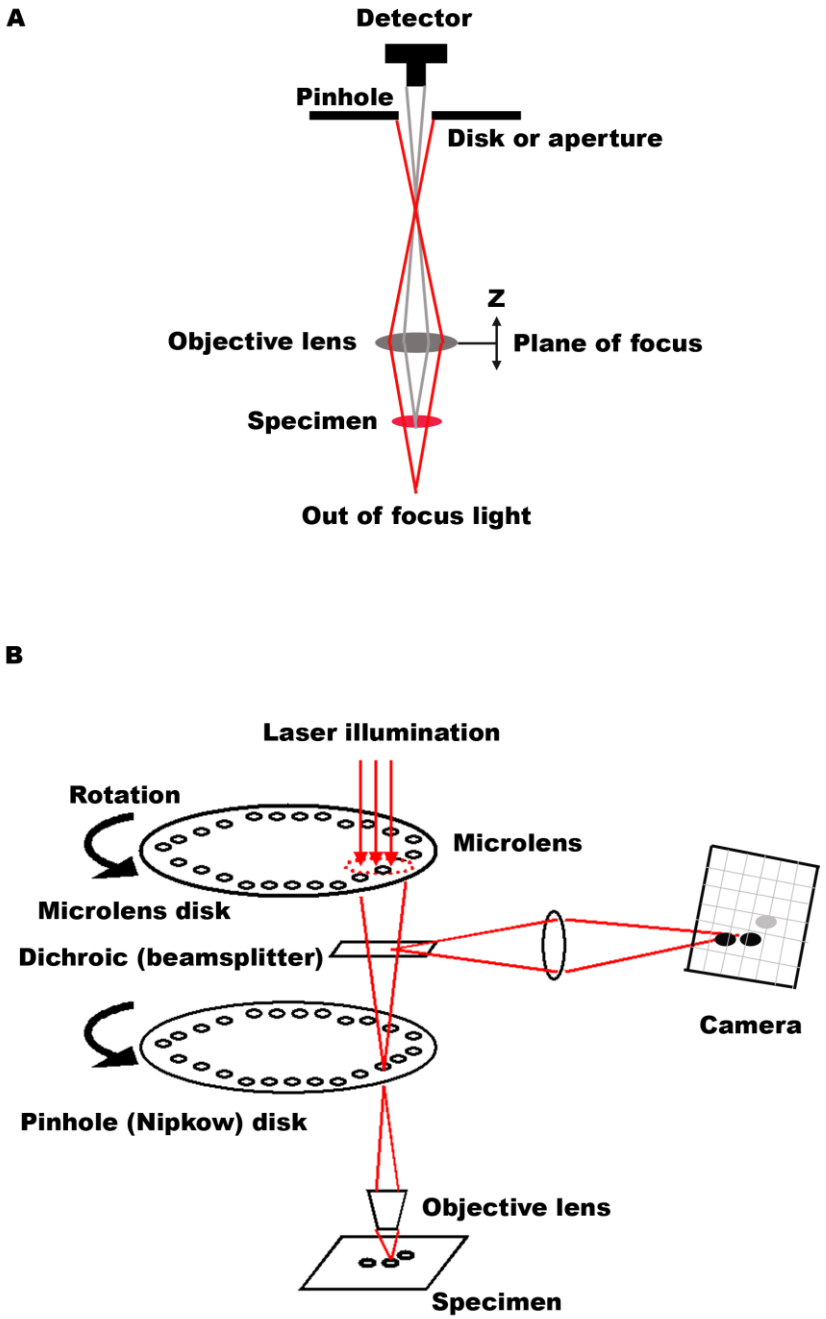

Figure 63: Confocal laser scanning microscopy (CLSM) and spinning disk confocal microscopy (SDCM) systems

Conventionally, linkage of organic fluorophores, such as biotin-conjugated fluorophores, either relies on a photoactivable cross-linker molecule such as psoralen that non-specifically labels the entire pDNA in a random fashion, or enzymatic methods such as digoxigenin and BrdU that perturbs the native transcriptional activity of the pDNA. In addition, if the pDNA carries labels in the transcriptional sensitive areas such as the promoter or transgene, it is likely to interfere with the biological activity. I, therefore, sought to use a conjugation strategy to attach a fluorochrome to pDNA that avoided loss of native transcriptional activity of pDNA. Our laboratory has successfully used this strategy of sequence-specific tagging the conventional organic fluorescent probe, Oregon Green 488, via a thiol-terminated PNA linker molecule, to a β-galactosidase reporter plasmid for imaging of pDNA-nuclear delivery [183;187]. More recently, a similar strategy has been used to link two small organic fluorophores, rhodamine and fluorescein, to the same pDNA in a sequence-specific manner [268]. However, this and other earlier attempts at labelling pDNA with organic fluorophores suffer from a major drawback: the rapid photo bleaching upon extended illumination required for real-time imaging [187;269-274]. In addition, their use is also restricted by their narrow excitation band widths and broad emission spectra, which limits the number of fluorophores that can be simultaneously resolved. In summary, relatively low emission (fluorescence) intensity, low photo-stability, low quantum yields, narrow excitation and broad emission spectra render them suboptimal for live-cell imaging.

Recently, quantum dots (QDots; also called semiconductor nanocrystals or particles) have gained attention as fluorescent labelling probes for fixed- and live-cell imaging studies using both wide field and confocal microscopy [275-280]. Although QDots are composed of semiconductor materials, their small size results in spectroscopic properties that differ from those of bulk semiconductors. Absorption of a photon causes an electron to move from the semiconductor valence band to the conductance band, creating an exciton (electron-hole

pair). Absorption occurs as long as the energy of the incident photons is higher than the semiconductor band-gap energy; thus, excitons can be created over a wide range of energies within the QDot core. The higher-energy excitons relax to the lowest band gap energy before they recombine and emit a photon. Therefore, the wavelength range of the absorption spectrum is broad, whereas that of the emission spectrum is narrow [281]. The most popular QDot currently used in fluorescence microscopy consists of an inner core made of a semiconductor, cadmium selenide (CdSe), which is encapsulated with zinc sulphide (ZnS) followed by a polymer coating and exterior hydrophilic ligand coating, which in turn can be conjugated to biological molecules. Their bio-compatibility with cellular substrates, high quantum yield, extremely high photo stability and non-toxicity make them suitable for long-term real-time imaging; an advantage over fluorescent organic dyes and fluorescent proteins as mentioned above. In addition, their broad absorption and narrow emission properties allow multicolour imaging with a single-wavelength excitation source for all emission profiles [275]. The different sizes of QDot particles have different absorption and emission range; thus the colour can be tuned in the same biological sample with a single excitation wavelength. This particular characteristic of QDots makes them excellent candidates for multiple labelling thus permitting the simultaneous visualisation of several fluorescent-(QDot-) labelled biomolecules in fixed or live cells [282]. Here, I used SDCM quantitatively to describe the distribution of pDNA in real time following non-viral gene transfection in human ALIs. In order to visualise the pDNA using fluorescence microscopy, I sequence-specifically labelled the pDNA with QDots in a similar fashion to the labelling of pDNA with electron-dense nanogold particles as probes for my previous TEM study.

Hypothesis

Increasing the transfection time of human ALIs with QDot-conjugated pDNA using cationic lipid GL67A results in enhanced nuclear delivery of the QDot-labelled pDNA as measured by TEM.

Aims

To assess real-time quantitative localisation of pDNA in human airway epithelial cells at different transfection time points using SDCM.

1) Prepared QDot-conjugated pDNA using cysteine-PNA as a linker molecule including a physical mix of pDNA and QDot (control unconjugated pDNA) in the absence of PNA.
2) Determined stoichiometric ratio of QDot to pDNA in the QDot-conjugated pDNA.
3) Assessed the effect of QDot conjugation on transcriptional activity of pDNA.
4) Visualised the intracellularly localised QDot-conjugated pDNA in HEK293T monolayers, mouse nasal epithelium and ALI by SDCM.
5) Assessed the real time quantitative localisation of pDNA in human airway epithelial cells at different transfection time points using SDCM.

6.2 Materials and Methods

All chemicals, reagents and doubly distilled de-ionised water used throughout the experiments were of analytical grade. Absorption spectra were captured on a Unicam UV1 spectrophotometer Thermo Scientific, Cambridge, UK) using 1 nm bandwidth.

6.2.1 Peptide nucleic acid

PNA with a terminal cysteine residue contained the following sequence: cLLLTTTCTCCCTTCLLLJTTJJJTJTTT (where c = cysteine, L = *N*-(2-aminoethyl) aspartic acid (AEAA) linker, C = cytosine, T = thymine, J = psuedocytosine) and has already been discussed in Chapter 2, Section 2.5.

6.2.2 Plasmid DNA

All the plasmids have been described previously in Chapter 2, Section 2.6.1. Briefly pCIKFluc (referred to as pCMV-Fluc) contains the Fluc reporter gene and possesses a specific PNA target site containing the 8-mer sequence (AAGGGAGA); pCIKGluc contains the secreted Gluc reporter gene; and pCIKCFTR contains the human CFTR cDNA.

6.2.3 Monomaleimido-quantum dots

The 5 nm monomaleimdo-QDot565 was purchased from Invitrogen, Molecular Probes, Paisley, UK.

6.2.4 Labelling of plasmid DNA with quantum dot

Plasmid pCIKFluc was labelled by hybridisation to PNA-cysteine covalently conjugated to QDot565-maleimide using a method described previously [187]. Briefly, the PNA-cysteine was activated prior to the conjugation reaction to expose free thiol residues by incubation with 0.1 μM Tris (2-carboxyl ethyl) phosphinehydrochloride (TCEP) (in 100 mM HEPES; pH 7.5) and used within 1 hour of activation. The QDot565-maleimide was activated as per manufacturer's instructions and also used within 1 hour of activation. The QDot565-maleimide was added to the PNA-cysteine (3 μM) at a 15 molar excess, and incubated at room temperature for 16 hours with end-to-end mixing. PNA-cysteine/QDot was reacted with the pCIKFluc at a 10:1 molar ratio in TE buffer (10 mM Tris, pH 6.5, 1 mM EDTA) overnight at 37^{o}C with end-to-end mixing, where the molarity of the pDNA was at 0.5 μM. The reactions were diluted into 2 ml of TE buffer and concentrated to 50 μl in a Centricon-30 microconcentration device (Millipore, Watford, UK). To remove further any unbound QDot565-PNA, the pDNA was re-precipitated using isopropanol. The solution containing the precipitated pDNA was centrifuged at 14,400 *g* for 25 min at 4˚C. The pellet was washed with 70% (v/v) ethanol and re-centrifuged. The supernatant was then removed, and the pellet allowed to air-dry. Sterile water was added and the pDNA allowed to resuspend overnight at 4˚C. Approximately 2.5 mg of pDNA was labelled in a typical experiment. Labelled pDNAs were stored in single-use aliquots at −80°C.

6.2.5 Spectrophotometric analysis of quantum dot conjugated plasmid DNA

The samples (1 μl) was added to WFI (500 μl) in duplicate in a quartz cuvette and gently mixed by inversion. The absorbance of pDNA and the QDot was measured at 260 nm and 405 nm respectively using a Unicam UV1 spectrophotometer (Thermospectronic, Cambridge, UK) using 1 nm bandwidth. The concentration of pDNA and QDot in the QDot-conjugated pDNA, and the concentration of pDNA in the control unconjugated pDNA, was determined from the absorbance values measured at 260 nm and 405 nm respectively.

6.2.6 Cell Culture

Briefly, the human embryonic kidney HEK293T cells (ATCC LGC Promochem, London, UK) were seeded at a density of 1×10^5 cells/glass coverslip (No. 1; 35 mm diameter) 24 hours before transfection. The cells were maintained in Dulbecco's Modified Eagle Medium (DMEM) media (supplemented with 10% FBS, 1 mM glucose, 5 mM L-glutamine, 100 IU/ml penicillin and 100 µg/ml streptomycin). Cells were cultured in a humidified atmosphere at 37 °C with 5% CO_2. All the experiments were carried out with cells at passage numbers between 1-10. Cultures of fully differentiated human airway epithelial cells grown at the air-liquid-interface (ALI), (MucilAir), were purchased from Epithelix SÀRL (Geneva, Switzerland) and cultured at 37 °C and 5% CO_2 in a humidified atmosphere in a standard tissue culture incubator according to manufacturer's recommendation. The basolateral culture medium (MucilAir culture medium, Epithelix) was replaced every 2–3 days.

6.2.7 Mouse nasal tissue

Mouse nasal epithelial tissue was freshly obtained from 8-10 weeks old FABP mice as detailed in Chapter 2, Section 2.2.

6.2.8 Custom-built perfusion chamber

The perfusion chamber, shown in Figure 64, consists of two apposed assemblies forming a functional unit, but containing two separate and sealed apical and basolateral compartments. Krebs-Henseleit buffer (composed of (in mM) 119 NaCl, 15 KCl, 0.8 $CaCl_2$, 5.2 $MgCl_2$, 25 $NaHCO_3$, 1.2 KH_2PO_4, and 5.6 glucose) flowed (~1 ml/hour, 37°C with 5% CO_2) through the

basolateral compartment. The upper (apical) compartment contained the water-immersion objective lens immersed in Krebs-Henseleit buffer. Temperature during imaging was maintained at 37°C using an in-line heating device. The chamber was constructed by Dr Stephen Smith (Department of Gene Therapy, Imperial College London).

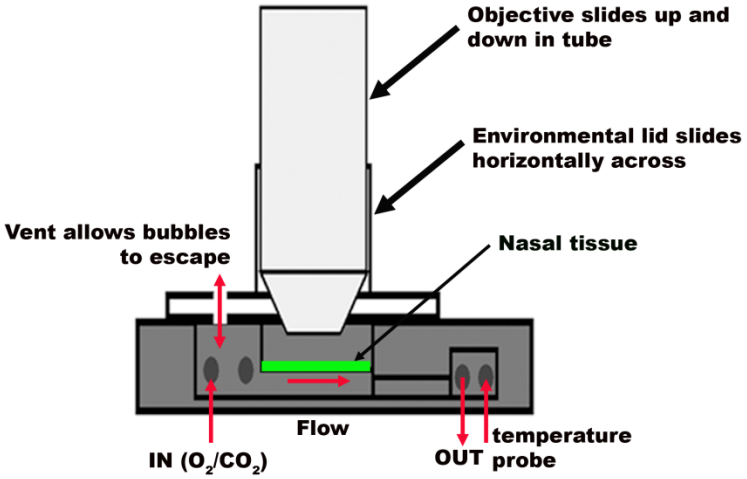

Figure 64: Overview of the perfusion chamber
Cross-section of the dual-chamber, showing the separated, sealed upper (apical) chamber, lower (basolateral) chamber, environmental lid/envelope around the water-immersion objective lens, and inlet and outlet ports.

6.2.9 Transfection

Coverglass-cultured HEK293T cells were transiently transfected using lipofectamine™ 2000 (Invitrogen, Paisley, UK) according to the manufacturer's directions. Briefly, plasmid DNA (1 μg) and 2.5 μl of the lipofectamine™ 2000 reagent were incubated in 400 μl of serum-free Opti-MEM medium (Invitrogen) for 20 min at room temperature. This solution was applied to the cells and incubated in a humidified atmosphere at 37°C with 5% CO_2. After 6 hours, the transfection media was discarded and replaced with 1 ml Opti-MEM media supplemented with 10% FBS. The Opti-MEM/FBS media was changed after 18 hours and further incubated at 37°C with 5% CO_2 for 24 hours prior to use. Human airway epithelial cells cultured at the ALI were transfected with pDNA complexed with the cationic lipid formulation GL67A as described previously.

6.2.10 *Firefly* and *Gaussia* luciferase reporter gene assays

Firefly luciferase or *Gaussia* reporter gene activities were routinely assessed in HEK293T cells or ALIs, respectively, as described in Chapter 2, Sections 2.14 and 2.15.

6.2.11 Live-cell confocal microscopy and image analysis

Live-cell imaging was performed using an Ultra View LCI confocal system (Perkin Elmer, Buckinghamshire, UK) equipped with Zeiss Axioplan 2 inverted microscope (Carl Zeiss Ltd, Hertfordshire, UK). All images were taken using a x63 Achroplan 0.95 numerical aperture (NA) water-immersion objective and acquisition was controlled by Ultra VIEW Imaging Suite software (Perkin-Elmer). Transfected HEKT293 cells were imaged in 35-mm dish

containing 1 ml of wash buffer (consisting of 20 mM HEPES (pH 7.3), 100 mM potassium acetate, 2 mM magnesium acetate, 1 mM EGTA, 0.25 M sucrose). To image human airway epithelial cells grown at the ALI, the permeable filters were carefully removed from the inserts and placed, apical side up, into the custom-built perfusion chamber. The apical compartment contained the objective lens immersed in 100 μl of pDNA/lipid complex made up to 500 μl with Krebs-Henseleit buffer. The 12-bit greyscale images were acquired using a cooled monochrome CCD camera (Orca-AG, Hamamatsu Photonics, Japan). QDot565 fluorescence was excited at 488 nm Krypton/Argon laser wavelength, and collected with a 575 ± 75 nm emission filter. In order to permit comparison of QDot565 fluorescence and brightness, images for each QDot565 scan were acquired using the same illumination and image acquisition settings. SYTO-16 (dissolved in DMSO at 0.1 mM, added at 10 μM, excited at 488 nm and collected using a 480 ± 50 nm emission filter) and di-4-ANEPPDHQ (dissolved in DMSO at 1 mM, added at 0.1 mM, excited at 488 nm and collected using a 620 ± 70 nm emission filter) vital dyes (both from Invitrogen) were used to counter-stain the nuclei and cell membranes, respectively. It is noteworthy that whilst preventing "contamination" of the QDot565-fluorescence signal, the above sequential imaging of QDot565, and the SYTO-16, and di-4-ANEPPDHQ channels meant only one field-of-view per individual cell monolayer, or ALI, could be sampled per experiment.

6.2.12 Image processing and analysis

Three-dimensional (3-D) reconstructions were made using Volocity imaging software (version 5.5; Perkin-Elmer) running on a Dell Precision T5400 computer (Dell Computer, UK) equipped with an nVidia GeForce 4 video card (nVidia, Santa Clara, CA). Images generated with the Volocity imaging program were converted to tagged image file format and

imported into Adobe Photoshop, version 6.0, software files (Adobe, Seattle, WA). In all figures, equivalent changes in contrast and brightness were applied to all photomicrographs to ensure that the images were directly comparable.

The studies in this Chapter were undertaken jointly with Dr Felix Munkonge (Department of Gene Therapy, Imperial College London).

6.3 Results

In order to visualise and quantitate QDot-conjugated plasmid DNA (QDot-pDNA) against a cellular background in living cultured cells, mouse nasal tissue as well as human airway epithelial cells, we chose covalently to label the pDNA (pCIKFluc; ~4,970 kDa; ~200 nm when fully condensed) with QDot565 (~ 5 nm when fully functionalised) via a peptide nucleic acid (PNA; 6.8 kDa) linker molecule. Our choice of ~565 nm-emitting QDot565 was primarily dictated by the need for our pDNA "marker" to be of a longer wavelength than any potential "contaminating" cellular autofluorescence emission in the UV range. As noted above, whereas the QDots exhibit narrow emission spectra, the wavelength range of the absorption spectrum is broad. Figure 65 shows the absorbance spectrum of QDot-pDNA compared to that of unconjugated pDNA. The pCIKFluc conjugated to QDot565 via a PNA linker molecule was compared with unconjugated pCIKFluc, subjected to a similar conjugation reaction, excluding the PNA. Figure 65A shows the broad absorbance of the conjugated pDNA due to QDot compared to its absence in the unconjugated (Figure 65B) and vehicle negative control (Figure 65C). In both cases, following the reaction of QDot565 with the PNA (or without the PNA in the control reaction) and subsequent hybridisation of the QDot565-PNA conjugate with pCIKFluc, the resultant QDot565-conjugated pDNA was purified by filtration using microconcentrator devices which efficiently excludes any free unreacted PNA, QDot565 and QDot565-PNA conjugate. Thus, the QDot-pDNA absorbance spectrum shown in Figure 65A is solely attributable to the conjugated pDNA free of any contaminating primary reactants.

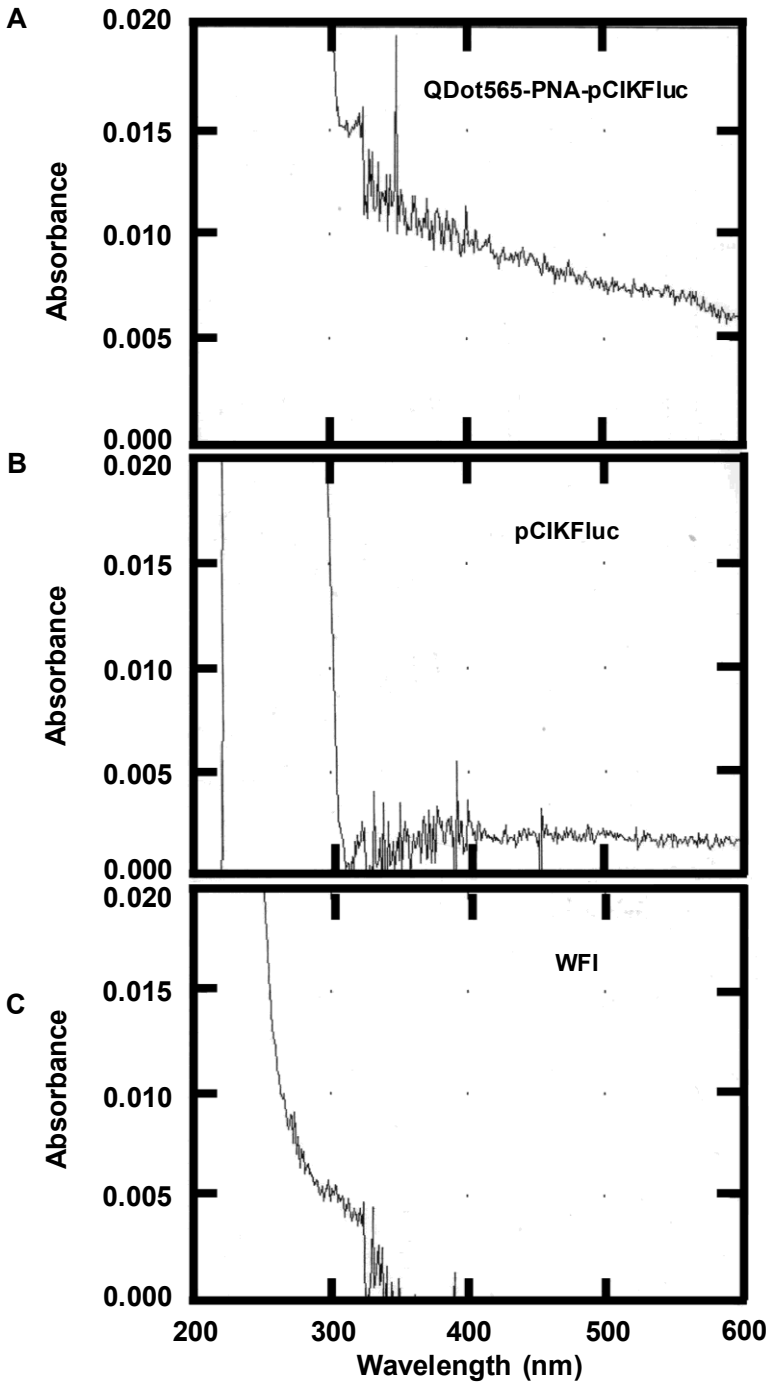

Figure 65: Absorption spectrum of quantum dot-conjugated plasmid DNA

Absorption spectra of (A) quantum dot-conjugated Qdot565-PNA-pCIKFluc (12 mg/ml with respect to pCIKFluc), (B) control pCIKFluc (12 mg/ml) subjected to the same conjugation reaction but without addition of peptide nucleic acid (PNA) linker molecule and final purification steps as detailed in Materials and Methods. (C) Control water-for-injection (WFI) used for dissolving the conjugated and the control unconjugated plasmid DNA. Bandwidth of excitation and emission slits: 1 nm. Representative of 6 independent experiments.

In order to correlate the QDot565 marker fluorescence to the conjugated pDNA, it was essential to determine the labelling density of quantum dots on the pDNA. To do this, the quantities of both QDot565 and pDNA were calculated using published extinction coefficients [283;284] and spectrophotometrically determined absorbances.

As the absorbance measurement is governed by Beer-Lambert's law.

$A = \varepsilon CL$ - *equation 1*

(where A is absorbance, ε is the molar extinction coefficient (1,100,000 cm^{-1} M^{-1} at 405 nm), L is the path length, and C is the QDot565 concentration), I was able to calculate the absolute quantity of QDot565 present on the final purified QDot565-PNA-pCIKFluc conjugate. Similarly, the absolute pDNA concentration was determined spectrophotometrically using the commonly accepted average extinction coefficients for 1 mg/ml nucleic acid solutions at 260 nm and 280 nm of 20 and 10 cm^{-1} M^{-1}, respectively [284]. Plasmid DNA absorbs maximally at 260 nm but suffers from low sensitivity and interference from molecules such as PNA and compounds used in its preparation. These "contaminants" also absorb at 280 nm permitting the estimation of pDNA purity by performing ratio absorbance measurements at A260/A280. Preparations with an A260/A280 greater than approximately 1.7 are termed "pure" [284]. I was thus able routinely to accurately determine the molar ratio (1:1; a single molecule of QDot565 per one pDNA molecule) of QDot565 to pDNA for the purified conjugated pDNA.

Having fluorescently labelled the pDNA by site-selective conjugation with QDot565 (via PNA), I next sought to examine the effect of this conjugation on the biological activity of the plasmid. HEK293T cells were transfected with the QDot565-PNA-pCIKFluc or unconjugated control pDNA using the cationic lipid formulation lipofectamine™ 2000. The pDNA biological activity of the conjugated pDNA, positive control unconjugated pDNA and

negative control pCMVβ-Gal were evaluated by monitoring *Firefly* luciferase (Fluc) activity present in cell lysates at indicated time-points immediately after the removal of the Lipofectamine/pDNA transfection mix**.**

Figure 66 shows that there was no significant difference in Fluc activity between the conjugated and unconjugated control pDNA at all transfection time-points. Thus, the pDNA hybridised to QDot565-PNA retains native transgene activity within mammalian cells.

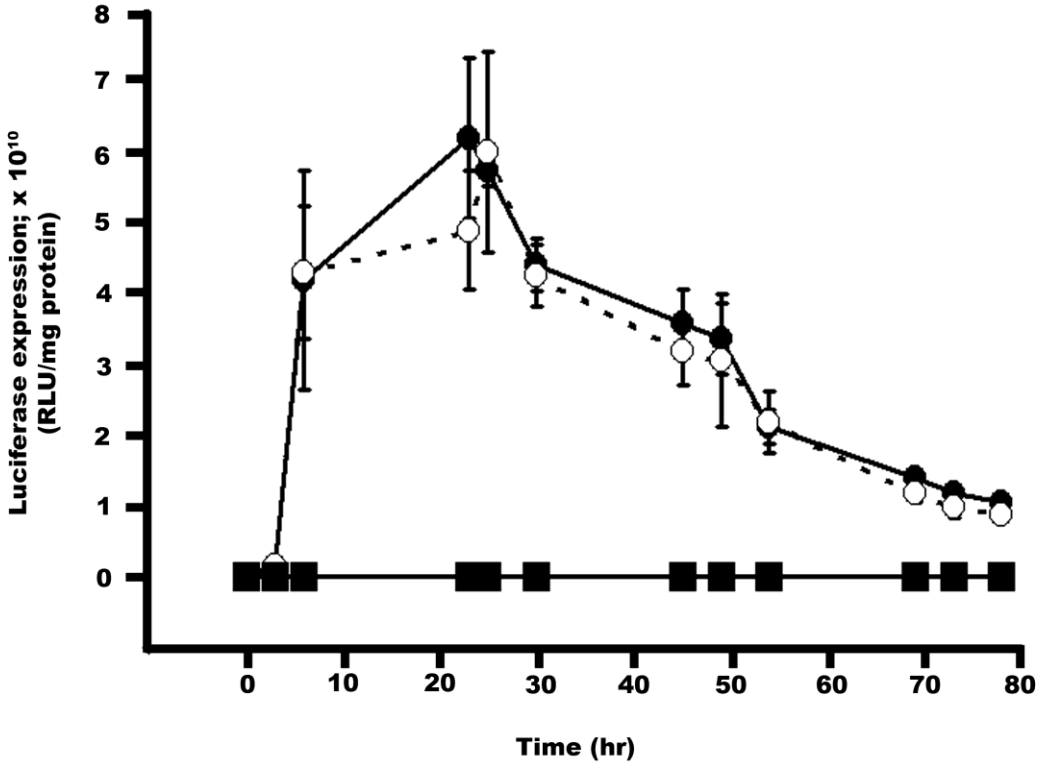

Figure 66: Effect on reporter gene activity of conjugating plasmid DNA with fluorescent quantum dots

HEK293T cells were transiently transfected using Lipofectamine 2000-mediated transfection of HEK293T cells with 1 μg of quantum dot (QDot) 565-conjugated pCIKFluc (QDot565 -PNA-pCIKFluc) (closed circles), unconjugated control pCIKFluc (open circles) and the negative control plasmid, pCMVβ-Gal (closed squares). Firefly luciferase (Fluc) activity was assayed (as described in Materials and Methods) at indicated time-points, immediately after the removal of the Lipofectamine 2000/pCIKFluc transfection mix. Data represent the mean ± SEM of Fluc activity (RLU/mg protein). N=6 dishes from 3 independent experiments.

The primary objective in this part of the study was to visualise and quantitate intracellular fluorescently-tagged pDNA following non-viral transfection. With this mind and to establish an appropriate imaging pipeline as a prelude to detection and quantitation in human airway epithelial cells, I therefore evaluated whether QDot-pDNA could be visualised in cultured cell monolayers. HEK293T cell monolayers were transiently transfected, 24 hours after seeding on glass coverslips, by incubation with QDot565-PNA-pCIKFluc complexed with the commercial cationic lipid lipofectamine™ 2000 for 6 hours as recommended by the suppliers. After replacing the cationic lipid/QDot-pDNA complex with media and culturing for a further 72 hours, the coverslips containing the living transfected cells were then imaged at room temperature by placing them in a Petri dish containing 1 ml HBSS/glucose buffer located on the SDCM stage. To eliminate the possibility of bleed-through of fluorescence emission from the SYTO-16 and di-4-ANEPPDHQ vital dyes used to counter-stain the nuclei and cell membranes, respectively, I first scanned the QDot565 fluorescence before adding any of the other contrast vital dyes. The SYTO-16 (10 μM) was then added and incubated for 15 minutes before re-scanning. Di-4-ANEPPDHQ (0.1 mM) was added next, incubated for 15 min before re-scanning.

Figure 67 shows merged pseudo-coloured red QDot565-PNA-pCIKFluc, SYTO-16-stained nuclei pseudo-coloured blue and di-4-ANEPPDHQ-stained cell membranes pseudo-coloured grey maximum intensity projected images generated from 130 *z*-sections (top panel of Figure 67) and the corresponding *x-z* projection (bottom panel of Figure 67) demonstrating the distribution of QDot565-conjugated pDNA in the transfected cells. Red QDot565 fluorescence (arrowheads), representing QDot-pDNA, is clearly visible together with distinct, strong, blue-stained nuclei in both the *x-y* and *x-z* views. Cell membrane fluorescence staining with ANEPPDHQ dye (arrows) was, however, not very distinct and the cell

boundaries were barely discernable. It was not clear from the images shown in Figure 67 whether the visualised QDot-pDNA is localised intracellularly, or for that matter, inside the nuclei. A major strength of confocal microscopy imaging is the capability of reconstructing 3-D images from serial optical *z*-sections. Thus, I next used this facility to visualise better the post-transfection intracellular distribution of QDot-pDNA using 3-D images re-constructed from 130 serial optical *z*-sections of the QDot-pDNA-transfected HEK293T cell monolayers.

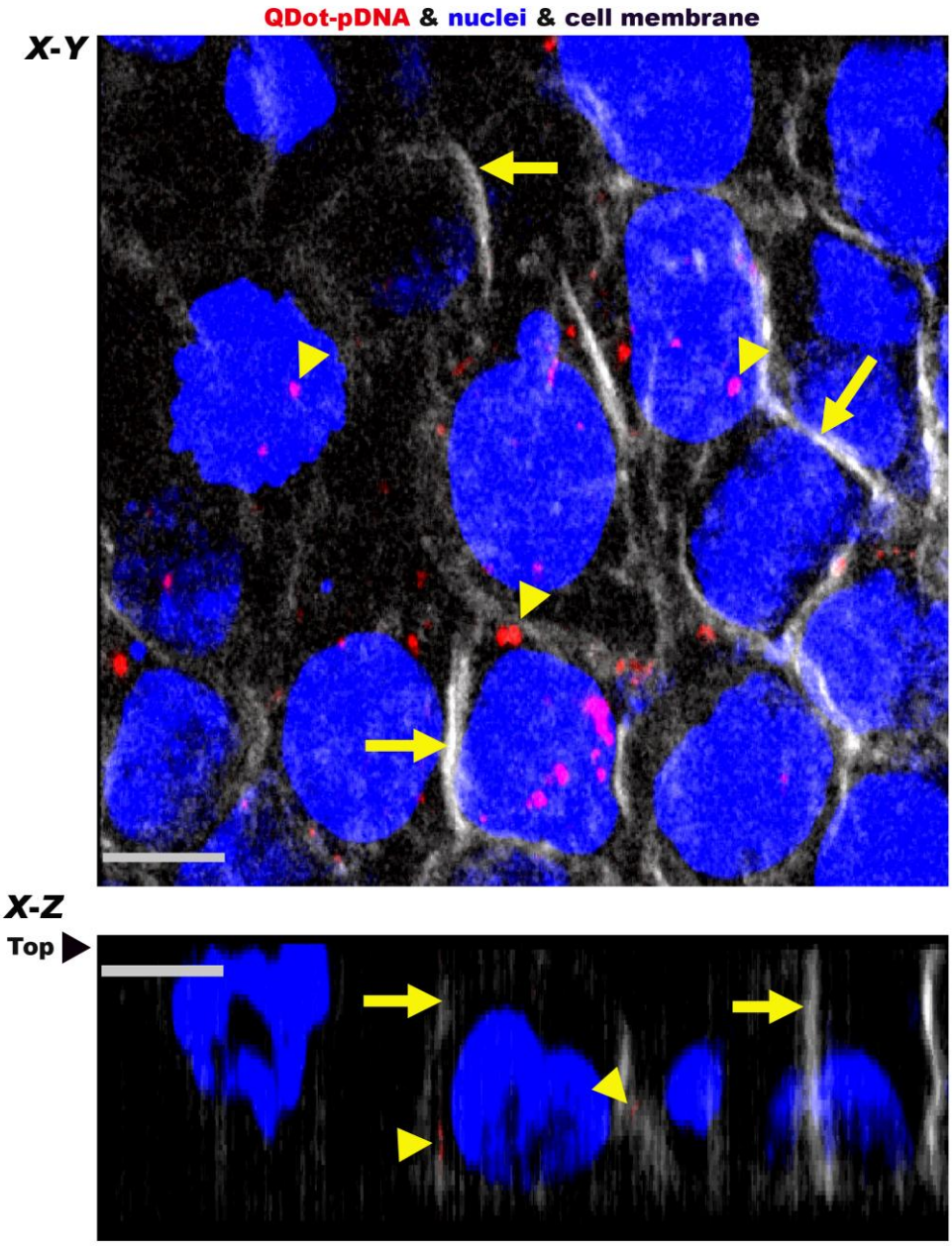

Figure 67: Subcellular localisation of quantum dot-conjugated plasmid DNA following cationic lipid-mediated transfection of HEK293T cells
HEK293T cell monolayers were transiently transfected with QDot565-conjugated pCIKFluc (QDot -pDNA) using Lipofectamine™ 2000, 24 hours after seeding. Seventy-two hours post-transfection, living HEK293T cells were imaged using Spinning Disk Confocal Microscopy. Representative *x-y* (top panel) and *x-z* (bottom panel) projection images from 130 serial optical *z*-sections (0.2 µm thick) are shown. The micrographs are merged fluorescent images of red pseudo-coloured QDot-pDNA, blue pseudo-coloured SYTO-16-stained nuclei and grey pseudo-coloured di-4-ANEPPDHQ-stained cell membranes. The arrowheads indicate QDot-pDNA and arrows indicate cell membrane fluorescence staining with di-4-ANEPPDHQ dye. Scale bars = 10 µm.

The left-hand panels of Figure 68 show representative *z*-sections (0.2 μm thick at 1 μm intervals) through the HEK293T cell monolayer. The micrographs are red pseudo-coloured QDot565-pDNA images, merged with corresponding blue pseudo-coloured SYTO-16-stained nuclei images (middle panels of Figure 68), as well as grey pseudo-coloured di-4-ANEPPDHQ-stained cell membrane images (right-hand panels of Figure 68). At a depth below ~3 μm, QDot565 fluorescence (arrow), representing intracellularly-localised QDot-pDNA, is clearly visible. When merged with blue and grey pseudo-coloured SYTO-16-stained nuclei and di-4-ANEPPDHQ-stained cells, respectively, it is clear that not only is the QDot565 fluorescence localised on the cell membrane but is visible within the cells (arrowheads). Some QDot565 fluorescence appears to be masked by the nuclei 4 to 9 μm below the apical surface, suggesting the internalisation of the QDot-pDNA in the nuclei of the transfected cells. I thus followed up this co-localisation of QDot565 fluorescence with the nuclei in transfected HEK293T cells using Volocity imaging software to reconstruct 3-D renderings of the cell monolayers using the above serial sections.

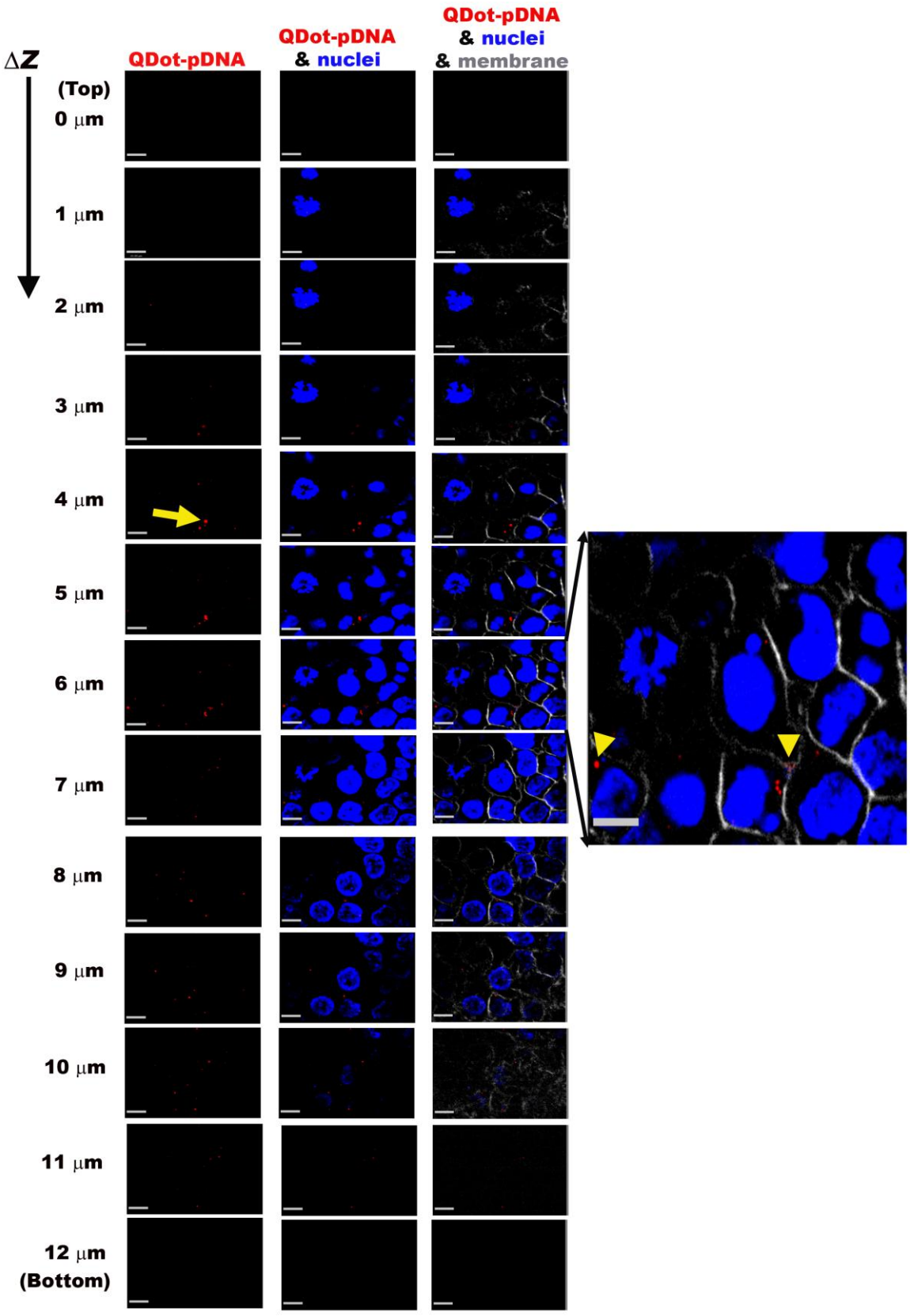
ΔZ
QDot-pDNA
QDot-pDNA & nuclei
QDot-pDNA & nuclei & membrane
(Top)
0 μm
1 μm
2 μm
3 μm
4 μm
5 μm
6 μm
7 μm
8 μm
9 μm
10 μm
11 μm
12 μm
(Bottom)

Figure 68: Subcellular localisation of quantum dot-conjugated plasmid DNA in optical sections following cationic lipid-mediated transfection of HEK293T cells
Confocal optical sections (0.2 µm thick) in 1 µm intervals through the HEK293T cellmonolayer shown in Figure 67. Red pseudo-coloured quantum dot 565-conjugated pCIKFluc (QDot-pDNA) (left-hand panels), merged with images of blue pseudo-coloured SYTO-16-stained nuclei (middle panels), and grey pseudo-coloured di-4-ANEPPDHQ-stained cell membranes (near right-hand panels). The arrows indicate QDot-pDNA. The insert on the far right-hand side is a magnified view of the QDot-pDNA, nuclear and cell surface membrane merged overlay, 6 µm below the top of the cell monolayer, showing cell membrane and cytoplasmicaly-localised QDot-pDNA indicated by arrowheads. Scale bars = 10 µm.

Three dimensional reconstruction and rendering of the confocal image stacks shown in Figure 69 permitted the separate visualisation of the QDot-pDNA channel alone, merged with the nuclei channel, and nuclei and cell surface membrane segmentation. Visualisation of the QDot-pDNA-transfected cells from these different perspectives allowed the unambiguous evaluation of cytoplasmicaly- and nuclear-localised pDNA. The QDot-pDNA shown in the top panel of Figure 69 represents the total amount of pDNA detected whilst the QDot-pDNA masked by the nuclei (middle panel of Figure 69) represents nuclear-localised pDNA. Plasmid DNA co-localising with the cytoplasmic compartment was demarcated by the grey pseudo-coloured di-4-ANEPPDHQ cell membrane stain (bottom panel of Figure 69). Thus, I was able to visualise QDot-pDNA in living HEK293 cells, 72 hours post-transfection using SDCM. In addition, I established conditions for staining nuclei of the living HEK293 cells with the biocompatible cell-permeant nucleic acid, SYTO-16 vital dye. Unfortunately, I did not achieve good staining of the cell surface membrane with the selected long wavelength vital dye, di-4-ANEPPDHQ, likely due to heterogeneous mixing in the apical compartment of the chamber which unlike the bottom (basolateral) was not continually perfused. I was, thus, unable to clearly discern all the cellular boundaries.

Prior to the ultimate aim of quantitatively describing the fate of pDNA in non-virally transfected human airway epithelial cells, I initially used freshly obtained mouse nasal tissue to facilitate the development of a custom-built perfusion chamber, as well as to optimise the concentrations and conditions of vital dyes used for staining the nuclei and cell surface membranes. Our laboratory has traditionally used mouse nasal epithelium as a convenient surrogate for human lung to evaluate the transfection of a mucus-enriched airway surface fluid layer in gene therapy for CF.

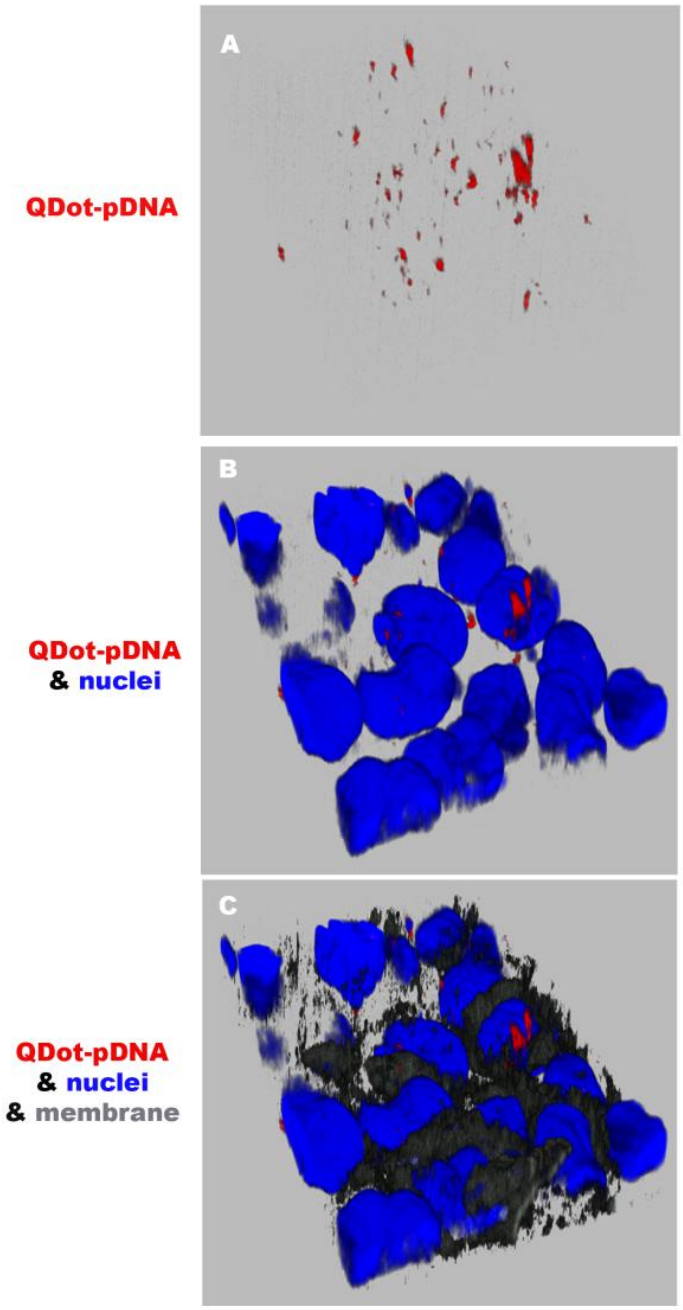

Figure 69: Three-dimensional visualisation of the quantum dot-conjugated plasmid DNA inside HEK293T cells following cationic lipid-mediated transfection
Three-dimensional volume rendering of the re-construction of the 130 serial z-sections (0.2 µ m thick) through the quantum dot-conjugated plasmid DNA (QDot-pDNA)-transfected HEK293T cell monolayer shown in Figures 67 and 68, showing (A) red pseudo-coloured QDot-pDNA, (B) merged with images of blue pseudo-coloured SYTO-16-stained nuclei, and (C) grey pseudo-coloured di-4-ANEPPDHQ-stained cell membranes. Representative of three independent experiments.

The mouse nasal epithelium models the fully differentiated, pseudostratified, polarised, ciliated airway epithelial cells. In contrast to the lower airways of CF knockout mice, mouse nasal tissue contains both submucosal glands, mucous-secreting cells and recapitulates the characteristic pathophysiological abnormalities of CF [12]. The correct modelling of transfection of the intact mouse, or for that matter human, apical surface of the airway epithelium *in vivo*, requires the separation of epithelial luminal compartment from its serosal side, whilst maintaining the tight epithelial seal. Thus, in order to provide a suitable chamber with separated apical and basolateral compartments, capability for transfection via the apical side, perfusion of oxygenated nutrient medium via the basolateral side with concomitant removal of depleted medium and catabolites, we constructed the modular dual-chamber perfusion chamber illustrated in Figure 70.

To image the transfection of mouse nasal tissue, the freshly obtained epithelium was carefully removed, as described in Materials and Methods Section in Chapter 2.2, and placed in the perfusion chamber, apical compartment side up as shown above in Figure 70. The basolateral compartment was continually perfused with warm (37°C) oxygenated Krebs-Henseleit buffer. The nasal tissue was then transfected for 15 minutes by introduction of the QDot-pDNA (10 μg DNA) using lipid GL67A (0.6 mM) in the apical compartment. One hour post-transfection, the pDNA/cationic lipid complex was removed by washing twice with freshly gassed Krebs-Henseleit buffer (at 37°C) for 1 hour. The tissue was then scanned for QDot565 fluorescence, prior to sequential staining with, and imaging of, SYTO-16 (10 μM) and di-4-ANEPPDHQ (0.1 mM) nuclear and cell surface membrane vital dyes as detailed above for HEK293Tcells.

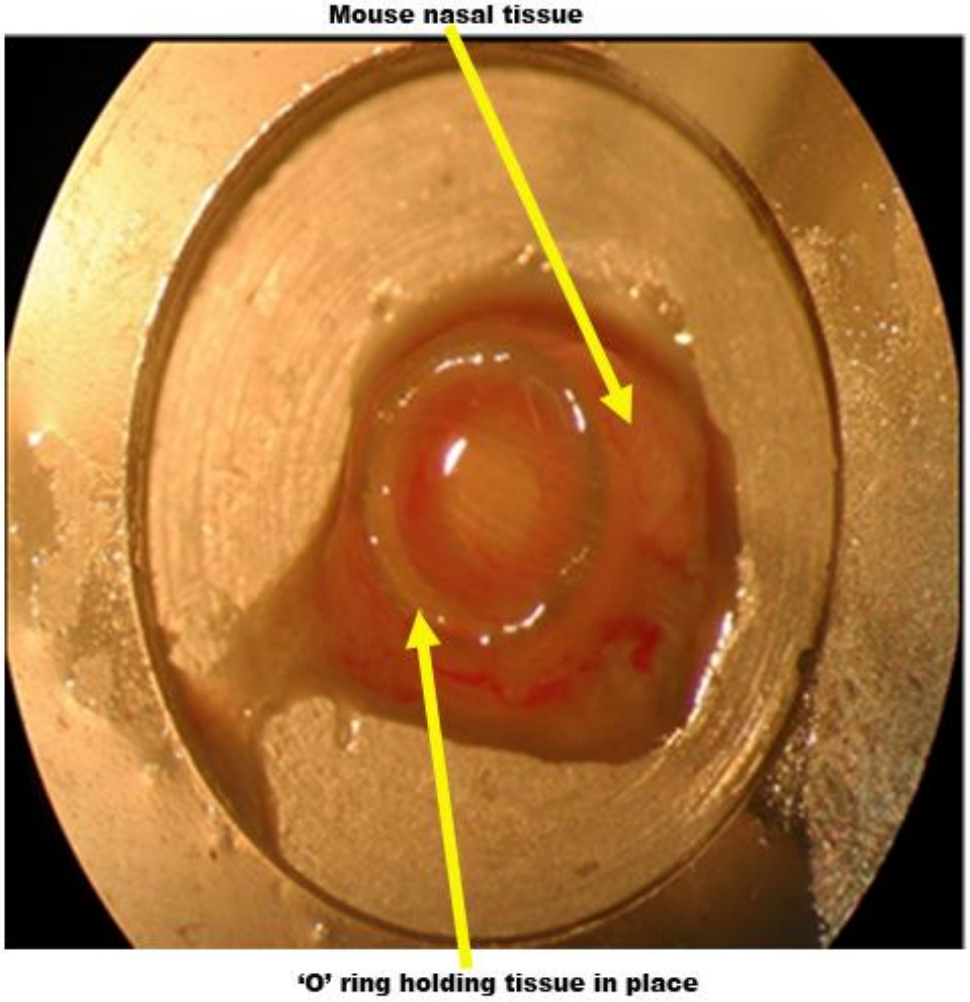

Figure 70: Mouse nasal epithelium mounted on the fully assembled dual-chamber. Such an arrangement can be used for both mouse nasal tissue and human airway epithelial cells grown at the air-liquid-interface on inserts

The confocal micrographs shown in Figure 71 depict merged red pseudo-coloured QDot565-PNA-pCIKFluc, SYTO-16-stained nuclei pseudo-coloured blue and di-4-ANEPPDHQ-stained cell membranes pseudo-coloured grey maximum intensity projected images generated from 134 *z*-sections (top panel of Figure 71) and the corresponding *x*-*z* projection (bottom panel of Figure 71) demonstrating the distribution of QDot-pDNA in the transfected mouse nasal epithelium. Red QDot-pDNA fluorescence (arrows) in both the *x*-*y* and *x*-*z* views are clearly visible. The blue SYTO-16-stained nuclei although visible were not good enough to permit the clear segmentation of distinct mouse nasal epithelial cell nuclei to enable QDot-pDNA/nuclei co-localisation. Also, as in the case for imaging of HEK293T cells, the ANEPPDHQ membrane dye fluorescence was not very distinct (arrowheads).

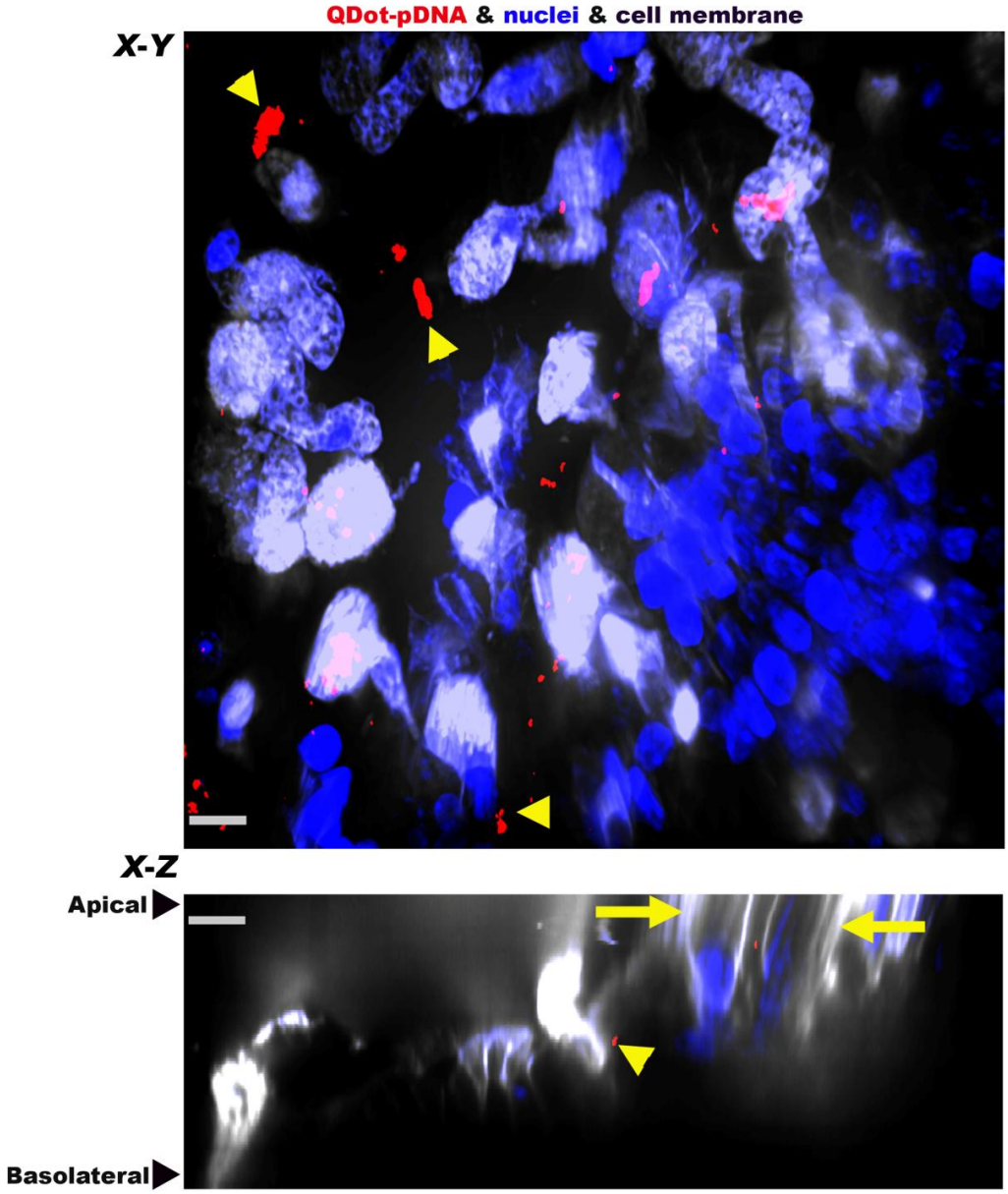

Figure 71: Subcellular localisation of quantum dot-conjugated plasmid DNA following cationic lipid-mediated transfection of mouse nasal tissue
Freshly obtained mouse airway tissue was transfected for 15 minutes with quantum dot (QDot)) 565-conjugated pCIKFluc (10 µg DNA) using cationic lipid GL67A. One hour post-transfection, living tissue (marked by cilia beating) was imaged below the epithelial apical surface using Spinning Disk Confocal Microscopy. Representative *x-y* projections (top panel) and orthogonal sections (bottom panel; with apical membrane at the top and basolateral membrane at the bottom) of 134 *z*-sections are shown. The micrographs are merged images of red pseudo-coloured QDot565-PNA-pCIKFluc, SYTO-16-stained nuclei pseudo-coloured blue and di-4-ANEPPDHQ-stained cell membranes pseudo-coloured grey. The arrowheads indicate QDot565-PNA-pCIKFluc fluorescence and the arrows indicate cell membrane fluorescence staining with di-4-ANEPPDHQ dye. Scale bars = 10 µm.

The confocal micrographs shown in Figure 72 depict *z*-sections (0.3 μm/ *z* –section; 3 μm intervals shown) through the epithelium represented by red pseudo-coloured QDot565-PNA (left-hand panels), merged with corresponding blue pseudo-coloured SYTO-16-stained nuclei images (middle panels), as well as grey pseudo-coloured di-4-ANEPPDHQ-stained cell membrane images (right-hand panels). Figure 72 shows QDot565 fluorescence visible at the top (marked by beating cilia in a respective bright field image) of the mouse nasal tissue (top left hand-panel of Figure 72). QDot565 fluorescence was also clearly present at 12 μm below this level (arrowheads). As shown previously for the subcellular distribution of QDot- DNA following cationic lipid-mediated transfection of HEK293T cells, whilst excellent nuclear-staining with SYTO-16 was achieved, di-4-ANEPPDHQ staining for cell surface membrane was incomplete (right-hand panels of Figure 72) making cell segmentation impossible. Thus, whilst the number of nuclei containing QDot-pDNA (QDot-pDNA-positive nuclei) could be seen clearly, it was not possible to directly determine the number of cells containing red fluorescently-labelled QDot-pDNA (QDot-pDNA-positive cells).

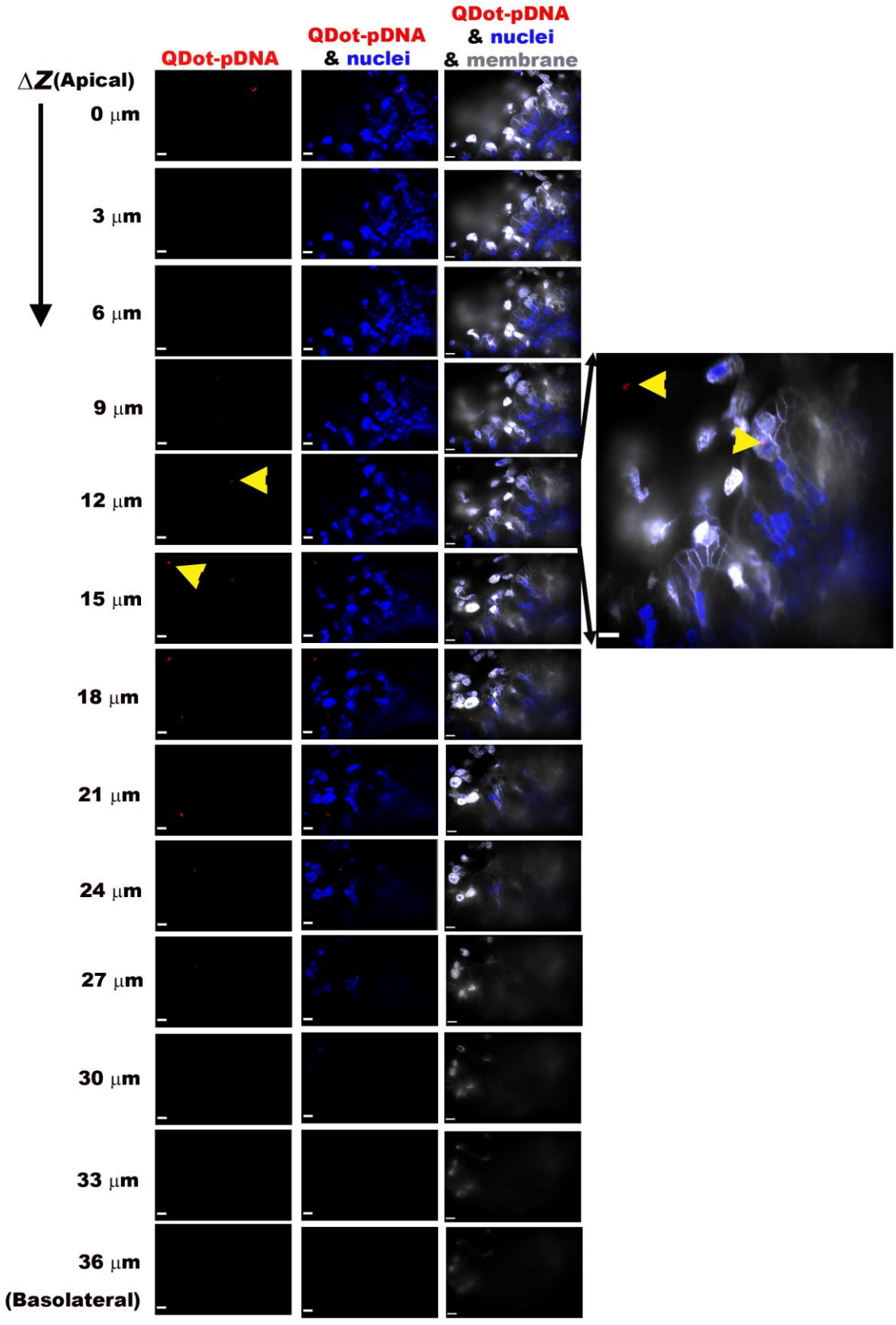
QDot-pDNA
QDot-pDNA & nuclei
QDot-pDNA & nuclei & membrane
ΔZ(Apical)
0 μm
3 μm
6 μm
9 μm
12 μm
15 μm
18 μm
21 μm
24 μm
27 μm
30 μm
33 μm
36 μm
(Basolateral)

Figure 72: Subcellular localisation of quantum dot-conjugated plasmid DNA in optical sections following cationic lipid-mediated transfection of mouse nasal tissue
Confocal optical sections (0.3 μm thick) in 3 μm intervals through the mouse nasal tissue shown in Figure 71. Red pseudo-coloured quantum dot (QDot) 565-PNA- pCIKFluc (left-hand panels), merged with images of blue pseudo-coloured SYTO-16-stained nuclei (middle panels), and grey pseudo-coloured di-4-ANEPPDHQ-stained cell membranes (near right-hand panels). The arrowheads indicate QDot-pDNA. The insert on the far right-hand side is a magnified views of the QDot-pDNA (indicated by arrowheads) 12 μm below the apical surface. Scale bars = 10 μm.

I next transfected human airway epithelial cells grown at the ALI in order to evaluate the visualisation of QDot565-conjugated pDNA in living terminally-differentiated ciliated human AECS, target cells for CF gene therapy. The airway epithelial cells on ALIs were mounted in the dual-chamber and transfected for 15 minutes by addition of QDot-pDNA (10 μg DNA) complexed to GL67A (0.6 mM; in a total volume of 100 μl) on the apical surface. One hour post-transfection, the pDNA/lipid complex was removed by washing twice with freshly gassed Krebs-Henseleit buffer (at 37°C), replaced with a 500 μl of buffer ready for imaging with a water-immersion objective and scanned for QDot565 fluorescence. Again, and as in the HEK293T cell imaging described above, nuclei and cell surface membranes were stained by incubating the airway epithelial cells apically for 15 minutes with SYTO-16 (10 μM) and di-4-ANEPPDHQ (0.1 mM), respectively, prior to re-scanning with the SDCM.

The confocal micrographs shown in Figure 73 depict a 2-D projection of red pseudo-coloured QDot-pDNA images, merged with blue pseudo-coloured SYTO-16-stained nuclei and grey pseudo-coloured di-4-ANEPPDHQ-stained cell membrane images from a 134 *z*-stack series (top panel of Figure 73) and corresponding *x*-*z* projection (bottom panel of Figure 73). The micrographs show the distribution of QDot-pDNA in the transfected human ALI. Red QDot-pDNA fluorescence (arrowheads) and the cell membrane fluorescence (arrows), together with blue-stained nuclei in both the *x*-*y* and *x*-*z* views are clearly visible.

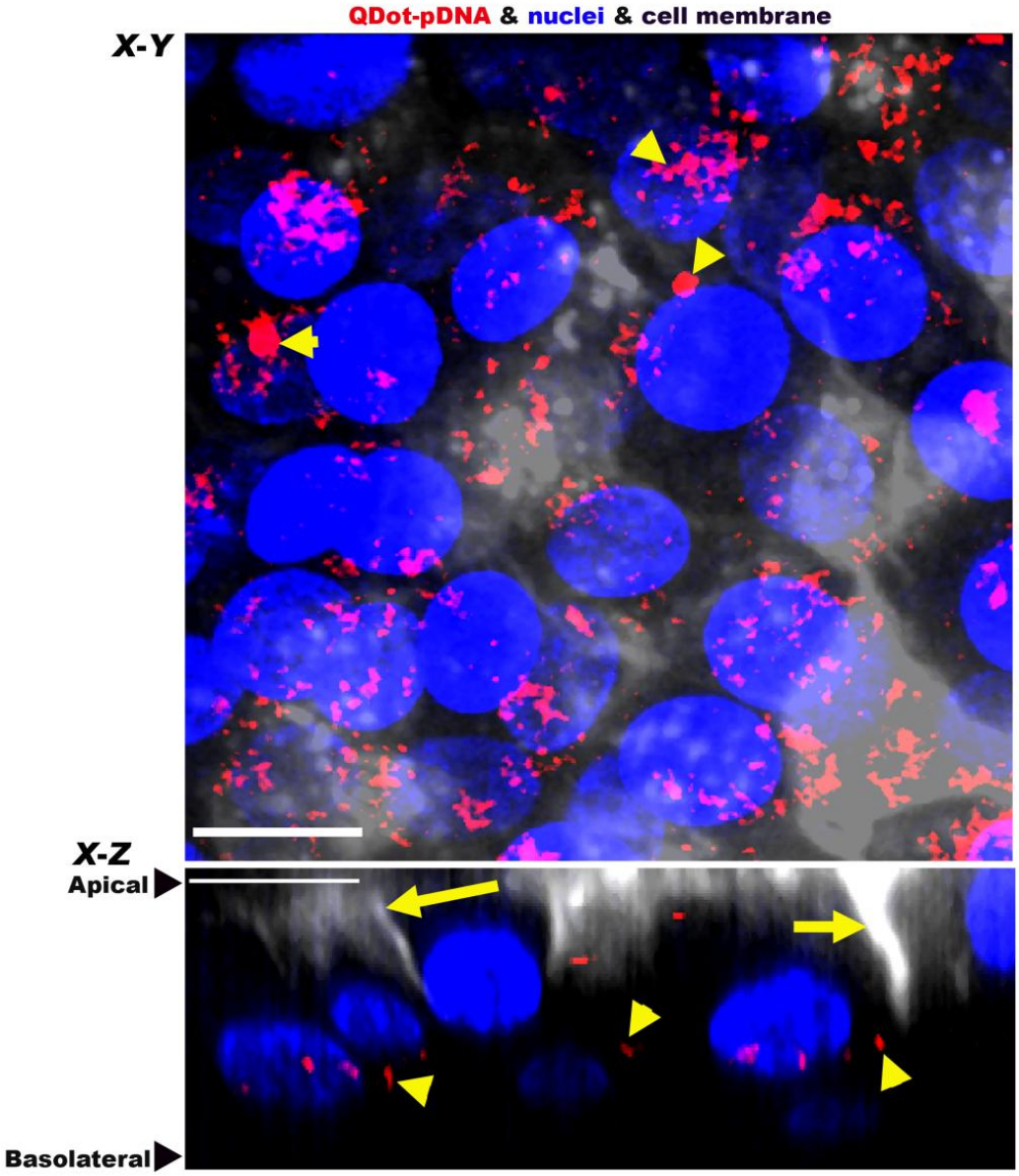

Figure 73: Subcellular localisation of quantum dot-conjugated plasmid DNA in living human airway epithelial cells following cationic lipid-mediated transfection
Cultures of fully differentiated human airway epithelial cells grown at the air-liquid-interface were transfected for 15 minutes with quantum dot (QDot) 565-conjugated pCIKFluc (10 µg DNA) using cationic lipid GL67A. One hour post-transfection, the airway epithelial cells (marked by beating cilia) were imaged using Spinning Disk Confocal Microscopy as described in Materials and Methods. Representative *x-y* (top panels) and *x-z* projections (bottom panels; with apical membrane at the top and basolateral membrane at the bottom) of 134 *z*-sections are shown. The micrographs are merged images of red pseudo-coloured QDot565-PNA-pCIKFluc (indicated by arrowheads), blue pseudo-coloured SYTO-16-stained nuclei and grey pseudo-coloured di-4-ANEPPDHQ-stained cell membranes (indicated by arrows). Scale bars = 10 µm.

The left-hand panels of Figure 74 show red pseudo-coloured QDot-pDNA *z*-sections (0.25 μm/ *z* -section; 2 μm intervals shown) through the airway epithelial cells, merged with corresponding blue pseudo-coloured nuclei (middle panels of Figure 74) showing the co-localisation of the QDot-pDNA with nuclei. The "honeycomb-like" structure is visible on the apical surface of the grey pseudo-coloured di-4-ANEPPDHQ-stained, QDot-pDNA and nuclei merged images down to a depth of ~ 12 μm (right-hand panels of Figure 74). As the cellular boundaries were discernable, I was able to detect apical surface-localised as well as cytoplasm-localised QDot565 fluorescence (arrowheads on top and bottom inserts). The lateral cell surface, deeper down into the epithelium (≥12 μm), was not stained, likely due to lack of penetration by the ANEPPDHQ dye. Thus, and as in the above cases for co-localisation of QDot- DNA with the insufficiently demarcated (cell surface membrane-di-4-ANEPPDHQ-stained) cells in both transfected HEK293T cell monolayers and pseudostratified mouse nasal epithelium, it was not possible to determine the number of cells containing cytoplasmic-localised QDot-pDNA fluorescence. Unambiguous co-localisation of QDot-pDNA and nuclei was however straightforward and I was able to distinguish between pDNA either outside, or inside, nuclei, between ~12 and 20 μm below the epithelial apical surface. To further visualise this sub-cellular distribution of QDot-pDNA in transfected airway epithelial cells and facilitate the counting of the number of QDot-pDNA-positive nuclei, I used Volocity imaging software to re-construct the serial sections in 3-D.

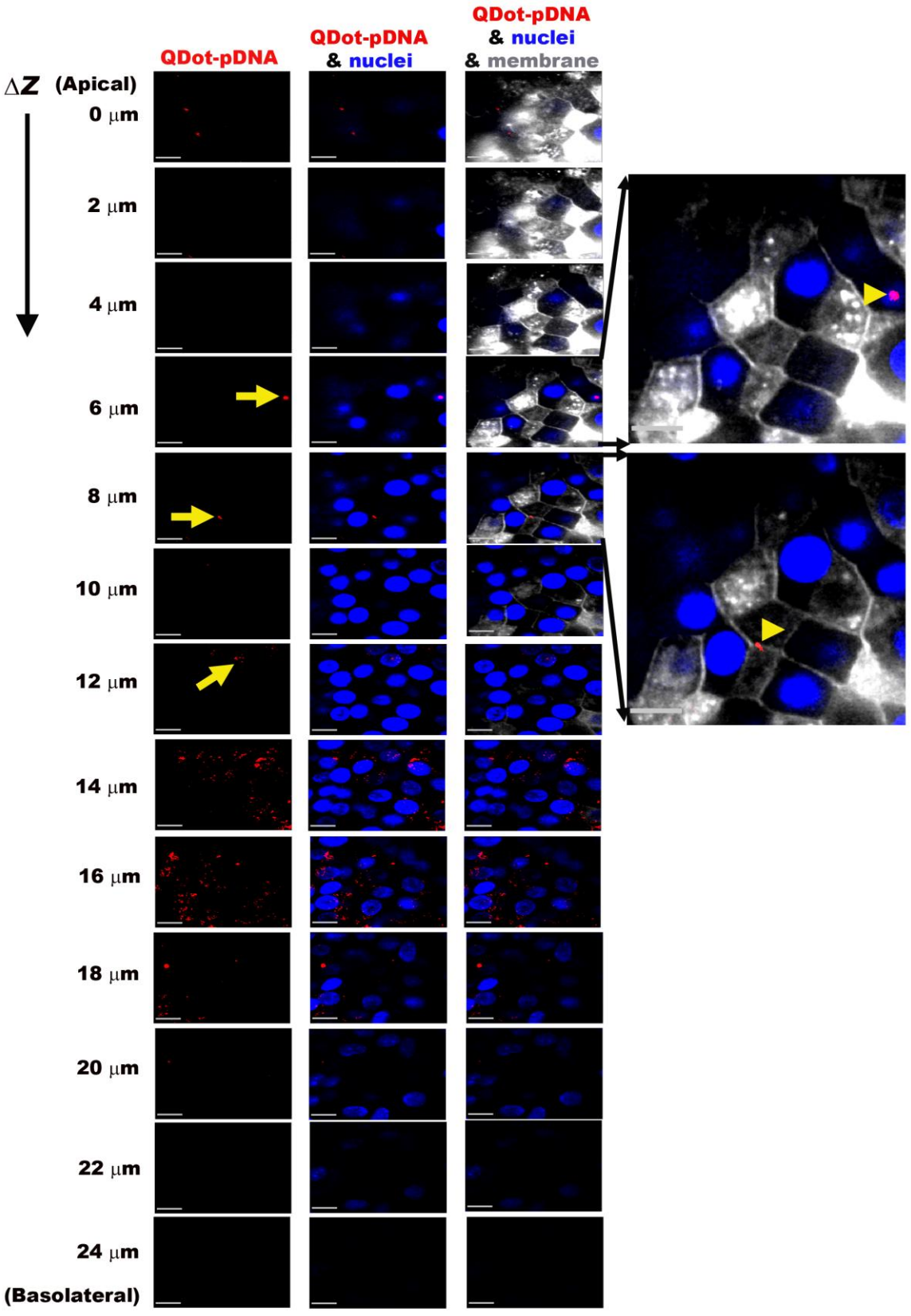
QDot-pDNA
QDot-pDNA & nuclei
QDot-pDNA & nuclei & membrane
ΔZ (Apical)
0 μm
2 μm
4 μm
6 μm
8 μm
10 μm
12 μm
14 μm
16 μm
18 μm
20 μm
22 μm
24 μm
(Basolateral)

Figure 74: Subcellular localisation of quantum dot-conjugated plasmid DNA in optical sections of living human airway epithelial cells following cationic lipid-mediated transfection

Confocal optical sections (0.25 μm thick) in 2.0 μm intervals through the human airway epithelial cells shown in Figure 73. Red pseudo-coloured quantum dot (QDot)565-PNA-pCIKFluc (left panels, indicated by arrows), merged with images of blue pseudo-coloured SYTO-16-stained nuclei (middle panels), and grey pseudo-coloured di-4-ANEPPDHQ-stained cell membranes (right panels). The insert on the far right-hand side is a magnified views of the QDot-pDNA (indicated by arrowheads) 12 μm below the apical surface. Scale bars = 10 μm.

Three dimensional reconstruction and rendering of the confocal image stacks shown in Figure 75 permitted the separate visualisation of the QDot-pDNA channel alone, QDot-pDNA/nuclear overlays, and QDot-pDNA/nuclear/cell membrane overlays. The QDot565 fluorescence shown in the top panel represents the total amount of pDNA detected whilst the QDot-pDNA masked by the nuclei (middle panel) represents nuclear-localised pDNA. QDot565 fluorescence masked by the cytoplasmic compartment demarcated by the grey pseudo-coloured di-4-ANEPPDHQ cell membrane stain (bottom panel of Figure 75) represents all QDot-pDNA either inside the airway epithelial cells or on the cell surface membranes. As mentioned above, this permitted better visualisation of QDot-pDNA against a clearer background of nuclei and limited cell membrane delineation, 3-D reconstruction of the transfected epithelium is the preliminary step in the quantitative assessment of co-localisation of QDot-pDNA and nuclei using Quantitation module of the Volocity imaging software.

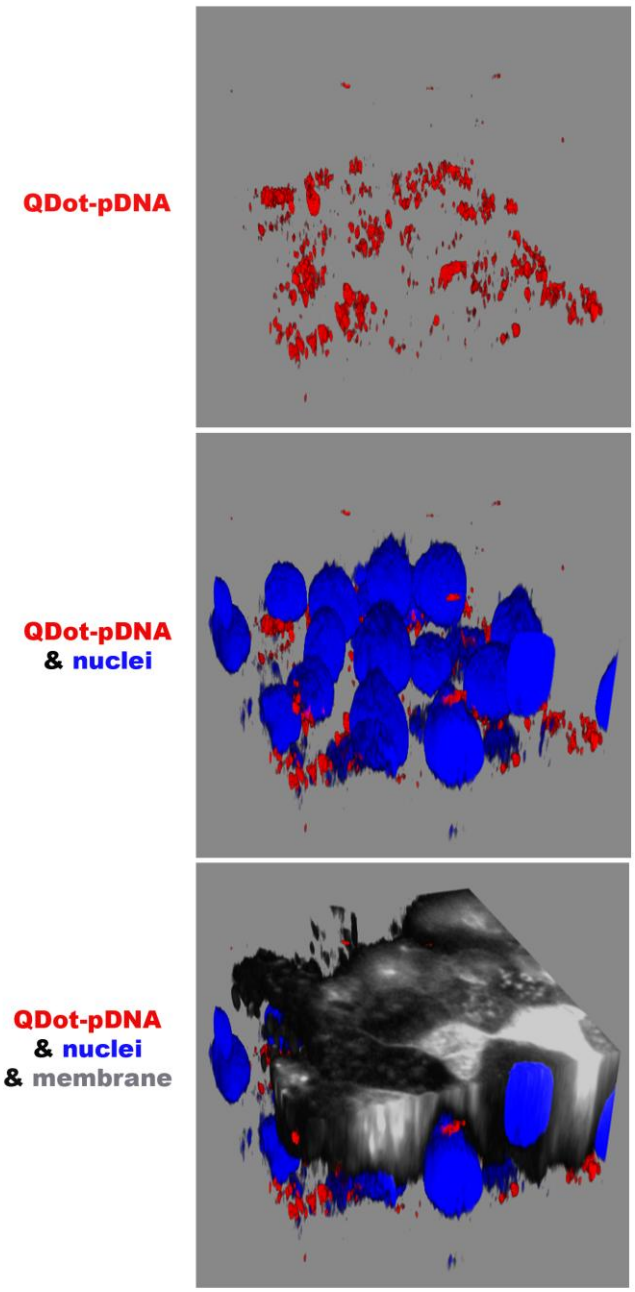

Figure 75: Three-dimensional visualization of the quantum dot-conjugated plasmid DNA inside human airway epithelial cells following cationic lipid-mediated transfection
A three-dimensional (3-D) volume rendering of the reconstructed quantum dot-conjugated plasmid DNA (QDot-pDNA)-transfected human airway epithelial cells, showing (A) QDot -pDNA (red), (B) merged QDot-pDNA and nuclei (blue), and merged QDot-pDNA, nuclei and cell surface membranes (grey).

Table 5 shows the quantitative evaluation of the accumulation of QDot-pDNA in nuclei of human epithelium 1 hour after transfection for 15 minutes represented in Figures 73, 74 and 75. The number of nuclei containing QDot565 fluorescent in the 3-D reconstructed epithelium was counted and the number of QDot-pDNA-positive nuclei expressed as a percentage (8±4 %; n=349 nuclei from 9 ALIs) of the total detected nuclei.

ALI*	Number of nuclei	Number of nuclei containing QDot565-conjugated plasmid DNA	Percent nuclei containing QDot565-conjugated plasmid DNA (%)
1	42	3	7
2	56	0	0
3	27	2	7
4	52	11	21
5	49	12	25
6	15	0	0
7	22	0	0
8	29	0	0
9	57	10	18
*Mean percent nuclei containing QDot-pDNA = 8 ± 4%; n=349 nuclei from independent experiments (9 ALIs)			

Table 5: Quantitative evaluation of the delivery of quantum dot-localised plasmid DNA to the nuclei of non-virally transfected living human airway epithelial cells
Three-dimensional (3-D) reconstructions and renderings of the confocal image *z*-stacks of red pseudo-coloured quantum dot (QDot)-565-conjugated plasmid DNA merged with blue pseudo-coloured SYTO-16-stained nuclei were used to segment the QDot565 fluorescence and nuclei in both 2-D and 3-D. Each number is from a single randomly selected field-of-view (84 μm x 55 μm x 30 μm) from the human airway epithelium shown in Figures 73,74,75 and represent: the total number of nuclei clearly delineated by the SYTO-16-stain; total number of nuclei containing QDot565 fluorescence (total number of QDot-pDNA-positive nuclei); QDot-pDNA-positive nuclei as a percentage of the total number of nuclei detected (% nuclei containing QDot565-PNA-pCIKFluc).

In summary, working with Drs Stephen Smith and Felix Munkonge, in our department, I used SDCM combined with a custom-built perfusion chamber to image the biodistribution of QDot-labelled pDNA in living non-viral transfected HEK293 cultured, mouse nasal and human airway epithelial cells. Whilst the counterstaining with cell surface membrane-di-4-ANEPPDHQ-stain to provide a cellular background for co-localisation was not successful, I was able effectively to stain human airway epithelial cell nuclei using the nucleic acid stain SYTO-16, which facilitated the co-localisation of the QDot-pDNA with blue pseudo-coloured nuclei. Using image analysis software, this permitted me to count the number of nuclei containing QDot-pDNA in 3-D reconstructions of the epithelium after non-viral transfection. Approximately 8% of the nuclei were QDot-pDNA-positive in the human airway epithelium 1 hour after transfection for 15 minutes.

The above experiments were undertaken during the process of constructing the perfusion chamber, evaluating the contrast surface membrane and nuclear vital stains, and establishing appropriate conditions and protocols for real-time confocal imaging of living airway epithelium. Having successfully used this resource to assess the nuclear delivery of QDot-pDNA in both mouse and human airway epithelium at an early time point, I next sought to follow and quantitate the dynamics of this nuclear delivery of QDot-pDNA in living human airway epithelial cells over a much longer time period. To do so, I applied the QDot-pDNA/Lipid GL-67 (in 500 μl Krebs-Henseleit buffer) complex onto the apical surface of the human airway epithelial cells grown at the ALI and continuously collected 130 *z*-series (0.25 μm/ *z* -section) for QDot565 fluorescence every 10 minutes up to a maximum of 120 min after addition of the complex. After 120 minutes, SYTO-16 (10 μM) was added, incubated for 15 minute, and scanned to image nuclei. Images were processed and QDot-pDNA/nuclei co-localisation was analysed using image analysis software (see Materials and Methods).

The confocal micrographs shown in Figure 76 each depict a maximum *x*-*y* intensity projected images of red pseudo-coloured QDot-pDNA and blue pseudo-coloured SYTO-16-stained nuclei post-acquisition merged images, generated by overlaying 130 *z*-sections. The projections demonstrate the distribution of QDot-pDNA in the living human airway epithelium transfected for 10, 30, 60, 90 and 120 minutes.

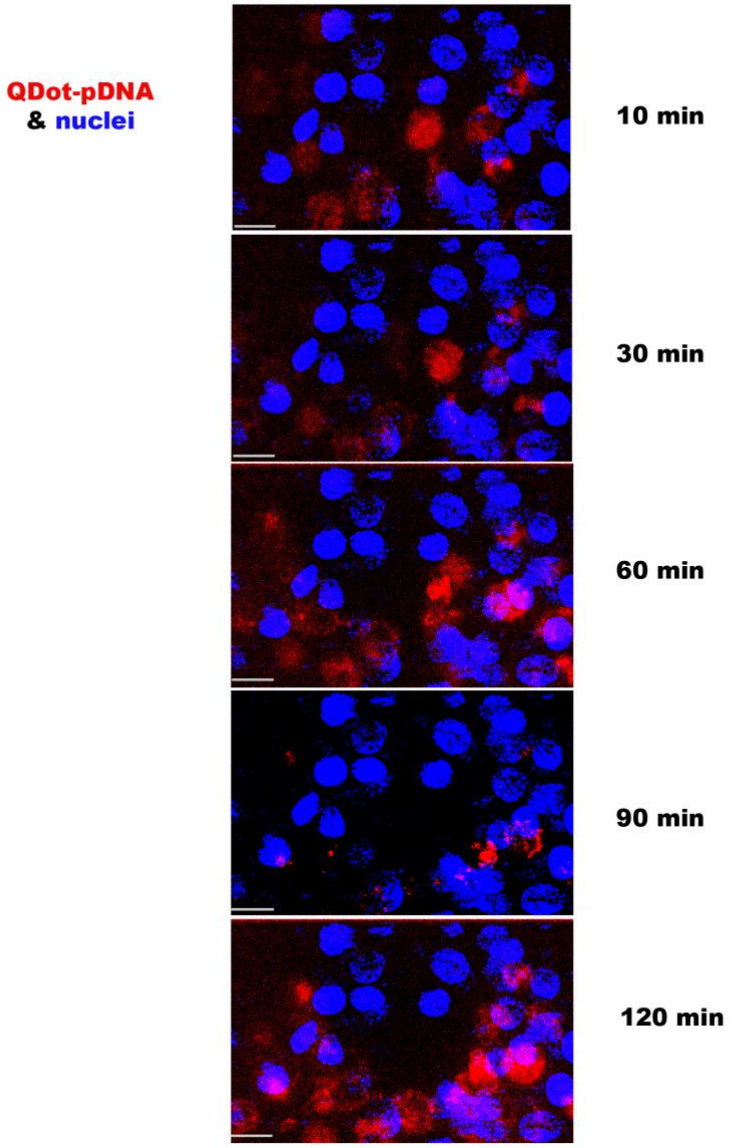

Figure 76: Confocal time-lapse imaging of subcellular localisation of quantum dot-conjugated plasmid DNA in living human airway epithelial cells following cationic lipid-mediated transfection

Cultures of fully differentiated human airway epithelial cells grown at the air-liquid-interface were transfected with quantum dot (QDot) 565-conjugated pCIKFluc (10 µg DNA) using cationic lipid GL67A and continuously imaged in real time using Spinning Disk Confocal Microscopy as described in Materials and Methods. Representative *x-y* projections of time-lapse series of 130 (0.25 µm thick) *z*-sections through the airway epithelial cells are shown. The micrographs are merged images of red pseudo-coloured QDot565-PNA-pCIKFluc, blue pseudo-coloured SYTO-16-stained nuclei. Representative of images from 7 independent experiments. All Scale bars = 10 µm.

Figure 77 shows a representative *z*-section series (0.25 μm/ *z* -section; 2.5 μm intervals shown) through the epithelium consisting of QDot-pDNA images merged with corresponding nuclei images here shown every 30 minutes (after the first ten minutes) for clarity. Although punctate QDot565 fluorescence can be seen on the top (marked by beating cilia in a respective brightfield image; data not shown) of the apical surface of the epithelium throughout the whole 120-minute transfection period (asterisk), a time-dependent net movement of the QDot-pDNA downwards through the epithelium is visible. Further clarifying and confirming the distribution pattern observed in the previous *x*,*y* and *x*,*z* projections, significant extra-nuclear (arrows) and "nuclear-associated" (arrowheads) QDot565 fluorescence was visible 10 μm below the apical surface. In order to analyse this time-dependent co-localisation of QDot-pDNA with the nuclei further, I next employed Volocity software first to visualise and then to quantitate, in 3-D, the co-localisation of QDot-pDNA with blue-stained nuclei during transfection over a period of 120 minutes.

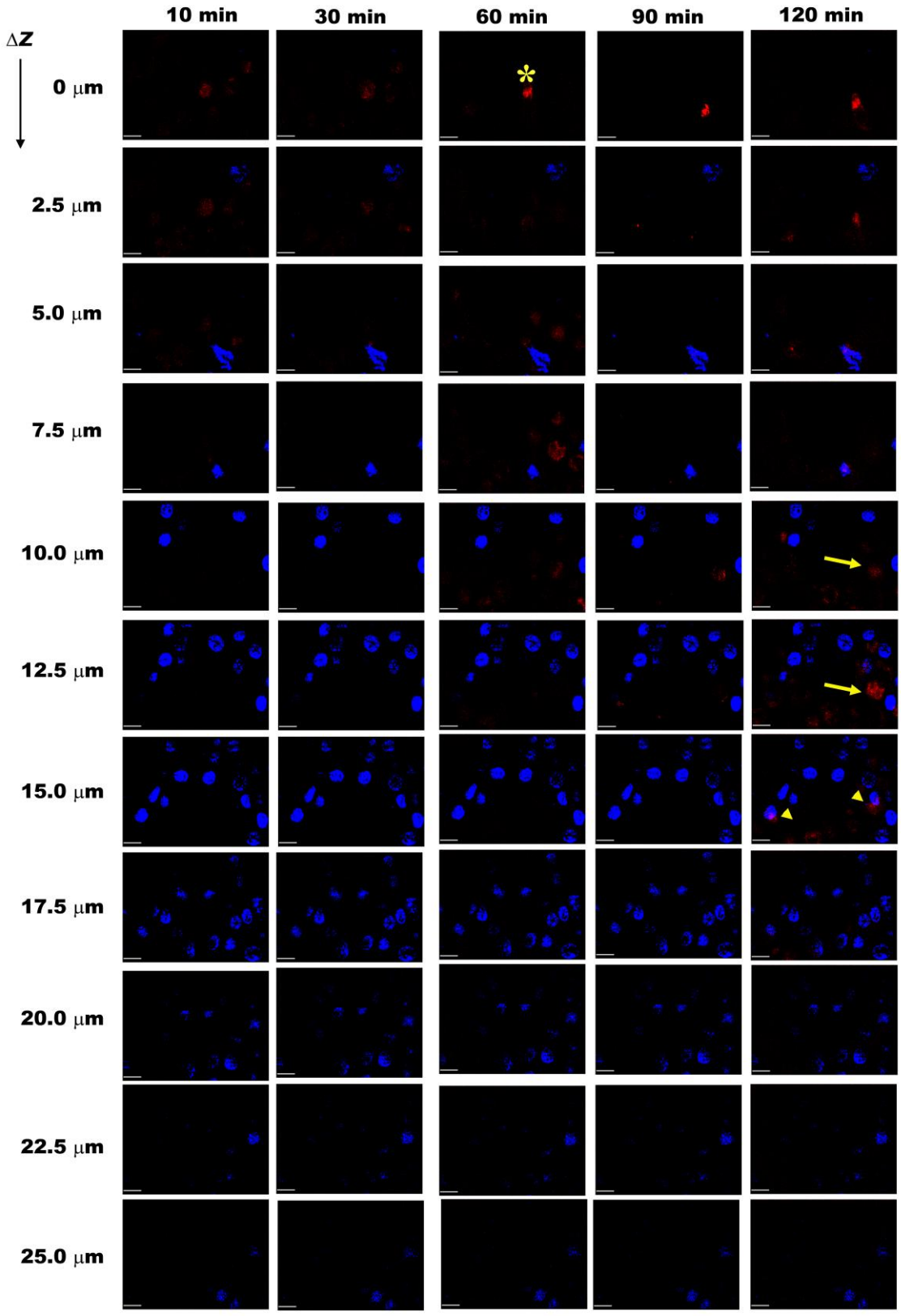
10 min
30 min
60 min
90 min
120 min
ΔZ
0 μm
2.5 μm
5.0 μm
7.5 μm
10.0 μm
12.5 μm
15.0 μm
17.5 μm
20.0 μm
22.5 μm
25.0 μm

Figure 77: Confocal time-lapse imaging of subcellular localisation of quantum dot-conjugated plasmid DNA in optical sections of living human airway epithelial cells following cationic lipid-mediated transfection

Cultures of fully differentiated human airway epithelial cells grown at the air-liquid-interface were transfected with QDot565-conjugated pCIKFluc (10 µg DNA) using cationic lipid GL67A and continuously imaged in real time using Spinning Disk Confocal Microscopy as described in Materials and Methods. Images representing time-lapse series of confocal optical *z*-sections (0.25 µm thick) in 2.5 µm intervals through the epithelium. Merged red pseudo-coloured QDot565-PNA-pCIKFluc (extra-nuclear and nuclear-associated indicated by arrows and arrowheads respectively) and blue pseudo-coloured SYTO-16-stained nuclei are shown. Punctuate red QDot565-PNA-pCIKFluc fluorescence on the top of the apical surface indicated by asterisk. Representative of images from 7 independent experiments. All Scale bars = 10 µm.

Figure 78 shows the distribution of QDot-pDNA in the living human airway epithelium during the continuous 120 minute transfection period. The number of nuclei containing QDot565 fluorescent in the 3-D reconstructed epithelium was counted and the number of QDot-pDNA-positive nuclei expressed as a percentage of the total detected nuclei at 30 minute time intervals. The data indicate an increase in the number of nuclei containing QDot-pDNA as early as 30 minutes during the transfection period reaching maximum levels of 8.2±4.8% (n=256 nuclei from 7 ALIs).

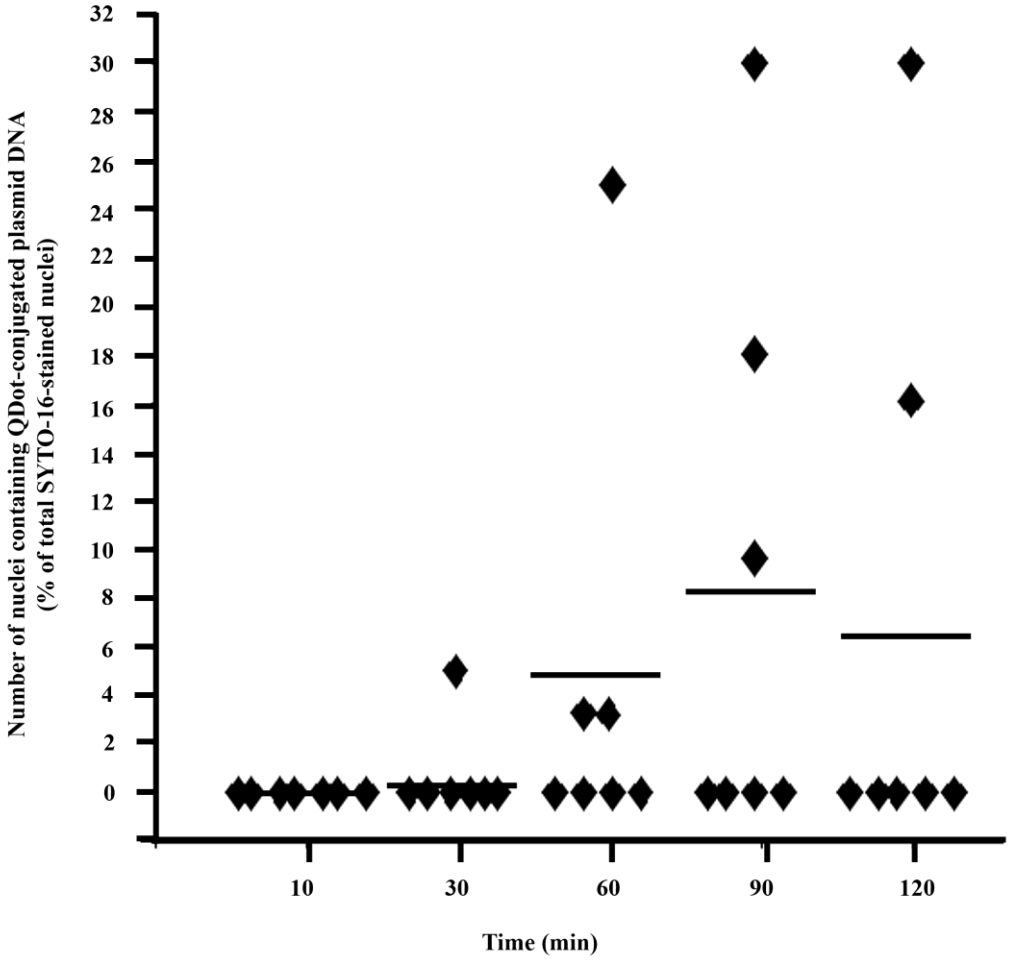

Figure 78: Quantitative evaluation of the delivery of quantum dot-localised plasmid DNA to the nuclei of living human airway epithelial cells during non-viral transfection
Three-dimensional reconstructions and renderings of the confocal image *z*-stacks of red pseudo-coloured quantum dot (QDot)565-conjugated plasmid DNA merged with blue pseudo-coloured SYTO-16-stained nuclei were used to segment the QDot565 fluorescence and nuclei in both 2-D and 3-D to permit co-localisation of QDot-pDNA and nuclei in a single randomly selected field-of-view (84 μm x 55 μm x 33 μm) from the human airway epithelium shown in Figures 76 and 77. Each number represents the QDot-pDNA-positive nuclei as a percentage of the total number of nuclei detected (% nuclei containing QDot565 -PNA-pCIKFluc). The bars indicate mean percent QDot-pDNA-positive nuclei. Representative of 7 independent experiments.

6.4 Discussion

In parallel to the TEM study which described the intracellular spatial distribution of gold-labelled plasmid DNA (nanogold-conjugated pDNA) in fixed human airway epithelial cells at the single-molecule resolution described in the previous chapter, I used a confocal-based study to monitor the intracellular progress of the pDNA in transfected living human airway epithelial cells, using an identical clinically relevant human model system (the human ALI) and materials. Plasmid DNA is not fluorescent so a prerequisite to its intracellular tracking is the need to label it with a suitable marker fluorochrome. I therefore tagged the pCIKFluc, a CMV promoter-driven plasmid encoding the Fluc reporter protein, with bright photostable semiconductor nanocrystal QDots. This was done using essentially the same strategy used to sequence-specifically conjugate nanogold at a 1:1 stoichiometry for the TEM study described in Chapters 4 and 5. The binding efficiency of the QDot conjugated to the PNA linker molecule (QDot-PNA) was assessed by spectrophotometry after stringent washing and purification to remove residue unbound QDot-PNA and unlabelled pDNA. Strong absorbance of the pDNA and QDot was seen at 260 nm and 405 nm, respectively. Using their respective extinction coefficients, I was able to determine the amounts present and the subsequent 1:1 stoichiometry of binding.

I next sought to demonstrate the above conjugation of pDNA with QDot using agarose gel electrophoresis to compare mobilities of covalently conjugated QDot-pDNA with control physical mixtures of the two separate components. As for the agarose gel electrophoretic analysis of nanogold-pDNA conjugation, there was no significant shift in the mobility of the QDot-conjugated pDNA compared to the unconjugated pDNA (Figure 79). This is perhaps

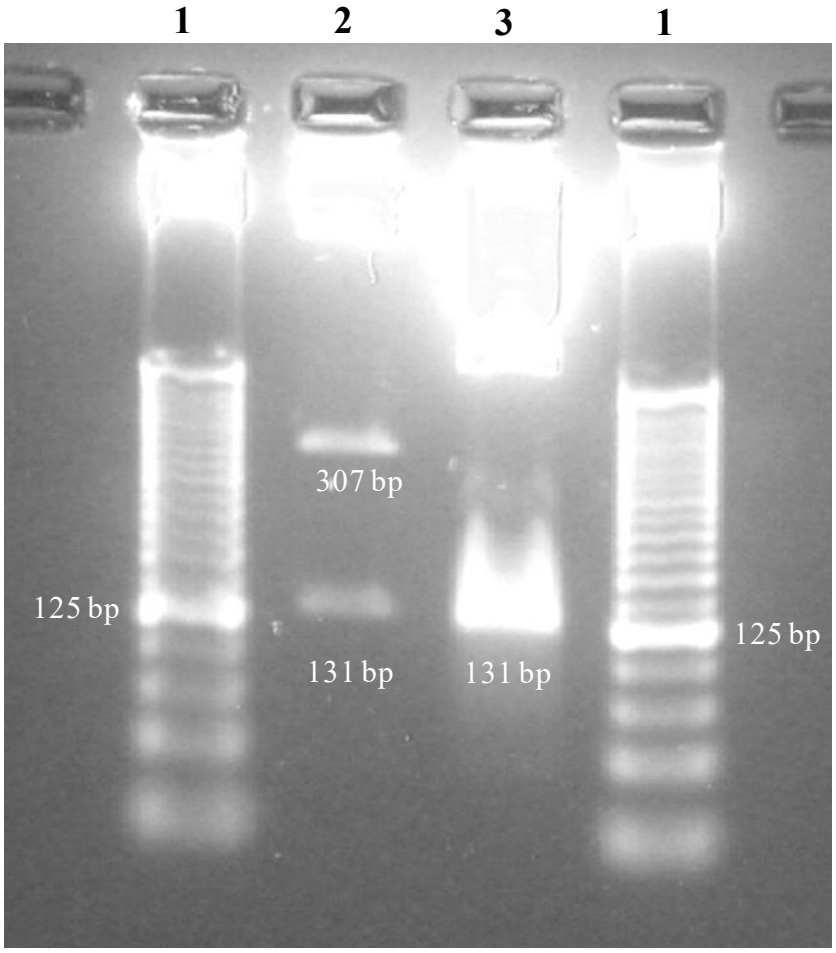

Figure 79: Agarose gel electrophoresis of restriction fragments of QDot-conjugated plasmid DNA and unconjugated plasmid DNA
Restriction fragments of QDot-conjugated pDNA and unconjugated pDNA were generated by treating QDot-conjugated pDNA and unconjugated pDNA with restriction enzymes namely endonucleases BssSI and BseYI. After digestion restriction fragments were run on a 3 % agarose gel for 90 minutes. Agarose gel was stained with Gel Red (10000x) for DNA detection. Lane 1: Ladder 25-500 bp, Lane 2: Restriction fragments of unconjugated conjugated pDNA and Lane 3: Restriction fragments of QDot-conjugated pDNA. Representative of three independent experiments.

not surprising considering the size of the QDot in relation to the pDNA. Despite numerous efforts I was unable to find a convenient alternative means of resolving any size differences between conjugated and unconjugated pDNA. A further difficulty with the gel analysis was that it was not possible to co-localise the Gel Red-based pDNA bands with their corresponding QDot bands. The very bright endogenous QDot emission masked the pDNA bands and extensive efforts to attenuate or find alternative gel-based QDot stains (readouts) were unsuccessful. Thus, despite the fact that any QDots present after the above mentioned rigorous purification and washing could only be attributed to that bound to the pDNA, I was not able directly to confirm the covalent linkage of the QDots to the pDNA.

After the labelling of the pDNA with the fluorescent QDot to facilitate confocal microscopy, I first needed to find out what effect this conjugation had on the biological activity of pDNA. To this end, the reporter gene activity of pDNA tagged with QDot-PNA conjugates was compared with that of unconjugated pDNA. It is clear that QDot-conjugated pDNA retained its activity following the conjugation with the fluorescent QDots. Having prepared and validated the QDot-conjugated pDNA I next evaluated its visualisation using SDCM in living HEK293T cell monolayers, mouse nasal epithelium and our ultimate experimental model ALI human airway epithelium. I helped evaluate a number of potential vital (compatible with live-cell imaging) fluorescent dyes suitable for counter-staining cellular surface membranes and nuclei to permit respective co-localisation of the QDot-conjugated pDNA following transfection. I demonstrated excellent nuclear-staining of both HEK293 and human airway epithelial cells with the nucleic acid stain SYTO-16 although nuclear staining in the mouse nasal epithelium was less distinct. The cell surface membrane dyes, including the best performing di-4-ANEPPDHQ, did not completely penetrate HEK293 cells, mouse nasal and human epithelium making clear delineation of cellular boundaries difficult. Thus, although

our ultimate goal of quantitating nuclear delivery of QDot-conjugated pDNA in transfected human ALI was realised, I was not able to visualise and quantitate levels of cell surface- and cytoplasmic-localised QDot-conjugated pDNA. Using the capability of the SDCM to provide confocal optical dissection, I was able to visualise the biodistribution of QDot-conjugated pDNA in transfected HEK293 cells, mouse nasal and human airway epithelium. Further, analysis, and 3-D reconstruction of, *z*-sections from human airway epithelia imaged 1 hour after a 15 minute transfection showed QDot-conjugated pDNA either outside, or inside, nuclei between ~12 and 20 μm below the epithelial apical surface with approximately 8% of total number of cells positive for QDot fluorescence.

Further development of our custom-built chamber to permit long-term separate perfusion of the epithelial apical and basolateral compartments on the SDCM permitted me to follow the progress of QDot-conjugated pDNA in living transfected human airway epithelium for extended time-points up to 120 minutes. As expected, there was a net movement of QDot-conjugated pDNA into the epithelium over the time period with nuclear-localised QDot fluorescence clearly visible at transfection times as early as 30 minutes. The number of nuclei containing QDot-conjugated pDNA reached a maximum of approximately 8% after 90 minutes of transfection. In the analysis of the data from experiments following the progress of fluorescent-labelled pDNA in transfected epithelium cells above, I have quantitated the fraction of nuclei containing QDot-conjugated pDNA over a given time during the transfection. Although no significant increase in the number of nuclei containing QDot-labelled pDNA following non-viral transfection for 0, 10, 30, 60, 90 and 120 minutes, a trend suggesting increased nuclear delivery of pDNA was observed, tentatively supporting our original hypothesis.

The next logical step in the analysis was to record the mobility of QDot- conjugated pDNA. The question then arises of how much pDNA is represented in each punctum of QDot fluorescence as observed in the confocal images. Of course each individual pDNA molecule is hybridised to a single QDot-pDNA conjugate molecule and should thus permit the study of single-pDNA intracellular detection, in theory. As mentioned previously, a single 5 nm QDot is too small to be resolved by SDCM (resolution about ~250 nm). Other optical systems such as multi-photon configurations [285] and the newer super-resolution microscopy techniques [286] are able to image beyond the diffraction limit (half the wavelength of the light employed) but are not suitable for this dynamic imaging of the relatively thick airway epithelium. In an effort to extract information on how the observed QDot fluorescence relates to the amount of labelled pDNA one needs to consider the QDot-conjugated pDNA's point-spread-function (PSF). The PSF describes fluorescence distribution that results from a single point source, such as the single QDot on a single pDNA in our case [287]. Although the source may be a point, the image visualised in our images is not. The two main reasons for this are: a) aberrations in the optical system will spread the image over a finite area, and b) diffraction effects will also spread the image, even in an ideal system with no aberrations. Thus, it is possible to derive the PSF from the emission of QDot-pDNA aggregates in order to compute the centre of the diffraction-limited fluorescence emanating from a single QDot by performing least-squares Gaussian fits. This information can then be used for the subsequent tracking of the QDot-conjugated pDNA in live-cell time-lapse sequences shown in Figure 77. Unfortunately, I did not have access to the very expensive software (Classification Module of Volocity) to permit me to extend the analysis in this way.

Chapter 7: General conclusion and future work

Non-viral gene therapy is a promising treatment for CF and is currently being actively pursued by the UKCFGTC, comprising the three leading CF gene therapy groups in the UK based at Edinburgh and Oxford Universities, and at Imperial College London. Despite the partial correction of the basic defect, without major safety issues, shown in the airways of CF subjects, gene transfer to the CF lung is still sub-optimal and likely needs further improvement. At the cellular level, a key limiting factor to successful delivery of therapeutic pDNA to the nuclei of the terminally differentiated ciliated human airway epithelial cell, for transcription in this target cell for CF gene therapy, includes a number of intracellular barriers. To provide insight into the intracellular bottlenecks pDNA encounters on its way to the nucleus of the transfected non-dividing target airway epithelial cells, and as part of laboratory-based experiments supporting the Consortium's clinical programme, I sought to visualise and quantitatively describe the intracellular fate of non-virally transferred pDNA using a clinically relevant human airway epithelial model system and materials.

Throughout the whole study, for the purposes pDNA quality control and future functional gene expression correlation studies, I used pCIKFluc, a CMV promoter-driven plasmid encoding the Fluc reporter protein, as a convenient surrogate for pGM169, the CFTR protein-encoding therapeutic plasmid developed and being used for CF gene therapy.

To visualise and quantitate reporter pDNA on sections with well-preserved ultra-structure from non-virally transfected human airway epithelial cells, using high-resolution TEM, I conjugated the pDNA to electron-dense nanogold particle tags. In a parallel study, I also followed the progress of the pDNA, conjugated to fluorescent QDots, in living transfected

human airway epithelial cell using SDCM. Both the nanogold particle and the QDot tags were conjugated to the reporter plasmid in a sequence-specific manner, via thiol-terminated PNA, using an identical strategy. I have previously successfully labelled pDNA with conventional organic fluorochrome. Great care was taken to remove residual unbound nanogold particles, PNA or QDots from the final nanogold- or QDot-pDNA using stringent washing and filtration steps leading one to conclude that all nanogold particles or QDots, detected spectrophometrically and visualised by microscopy, were covalently linked and that the two tags are *bona fide* reporters of the pDNA. Gel-based approaches to confirm the labelling density of nanogold particles or fluorescent QDots here was not successful for technical reasons. Nanogold- and QDot particles are much smaller (~1.4 nm and ~5 nm, respectively) than the pDNA (typically ~200 nm when fully condensed with cationic lipid GL67A) so size is unlikely to be a factor in tag-pDNA interactions confirmed by the retention of reporter gene activity of the nanogold- or QDot-conjugated pDNAs compared with their respective unconjugated control pDNA.

I next worked up a methodology for the visualisation of intracellular-localised nanogold-pDNA probe within transfected airway epithelial cells using TEM. For these pilot experiments, I first used cultured HEK293T cell monolayers and, more importantly, mouse nasal tissue, a readily available surrogate for lung transfection in the context of CF gene transfer, to optimise the conventional chemical fixation technique in order to obtain the best preservation of intracellular ultra-structure. I evaluated a number of cytoskeleton-interacting compounds for the preservation of ultra-structure and found that fixation of tissue in glutaraldehyde in PBS at 37˚C provides the optimal preservation of key intracellular structures. I found that despite a well-preserved cellular background, the very small 1.4 nm nanogold particle tags conjugated to pDNA were not sufficiently electron-dense enough to be

visualised by TEM. The nanogold tags were thus made TEM-opaque by amplification with gold-enhancement to reveal distinct dark spots on the well-preserved ultrastructure. The randomly dispersed background black spots in cells transfected with control unconjugated pDNA are likely due to auto-nucleation following gold-enhancement, a common phenomenon in TEM autometallography. Crucially, and in contrast to other reported studies, I have presented representative micrographs showing background dark spots on sections from airway epithelial cells contemporaneously transfected with control unconjugated pDNA. Furthermore, all levels of nanogold-pDNA shown in this study show background-subtracted (i.e. levels of dark spots on sections from control unconjugated pDNA-transfected airway epithelial cells) levels of dark spots seen on sections from nanogold-conjugated pDNA-transfected airway epithelial cells. I cannot, however, exclude the possibility that the intracellular-localised positive dark spots observed might represent nanogold particles detached from the pDNA during uptake or cell transit, and which do not stay covalently linked to the pDNA. For the future therefore, it may be useful to confirm that the dark spots, representing nanogold particles covalently tagged to pDNA, co-localise with the pDNA by *in situ* hybridisation, using suitable specific gold-tagged probes. The use of gold-enhancement to amplify the electron-density of the 1.4 nm nanogold particle for TEM introduces additional handling steps to the already complicated TEM processing. For future work, I have made initial attempts, in collaboration with the manufacturer (Nanoprobes), aimed at evaluating TEM-opaque, 10 nm mono-maleimide-terminated nanogold particles for use as tags for pDNA. Conjugation with these larger particle would obviate the need for the use of the gold-enhancement step.

Once I could visualise the nanogold-labelled pDNA probes against well-preserved ultra-structure, I next translated the protocol for use in my ultimate objective i.e. the visualisation

of nanogold-conjugated pDNA in human airway epithelial cells grown at an ALI, a tractable clinically-relevant experimental model of the conducting human airway epithelium. Interestingly, I found that following the transfection of airway epithelial cells with nanogold-conjugated pDNA complexed with GL67A cationic lipid as early as 15 minutes, I could visualise nanogold-conjugated pDNA in the nuclear compartment, as well as the cytoplasm, cilia and on the cell surface membranes. The levels of nanogold-conjugated pDNA seen in the cytoplasm rose on further increasing the transfection time from 15 to 60 and 360 minutes. In addition, I also found nanogold-conjugated pDNA in the nucleus of ~7-8 % of the cells transfected over these extended time-points (Figure 62). I therefore concluded that pDNA was delivered to the nucleus as early as 15 minutes of transfection. Increasing the contact time to 60 minutes between the pDNA/lipid complex and the apical surface increased pDNA uptake into the nucleus. There was, however, no further increase in nuclear delivery to the nucleus after the much longer transfection time of 360 minutes.

Interestingly, it has been previously suggested that transfecting 5-10% cells with pDNA is likely to be of clinical benefit for CF patients (288-290). To the best of our knowledge, this is the first time this observation has been made in a clinically relevant model of the human conducting airway epithelium, the target site for CF gene therapy. Whilst appreciating the significance of this finding, it is worth bearing in mind potential limitations of our TEM study. The most important amongst these is that the ultra-thin sections showing nanogold-conjugated pDNA co-localised with intracellular compartments (i.e. cytoplasm or nuclear) visualised in our 2-D images may not give an accurate view of its localisation in depth. Future work to overcome this limitation will involve the taking of serial sections which can then be used to generate 3-D image volumes. The imaging of large volumes of tissue with serial section TEM relies on the acquisition of large sets of aligned micrographs. The

experiments are technically challenging and were beyond the scope of the present study. A further improvement to our TEM strategy would be to confirm co-localisation of nanogold-conjugated pDNA with intracellular entities such as cytoskeletal elements, endocytic vesicles etc, by unambiguously identifying the structures with specific gold-labelled antibodies using immunogold TEM.

A further limitation inherent to the TEM technique is that sample preparation involves fixing of the tissue and therefore, for our study, precludes the study of pDNA intracellular transport during transfection in real-time, in living airway epithelial cells. To circumvent this technical limitation and reveal detailed dynamic progress of pDNA in living airway epithelial cells without prior fixation of the sample, I have used SDCM to quantitatively describe the distribution of pDNA in real time following non-viral gene transfection in human airway epithelial cell model.

As noted above, for the confocal studies, I tagged pDNA with fluorescent QDot particles sequence-specifically, in a similar fashion to the labelling of pDNA with electron-dense gold particles used in our TEM study. The bright fluorescent QDot565 nanoparticles were chosen for their high photostability and non-toxicity which permits long-term real-time imaging with reduced overlap from background autofluorescence. As a first step in visualising the QDot-tagged pDNA in transfected cells, I initially transfected HEK293T immortalised cultured cells using standard commercially-available cationic lipid and used SDCM together with imaging software to visualise the post-transfection intracellular distribution of QDot-labelled pDNA. Because I needed to image the cellular uptake and nuclear delivery of pDNA, high contrast fluorescent staining of the outer cell membrane as well as the nucleus was an absolute requirement. Motivated by this need, I initially evaluated a number of commercially

available fluorescent vital cytoplasm, cell surface membrane stains, compatible with live-cell fluorescent imaging. The main criteria of suitability in our search for ideal cell and nuclear staining vital dyes were brightness and permeability. I found the lipophilic membrane-staining dye di-4-ANEPPDHQ to be the optional stain of cell boundaries for our purposes. Di-4-ANEPPDHQ exhibits very low internalisation and good signal-to-noise ratio and clearly stained the HEK293T cell membranes. For nuclear staining, the cell-permeant SYTO-16 fluorescent nucleic acid stain, which exhibits bright fluorescence upon binding to nucleic acids, was optimal compared to several commercially alternatives tested. QDot fluorescence, co-localised with fluorescent SYTO-16-stained nuclei in di-4-ANEPPDHQ-stained delineated cells, was clearly visible in confocal micrographs as well as 3-D reconstructions of transfected cell monolayers, confirming the TEM results.

In order to facilitate the SDCM imaging of non-virally transfected polarised ciliated airway epithelial cells, we next constructed a perfusion chamber with separately perfused apical and basolateral compartments. To evaluate the utility of this dual-chamber for use in the introduction of QDot-conjugated pDNA/lipid complex on the apical surface and subsequent visualisation, in real-time, of the QDot-conjugated pDNA during prolonged transfection times, I carried out preliminary experiments using transfected mouse nasal tissue. QDot fluorescence was clearly visible in living mouse nasal tissue imaged 1 hour after transfection for 15 minutes, again confirming the TEM results. Finally, to address the primary goal of imaging the progress of pDNA in living transfected fully differentiated human airway epithelial cells, I transfected human airway epithelial cells with QDot-conjugated pDNA and imaged QDot565 fluorescence in SYTO-16 nuclear-stained in cell surface membrane di-4-ANEPPDHQ-stain delineated cells. The image series had sufficient contrast and resolution clearly to identify QDot-conjugated pDNA in epithelia (~12 μm below the apical surface)

after transfection for only 15 minutes, consistent with the earlier observations. Using the capability offered by imaging analysis tools for 3-D reconstruction and rendering of confocal image stacks generated from living epithelia I was able to pinpoint the positions of QDot-conjugated pDNA within the x-, *y*- and *z*-planes, allowing quantitative evaluation of the accumulation of QDot-DNA in the nuclei of transfected cells.

In order to further follow nuclear delivery of pDNA in living human airway epithelial cells over a prolonged transfection, I applied QDot-conjugated pDNA/lipid complex onto the apical surface and continuously collected QDot565 fluorescence confocal *z*-stacks every 10 minutes up to a maximum of 120 min after addition of the complex. Ten minutes following the introduction of QDot-conjugated pDNA/lipid complex, the pDNA was observed on top of the epithelial surface. As expected, some surface QDot-conjugated pDNA remained on the epithelial apical surface throughout the overall 120 min transfection period. Importantly though, by 60 min, there was a time-dependent net movement of the QDot565 fluorescence downwards through the epithelium. The close association of a portion of the QDot565 fluorescence with nuclei raised the question whether the QDot-pDNA enters the nuclei, its ultimate destination for gene expression. To address this question, I used imaging analysis software accurately to identify and quantitate the number of cell nuclei containing QDot-plasmid through time. Strikingly the percentage of nuclei positive for QDot-conjugated pDNA found in cells transfected for between 30 to 60 minutes was in good agreement with the number of nanogold-conjugated pDNA seen in TEM study following transfection for 15 and 60 minutes. To the best of my knowledge, this is the first demonstration of the progress of pDNA in living human airway epithelial cells, the target cells for CF gene therapy, at these early time points.

Unfortunately, I could not track the progress of QDot-conjugated pDNA in living ALI because of technical issues to keep these ALI alive after 120 minutes transfection. However, for future work it may be worthwhile to improve the perfusion chamber in order to keep the ALIs alive for longer time points, thus allowing the tracking of QDot-conjugated pDNA for extended transfection times. Since SDCM study allowed the quantification of QDot-conjugated pDNA inside or outside the nuclei because of less penetration of the cell surface membrane dye (used here), it is also worthwhile to look in future for compatible dyes which can penetrates the cells deeply enough laterally thus, allowing the compartmentation of cells from each other. This will allow confirmation of the percentage of cells containing internalised QDot-conjugated pDNA in the cytoplasm as well as in the nucleus, similar to TEM study. Thus, I confirmed the quantitative intracellular localisation of pDNA following transfection; the next exciting step would be to study the trafficking events exploited by pDNA to reach the nucleus using specific immunolabelling of various intracellular structures like actin, microtubules, various endocytic vesicles etc. The different fluorescent emission of QDots can be tuned to their size, thus allowing the simultaneous association of QDot-conjugated pDNA with different intracellular structures in living airway epithelial cells, and thereby continuously following transfection over time.

In conclusion, the above spatial and temporal description of the progress of pDNA in clinically relevant model of the human airway epithelia, the target site for CF gene therapy, should provide a useful resource to help guide the development and application of gene transfer materials and agents. The description presented herein provides some insight into the progress of the pDNA to the nucleus. For instance, both the TEM and confocal studies demonstrate that contact time (between the pDNA-lipid complex and the apical surface) is not limiting for effective nuclear delivery. Therefore, strategies aimed at increasing the

delivery of pDNA for clinical benefit would perhaps be better focussed on means of overcoming cytoplasmic and nuclear barriers.

References

(1) Collins FS. Cystic fibrosis: molecular biology and therapeutic implications. *Science* 1992 May 8;256(5058):774-9.

(2) O'Sullivan BP, Freedman SD. Cystic fibrosis. *Lancet* 2009 May 30;373(9678):1891-904.

(3) Tsui LC, Buchwald M, Barker D, Braman JC, Knowlton R, Schumm JW, et al. Cystic fibrosis locus defined by a genetically linked polymorphic DNA marker. *Science* 1985 Nov 29;230(4729):1054-7.

(4) Kerem B, Rommens JM, Buchanan JA, Markiewicz D, Cox TK, Chakravarti A, et al. Identification of the cystic fibrosis gene: genetic analysis. *Science* 1989 Sep 8;245(4922):1073-80.

(5) Riordan JR, Rommens JM, Kerem B, Alon N, Rozmahel R, Grzelczak Z, et al. Identification of the cystic fibrosis gene: cloning and characterization of complementary DNA. *Science* 1989 Sep 8;245(4922):1066-73.

(6) Davies JC, Alton EW, Bush A. Cystic fibrosis. *BMJ* 2007 Dec 15;335(7632):1255-9.

(7) Matsui H, Grubb BR, Tarran R, Randell SH, Gatzy JT, Davis CW, et al. Evidence for periciliary liquid layer depletion, not abnormal ion composition, in the pathogenesis of cystic fibrosis airways disease. *Cell* 1998 Dec 23;95(7):1005-15.

(8) Boucher RC. Molecular insights into the physiology of the 'thin film' of airway surface liquid. *J Physiol* 1999 May 1;516 (Pt 3):631-8.

(9) Davis PB. Cystic fibrosis since 1938. *Am J Respir Crit Care Med* 2006 Mar 1;173(5):475-82.

(10) Frerichs C, Smyth A. Treatment strategies for cystic fibrosis: what's in the pipeline? *Expert Opin Pharmacother* 2009 May;10(7):1191-202.

(11) White R, Woodward S, Leppert M, O'Connell P, Hoff M, Herbst J, et al. A closely linked genetic marker for cystic fibrosis. *Nature* 1985 Nov 28;318(6044):382-4.

(12) Kreda SM, Mall M, Mengos A, Rochelle L, Yankaskas J, Riordan JR, et al. Characterization of wild-type and deltaF508 cystic fibrosis transmembrane regulator in human respiratory epithelia. *Mol Biol Cell* 2005 May;16(5):2154-67.

(13) Wu JV, Krouse ME, Wine JJ. Acinar origin of CFTR-dependent airway submucosal gland fluid secretion. *Am J Physiol Lung Cell Mol Physiol* 2007 Jan;292(1):L304-L311.

(14) Boucher RC. New concepts of the pathogenesis of cystic fibrosis lung disease. *Eur Respir J* 2004;23(1):146-58.

(15) Riordan JR. Assembly of functional CFTR chloride channels. *Annu Rev Physiol* 2005;67:701-18.

(16) Alton EW, Kitson C. Gene therapy for cystic fibrosis. *Expert Opin Investig Drugs* 2000;9(7):1523-35.

(17) Proesmans M, Vermeulen F, De BK. What's new in cystic fibrosis? From treating symptoms to correction of the basic defect. *Eur J Pediatr* 2008 Aug;167(8):839-49.

(18) Pier GB. Role of the cystic fibrosis transmembrane conductance regulator in innate immunity to Pseudomonas aeruginosa infections. *Proc Natl Acad Sci U S A* 2000;97(16):8822-8.

(19) Gail DB, Lenfant CJ. Cells of the lung: biology and clinical implications. *Am Rev Respir Dis* 1983 Mar;127(3):366-87.

(20) Engelhardt JF, Yankaskas JR, Ernst SA, Yang Y, Marino CR, Boucher RC, et al. Submucosal glands are the predominant site of CFTR expression in the human bronchus. *Nat Genet* 1992 Nov;2(3):240-8.

(21) Joo NS, Cho HJ, Khansaheb M, Wine JJ. Hyposecretion of fluid from tracheal submucosal glands of CFTR-deficient pigs. *J Clin Invest* 2010 Sep 1;120(9):3161-6.

(22) Cho HJ, Joo NS, Wine JJ. Mucus secretion from individual submucosal glands of the ferret trachea. *Am J Physiol Lung Cell Mol Physiol* 2010 Jul;299(1):L124-L136.

(23) Cliff WH, Frizzell RA. Separate Cl- conductances activated by cAMP and Ca2+ in Cl(-)-secreting epithelial cells. *Proc Natl Acad Sci U S A* 1990 Jul;87(13):4956-60.

(24) Conese M, Boyd AC, Di GS, Auriche C, Ascenzioni F. Genomic context vectors and artificial chromosomes for cystic fibrosis gene therapy. *Curr Gene Ther* 2007 Jun;7(3):175-87.

(25) Daniels SE, Bhattacharrya S, James A, Leaves NI, Young A, Hill MR, et al. A genome-wide search for quantitative trait loci underlying asthma. *Nature* 1996 Sep 19;383(6597):247-50.

(26) Drumm ML, Pope HA, Cliff WH, Rommens JM, Marvin SA, Tsui LC, et al. Correction of the cystic fibrosis defect in vitro by retrovirus-mediated gene transfer. *Cell* 1990 Sep 21;62(6):1227-33.

(27) Hyde SC, Gill DR, Higgins CF, Trezise AE, MacVinish LJ, Cuthbert AW, et al. Correction of the ion transport defect in cystic fibrosis transgenic mice by gene therapy. *Nature* 1993 Mar 18;362(6417):250-5.

(28) Alton EW, Middleton PG, Caplen NJ, Smith SN, Steel DM, Munkonge FM, et al. Non-invasive liposome-mediated gene delivery can correct the ion transport defect in cystic fibrosis mutant mice. *Nat Genet* 1993 Oct;5(2):135-42.

(29) Alton EW, Stern M, Farley R, Jaffe A, Chadwick SL, Phillips J, et al. Cationic lipid-mediated CFTR gene transfer to the lungs and nose of patients with cystic fibrosis: a double-blind placebo-controlled trial. *Lancet* 1999 Mar 20;353(9157):947-54.

(30) Ferrari S, Griesenbach U, Shiraki-Iida T, Shu T, Hironaka T, Hou X, et al. A defective nontransmissible recombinant Sendai virus mediates efficient gene transfer to airway epithelium in vivo. *Gene Ther* 2004 Nov;11(22):1659-64.

(31) Zhang L, Bukreyev A, Thompson CI, Watson B, Peeples ME, Collins PL, et al. Infection of ciliated cells by human parainfluenza virus type 3 in an in vitro model of human airway epithelium. *J Virol* 2005 Jan;79(2):1113-24.

(32) Ferrari S, Griesenbach U, Iida A, Farley R, Wright AM, Zhu J, et al. Sendai virus-mediated CFTR gene transfer to the airway epithelium. *Gene Ther* 2007 Oct;14(19):1371-9.

(33) Hyde SC, Pringle IA, Abdullah S, Lawton AE, Davies LA, Varathalingam A, et al. CpG-free plasmids confer reduced inflammation and sustained pulmonary gene expression. *Nat Biotechnol* 2008 May;26(5):549-51.

(34) Sinn PL, Arias AC, Brogden KA, McCray PB, Jr. Lentivirus vector can be readministered to nasal epithelia without blocking immune responses. *J Virol* 2008 Nov;82(21):10684-92.

(35) Griesenbach U, Alton EW. Gene transfer to the lung: lessons learned from more than 2 decades of CF gene therapy. *Adv Drug Deliv Rev* 2009 Feb 27;61(2):128-39.

(36) Pringle IA, Hyde SC, Gill DR. Non-viral vectors in cystic fibrosis gene therapy: recent developments and future prospects. *Expert Opin Biol Ther* 2009 Aug;9(8):991-1003.

(37) Zhang L, Button B, Gabriel SE, Burkett S, Yan Y, Skiadopoulos MH, et al. CFTR delivery to 25% of surface epithelial cells restores normal rates of mucus transport to human cystic fibrosis airway epithelium. *PLoS Biol* 2009 Jul;7(7):e1000155.

(38) Kwilas AR, Yednak MA, Zhang L, Liesman R, Collins PL, Pickles RJ, et al. Respiratory syncytial virus engineered to express the cystic fibrosis transmembrane conductance regulator corrects the bioelectric phenotype of human cystic fibrosis airway epithelium in vitro. *J Virol* 2010 Aug;84(15):7770-81.

(39) Mitomo K, Griesenbach U, Inoue M, Somerton L, Meng C, Akiba E, et al. Toward gene therapy for cystic fibrosis using a lentivirus pseudotyped with Sendai virus envelopes. *Mol Ther* 2010 Jun;18(6):1173-82.

(40) Davies JC, Alton EW. Gene therapy for cystic fibrosis. *Proc Am Thorac Soc* 2010 Nov;7(6):408-14.

(41) Griesenbach U, McLachlan G, Owaki T, Somerton L, Shu T, Baker A, et al. Validation of recombinant Sendai virus in a non-natural host model. *Gene Ther* 2011 Feb;18(2):182-8.

(42) Crystal RG, McElvaney NG, Rosenfeld MA, Chu CS, Mastrangeli A, Hay JG, et al. Administration of an adenovirus containing the human CFTR cDNA to the respiratory tract of individuals with cystic fibrosis. *Nat Genet* 1994 Sep;8(1):42-51.

(43) Harvey BG, Leopold PL, Hackett NR, Grasso TM, Williams PM, Tucker AL, et al. Airway epithelial CFTR mRNA expression in cystic fibrosis patients after repetitive

administration of a recombinant adenovirus. *J Clin Invest* 1999 Nov;104(9):1245-55.

(44) Griesenbach U, Alton EW. Current status and future directions of gene and cell therapy for cystic fibrosis. *BioDrugs* 2011 Apr 1;25(2):77-88.

(45) Conese M, Ascenzioni F, Boyd AC, Coutelle C, De F, I, De SS, et al. Gene and cell therapy for cystic fibrosis: from bench to bedside. *J Cyst Fibros* 2011 Jun;10 Suppl 2:S114-S128.

(46) Hyde SC, Southern KW, Gileadi U, Fitzjohn EM, Mofford KA, Waddell BE, et al. Repeat administration of DNA/liposomes to the nasal epithelium of patients with cystic fibrosis. *Gene Ther* 2000 Jul;7(13):1156-65.

(47) Griesenbach U, Sumner-Jones SG, Holder E, Munkonge FM, Wodehouse T, Smith SN, et al. Limitations of the murine nose in the development of nonviral airway gene transfer. *Am J Respir Cell Mol Biol* 2010 Jul;43(1):46-54.

(48) Zabner J, Couture LA, Gregory RJ, Graham SM, Smith AE, Welsh MJ. Adenovirus-mediated gene transfer transiently corrects the chloride transport defect in nasal epithelia of patients with cystic fibrosis. *Cell* 1993 Oct 22;75(2):207-16.

(49) Hay JG, McElvaney NG, Herena J, Crystal RG. Modification of nasal epithelial potential differences of individuals with cystic fibrosis consequent to local administration of a normal CFTR cDNA adenovirus gene transfer vector. *Hum Gene Ther* 1995 Nov;6(11):1487-96.

(50) Zabner J, Ramsey BW, Meeker DP, Aitken ML, Balfour RP, Gibson RL, et al. Repeat administration of an adenovirus vector encoding cystic fibrosis transmembrane conductance regulator to the nasal epithelium of patients with cystic fibrosis. *J Clin Invest* 1996 Mar 15;97(6):1504-11.

(51) Perricone MA, Morris JE, Pavelka K, Plog MS, O'Sullivan BP, Joseph PM, et al. Aerosol and lobar administration of a recombinant adenovirus to individuals with cystic fibrosis. II. Transfection efficiency in airway epithelium. *Hum Gene Ther* 2001 Jul 20;12(11):1383-94.

(52) Moss RB, Rodman D, Spencer LT, Aitken ML, Zeitlin PL, Waltz D, et al. Repeated adeno-associated virus serotype 2 aerosol-mediated cystic fibrosis transmembrane regulator gene transfer to the lungs of patients with cystic fibrosis: a multicenter, double-blind, placebo-controlled trial. *Chest* 2004 Feb;125(2):509-21.

(53) Moss RB, Milla C, Colombo J, Accurso F, Zeitlin PL, Clancy JP, et al. Repeated aerosolized AAV-CFTR for treatment of cystic fibrosis: a randomized placebo-controlled phase 2B trial. *Hum Gene Ther* 2007 Aug;18(8):726-32.

(54) Yonemitsu Y, Kitson C, Ferrari S, Farley R, Griesenbach U, Judd D, et al. Efficient gene transfer to airway epithelium using recombinant Sendai virus. *Nat Biotechnol* 2000 Sep;18(9):970-3.

(55) Griesenbach U, Boyton RJ, Somerton L, Garcia SE, Ferrari S, Owaki T, et al. Effect of tolerance induction to immunodominant T-cell epitopes of Sendai virus on gene

expression following repeat administration to lung. *Gene Ther* 2006 Mar;13(5):449-56.

(56) Thomas CE, Ehrhardt A, Kay MA. Progress and problems with the use of viral vectors for gene therapy. *Nat Rev Genet* 2003 May;4(5):346-58.

(57) Woods NB, Bottero V, Schmidt M, von KC, Verma IM. Gene therapy: therapeutic gene causing lymphoma. *Nature* 2006 Apr 27;440(7088):1123.

(58) Meyer KB, Thompson MM, Levy MY, Barron LG, Szoka FC, Jr. Intratracheal gene delivery to the mouse airway: characterization of plasmid DNA expression and pharmacokinetics. *Gene Ther* 1995 Sep;2(7):450-60.

(59) Gill DR, Smyth SE, Goddard CA, Pringle IA, Higgins CF, Colledge WH, et al. Increased persistence of lung gene expression using plasmids containing the ubiquitin C or elongation factor 1alpha promoter. *Gene Ther* 2001 Oct;8(20):1539-46.

(60) Yew NS, Wang KX, Przybylska M, Bagley RG, Stedman M, Marshall J, et al. Contribution of plasmid DNA to inflammation in the lung after administration of cationic lipid:pDNA complexes. *Hum Gene Ther* 1999 Jan 20;10(2):223-34.

(61) Gill DR, Pringle IA, Hyde SC. Progress and prospects: the design and production of plasmid vectors. *Gene Ther* 2009 Feb;16(2):165-71.

(62) Boussif O, Lezoualc'h F, Zanta MA, Mergny MD, Scherman D, Demeneix B, et al. A versatile vector for gene and oligonucleotide transfer into cells in culture and in vivo: polyethylenimine. *Proc Natl Acad Sci U S A* 1995 Aug 1;92(16):7297-301.

(63) Kichler A. Gene transfer with modified polyethylenimines. *J Gene Med* 2004 Feb;6 Suppl 1:S3-10.

(64) Lungwitz U, Breunig M, Blunk T, Gopferich A. Polyethylenimine-based non-viral gene delivery systems. *Eur J Pharm Biopharm* 2005 Jul;60(2):247-66.

(65) Neu M, Fischer D, Kissel T. Recent advances in rational gene transfer vector design based on poly(ethylene imine) and its derivatives. *J Gene Med* 2005 Aug;7(8):992-1009.

(66) Sonawane ND, Szoka FC, Jr., Verkman AS. Chloride accumulation and swelling in endosomes enhances DNA transfer by polyamine-DNA polyplexes. *J Biol Chem* 2003 Nov 7;278(45):44826-31.

(67) Ferrari S, Pettenazzo A, Garbati N, Zacchello F, Behr JP, Scarpa M. Polyethylenimine shows properties of interest for cystic fibrosis gene therapy. *Biochim Biophys Acta* 1999 Oct 28;1447(2-3):219-25.

(68) Wiseman JW, Goddard CA, McLelland D, Colledge WH. A comparison of linear and branched polyethylenimine (PEI) with DCChol/DOPE liposomes for gene delivery to epithelial cells in vitro and in vivo. *Gene Ther* 2003 Sep;10(19):1654-62.

(69) Bragonzi A, Dina G, Villa A, Calori G, Biffi A, Bordignon C, et al. Biodistribution and transgene expression with nonviral cationic vector/DNA complexes in the lungs. *Gene Ther* 2000 Oct;7(20):1753-60.

(70) Rudolph C, Ortiz A, Schillinger U, Jauernig J, Plank C, Rosenecker J. Methodological optimization of polyethylenimine (PEI)-based gene delivery to the lungs of mice via aerosol application. *J Gene Med* 2005 Jan;7(1):59-66.

(71) Gautam A, Densmore CL, Xu B, Waldrep JC. Enhanced gene expression in mouse lung after PEI-DNA aerosol delivery. *Mol Ther* 2000 Jul;2(1):63-70.

(72) Gautam A, Densmore CL, Waldrep JC. Pulmonary cytokine responses associated with PEI-DNA aerosol gene therapy. *Gene Ther* 2001 Feb;8(3):254-7.

(73) Rudolph C, Muller RH, Rosenecker J. Jet nebulization of PEI/DNA polyplexes: physical stability and in vitro gene delivery efficiency. *J Gene Med* 2002 Jan;4(1):66-74.

(74) Rudolph C, Lausier J, Naundorf S, Muller RH, Rosenecker J. In vivo gene delivery to the lung using polyethylenimine and fractured polyamidoamine dendrimers. *J Gene Med* 2000 Jul;2(4):269-78.

(75) Davies LA, McLachlan G, Sumner-Jones SG, Ferguson D, Baker A, Tennant P, et al. Enhanced lung gene expression after aerosol delivery of concentrated pDNA/PEI complexes. *Mol Ther* 2008 Jul;16(7):1283-90.

(76) Rudolph C, Schillinger U, Ortiz A, Plank C, Golas MM, Sander B, et al. Aerosolized nanogram quantities of plasmid DNA mediate highly efficient gene delivery to mouse airway epithelium. *Mol Ther* 2005 Sep;12(3):493-501.

(77) Koping-Hoggard M, Varum KM, Issa M, Danielsen S, Christensen BE, Stokke BT, et al. Improved chitosan-mediated gene delivery based on easily dissociated chitosan polyplexes of highly defined chitosan oligomers. *Gene Ther* 2004 Oct;11(19):1441-52.

(78) Fasbender A, Marshall J, Moninger TO, Grunst T, Cheng S, Welsh MJ. Effect of co-lipids in enhancing cationic lipid-mediated gene transfer in vitro and in vivo. *Gene Ther* 1997 Jul;4(7):716-25.

(79) Goddard CA, Ratcliff R, Anderson JR, Glenn E, Brown S, Gill DR, et al. A second dose of a CFTR cDNA-liposome complex is as effective as the first dose in restoring cAMP-dependent chloride secretion to null CF mice trachea. *Gene Ther* 1997 Nov;4(11):1231-6.

(80) Caplen NJ, Alton EW, Middleton PG, Dorin JR, Stevenson BJ, Gao X, et al. Liposome-mediated CFTR gene transfer to the nasal epithelium of patients with cystic fibrosis. *Nat Med* 1995 Jan;1(1):39-46.

(80a) Rawlins EL and Hogan BLM. Ciliated epithelial cell lifespan in the mouse trachea and lung. *Am J Physiol Lung Cell Mol Physiol* 2008 May;295:L231-L234.

(81) Gill DR, Southern KW, Mofford KA, Seddon T, Huang L, Sorgi F, et al. A placebo-controlled study of liposome-mediated gene transfer to the nasal epithelium of patients with cystic fibrosis. *Gene Ther* 1997 Mar;4(3):199-209.

(82) Lee ER, Marshall J, Siegel CS, Jiang C, Yew NS, Nichols MR, et al. Detailed analysis of structures and formulations of cationic lipids for efficient gene transfer to the lung. *Hum Gene Ther* 1996 Sep 10;7(14):1701-17.

(83) Eastman SJ, Tousignant JD, Lukason MJ, Murray H, Siegel CS, Constantino P, et al. Optimization of formulations and conditions for the aerosol delivery of functional cationic lipid:DNA complexes. *Hum Gene Ther* 1997 Feb 10;8(3):313-22.

(84) Jaffe A, Judd D, Ratcliffe C, Cheng SH, Bush A, Geddes DM, et al. Cationic lipid-mediated gene transfer to the growing murine and human airway. *Gene Ther* 2000 Feb;7(4):273-8.

(85) Ruiz FE, Clancy JP, Perricone MA, Bebok Z, Hong JS, Cheng SH, et al. A clinical inflammatory syndrome attributable to aerosolized lipid-DNA administration in cystic fibrosis. *Hum Gene Ther* 2001 May 1;12(7):751-61.

(86) Wu GY, Wu CH. Receptor-mediated in vitro gene transformation by a soluble DNA carrier system. *J Biol Chem* 1987 Apr 5;262(10):4429-32.

(87) Smith JG, Walzem RL, German JB. Liposomes as agents of DNA transfer. *Biochim Biophys Acta* 1993 Dec 21;1154(3-4):327-40.

(88) Ledley FD. Non-viral gene therapy. *Curr Opin Biotechnol* 1994 Dec;5(6):626-36.

(89) Bally MB, Harvie P, Wong FM, Kong S, Wasan EK, Reimer DL. Biological barriers to cellular delivery of lipid-based DNA carriers. *Adv Drug Deliv Rev* 1999 Aug 20;38(3):291-315.

(90) Warburton D, Wuenschell C, Flores-Delgado G, Anderson K. Commitment and differentiation of lung cell lineages. *Biochem Cell Biol* 1998;76(6):971-95.

(91) Johnson LG, Boyles SE, Wilson J, Boucher RC. Normalization of raised sodium absorption and raised calcium-mediated chloride secretion by adenovirus-mediated expression of cystic fibrosis transmembrane conductance regulator in primary human cystic fibrosis airway epithelial cells. *J Clin Invest* 1995 Mar;95(3):1377-82.

(92) Danel C, Erzurum SC, McElvaney NG, Crystal RG. Quantitative assessment of the epithelial and inflammatory cell populations in large airways of normals and individuals with cystic fibrosis. *Am J Respir Crit Care Med* 1996 Jan;153(1):362-8.

(93) Penque D, Mendes F, Beck S, Farinha C, Pacheco P, Nogueira P, et al. Cystic fibrosis F508del patients have apically localized CFTR in a reduced number of airway cells. *Lab Invest* 2000 Jun;80(6):857-68.

(94) Behr JP, Demeneix B, Loeffler JP, Perez-Mutul J. Efficient gene transfer into mammalian primary endocrine cells with lipopolyamine-coated DNA. *Proc Natl Acad Sci U S A* 1989 Sep;86(18):6982-6.

(95) Labat-Moleur F, Steffan AM, Brisson C, Perron H, Feugeas O, Furstenberger P, et al. An electron microscopy study into the mechanism of gene transfer with lipopolyamines. *Gene Ther* 1996 Nov;3(11):1010-7.

(96) Tyagi M, Rusnati M, Presta M, Giacca M. Internalization of HIV-1 tat requires cell surface heparan sulfate proteoglycans. *J Biol Chem* 2001 Feb 2;276(5):3254-61.

(97) Richard JP, Melikov K, Brooks H, Prevot P, Lebleu B, Chernomordik LV. Cellular uptake of unconjugated TAT peptide involves clathrin-dependent endocytosis and heparan sulfate receptors. *J Biol Chem* 2005 Apr 15;280(15):15300-6.

(98) Luc W, Dick H. Cationic lipids, lipoplexes and intracellular delivery of genes. *J Control Release* 2006;112:362-8.

(99) Mislick KA, Baldeschwieler JD. Evidence for the role of proteoglycans in cation-mediated gene transfer. *Proc Natl Acad Sci U S A* 1996 Oct 29;93(22):12349-54.

(100) Kopatz I, Remy JS, Behr JP. A model for non-viral gene delivery: through syndecan adhesion molecules and powered by actin. *J Gene Med* 2004 Jul;6(7):769-76.

(101) Felgner PL, Tsai YJ, Sukhu L, Wheeler CJ, Manthorpe M, Marshall J, et al. Improved cationic lipid formulations for in vivo gene therapy. *Ann N Y Acad Sci* 1995 Nov 27;772:126-39.

(102) Felgner PL, Gadek TR, Holm M, Roman R, Chan HW, Wenz M, et al. Lipofection: a highly efficient, lipid-mediated DNA-transfection procedure. *Proc Natl Acad Sci U S A* 1987 Nov;84(21):7413-7.

(103) Friend DS, Papahadjopoulos D, Debs RJ. Endocytosis and intracellular processing accompanying transfection mediated by cationic liposomes. *Biochim Biophys Acta* 1996 Jan 12;1278(1):41-50.

(104) Matsui H, Johnson LG, Randell SH, Boucher RC. Loss of binding and entry of liposome-DNA complexes decreases transfection efficiency in differentiated airway epithelial cells. *J Biol Chem* 1997 Jan 10;272(2):1117-26.

(105) Zuhorn IS, Kalicharan R, Hoekstra D. Lipoplex-mediated transfection of mammalian cells occurs through the cholesterol-dependent clathrin-mediated pathway of endocytosis. *J Biol Chem* 2002 May 17;277(20):18021-8.

(106) Stuart LM, Ezekowitz RA. Phagocytosis: elegant complexity. *Immunity* 2005 May;22(5):539-50.

(107) Swanson JA, Watts C. Macropinocytosis. *Trends Cell Biol* 1995 Nov;5(11):424-8.

(108) Mellman I. Endocytosis and molecular sorting. *Annu Rev Cell Dev Biol* 1996;12:575-625.

(109) Conner SD, Schmid SL. Regulated portals of entry into the cell. *Nature* 2003 Mar 6;422(6927):37-44.

(110) Nichols B. Caveosomes and endocytosis of lipid rafts. *J Cell Sci* 2003 Dec 1;116(Pt 23):4707-14.

(111) Pelkmans L, Puntener D, Helenius A. Local actin polymerization and dynamin recruitment in SV40-induced internalization of caveolae. *Science* 2002 Apr 19;296(5567):535-9.

(112) Ehrlich M, Boll W, Van OA, Hariharan R, Chandran K, Nibert ML, et al. Endocytosis by random initiation and stabilization of clathrin-coated pits. *Cell* 2004 Sep 3;118(5):591-605.

(113) Noguchi A, Kawaura C, Nakanishi M, et al. Membrane fusion plays an important role in gene transfection mediated by cationic liposomes. *FEBS Lett* 1999;433:169-73.

(114) Takei K, Haucke V. Clathrin-mediated endocytosis: membrane factors pull the trigger. *Trends Cell Biol* 2001 Sep;11(9):385-91.

(115) Zhou X, Huang L. DNA transfection mediated by cationic liposomes containing lipopolylysine: characterization and mechanism of action. *Biochim Biophys Acta* 1994 Jan 19;1189(2):195-203.

(116) Rejman J, Oberle V, Zuhorn IS, Hoekstra D. Size-dependent internalization of particles via the pathways of clathrin- and caveolae-mediated endocytosis. *Biochem J* 2004 Jan 1;377(Pt 1):159-69.

(117) Rejman J, Bragonzi A, Conese M. Role of clathrin- and caveolae-mediated endocytosis in gene transfer mediated by lipo- and polyplexes. *Mol Ther* 2005 Sep;12(3):468-74.

(118) Matveev S, Li X, Everson W, Smart EJ. The role of caveolae and caveolin in vesicle-dependent and vesicle-independent trafficking. *Adv Drug Deliv Rev* 2001 Jul 28;49(3):237-50.

(119) Harris J, Werling D, Hope JC, Taylor G, Howard CJ. Caveolae and caveolin in immune cells: distribution and functions. *Trends Immunol* 2002 Mar;23(3):158-64.

(120) Ferrari A, Pellegrini V, Arcangeli C, Fittipaldi A, Giacca M, Beltram F. Caveolae-mediated internalization of extracellular HIV-1 tat fusion proteins visualized in real time. *Mol Ther* 2003 Aug;8(2):284-94.

(121) Fittipaldi A, Ferrari A, Zoppe M, Arcangeli C, Pellegrini V, Beltram F, et al. Cell membrane lipid rafts mediate caveolar endocytosis of HIV-1 Tat fusion proteins. *J Biol Chem* 2003 Sep 5;278(36):34141-9.

(122) Kleuss C, Hescheler J, Ewel C, Rosenthal W, Schultz G, Wittig B. Assignment of G-protein subtypes to specific receptors inducing inhibition of calcium currents. *Nature* 1991 Sep 5;353(6339):43-8.

(123) Leonetti JP, Mechti N, Degols G, Gagnor C, Lebleu B. Intracellular distribution of microinjected antisense oligonucleotides. *Proc Natl Acad Sci U S A* 1991 Apr 1;88(7):2702-6.

(124) Barry EL, Gesek FA, Friedman PA. Introduction of antisense oligonucleotides into cells by permeabilization with streptolysin O. *Biotechniques* 1993 Dec;15(6):1016-8, 1020.

(125) Midoux P, Mayer R, Monsigny M. Membrane permeabilization by alpha-helical peptides: a flow cytometry study. *Biochim Biophys Acta* 1995 Nov 1;1239(2):249-56.

(126) Bergan R, Connell Y, Fahmy B, Neckers L. Electroporation enhances c-myc antisense oligodeoxynucleotide efficacy. *Nucleic Acids Res* 1993 Jul 25;21(15):3567-73.

(127) Gumbiner BM. Breaking through the tight junction barrier. *J Cell Biol* 1993 Dec;123(6 Pt 2):1631-3.

(128) Rose JK, Buonocore L, Whitt MA. A new cationic liposome reagent mediating nearly quantitative transfection of animal cells. *Biotechniques* 1991 Apr;10(4):520-5.

(129) Caplen NJ, Kinrade E, Sorgi F, Gao X, Gruenert D, Geddes D, et al. In vitro liposome-mediated DNA transfection of epithelial cell lines using the cationic liposome DC-Chol/DOPE. *Gene Ther* 1995 Nov;2(9):603-13.

(130) Holmen SL, Vanbrocklin MW, Eversole RR, Stapleton SR, Ginsberg LC. Efficient lipid-mediated transfection of DNA into primary rat hepatocytes. *In Vitro Cell Dev Biol Anim* 1995 May;31(5):347-51.

(131) Trivedi RA, Dickson G. Liposome-mediated gene transfer into normal and dystrophin-deficient mouse myoblasts. *J Neurochem* 1995 May;64(5):2230-8.

(132) Fasbender A, Zabner J, Zeiher BG, Welsh MJ. A low rate of cell proliferation and reduced DNA uptake limit cationic lipid-mediated gene transfer to primary cultures of ciliated human airway epithelia. *Gene Ther* 1997 Nov;4(11):1173-80.

(133) Zabner J, Cheng SH, Meeker D, Launspach J, Balfour R, Perricone MA, et al. Comparison of DNA-lipid complexes and DNA alone for gene transfer to cystic fibrosis airway epithelia in vivo. *J Clin Invest* 1997 Sep 15;100(6):1529-37.

(134) Jiang C, O'Connor SP, Fang SL, Wang KX, Marshall J, Williams JL, et al. Efficiency of cationic lipid-mediated transfection of polarized and differentiated airway epithelial cells in vitro and in vivo. *Hum Gene Ther* 1998 Jul 20;9(11):1531-42.

(135) Chu Q, Tousignant JD, Fang S, Jiang C, Chen LH, Cheng SH, et al. Binding and uptake of cationic lipid:pDNA complexes by polarized airway epithelial cells. *Hum Gene Ther* 1999 Jan 1;10(1):25-36.

(136) Zabner J, Fasbender AJ, Moninger T, Poellinger KA, Welsh MJ. Cellular and molecular barriers to gene transfer by a cationic lipid. *J Biol Chem* 1995 Aug 11;270(32):18997-9007.

(137) Wilke M, Fortunati E, van den Broek M, Hoogeveen AT, Scholte BJ. Efficacy of a peptide-based gene delivery system depends on mitotic activity. *Gene Ther* 1996 Dec;3(12):1133-42.

(138) Oudrhiri N, Vigneron JP, Peuchmaur M, Leclerc T, Lehn JM, Lehn P. Gene transfer by guanidinium-cholesterol cationic lipids into airway epithelial cells in vitro and in vivo. *Proc Natl Acad Sci U S A* 1997 Mar 4;94(5):1651-6.

(139) Leigh MW, Kylander JE, Yankaskas JR, Boucher RC. Cell proliferation in bronchial epithelium and submucosal glands of cystic fibrosis patients. *Am J Respir Cell Mol Biol* 1995 Jun;12(6):605-12.

(140) Pickles RJ, McCarty D, Matsui H, Hart PJ, Randell SH, Boucher RC. Limited entry of adenovirus vectors into well-differentiated airway epithelium is responsible for inefficient gene transfer. *J Virol* 1998 Jul;72(7):6014-23.

(141) Duan D, Yue Y, Yan Z, McCray PB, Jr., Engelhardt JF. Polarity influences the efficiency of recombinant adenoassociated virus infection in differentiated airway epithelia. *Hum Gene Ther* 1998 Dec 10;9(18):2761-76.

(142) Keefer JR, Limbird LE. The alpha 2A-adrenergic receptor is targeted directly to the basolateral membrane domain of Madin-Darby canine kidney cells independent of coupling to pertussis toxin-sensitive GTP-binding proteins. *J Biol Chem* 1993 May 25;268(15):11340-7.

(143) Du J, Wilson PD. Abnormal polarization of EGF receptors and autocrine stimulation of cyst epithelial growth in human ADPKD. *Am J Physiol* 1995 Aug;269(2 Pt 1):C487-C495.

(144) Bhat M, Toledo-Velasquez D, Wang L, Malanga CJ, Ma JK, Rojanasakul Y. Regulation of tight junction permeability by calcium mediators and cell cytoskeleton in rabbit tracheal epithelium. *Pharm Res* 1993 Jul;10(7):991-7.

(145) Denker BM, Nigam SK. Molecular structure and assembly of the tight junction. *Am J Physiol* 1998 Jan;274(1 Pt 2):F1-F9.

(146) Tomita M, Hayashi M, Awazu S. Absorption-enhancing mechanism of EDTA, caprate, and decanoylcarnitine in Caco-2 cells. *J Pharm Sci* 1996 Jun;85(6):608-11.

(147) Parsons DW, Grubb BR, Johnson LG, Boucher RC. Enhanced in vivo airway gene transfer via transient modification of host barrier properties with a surface-active agent. *Hum Gene Ther* 1998 Dec 10;9(18):2661-72.

(148) Weiss DJ, Strandjord TP, Jackson JC, Clark JG, Liggitt D. Perfluorochemical liquid-enhanced adenoviral vector distribution and expression in lungs of spontaneously breathing rodents. *Exp Lung Res* 1999 Jun;25(4):317-33.

(149) Weiss DJ, Bonneau L, Allen JM, Miller AD, Halbert CL. Perfluorochemical liquid enhances adeno-associated virus-mediated transgene expression in lungs. *Mol Ther* 2000 Dec;2(6):624-30.

(150) Wang G, Zabner J, Deering C, Launspach J, Shao J, Bodner M, et al. Increasing epithelial junction permeability enhances gene transfer to airway epithelia In vivo. *Am J Respir Cell Mol Biol* 2000 Feb;22(2):129-38.

(151) Chu Q, St George JA, Lukason M, Cheng SH, Scheule RK, Eastman SJ. EGTA enhancement of adenovirus-mediated gene transfer to mouse tracheal epithelium in vivo. *Hum Gene Ther* 2001 Mar 20;12(5):455-67.

(152) Das A, Niven R. Use of perfluorocarbon (fluorinert) to enhance reporter gene expression following intratracheal instillation into the lungs of Balb/c mice: implications for nebulized delivery of plasmids. *J Pharm Sci* 2001 Sep;90(9):1336-44.

(153) Zelphati O, Szoka FC, Jr. Mechanism of oligonucleotide release from cationic liposomes. *Proc Natl Acad Sci U S A* 1996 Oct 15;93(21):11493-8.

(154) Xu Y, Szoka FC, Jr. Mechanism of DNA release from cationic liposome/DNA complexes used in cell transfection. *Biochemistry* 1996 May 7;35(18):5616-23.

(155) Tachibana R, Harashima H, Shono M, Azumano M, Niwa M, Futaki S, et al. Intracellular regulation of macromolecules using pH-sensitive liposomes and nuclear localization signal: qualitative and quantitative evaluation of intracellular trafficking. *Biochem Biophys Res Commun* 1998 Oct 20;251(2):538-44.

(156) Midoux P, LeCam E, Coulaud D, Delain E, Pichon C. Histidine containing peptides and polypeptides as nucleic acid vectors. *Somat Cell Mol Genet* 2002 Nov;27(1-6):27-47.

(157) Medina-Kauwe LK, Xie J, Hamm-Alvarez S. Intracellular trafficking of nonviral vectors. *Gene Ther* 2005 Dec;12(24):1734-51.

(158) Coonrod A, Li FQ, Horwitz M. On the mechanism of DNA transfection: efficient gene transfer without viruses. *Gene Ther* 1997 Dec;4(12):1313-21.

(159) Dowty ME, Williams P, Zhang G, Hagstrom JE, Wolff JA. Plasmid DNA entry into postmitotic nuclei of primary rat myotubes. *Proc Natl Acad Sci U S A* 1995 May 9;92(10):4572-6.

(160) Lukacs GL, Haggie P, Seksek O, Lechardeur D, Freedman N, Verkman AS. Size-dependent DNA mobility in cytoplasm and nucleus. *J Biol Chem* 2000 Jan 21;275(3):1625-9.

(161) Vallee RB, Sheetz MP. Targeting of motor proteins. *Science* 1996 Mar 15;271(5255):1539-44.

(162) Rogers SL, Gelfand VI. Membrane trafficking, organelle transport, and the cytoskeleton. *Curr Opin Cell Biol* 2000 Feb;12(1):57-62.

(163) Vaughan EE, Dean DA. Intracellular trafficking of plasmids during transfection is mediated by microtubules. *Mol Ther* 2006 Feb;13(2):422-8.

(164) Vaughan EE, DeGiulio JV, Dean DA. Intracellular trafficking of plasmids for gene therapy: mechanisms of cytoplasmic movement and nuclear import. *Curr Gene Ther* 2006 Dec;6(6):671-81.

(165) Grosse S, Aron Y, Thevenot G, Monsigny M, Fajac I. Cytoskeletal involvement in the cellular trafficking of plasmid/PEI derivative complexes. *J Control Release* 2007 Sep 11;122(1):111-7.

(166) Giannakakou P, Sackett DL, Ward Y, Webster KR, Blagosklonny MV, Fojo T. p53 is associated with cellular microtubules and is transported to the nucleus by dynein. *Nat Cell Biol* 2000 Oct;2(10):709-17.

(167) Giannakakou P, Nakano M, Nicolaou KC, O'Brate A, Yu J, Blagosklonny MV, et al. Enhanced microtubule-dependent trafficking and p53 nuclear accumulation by suppression of microtubule dynamics. *Proc Natl Acad Sci U S A* 2002 Aug 6;99(16):10855-60.

(168) Hasegawa S, Hirashima N, Nakanishi M. Microtubule involvement in the intracellular dynamics for gene transfection mediated by cationic liposomes. *Gene Ther* 2001 Nov;8(21):1669-73.

(169) Suh J, Wirtz D, Hanes J. Efficient active transport of gene nanocarriers to the cell nucleus. *Proc Natl Acad Sci U S A* 2003 Apr 1;100(7):3878-82.

(170) Dauty E, Verkman AS. Actin cytoskeleton as the principal determinant of size-dependent DNA mobility in cytoplasm: a new barrier for non-viral gene delivery. *J Biol Chem* 2005 Mar 4;280(9):7823-8.

(171) Yoneda Y. Nuclear pore-targeting complex and its role on nuclear protein transport. *Arch Histol Cytol* 1996 May;59(2):97-107.

(172) Stoffler D, Fahrenkrog B, Aebi U. The nuclear pore complex: from molecular architecture to functional dynamics. *Curr Opin Cell Biol* 1999 Jun;11(3):391-401.

(173) Munkonge FM, Dean DA, Hillery E, Griesenbach U, Alton EW. Emerging significance of plasmid DNA nuclear import in gene therapy. *Adv Drug Deliv Rev* 2003 Jun 16;55(6):749-60.

(174) Brunner S, Sauer T, Carotta S, Cotten M, Saltik M, Wagner E. Cell cycle dependence of gene transfer by lipoplex, polyplex and recombinant adenovirus. *Gene Ther* 2000 Mar;7(5):401-7.

(175) Kitson C, Angel B, Judd D, Rothery S, Severs NJ, Dewar A, et al. The extra- and intracellular barriers to lipid and adenovirus-mediated pulmonary gene transfer in native sheep airway epithelium. *Gene Ther* 1999 Apr;6(4):534-46.

(176) Breeze RG, Wheeldon EB. The cells of the pulmonary airways. *Am Rev Respir Dis* 1977 Oct;116(4):705-77.

(177) Dean DA. Import of plasmid DNA into the nucleus is sequence specific. *Exp Cell Res* 1997 Feb 1;230(2):293-302.

(178) Mortimer I, Tam P, MacLachlan I, Graham RW, Saravolac EG, Joshi PB. Cationic lipid-mediated transfection of cells in culture requires mitotic activity. *Gene Ther* 1999 Mar;6(3):403-11.

(179) Gorlich D, Kutay U. Transport between the cell nucleus and the cytoplasm. *Annu Rev Cell Dev Biol* 1999;15:607-60.

(180) Zanta MA, Belguise-Valladier P, Behr JP. Gene delivery: a single nuclear localization signal peptide is sufficient to carry DNA to the cell nucleus. *Proc Natl Acad Sci U S A* 1999 Jan 5;96(1):91-6.

(181) Branden LJ, Mohamed AJ, Smith CI. A peptide nucleic acid-nuclear localization signal fusion that mediates nuclear transport of DNA. *Nat Biotechnol* 1999 Aug;17(8):784-7.

(182) Cartier R, Reszka R. Utilization of synthetic peptides containing nuclear localization signals for nonviral gene transfer systems. *Gene Ther* 2002 Feb;9(3):157-67.

(183) Munkonge FM, Amin V, Hyde SC, Green AM, Pringle IA, Gill DR, et al. Identification and functional characterization of cytoplasmic determinants of plasmid DNA nuclear import. *J Biol Chem* 2009 Sep 25;284(39):26978-87.

(184) Pollard H, Remy JS, Loussouarn G, Demolombe S, Behr JP, Escande D. Polyethylenimine but not cationic lipids promotes transgene delivery to the nucleus in mammalian cells. *J Biol Chem* 1998 Mar 27;273(13):7507-11.

(185) Remy JS, Kichler A, Mordvinov V, Schuber F, Behr JP. Targeted gene transfer into hepatoma cells with lipopolyamine-condensed DNA particles presenting galactose ligands: a stage toward artificial viruses. *Proc Natl Acad Sci U S A* 1995 Feb 28;92(5):1744-8.

(186) Zhang XX, McIntosh TJ, Grinstaff MW. Functional lipids and lipoplexes for improved gene delivery. *Biochimie* 2012 Jan;94(1):42-58.

(187) Hillery E, Munkonge FM, Xenariou S, Dean DA, Alton EW. Nondisruptive, sequence-specific coupling of fluorochromes to plasmid DNA. *Anal Biochem* 2006 May 15;352(2):169-75.

(188) Wilson RW, Bloomfield VA. Counterion-induced condensation of deoxyribonucleic acid. a light-scattering study. *Biochemistry* 1979 May 29;18(11):2192-6.

(189) Wiszniewski L, Jornot L, Dudez T, Pagano A, Rochat T, Lacroix JS, et al. Long-term cultures of polarized airway epithelial cells from patients with cystic fibrosis. *Am J Respir Cell Mol Biol* 2006 Jan;34(1):39-48.

(190) Zhou L, Dey CR, Wert SE, DuVall MD, Frizzell RA, Whitsett JA. Correction of lethal intestinal defect in a mouse model of cystic fibrosis by human CFTR. *Science* 1994 Dec 9;266(5191):1705-8.

(191) Gomi K, Kajiyama N. Oxyluciferin, a luminescence product of firefly luciferase, is enzymatically regenerated into luciferin. *J Biol Chem* 2001 Sep 28;276(39):36508-13.

(192) Holder E, Stevenson B, Farley R, Hilliard T, Wodehouse T, Somerton L, et al. Detection of CFTR transgene mRNA expression in respiratory epithelium isolated from the murine nasal cavity. *J Gene Med* 2010 Jan;12(1):55-63.

(193) Constant S, Huang S, Derouette JP, Wiszniewski L. MucilAir: A novel *in vitro* human 3D airway epithelium model for assessing the potential hazard of nanoparticles and chemical coumpounds. *Toxicol Lett* 2008;180:S233.

(194) SABATINI DD, BENSCH K, BARRNETT RJ. Cytochemistry and electron microscopy. The preservation of cellular ultrastructure and enzymatic activity by aldehyde fixation. *J Cell Biol* 1963 Apr;17:19-58.

(195) Apodaca G. Endocytic traffic in polarized epithelial cells: role of the actin and microtubule cytoskeleton. *Traffic* 2001 Mar;2(3):149-59.

(196) Liu C, Liu M, Zhou J. Analysis of microtubule-mediated intracellular viral transport. *Methods Mol Med* 2007;137:175-80.

(197) Ondrej V, Lukasova E, Falk M, Kozubek S. The role of actin and microtubule networks in plasmid DNA intracellular trafficking. *Acta Biochim Pol* 2007;54(3):657-63.

(198) Vaughan EE, Geiger RC, Miller AM, Loh-Marley PL, Suzuki T, Miyata N, et al. Microtubule acetylation through HDAC6 inhibition results in increased transfection efficiency. *Mol Ther* 2008 Nov;16(11):1841-7.

(199) Katchburian E, Holt SJ. Studies on the development of ameloblasts. I. Fine structure. *J Cell Sci* 1972 Sep;11(2):415-47.

(200) Weatherbee JA, Luftig RB, Weihing RR. In vitro polymerization of microtubules from HeLa cells. *J Cell Biol* 1978 Jul;78(1):47-57.

(201) Massa LF, Arana-Chavez VE. Ultrastructural preservation of rat embryonic dental tissues after rapid fixation and dehydration under microwave irradiation. *Eur J Oral Sci* 2000 Feb;108(1):74-7.

(202) Suikkanen S, Aaltonen T, Nevalainen M, Valilehto O, Lindholm L, Vuento M, et al. Exploitation of microtubule cytoskeleton and dynein during parvoviral traffic toward the nucleus. *J Virol* 2003 Oct;77(19):10270-9.

(203) Reipert S, Kotisch H, Wysoudil B, Wiche G. Rapid microwave fixation of cell monolayers preserves microtubule-associated cell structures. *J Histochem Cytochem* 2008 Jul;56(7):697-709.

(204) Luftig RB, McMillan PN, Weatherbee JA, Weihing RR. Increased visualization of microtubules by an improved fixation procedure. *J Histochem Cytochem* 1977 Mar;25(3):175-87.

(205) Lin A, Krockmalnic G, Penman S. Imaging cytoskeleton--mitochondrial membrane attachments by embedment-free electron microscopy of saponin-extracted cells. *Proc Natl Acad Sci U S A* 1990 Nov;87(21):8565-9.

(206) Araki N, Lee T, Matsubara H, Takashima Y. An improved technique for observing both membranous organelles and cytoskeleton in saponin-extracted cells. *J Electron Microsc (Tokyo)* 1993 Feb;42(1):51-4.

(207) Hirokawa N. Kinesin and dynein superfamily proteins and the mechanism of organelle transport. *Science* 1998 Jan 23;279(5350):519-26.

(208) Faulk WP, Taylor GM. An immunocolloid method for the electron microscope. *Immunochemistry* 1971 Nov;8(11):1081-3.

(209) Romano EL, Stolinski C, Hughes-Jones NC. An antiglobulin reagent labelled with colloidal gold for use in electron microscopy. *Immunochemistry* 1974;11:521-2.

(210) Bauer H, Gerber H, Horisberger M. Morphology of colloidal gold, ferritin and anti-ferritin antibody complexes. *Experientia* 1975 Oct 15;31(10):1149-51.

(211) Goodman SL, Hodges GM, Livingston DC. A review of the colloidal gold marker system. *Scan Electron Microsc* 1980;(Pt 2):133-46.

(212) Stirling JW. Immuno- and affinity probes for electron microscopy: a review of labeling and preparation techniques. *J Histochem Cytochem* 1990 Feb;38(2):145-57.

(213) Oliver C. Colloidal gold/streptavidin methods. *Methods Mol Biol* 2010;588:375-80.

(214) Dowty ME, Gurevich V, Berg RK, Repetto G, Wolff JA. Characterisation of biotinylated and gold-labelled plasmid DNA. *Methods in Cell and Mol Biol* 1992;3:167-74.

(215) Kitson C. The mechanisms of, and barriers to cationic liposome-mediated gene transfer 1997.

(216) Sakamoto H, Traincard F, Vo-Quang T, Ternynck T, Guesdon JL, Avrameas S. 5-Bromodeoxyuridine in vivo labelling of M13 DNA, and its use as a non-radioactive probe for hybridization experiments. *Mol Cell Probes* 1987 Mar;1(1):109-20.

(217) Kitazawa S, Takenaka A, Abe N, Maeda S, Horio M, Sugiyama T. In situ DNA-RNA hybridization using in vivo bromodeoxyuridine-labeled DNA probe. *Histochemistry* 1989;92(3):195-9.

(218) Tamatani R, Taniguchi Y, Kawarai Y. Ultrastructural study of proliferating cells with an improved immunocytochemical detection of DNA-incorporated bromodeoxyuridine. *J Histochem Cytochem* 1995 Jan;43(1):21-9.

(219) Troxler M, Pasamontes L, Egger D, Bienz K. In situ hybridization for light and electron microscopy: a comparison of methods for the localization of viral RNA using biotinylated DNA and RNA probes. *J Virol Methods* 1990 Oct;30(1):1-14.

(220) Lockard VG. A simple technique for post embedding ultrastructural immunogold labelling. *Ultrastructural pathology* 1992;16:47-50.

(221) Lappalainen K, Miettinen R, Kellokoski J, Jaaskelainen I, Syrjanen S. Intracellular distribution of oligonucleotides delivered by cationic liposomes: light and electron microscopic study. *J Histochem Cytochem* 1997 Feb;45(2):265-74.

(222) Egholm M, Buchardt O, Christensen L, Behrens C, Freier SM, Driver DA, et al. PNA hybridizes to complementary oligonucleotides obeying the Watson-Crick hydrogen-bonding rules. *Nature* 1993 Oct 7;365(6446):566-8.

(223) Nielsen PE, Egholm M, Buchardt O. Evidence for (PNA)2/DNA triplex structure upon binding of PNA to dsDNA by strand displacement. *J Mol Recognit* 1994 Sep;7(3):165-70.

(224) Egholm M, Christensen L, Dueholm KL, Buchardt O, Coull J, Nielsen PE. Efficient pH-independent sequence-specific DNA binding by pseudoisocytosine-containing bis-PNA. *Nucleic Acids Res* 1995 Jan 25;23(2):217-22.

(225) Zelphati O, Liang X, Hobart P, Felgner PL. Gene chemistry: functionally and conformationally intact fluorescent plasmid DNA. *Hum Gene Ther* 1999 Jan 1;10(1):15-24.

(226) Wilson GL, Dean BS, Wang G, Dean DA. Nuclear import of plasmid DNA in digitonin-permeabilized cells requires both cytoplasmic factors and specific DNA sequences. *J Biol Chem* 1999 Jul 30;274(31):22025-32.

(227) Hainfeld JF, Furuya FR. A 1.4-nm gold cluster covalently attached to antibodies improves immunolabeling. *J Histochem Cytochem* 1992 Feb;40(2):177-84.

(228) Hainfeld JF, Powell RD. New frontiers in gold labeling. *J Histochem Cytochem* 2000 Apr;48(4):471-80.

(229) Hainfeld JF, Powell RD, Stein J.K, Hacker G.W, Hauser-Kronberger c, Cheung A.L.M, et al. Gold-based autometallography. 1999; In: Bailey G.W., Jerome W.G, McKernan S, Mansfield J.F, Price RL, eds. Proc. 57th Ann. Mtg., Micros. Soc. Amer.: 486-487.

(230) Danscher G, Norgaard JO. Light microscopic visualization of colloidal gold on resin-embedded tissue. *J Histochem Cytochem* 1983 Dec;31(12):1394-8.

(231) Danscher G. Autometallography. A new technique for light and electron microscopic visualization of metals in biological tissues (gold, silver, metal sulphides and metal selenides). *Histochemistry* 1984;81(4):331-5.

(232) Danscher G, Hacker GW, Grimelius L, and Norgaard JOR. Autometallographic silver amplification of colloidal gold. *J Histotechnol* 1993;16:201-7.

(233) Leahy P, Carmichael GG, Rossomando EF. Novel biotinylated plasmid expression vectors retain biological function and can bind streptavidin. *Bioconjug Chem* 1996 Sep;7(5):545-51.

(234) Tannous BA, Kim DE, Fernandez JL, Weissleder R, Breakefield XO. Codon-optimized Gaussia luciferase cDNA for mammalian gene expression in culture and in vivo. *Mol Ther* 2005 Mar;11(3):435-43.

(235) Griesenbach U, Vicente CC, Roberts MJ, Meng C, Soussi S, Xenariou S, et al. Secreted Gaussia luciferase as a sensitive reporter gene for in vivo and ex vivo studies of airway gene transfer. *Biomaterials* 2011 Apr;32(10):2614-24.

(236) Wurdinger T, Badr C, Pike L, de KR, Weissleder R, Breakefield XO, et al. A secreted luciferase for ex vivo monitoring of in vivo processes. *Nat Methods* 2008 Feb;5(2):171-3.

(237) Badr CE, Hewett JW, Breakefield XO, Tannous BA. A highly sensitive assay for monitoring the secretory pathway and ER stress. *PLoS One* 2007;2(6):e571.

(238) Tannous BA. Gaussia luciferase reporter assay for monitoring biological processes in culture and in vivo. *Nat Protoc* 2009;4(4):582-91.

(239) Chung E, Yamashita H, Au P, Tannous BA, Fukumura D, Jain RK. Secreted Gaussia luciferase as a biomarker for monitoring tumor progression and treatment response of systemic metastases. *PLoS One* 2009;4(12):e8316.

(240) Enjalbert B, Rachini A, Vediyappan G, Pietrella D, Spaccapelo R, Vecchiarelli A, et al. A multifunctional, synthetic Gaussia princeps luciferase reporter for live imaging of Candida albicans infections. *Infect Immun* 2009 Nov;77(11):4847-58.

(241) Lwa TR, Tan CH, Lew QJ, Chu KL, Tan J, Lee YY, et al. Identification of cellular genes critical to recombinant protein production using a Gaussia luciferase-based siRNA screening system. *J Biotechnol* 2010 Apr 15;146(4):160-8.

(242) Nakanishi H, Higuchi Y, Kawakami S, Yamashita F, Hashida M. piggyBac transposon-mediated long-term gene expression in mice. *Mol Ther* 2010 Apr;18(4):707-14.

(243) Abbe E. Bbeitraege zur Theorie des Mikroskops und der mikroskopischen Wahrnehmung. *Arch Mikrosk Anatomie* 1873;9:413-20.

(244) Weber K, Rathke PC, Osborn M. Cytoplasmic microtubular images in glutaraldehyde-fixed tissue culture cells by electron microscopy and by immunofluorescence microscopy. *Proc Natl Acad Sci U S A* 1978 Apr;75(4):1820-4.

(245) Larsen MDB. Strategies to increase gene transfer to the lung 2011.

(246) Ouahabi AE, Thiry M, Schiffmann S, Fuks R, Nguyen-Tran H, Ruysschaert JM, et al. Intracellular visualisation of Brdu-labeled plasmid DNA/cationic liposome complexes. *J Histo & Cytochem* 1999;47(9):1159-66.

(247) Briane D, LLesage D, Cao A, Coudert R, Lievre N, Salzmann JL, et al. Cellular pathway of plasmids vectorized by cholesterol-based cationic liposomes. *J Histo & Cytochem* 2002;50(7):983-91.

(248) Thomas M, Klibanov AM. Conjugation to gold nanoparticles enhances polyethylenimine's transfer of plasmid DNA into mammalian cells. *Proc Natl Acad Sci U S A* 2003 Aug 5;100(16):9138-43.

(249) Li P, Li D, Zhang L, Li G, Wang E. Cationic lipud bilayer coated gold nanoparticles-mediated transfection of mammalian cells. *Biomaterials* 2008;29:3617-24.

(250) Wilson T. Optical sectioning in confocal fluorescence microscopes. *Journal of Microscopy* 1989;154:143-56.

(251) Paddock SW. Principles and practices of laser scanning confocal microscopy. *Mol Biotechnol* 2000 Oct;16(2):127-49.

(252) Ichihara A, Tanaami T, Isozaki K, Sugiyama Y, Kosugi Y, Mikuriya K, et al. High-speed confocal fluorescence microscopy using a Nipkow scanner with microlenses-for 3-D imaging of fluorescent molecules in real time. *Bioimages* 1996;4:57-62.

(253) Graf R, Rietdorf J, Zimmermann T. Live cell spinning disk microscopy. *Adv Biochem Eng Biotechnol* 2005;95:57-75.

(254) Tsien RY. The green fluorescent protein. *Annu Rev Biochem* 1998;67:509-44.

(255) Griffin BA, Adams SR, Tsien RY. Specific covalent labeling of recombinant protein molecules inside live cells. *Science* 1998 Jul 10;281(5374):269-72.

(256) Martin BR, Giepmans BN, Adams SR, Tsien RY. Mammalian cell-based optimization of the biarsenical-binding tetracysteine motif for improved fluorescence and affinity. *Nat Biotechnol* 2005 Oct;23(10):1308-14.

(257) Forster AC, McInnes JL, Skingle DC, Symons RH. Non-radioactive hybridization probes prepared by the chemical labelling of DNA and RNA with a novel reagent, photobiotin. *Nucleic Acids Res* 1985 Feb 11;13(3):745-61.

(258) Geselowitz DA, Neumann RD. Quantitation of triple-helix formation using a photo-cross-linkable aryl azide/biotin/oligonucleotide conjugate. *Bioconjug Chem* 1995 Jul;6(4):502-6.

(259) Waring MJ. Complex formation between ethidium bromide and nucleic acids. *J Mol Biol* 1965 Aug;13(1):269-82.

(260) Arndt-Jovin DJ, Jovin TM. Fluorescence labeling and microscopy of DNA. *Methods Cell Biol* 1989;30:417-48.

(261) Loewe H, Urbanietz J. [Basic-substituted 2,6-bisbenzimidazole derivates, a novel class of substances with chemotherapeutic activity]. *Arzneimittelforschung* 1974 Dec;24(12):1927-33.

(262) Arndt-Jovin DJ, Jovin TM. Analysis and sorting of living cells according to deoxyribonucleic acid content. *J Histochem Cytochem* 1977 Jul;25(7):585-9.

(263) Durand RE, Olive PL. Cytotoxicity, Mutagenicity and DNA damage by Hoechst 33342. *J Histochem Cytochem* 1982 Feb;30(2):111-6.

(264) Kubista M, Akerman B, Norden B. Characterization of interaction between DNA and 4',6-diamidino-2-phenylindole by optical spectroscopy. *Biochemistry* 1987 Jul 14;26(14):4545-53.

(265) Johnson I. Fluorescent probes for living cells. *Histochem J* 1998 Mar;30(3):123-40.

(266) Mujumdar RB, Ernst LA, Mujumdar SR, Lewis CJ, Waggoner AS. Cyanine dye labeling reagents: sulfoindocyanine succinimidyl esters. *Bioconjug Chem* 1993 Mar;4(2):105-11.

(267) Ballou B, Fisher GW, Waggoner AS, Farkas DL, Reiland JM, Jaffe R, et al. Tumor labeling in vivo using cyanine-conjugated monoclonal antibodies. *Cancer Immunol Immunother* 1995 Oct;41(4):257-63.

(268) Sirinivasan C, Siddiqui S, Silbart LK, Papadimitrakoapoulos F, burgess DJ. Dual fluorescent labelling method to visualize plasmid DNA degradation. *Bioconjug Chem* 2009;20(1):163-9.

(269) Sirinivasan C, Lee J., Papadimitrakoapoulos F, Silbart LK, Zhao M, burgess DJ. Labeling and intracellular tracking of functionally active plasmid DNA with semiconductor quantum dots. *Molecular therapy* 2006;14(2):192-201.

(270) Song L, Hennink EJ, Young IT, Tanke HJ. Photobleaching kinetics of fluorescein in quantitative fluorescence microscopy. *Biophys J* 1995 Jun;68(6):2588-600.

(271) Berrios M, Conlon KA, Colflesh DE. Antifading agents for confocal fluorescence microscopy. *Methods Enzymol* 1999;307:55-79.

(272) Song L, Varma CA, Verhoeven JW, Tanke HJ. Influence of the triplet excited state on the photobleaching kinetics of fluorescein in microscopy. *Biophys J* 1996 Jun;70(6):2959-68.

(273) Bunting JR. A test of the singlet oxygen mechanism of cationic dye photosensitization of mitochondrial damage. *Photochem Photobiol* 1992 Jan;55(1):81-7.

(274) Byers GW, Gross S, Henrichs PM. Direct and sensitized photooxidation of cyanine dyes. *Photochem Photobiol* 1976 Jan;23(1):37-43.

(275) Chan CWC. Luminescent quantum dots for multiplexed bilological detection and imaging. *Curr Opin Biotechnol* 2002;13:40-6.

(276) Jaiswal JK, Mattoussi H, Mauro JM, Simon SM. Long-term multiple color imaging of live cells using quantum dot bioconjugates. *Nat Biotechnol* 2003 Jan;21(1):47-51.

(277) Larson DR, Zipfel WR, Williams RM, Clark SW, Bruchez MP, Wise FW, et al. Water-soluble quantum dots for multiphoton fluorescence imaging in vivo. *Science* 2003 May 30;300(5624):1434-6.

(278) Watson A, Wu X, Bruchez M. Lighting up cells with quantum dots. *Biotechniques* 2003 Feb;34(2):296-300.

(279) Michalet X, Pinaud FF, Bentolila LA, Tsay JM, Doose S, Li JJ, et al. Quantum dots for live cells, in vivo imaging, and diagnostics. *Science* 2005 Jan 28;307(5709):538-44.

(280) Gao X, Yang L, Petros JA, Marshall FF, Simons JW, Nie S. In vivo molecular and cellular imaging with quantum dots. *Curr Opin Biotechnol* 2005 Feb;16(1):63-72.

(281) Resch-Genger U, Grabolle M, Cavaliere-Jaricot S, Nitschke R, Nann T. Quantum dots versus organic dyes as fluorescent labels. *Nat Methods* 2008 Sep;5(9):763-75.

(282) Lacoste TD, Michalet X, Pinaud F, Chemla DS, Alivisatos AP, Weiss S. Ultrahigh-resolution multicolor colocalization of single fluorescent probes. *Proc Natl Acad Sci U S A* 2000 Aug 15;97(17):9461-6.

(283) Invitrogen, Molecular Probes Handbook. 1989.

(284) Sambrook J, Fritsch EF, Manniatis T. Molecular Cloning. A Laboratory Manual. 1989; Second.

(285) Straub M, Hell SW. Multifocal multiphoton microscopy: a fast and efficient tool for 3-D fluorescence imaging. *Bioimaging* 1998;6:177-85.

(286) Chi KR. Super-resolution micrscopy: breaking the limits. *Nature Methods 6* 2009;15-8.

(287) Thomann D, Rines DR, Sorger PK, Danuser G. Automatic fluorescent tag detection in 3D with super-resolution: application to the analysis of chromosome movement. *J Microsc* 2002 Oct;208(Pt 1):49-64.

(288) Johnson LG, Olsen JC, Sarkadi B, Moore KL, Swanstrom R, Boucher RC. Efficiency of gene transfer for restoration of normal airway epithelial function in cystic fibrosis. *Nature genetics* 1992 Sept;(2):21-25.

(289) Farmen SL, Karp PH, Ng P, Palmer DJ, Koehler DR, Hu J, Beaudet AL, Zabner J, Welsh MJ. Gene transfer of CFTR to airway epithelia: low levels of expression are sufficient to correct Cl transport and overexpression can generate basolateral CFTR. *Am J Physiol Lung Cell Mol Physiol* 2005 August;289:L1123-L1130.

(290) Dannhoffer L, Blouquit-Laye S, Regnier A, Chinet T. Functional properties of mixed cystic fibrosis and normal bronchial epithelial cell cultures. *Am J Respir Cell Mol Biol* 2009 Jun;40(6):717-723.